

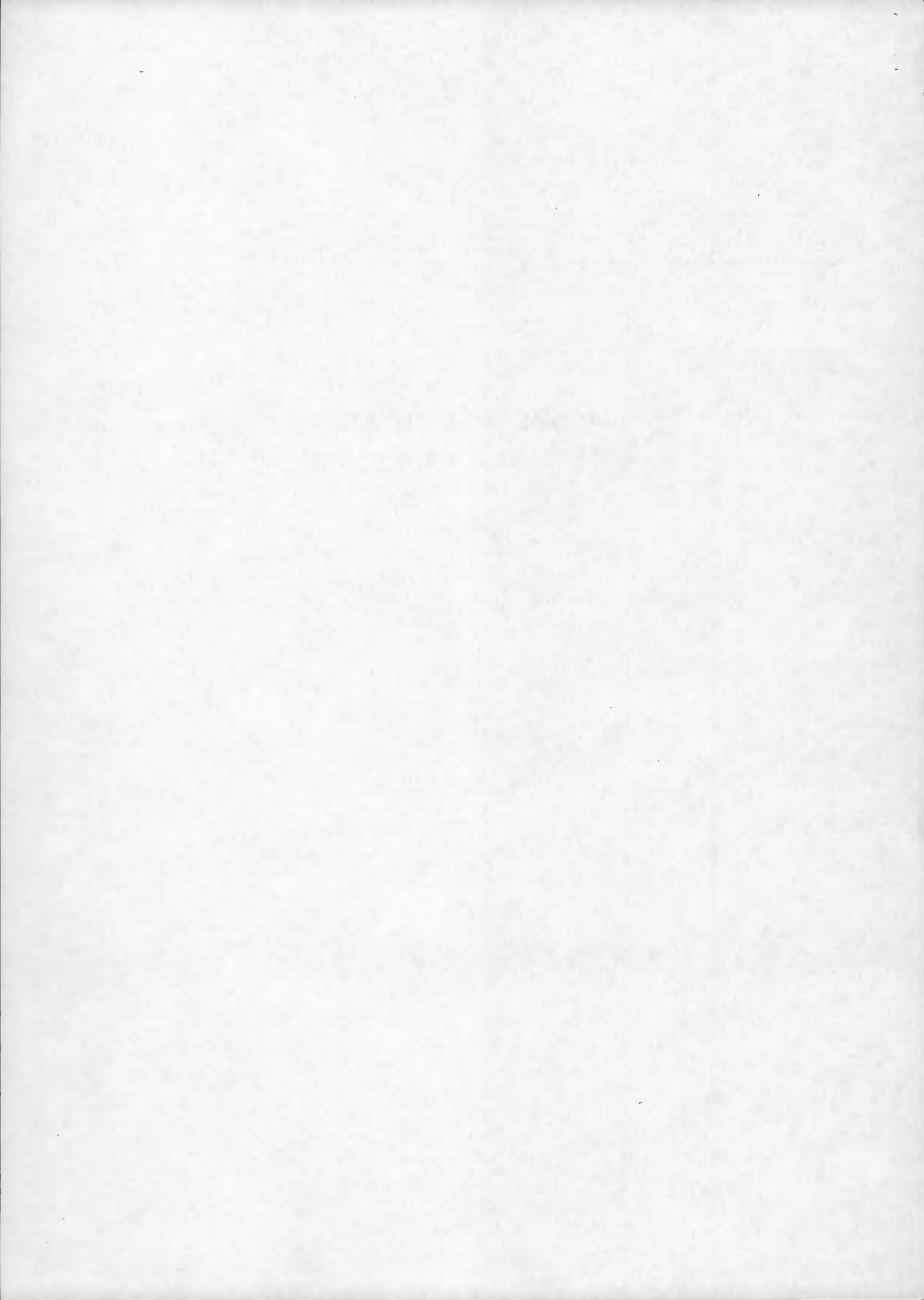
**THE ATSR INSTRUMENT**

*Various Extracts  
From  
The First And Second ERS Symposia*



**SPECIAL SESSION: ATSR/M**

**Chairman: D. Llewellyn-Jones**



## **ATSR**

The ATSR primary objective is to provide measurements of global sea surface temperature with the level of accuracy required for climate research i.e. better than 0.5 degrees.

This level of accuracy has been today demonstrated (even if the work will continue; particularly to optimize the performance of the radiative transfer models in the tropics) by a number of validation campaigns as well as global analysis, for a spatial resolution of 50 km and considerable cloud cover conditions. Of course, 1 km pixel products are also available. The good results have been shown to actually depend on the dual view (nadir plus forward), an essential feature of the instrument to better correct for the intervening atmosphere.

From 15.09.91 up to 27.05.92, the ATSR 3.7 micron channel has produced data of very good quality, then it suddenly failed. The 3.7 micron channel was used ( in terms of the main mission) only to improve the derivation of the sea surface temperature during the night scans. Therefore, ATSR global mission objectives are still being maintained with the 10, 11 microns channels. The analysis is still under way but there are good reasons to believe that the impact on the mission will not be important.

## **The Microwave Sounder**

The microwave sounder was designed to correct the altimeter path for the effect of water vapour content in the atmosphere.

The brightness temperatures of the two microwave channels are combined

together with the altimeter derived wind to provide this correction. Also, the cloud liquid water content is retrieved. In flight calibration and data validation were performed. The system requires continuous monitoring so as to detect possible instabilities.

The water vapour retrieval has been validated and it is operationally used at the F-PAF for the generation of the altimeter level 2 data. The liquid water retrieval is still under study and the work is not completed. Actually, only the water vapour correction is essential for the altimetric missions.

G. Paci  
06.11.92



## VALIDATION OF THE ATSR/M MICROWAVE RADIOMETER DATA

Laurence Eymard, Luc Tabary and Alain Le Cornec

Centre de Recherche en Physique de l'Environnement  
Centre Universitaire, 10-12 avenue de l'Europe  
78140 Vélizy, France

## ABSTRACT

The ERS-1 microwave radiometer has been designed to correct the altimeter tropospheric path for the delay due to humidity. The data quality assessment has consisted of verifying the instrument calibration, then of comparing the retrieved geophysical products with available observations. The in-flight calibration includes control of gain stability and long term survey of internal and brightness temperature variations, as well as footprint location verification. No anomaly has been detected after one year. Data validation is performed by comparing routine radiosonde measurements with the retrieved water vapours and altimeter path corrections. There is no routine measurement of cloud water content, so this retrieval cannot be simply tested. The water vapour content and altimeter tropospheric path correction retrievals have been validated, and are operationally used at the French PAF.

## 1. INTRODUCTION

The microwave radiometer aboard ERS-1 has been designed for the determination of the altimeter path delay due to tropospheric humidity. It is a two channel radiometer, nadir viewing (fig.1). The two frequencies, 23.8 and 36.5 GHz, have been selected to allow the retrieval of the columnar water vapour content (or the altimeter path correction), with a good sensitivity to cloud liquid water content.

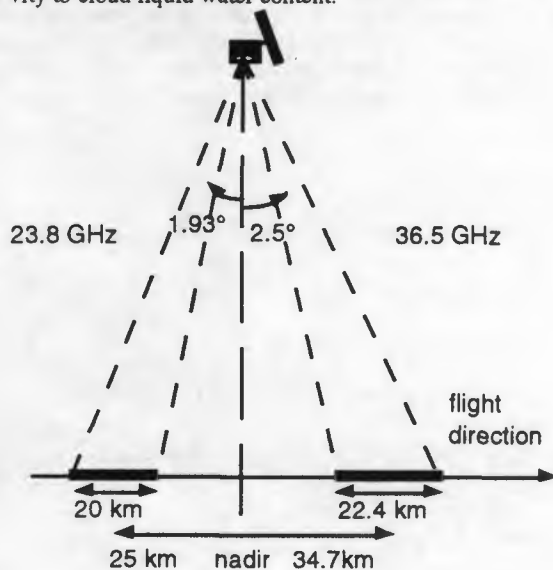


Fig.1 : geometry of the two channel field of view. The diameter of the footprints is indicated (3 dB level).

Since launch, the radiometer has worked nominally, but the absolute calibration can hardly be verified in flight. The in flight calibration procedure consists of switching the instrument to either a sky horn (cold reference) or a hot internal load at ambient temperature. It cannot account for calibration errors in the main antenna circuit, and particularly to those due to the horns and the reflector.

After computing the brightness temperatures, the geophysical parameters are retrieved, using algorithms developed before

launch (Refs. 1, 2) : a radiative transfer model (including surface emissivity effects) was applied to a large number of meteorological profiles, then the algorithm coefficients (assuming a log-linear function of the brightness temperatures) were determined using a linear regression method. The surface wind effect was included as a correcting term (linear function of the wind) in the algorithms. Validation of the retrieved values is achieved by comparison with in-situ measurements. Thus water vapour and altimeter correction values can easily be validated using radiosounding measurements from ships or small islands, but there is no routine measurement of the cloud liquid water content.

Such a comparison is the only method to assess the radiometer data quality. However, if a deviation is found, it is difficult to distinguish between radiometer errors and model / algorithm errors. In this paper, we present results of the calibration and validation tests we have performed since launch.

## 2. IN-FLIGHT CALIBRATION RESULTS

To obtain the brightness temperatures, the radiometer equation was established. The transmission and loss coefficients of each element are taken into account, as well as the antenna and sky horn side lobe contributions. A complete description of the radiometer model is given in Bernard et al (Ref. 3).

Each radiometric count (from the main antenna, hot load and sky horn) is related to the instrument gain  $G$ , the antenna (or load, respectively) temperature and the reference load temperature to which it is compared. Because the instrument is not perfectly isothermal, due to temperature exchanges with the exterior, the internal temperature gradients must be taken into account, as well as transmission and loss factors of each microwave element (wave-guides, circulators). The gain is deduced from the difference between the sky horn and hot load counts. Its value is used to compute the antenna temperature.

## 2.1 On-ground calibration.

The determination of the radiometer model coefficients was the purpose of the ground calibration (Ref. 3) which was realized in three steps : a measurement of the transmission and loss coefficients of the microwave elements was made in the laboratory, before the instrument was assembled; thermal vacuum (T/V) calibration; antenna modelling and calibration. From the results of the ground calibration and radiometer modelling, the radiometric error budget was deduced, assuming all errors sources are uncorrelated. The error budget contributions result in a RMS error of about 3 K.

## 2.2 In-flight calibration tests

The first tests, undertaken during the first four months after launch, concerned the internal behaviour, antenna field of view characterization, and the brightness temperature stability.

2.2.1 Internal behaviour. Two main series of tests were performed to verify the radiometer behaviour. A first series concerns the radiometer gain, and the internal sources of errors affecting the antenna temperature. The second series

concerns the antenna field-of-view, including the side lobe contributions and antenna mis-pointing.

We compared data from the same series of orbits from month to month. The mean stability with time of all parameters could be verified, as well as the orbital variation (fig. 2). This analysis, was undertaken during the first 4 months in orbit. It has been continued since this date, giving the following results :

- gain stability : after correction of orbital temperature variations and smoothing within 12 calibration scans, the gain variation is less than 4‰ of its mean value (for the two channels), as shown in fig. 3;
- radiometer model coefficients : the coefficient set produced after ground calibration has been updated, by accounting for the reduced temperature range of orbital variations (16 K).

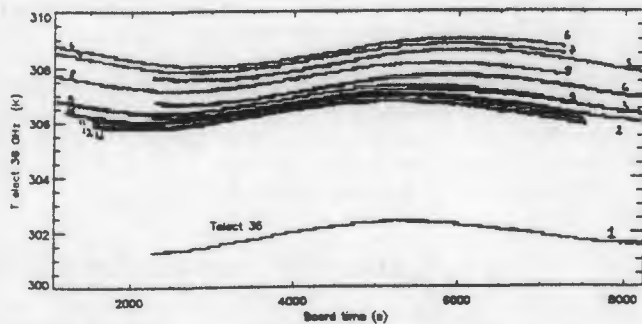


Fig. 2 : internal temperature variations (36.5 GHz channel) from month to month, between August, 1991 and August, 1992. The same orbits are used within each phase.

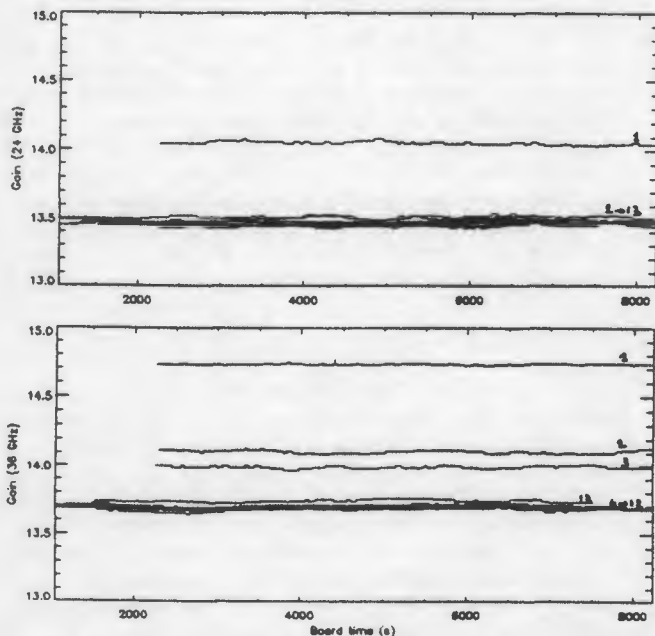


Fig. 3 : gain variations from month to month (same orbits as in fig. 2). The gain temperature dependence is filtered out using a polynomial function established before launch.

As the radiometer is nadir-viewing to permit the correction of the altimeter path delay, it is important to detect any mispointing with respect to the satellite attitude, which would degrade the measurement quality. Beyond this pointing aspect, the contribution of the surrounding elements to the brightness temperature has to be estimated to eliminate measurements contaminated by lands before retrieving geophysical parameters over oceans.

- Antenna pointing : the two channel field-of-view locations were examined with respect to the satellite ground-track to detect any mispointing effect. Coastal transitions were used as they correspond to strong radiometric count contrasts (about 100 K variations). The mispointing has been estimated to be less than 0.2° and 0.5° between the two channels (respectively along-track and across-track).

- Main antenna sidelobes : using again antenna measurements over coastal transitions, the side lobe contribution was examined, and successfully compared to prelaunch simulations, using antenna pattern measurements. The maximum contamination distance of such a transition was found to be negligible when the field of view is centered 30 km off the coast.

2.2.2 Brightness temperature stability. Over sea ice and Antarctic glaciers, the brightness temperature is rather different, respectively ranging between 190 and 250 K, and between 130 and 200 K : over sea ice, it depends on the ice concentration, and on the surface ice age, among other parameters. On the contrary, the Antarctic plateau is known for its very stable surface properties (Ref. 4), and the atmospheric contribution is negligible (very low water vapour content). Thus the brightness temperatures are simply related to the surface temperature and the surface emissivity. The gradient ratio, given by :

$$GR = (Tb1 - Tb2) / (Tb1 + Tb2)$$

where Tb1 and Tb2 are respectively the brightness temperatures at 23.8 GHz and 36.5 GHz, is a function of emissivity, the surface temperature being eliminated. In figure 4, the brightness temperatures and the gradient ratio are plotted as a function of time for four orbits in the area of the Wilkes land, (115 - 130°E, 67 - 70°S). The brightness temperatures present a very weak variation with time, essentially due to the seasonal surface temperature variation, and the gradient ratio is nearly constant. This parameter is therefore a good indicator of the instrument stability with time, very simple to compute to survey the radiometer evolution during its life.

Wilkes Land traverse

orbite	latitude	longitude	TB1min	TB1max	TB2min	TB2max	GRmin	GRmax
3	-67.6	115.6	211.7	221.3	219.7	234.6	17.5	29
17	-67.6	123.9	200	208.3	209	220.2	22	31.9
26	-69.4	119.7	205.3	210.6	213.3	220.9	14.6	23.6
40	-69.4	122.1	207.2	215	212.3	225.9	11.9	24.2

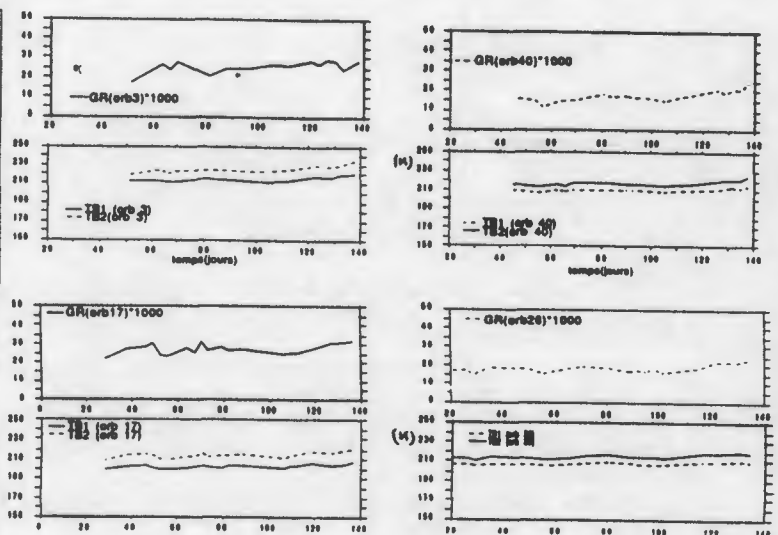


Fig. 4 : brightness temperatures and gradient ratio plotted as a function of time for four orbits overpassing the Wilkes land (Antarctic continent).

### 3. VALIDATION OF THE GEOPHYSICAL PRODUCTS

#### 3.1 Retrieval method

A radiative transfer model has been developed, including an atmospheric radiative transfer model (Ref. 5) and the sea surface emissivity contribution (Refs. 6, 7, 8). It provides the brightness temperature at frequencies lower than 40 GHz. Its complete description can be found in Lojou et al (Ref. 1).

A data set has been created, containing the integrated water vapour, liquid water contents and altimeter path correction, the surface temperature and wind, and the brightness temperatures. The source of the meteorological data were analyses of the European Centre for Medium range Weather Forecasting (ECMWF) meteorological model within 5 months (Ref. 1). As meteorological profiles do not contain informations about cloud liquid water, we used a simple random generation of liquid water at saturation levels

Relationships between the precipitable water  $W$ , the cloud liquid water content  $L$ , the altimeter tropospheric correction  $dh$  and a combination of brightness temperatures  $T_{bi}$  and surface wind  $U$  (as it can be deduced from the altimeter received power) were then obtained from multilinear regression analysis, using the following form :

$$L = \sum a_i \text{Log}(T_{oi} - T_{bi}) + a_0 + b U$$

$T_{oi}$  is a reference atmospheric temperature for the frequency considered, and  $a_0$ ,  $a_i$  and  $b$  are constant coefficients (see in Ref. 2 for more details).

#### 3.2 Validation of the retrieved water vapour and altimeter correction

The water vapour validation is achieved by statistically comparing the retrieved value from the two brightness temperatures with integrated contents from radiosounding data over oceans. The difficulty of this validation lies in the selection of a sufficient number of colocated (in the range  $\pm 200$  km) and synchronized data (within the interval  $\pm 3$  hours) : shipborne radiosoundings are sparse, and the ATSR/M microwave radiometer data are along track only.

However we have undertaken this validation by extracting a first set of about 700 coincident radiosounding data from ECMWF archives for the months of August, 1991 to March, 1992, over the global oceans. The comparison showed a rather good agreement between local measurements and retrieved values, but mean bias of  $0.18 \text{ g/cm}^2$  was found, due to an underestimate at very low water vapour values.

This deviation is probably due to a radiometer calibration problem. By comparing brightness temperatures with direct simulations at coincident locations, we found similar deviations at low values, larger on the 36.5 GHz channel than on the 23.8 GHz channel. We interpret this error as due to a change in a transmission factor after launch. By modifying it in the radiometer model, we correct the 36.5 GHz brightness temperature, and the retrieved water vapour: the scatter plot in fig. 5 shows that the mean bias has been completely suppressed, the RMS error is  $0.5 \text{ g/cm}^2$ . At high water vapour values, the retrieved water vapour appears overestimated. This deviation is caused by an algorithm problem, particularly when the large water vapour content is associated with clouds and rain (mainly at tropical latitudes).

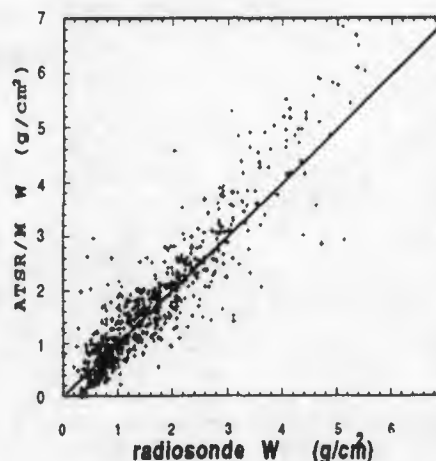


Fig. 5: comparison of retrieved water vapour contents ( $W$ ), in ordinate, with radiosonde data (abscissa) over oceans.

A similar result is obtained for the altimeter correction, presented in fig. 7 : RMS error 3 cm, same slope and no bias.

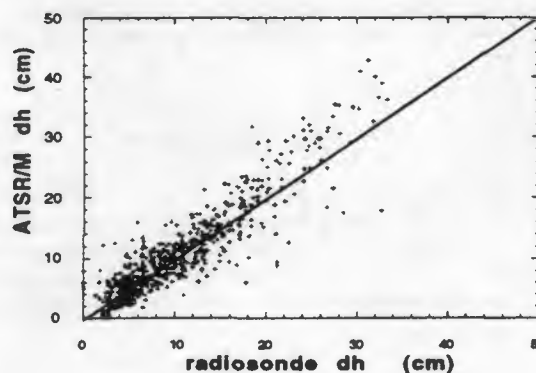


Fig. 6: comparison of retrieved altimeter correction  $dh$ , in ordinate, with radiosonde data (abscissa) over oceans.

#### 3.3 Cloud liquid water content

As explained in section 3.1, the algorithm was developed using a simulation of the cloud liquid water. There is no routine measurement of this parameter, which can only be obtained using aircraft measurements in clouds. Such data are very sparse over the globe, and their representativity is not assessed. Thus all liquid water retrieval algorithms (Refs. 6, 7, among others) are based on a small data set and/or assumptions on the distribution of cloud properties. Similar studies using the optical properties of cloud top (visible and IR radiances measured by meteorological satellites) present the same limitations. Lojou et al (Ref. 8) compared SMMR and GOES retrievals of cloud liquid water contents, and concluded to a rather good qualitative agreement, but found a large mean deviation between retrieved values.

To test our retrieval of liquid water content, we had no in-situ measurement. However, we performed some tests to evaluate the reliability of this retrieval. The main test consisted of applying the algorithm to clear air pixels. Their location was

determined using the cloud clearing procedure on the ATSR/IR data, developed by RAL.

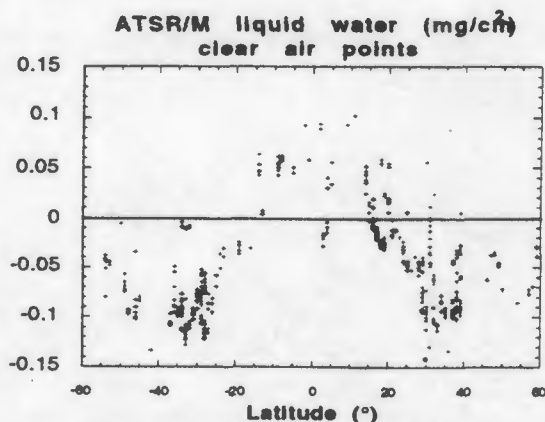


Fig. 7 : Computed liquid water content as function of latitude for clear air places (selected using the ATSR/IR data).

The figure 8 presents the retrieved cloud liquid water as a function of latitude over oceans, for cloud free locations (one 3-day cycle in November), showing negative values at temperate latitudes, and positive values in tropical regions. Analyzing this result leads to the conclusion that the present algorithm is too sensitive to water vapour (tropics) and to the surface wind (occurring at high latitudes). A more complete study will be necessary to establish a better algorithm, at least qualitatively. A large set of in-situ measurements would be necessary to improve the quantitative retrieval of this parameter.

#### 4. CONCLUSION

After one year, the microwave radiometer on board ERS-1 has still a nominal behaviour. Among other parameters, the thermal stability has been verified and the antenna pointing is normal. The survey of brightness temperatures is continuing over particular areas, characterized by stable surface properties.

Validation of retrieved geophysical parameters (water vapour, altimeter correction and cloud liquid water content) has been undertaken. The latter parameter cannot be correctly retrieved using the present algorithm, and a particular study is necessary. Water vapour and altimeter correction retrieval has been validated, using comparisons with about 700 radiosonde data at coincident locations. They result in no bias, nearly no tilt and a RMS error  $0.5 \text{ g/cm}^2$ . This comparison will be continued with other radiosonde data to get statistically representative results.

#### References :

1. Lojou, J.Y. & al 1992, A simple method for testing brightness temperatures from satellite microwave radiometers. Submitted to *J. Atmos. Oceanic Tech.*
2. Eymard, L. & al 1992 The ERS-1 microwave radiometer. To be published in *Intern. J. Remote Sensing*.
3. Bernard, R. & al 1992 The microwave radiometer aboard ERS-1 : Characteristics and Performances. Accepted for publication in *IEEE Trans. Geosci. Remote Sensing*.
4. Fily, M. and J.P. Benoist 1991 Large scale study of the microwave signature of the Antarctic ice sheet. *Proc Physical Measurements and signatures in Remote Sensing*, Courchevel, 14 - 18 Jan. 1991, ESA SP-319, 347 - 350.
5. Ulaby, F.T. & al 1981 Microwave Rensing. Vol. 1: Fundamentals and radiometry. Artec house Inc. 456 pp.
6. Wilheit T.T. and A.T.C. Chang 1980 An algorithm for retrieval of ocean surface and atmospheric parameters from the observations of the Scanning Multichannel Microwave Radiometer. *Radio Science*, 15, 3, 525 - 544.
7. Wentz, F.J. 1988 User's manual. SSM/I ocean product tapes. *RSS technical report 033088*.
8. Lojou J.Y. & al 1991 Comparison of Nimbus-7 SMMR and GOES-1 VISSR atmospheric liquid water content. *J. Appl. Meteor.*, 30, 2, 187 - 198.

MULTICHANNEL DUAL ANGLE APPROACH FOR SEA SURFACE  
TEMPERATURE RETRIEVAL - IN CONTEXT OF ERS-1 SCENARIO

Aloke K. Mathur and V.K. Agarwal

Meteorology and Oceanography Division  
Space Applications Centre (ISRO)  
Ahmedabad 380 053 INDIA

ABSTRACT

Observations from Along Track Scanning Radiometer (ATSR) and Microwave Sounder (MWS) onboard the first European Remote Sensing Satellite (ERS-1) enable retrieval of Sea Surface Temperature (SST) within an accuracy of 0.3 K because dual angle capability by ATSR accompanied by total water vapour content (WVC) retrieved by MWS is expected to reduce the existing ambiguities due to atmospheric stratifications especially in tropics. This paper describes an algorithm to retrieve SST based on the simulated ATSR data over Indian Ocean with the help of radiative transfer models.

Keywords: Sea Surface Temperature, Water vapor effect, dual angle, ATSR.

1. INTRODUCTION

Satellite IR observations are well known to be affected by the intervening atmospheric CO<sub>2</sub>, water vapor and Ozone. For atmospheric window region the absorption by water vapor dominates over other absorbers. McClain et al (Ref. 8) suggested a Multichannel retrieval scheme to remove this water vapor affect. The proposed algorithm did retrieve SST within an accuracy of 0.5 K in the region of low atmospheric water vapor content, but could not do so in the tropics where water vapor content exceeds 35 mm (Ref. 2). It was found (Ref. 1) that radiance in this spectral region is significantly dependent upon the distribution (rather than the total water vapor content) of water vapor and possibly vertical profile of temperature in the lower levels of the troposphere. Since then a number of alternative methods have been developed to account for the water vapor by combining AVHRR and TOVS observations and thereby making use of the simultaneous measurement of actual water vapor content (Ref. 2 & 11). But these schemes' error increases with a slight error in collocating the two sensors' observations. Recently, following the theoretical basis by McMillin (Ref. 9),

Dudhia (Ref. 6) showed the feasibility of removing the water vapor effect by taking the observations made by two different satellites viz. NOAA and METEOSAT at two different angles. But this again could not be operationalised because of paucity of simultaneous coverage of NOAA and METEOSAT over a region. With the launch of the first ERS-1 satellite which carries onboard ATSR and MWS, SST retrieval problem has got a new dimension for removing the atmospheric effect.

The first European Remote Sensing Satellite (ERS-1) carries onboard the instruments called ATSR and MWS specifically designed for retrieving SST within the accuracy of 0.5K even in the 80% of cloudiness. These sensors share the satellite platform alongwith other payloads like wind scatterometer, radar altimeter and Synthetic Aperture Radar (SAR). ATSR senses the earth under a nadir angle of 55° in forward scan and near vertically downwards in the nadir scan. So the scan line of this conical scanner is the intersection of the earth's surface making an ellipse at the ground. Although ATSR contains all the channels which AVHRR onboard NOAA satellite has, still there are many new hardware features alongwith the dual angle viewing capability in ATSR that are expected to provide more accurate SST measurements than is currently available from satellite data. These features include improved onboard calibration, more efficient cooling of detectors and 12 bit resolution data transmission. ATSR design characteristics are described in detail by Delderfield et al (Ref. 5). As suggested in several studies (Refs. 2-4) the estimation of total WVC in the atmospheric column is strongly needed for atmospheric correction in SST retrieval. MWS measures WVC in its two absorbing bands of 23.8 GHz and 36.5 GHz with a resolution of 20 km. Making use of dual angle scanning by ATSR and WVC by MWS we have attempted to suggest an algorithm to retrieve SST with better accuracy in section 3. Section 2 deals with the details of the atmospheric profiles used for ATSR data simulation representing the Indian Tropical conditions. Error estimate, advantages and disadvantages of such retrieval are discussed in section 4.

2. DATA USED FOR ATSR SIMULATION

The tropical temperature and humidity fluctuate very widely, so in any kind of simulation for tropical atmospheres one has to incorporate these extremes. We also have simulated the observations of ATSR IR channels using LOWTRAN software package (Ref. 7) keeping in view the seasonal variations of these parameters. The surface temperature was subjected to vary from 295 K to 306 K alongwith the near surface relative humidity of 60% to 95%. A distinctive feature of Indian Ocean is the Inversion phenomenon i.e. increase in temperature in the lower troposphere. So it was also introduced in the profiles of temperature by putting an artificial negative lapse rate just above the ocean surface. The whole data set was divided into two groups, one being "Normal" profiles (hereafter called 'N' type) and the other being "Inversion" ( hereafter called 'I' type) profiles.

3.0 ATMOSPHERIC CORRECTION FROM MULTIPLE ABSORPTION OBSERVATIONS:

From the simulation work of McMillin (Ref. 9), it was shown that to remove water vapor effect in retrieving SST from satellite observations, one should either have dual wavelength observations or dual angle observations in the window region. The obvious reason being that the differential absorption due to different wavelength or different optical pathlengths can be approximated as proportional to the intervening water vapor content. In radiative transfer terms, we can write the upwelling radiance in the simplest form as

$$I(v) = B(v, T_s) \tau(v, p_0, \theta) + B_a(v) [1 - \tau(v, p_0, \theta)] \dots\dots(1)$$

where I is the radiance reaching at the satellite sensor, v is the wavenumber, T is the atmospheric temperature at pressure p, T<sub>s</sub> is the surface temperature, p<sub>0</sub> is the surface pressure, τ is the transmittance, θ is the zenith angle and B is the Planck function. B<sub>a</sub> is the mean radiance of the atmosphere for the given τ and θ. It is clear from equation (1) that SST estimate (i.e. B(v, T<sub>s</sub>)) involves elimination of terms, B<sub>a</sub>(v).

3.1 Dual frequency

If measurements at different wavelengths are used, the dependence of B and I on wavelength must be determined. This is needed because in multiwavelengths mode, elimination of B<sub>a</sub> and estimate for B(v, T<sub>s</sub>) is possible only when the atmospheric term B<sub>a</sub> is approximately same for the two wavelengths. Then we can expand Planck function about the reference frequency as

$$B(v_r, T) = B(v, T) + [\delta B(v, T) / \delta v] [v_r - v] \dots\dots\dots(2)$$

similarly we can expand the radiance in terms of expected radiance of a reference frequency v<sub>r</sub>, as

$$I(v_r) = I(v) + [\delta I(v, T) / \delta v] [v_r - v] \dots\dots\dots(3)$$

where T is the equivalent blackbody temperature determined by the value of B(v, T) by setting it equal to I(v). In the atmospheric window region, δB(v, T)/δv is very weakly dependent on the temperature. So if values of v and v<sub>r</sub> are sufficiently close, it is possible to neglect the dependence of δB(v, T)/δv on temperature and then Eq.(2) can be written for two channels as

$$I_1(v_r) = B(v_r, T_s) \tau(v_1, p_0, \theta) + B_a(v_r) [1 - \tau(v_1, p_0, \theta)] \dots\dots\dots(4)$$

$$I_2(v_r) = B(v_r, T_s) \tau(v_2, p_0, \theta) + B_a(v_r) [1 - \tau(v_2, p_0, \theta)] \dots\dots\dots(5)$$

As suggested by McMillin (Ref. 9) if values of B<sub>a</sub> are nearly same for two different values of τ(v<sub>i</sub>, p<sub>0</sub>, θ), then differences in I<sub>i</sub>(v<sub>r</sub>) can be related to the differences in τ. Through simulations it was found that for a typical atmosphere, values of B<sub>a</sub>(v<sub>r</sub>) at 10.8 μm and 11.5 μm are 294.25 and 294.14 respectively. If values of B<sub>a</sub>(v<sub>r</sub>) are assumed to be equal for two different wavelengths, equation (4) and (5) can be solved for B<sub>s</sub> to give

$$B(v_r, T_s) = \frac{I_1(v_r) + [I_1(v_r) - I_2(v_r)] \cdot [1 - \tau(v_1, p_0, \theta)]}{[\tau(v_1, p_0, \theta) - \tau(v_2, p_0, \theta)]} \dots\dots\dots(6)$$

which can be simplified as

$$B(v_r, T_s) = I_1(v_r) + G [I_1(v_r) - I_2(v_r)] \dots\dots\dots(7)$$

where

$$G = \frac{[1 - \tau(v_1, p_0, \theta)]}{[\tau(v_1, p_0, \theta) - \tau(v_2, p_0, \theta)]} \dots\dots\dots(8)$$

In order to assess characteristics of expression (9), we used the simulated data (as described in section 2.0) of 'N' and 'I' types of the atmospheres separately as well as a composite of the two. If we plot G function and water vapor content for 'N' and 'I' type of atmospheres, we can see from figures(1 & 2) that in both the cases G decreases with WVC for lower WVC i.e. <15 mm and then increases for higher WVC (>30 mm), thus functional form of G can be determined with respect to WVC. But in region where WVC is between 15 and 30 mm, G can not be represented by a particular function in terms of WVC and so the usual relationship between G and WVC breaks down in this region. It is imperative to say that split channel observations alone are inadequate to retrieve SST in all the water vapor conditions.

3.2 Dual angle

For the case when the observations are made in optically related view angles rather than at different wavelengths, selection of a reference frequency is not required and G is given by

$$G = \frac{[1 - \tau(v, p_0, \theta_1)] / [\tau(v, p_0, \theta_1) - \tau(v, p_0, \theta_2)]}{\dots\dots\dots(9)}$$

Again through simulations, values of G were calculated by solving equation (8) for different atmospheres. The plot (figure

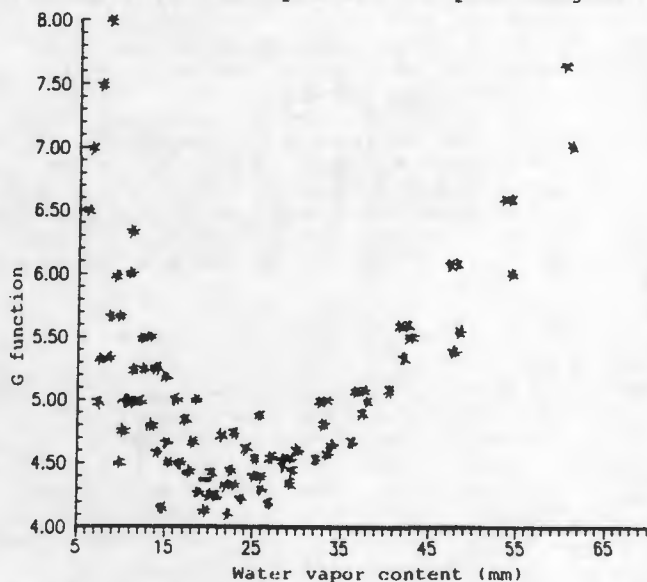


Figure 1. Scatter plot of G function and WVC for 'N' type of atmospheres (Dual frequency case).

$$B(v, T_s) = I_1(v) + G[I_1(v) - I_2(v)] \dots\dots\dots(10)$$

Seeing the figures(4 & 5) for dual angle cases, it is clear that a simple function can be established between G function and

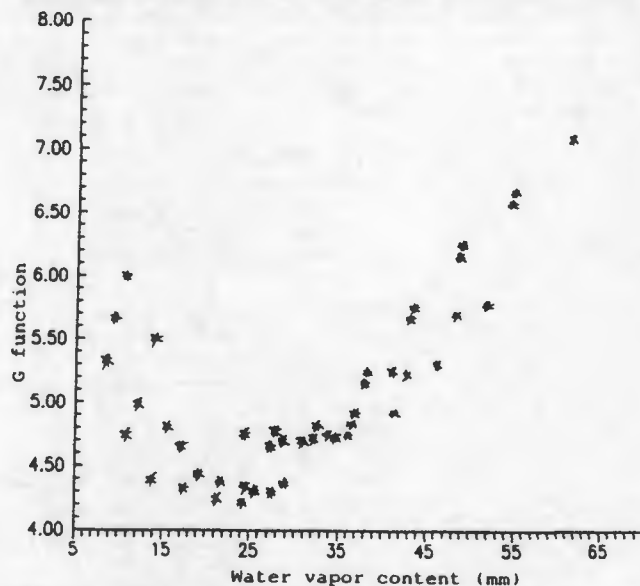


Figure 2. Same as figure 1 but for 'I' type of atmospheres.

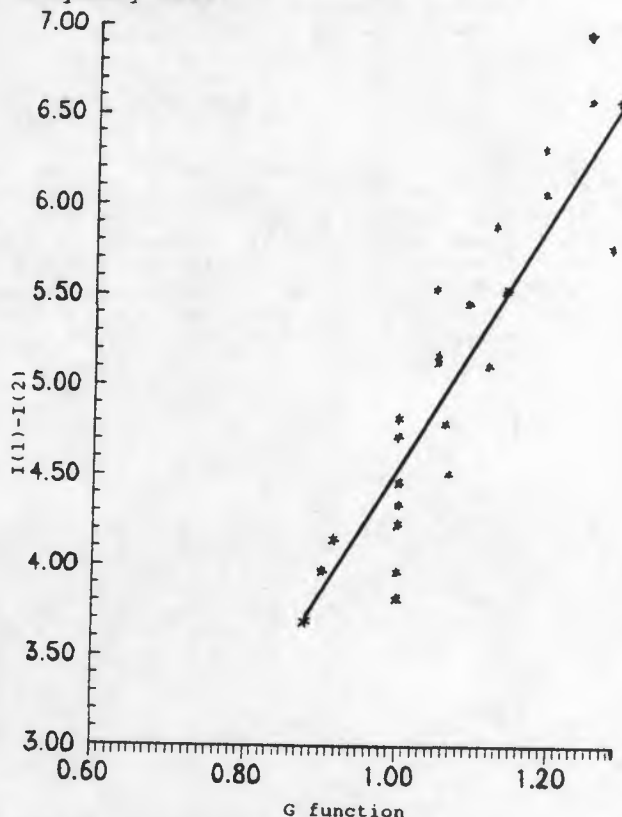


Figure 3. Scatter plot of G function and  $I(\theta_1) - I(\theta_2)$ .

3) of G against the term  $[I_1(v_r) - I_2(v_r)]$  suggests that G is a linear function of the difference term. This means that for dual angle measurements, T is dependent on WVC alone in a simpler form. Once we know the value of G in terms of  $[I_1(v) - I_2(v)]$ , we can very well write the equation (7) as

WVC in both 'N' type and 'I' type of atmospheres. If we combine the two atmospheres then there is a slight change in the function form. So theoretically it is imperative to say that neither split channel nadir observations alone nor single channel dual angle observations are sufficient to retrieve SST in all the types of atmospheres in all the seasons.

4. ALGORITHM FOR SST RETRIEVAL FROM ATSR/M

As discussed above, it has been established that multiple window observations can retrieve SST with an accuracy of 0.5 K in the low humidity regions but are unable to retrieve SST with the same accuracy in the regions of high humidity and stratifications unless these observations are supported by water vapor and it's vertical profile. A part of the uncertainty is removed by using the multiple angle observations. This, however, is also found to be inadequate because it needed a different sets of coefficients for 'N' type and 'I' type of atmospheres. An alternative approach then can be put forward where we combine the multichannel with multiview observations.

In order to account for the water vapor content, multiwavelength observations are required while its stratifications is taken care of by using the multiangle measurements. Therefore, if we use a combination of multiview and multiwavelength observations, both of these atmospheric conditions can be taken into account. Following this rationale, we have simulated the radiances and equivalent blackbody brightness temperatures for ATSR IR channels for forward scan as well as nadir scan and then we have regressed the input surface temperature taking the following relation:

$$\begin{aligned}
 SST = & a + b (T(840,0)) + c (T(925,0)) \\
 & + d (T(925,0)-T(925,55)) \\
 & + e (T(840,0)-T(840,55)) \dots\dots(12)
 \end{aligned}$$

Since ATSR carries Microwave sounder which retrieves the total Water vapor content, it is worth while to incorporate this information in the SST retrieval and hence the following combination was found to be the most suitable

$$\begin{aligned}
 SST = & a + b (T(840,0)) + c (T(925,0)) + \\
 & d (T(925,0)-T(925,55)) + \\
 & e (T(840,0)-T(840,55)) + \\
 & W*(T(925,0)-T(925,55)) + \\
 & W*(T(840,0)-T(840,55)) \dots\dots(13)
 \end{aligned}$$

Table 1: Coefficients for the relation  
 $SST = a + b(T(840,0)) + c(T(925,0)) + d(T(840,0)-T(840,55)) + e(T(925,0)-T(925,55))$

a	b	c	d	e	Correlation coeffts	RMS	Goodness
-7.81	-3.62	4.66	-2.73	2.52	0.93,0.96,0.56,0.63	0.06	0.9

Table 2: Coefficients for the relation:  
 $SST = a + b (T(840,0)) + c (T(925,0)) + d (T(925,0)-T(925,55)) + e (T(840,0)-T(840,55)) + f [W*(T(925,0)-T(925,55))] + g [W*(T(840,0)-T(840,55))]$

a	b	c	d	e	f	g	Corr coeffts	RMS	Goodness
11.66	1.16	-0.2	-1.17	-0.06	3.30	0.06	.93,.96,.56,.63 .63,.57,.63	0.03	0.9

where T(840,0) is the equivalent blackbody brightness temperature of the channel wavenumber 840 cm<sup>-1</sup> for nadir scan and W is water vapor retrieved by MWS. The regression coefficients alongwith the RMS error, correlation coefficients and goodness test coefficient are given in Table-1 and 2.

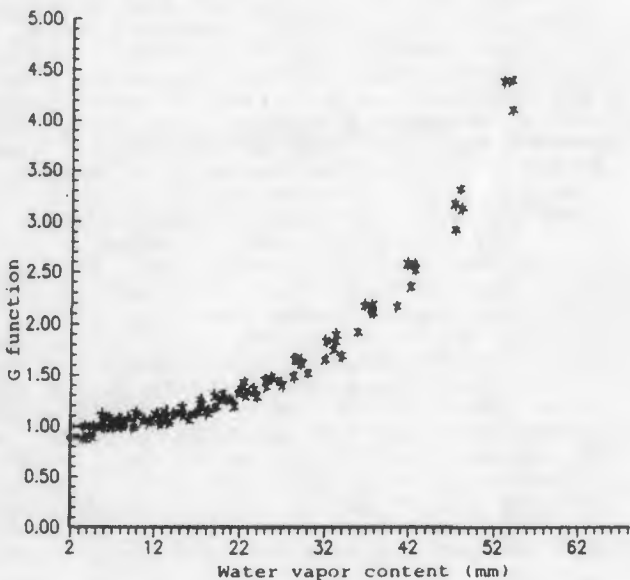


Figure 4. Scatter plot of G and WVC for 'N' type of atmospheres (Dual angle case).

5.0 DISCUSSION

As shown in Table-1 & 2 the r.m.s error of retrieval decreases from 0.06 to 0.03 if we incorporate the WVC retrieved from MWS. So theoretically dual angle technique for retrieving SST looks very promising and in the present scenario, ERS-1 can cater to such a technique, yet the technique has to be used after a lot of preprocessing and analytical efforts. For example the geometric distortion in the image due to the conical scanning of ATSR and due to obliqueness of the earth when the scanner's view angle is 55°, needs to be corrected carefully. Navigation of ATSR images as suggested by D.M.O'Brien & A.J.Prata (Ref. 10) can be a good tool to

calculate latitude and longitude corresponding to ATSR scan line and pixel. Similarly the corrections arising out of the Roll, Pitch and Yaw steering of the satellite will certainly make the retrieval algorithm more complex but accurate. Since ATSR will have much improved cooling and calibration capabilities than AVHRR, the

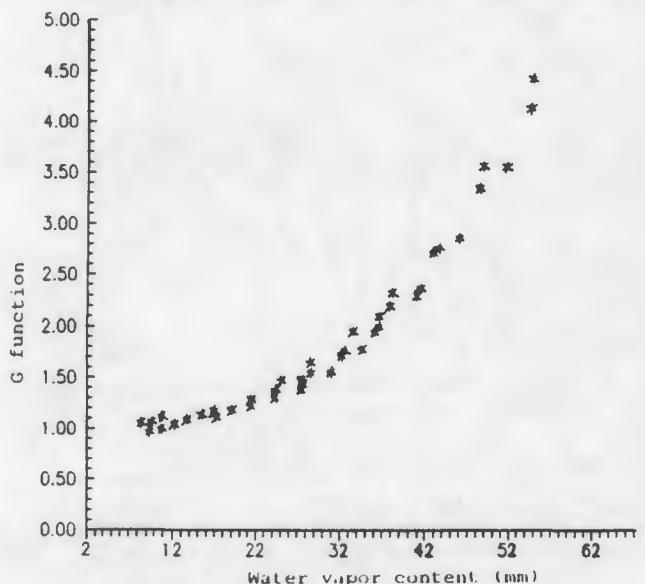


Figure 5. Same as figure 4 but for 'I' type of atmospheres.

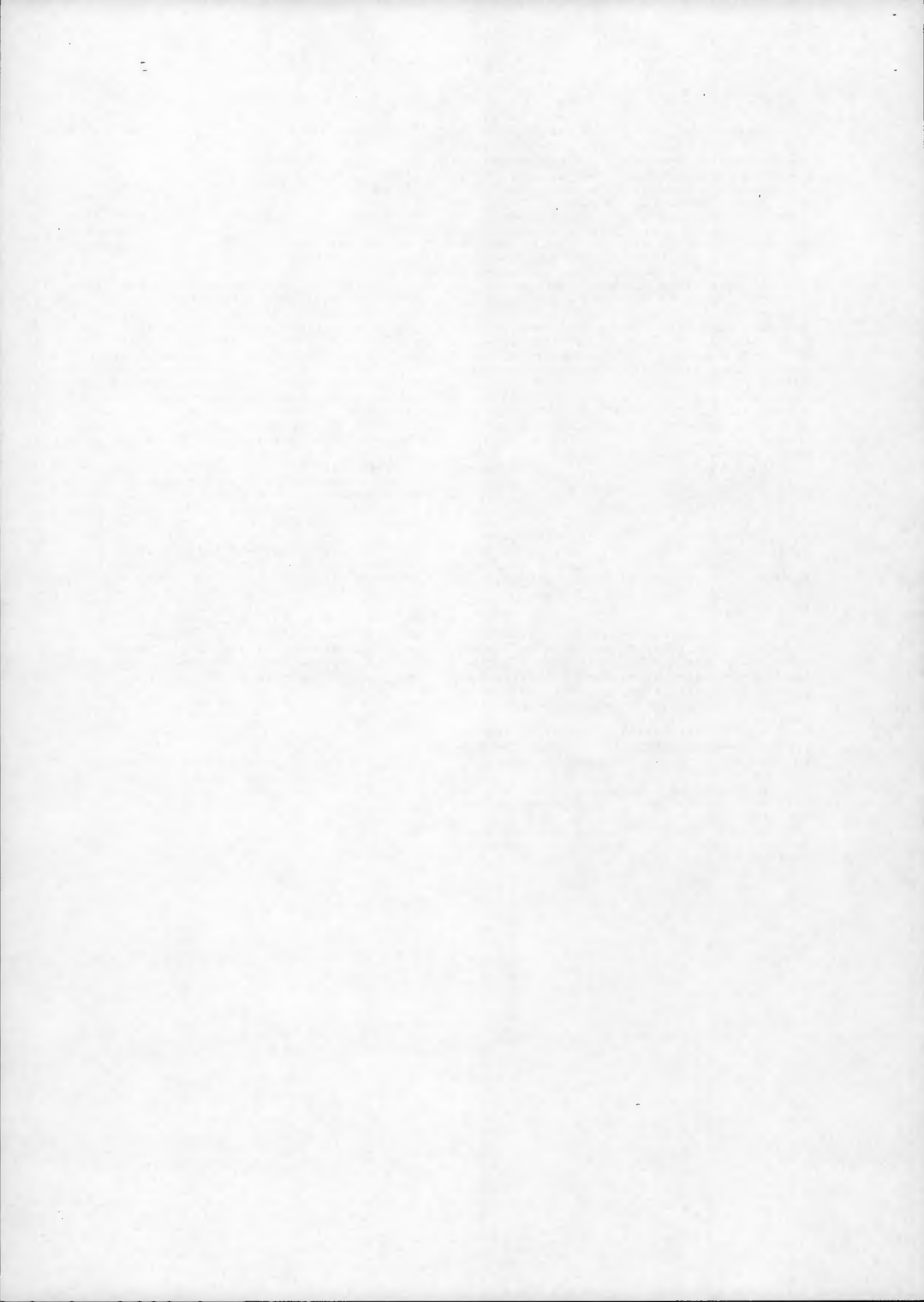
corresponding  $NE/\Delta T$  is also improved to be 0.1 K. Furthermore the error in retrieval will also be reduced if minimum number of channels are used (because the noise in multichannel retrieval is  $m \cdot NE/\Delta T$  where  $m$  is the number of channels used in retrieval). On the other hand the error in retrieving water vapor will also add to the overall error in SST retrieval. It was found that 1 cm error in WVC produces an error of  $0.06 \text{ mw/m}^2 \text{ Srcm}^{-1}$  in radiance of channel centering around  $840 \text{ cm}^{-1}$  i.e. nearly 0.18 K if surface temperature is assumed to be 300 K. So in effect if the maximum error in WVC estimation is 2 cm (as quoted in the literature), the error in SST retrieval due to water vapor will be 0.36 K. The breakup of both the possible errors is given below

Error due to  $NE/\Delta T$  in  $11 \mu\text{m}$  channel = 0.1 K  
 Error due to water vapor estimation = 0.36K

Total maximum error using single channel data = 0.46K

#### 6.0 REFERENCES

1. Agarwal V.K. and A.V.Ashajayanthi (1983)' Boundary Layer Structure over Tropical Oceans from TIROS-N Infrared Sounder Observations.' Journal of Climate and Applied Meteorology, 22, pp 1305-1311.
2. Mathur A K & Agarwal V K (1991)' A quantitative study on the effect of water vapor on estimation of sea surface temperature using satellite IR observations Oceanography of the Indian Ocean, edited by B N Desai, Oxford-IBH publications, New Delhi.
3. Barton I.J.(1983), ' Dual channel satellite measurements of Sea Surface Temperature.' Q. J. R. Meteorol. Soc., 109 pp 365-378.
4. Dalu G.C. and R.Prabhakara, C. Lo and M.J.Mack (1979)' An improved scheme for the remote sensing of sea surface temperature.' NASA Tech. Mem 80332 Goddard Space Flight Centre, Greenbelt, Maryland.
5. Delderfield J. et al.(1986), 'The Along-Track Scanning Radiometer(ATSR) for ERS-1,' Instrumentation for optical remote sensing from space, Proc. SPIE vol. 589, pp 114-120.
6. Dudhia Anu, 'A dual satellite algorithm for deriving sea surface temperature'(1988).Q. J. R. Meteorol. Soc., 114, pp 1305-1319.
7. Kneizys FOX., J.H.Chetwind, R.W.Fenn, E.P. Shettle, L.W.Abreu, R.A.McClatchey, W.O.Gallery and J.E.A.Selby (1980). ' Atmospheric Transmittance/Radiance computer code-LOWTRAN-5. Report no. AFGL TR 80-0067, Air Force Geophysics Lab. Massachusetts.
8. McClain E.P.(1980)' Multiple atmospheric window techniques for satellite derived sea surface temperatures.' Oceanography from space (Editor, J.F.R.Gower), Plenum Press. N. York.
9. McMillin L. (1975)' Estimation of sea surface temperature from two IR window measurements with different absorptions'. Journal of Geophysical Research Vol.80 No.36. pp 5133-5117.
10. O'Brien D.M. and A.J. Prata (1990) 'Navigation of ERS-1 Along-Track Scanning Radiometer (ATSR) images', ESA Journal 1990, vol. 14 no.4 pp 447-465.
11. Schluessal P., H.Y.Shin, W.J.Emery and H.Grassl(1987). 'Computation of satellite derived sea surface temperature with insitu skin measurements.' Journal of Geophysical Research vol.92 no.c2 pp 2859-2874.



**Estimations of the surface fluxes from satellite observations of  
boundary layer and the surface**

Vijay K Agarwal, Alope K Mathur and S Ilanthirayan  
Meteorology and Oceanography Division  
Space Applications Centre (ISRO)  
AHMEDABAD 380 053  
INDIA

**ABSTRACT**

In this paper, we describe a possible method for these calculations based on the data from ERS-1 ATSR/M, Scatterometer, and the NOAA-TOVS. The NOAA-TOVS can provide information about the vertical structures of the humidity and the temperature at coarse levels. The oblique view angles of the ERS-1 ATSR/M observations in the thermal spectral bands have capability to detect the stratifications in the boundary layer. These combined with NOAA inferences are found to provide adequate representation of the lower boundary layer.

"atmospheric corrections" for the retrieval of the sea-surface-temperature (SST). It has been observed (WMO 1986, Agarwal and Ashajayanti 1983, 1981) that the radiation in the spectral "window regions" (10-12  $\mu\text{m}$ ) has a direct dependence on the vertical distribution of the water vapor rather than the total water vapor content (WVC) of the atmospheric column. This means the radiance measured in the window channels will have, at least an indirect, dependence on the thermal and the humidity structure in the planetary boundary layer. Though such inferences put tremendous difficulties for the retrieval of the SST from these channels (specially where the water vapor absorption terms show higher variations). The "rosy side" of the picture is that it raises the possibility of information retrieval about the boundary structures. A successful demonstration of the detection and the estimates of the intensity of the monsoonal inversions in the central and western Arabian sea during and before monsoon (Agarwal and Ashajayanti 1983, Narayanan and Rao 1981) using a combination of the observations in the "window channels" and the sounding data from the satellite, leads credence to such speculations.

**1.0 INTRODUCTION:**

The information about the boundary layer and the interfacial layer at the earth-atmosphere boundary is essential for the understanding of the energy exchange processes. This problem assumes greater dimensions when, it is noted that the air-surface interaction is one of the most important processes after the radiative forcings, which completely specify the cloud fields on the climatic scale (see Agarwal 1992, 1991, Road 1978, Wetherald and Manabe 1986). The parametrization of these processes is generally based on very sparsely available data sets e.g. from a few towers near coastal regions and a few atolls mainly scattered in the Pacific and Atlantic oceans. A synoptic analysis is, therefore, not possible most of the time.

In this article, we suggest some innovative methods to get these boundary layer fluxes from satellite data on synoptic scales. The earlier indications of the possible inference of the planetary boundary layer structure using satellite data have been provided in the simulations exercises to try to understand the

Now that the satellite SST retrievals can be made independent of the stratifications of the boundary layer (Mathur and Agarwal 1991, Agarwal and Mathur 1985, Grassel et al 1986), together with the retrievals of the vertical temperature profiles (from NOAA), the winds and the wind-stress (from satellite scatterometer) and the WVC (from microwave radiometer), make it imperative to seek methods for the detailed investigation of the boundary layer structures from the satellite data. These studies have great potential for providing means for the calculations of energy and the mass fluxes in the planetary boundary layer on synoptic scale.

## 2.0 THE SIMULATIONS:

The initial exercise to demonstrate our suggestion is based on the radiative transfer calculations for the various spectral channels of the sensors under question. The calculations have been performed on a variety of the atmospheres simulated within a set of families of the vertical profiles of temperatures and the humidity corresponding to the standard tropical, mid-latitude and the sub-arctic atmospheres as specified under U.S. Standard (Valley 1965). The boundary layers have been perturbed to incorporate effects of the stratifications. It has been found that the 15 $\mu$ m CO<sub>2</sub> band spectral observations as in HIRS/2 on NOAA-TOVS not only depend on the vertical temperature profile but also the moisture content in the lower troposphere (Agarwal and Ashajayanthi 1981, 1983, Agarwal and Mathur 1992). This information when used in conjunction with the retrieved SST, can provide corrections for the moisture estimates obtained by using spectral observations in the 6.7 $\mu$ m H<sub>2</sub>O band. Such a multi-channel analysis can provide water vapour content retrievals in more layers than the customary three layers as reported by the NOAA/USA finished products. As a precursor to this contention, these spectral channels have been specifically used to derive the moisture depletion or enhancement in the planetary boundary layer. Of course, the underlying assumption that a robust SST retrieval is available from some other source is inherent in all these speculations.

## 3.0 SST FROM COMBINATION OF MULTIPLE OBSERVATIONS:

Normally, SST can be derived from satellite IR observations by viewing the surface through two or more windows using a radiative transfer equation as

$$I(\nu) = B(\nu, T_s) \tau(\nu, p_0, \theta) + \int B[\nu, T(p)] d\tau(\nu, p, \theta)$$

where  $I$  is the radiance reaching at the satellite sensor,  $\nu$  is the wavenumber,  $T$  is the atmospheric temperature at pressure  $p$ ,  $T_s$  is the surface temperature,  $p_0$  is the surface pressure,  $\tau$  is the transmittance,  $\theta$  is the zenith angle and  $B$  is the Planck function. In this equation, the effect of the surface reflection of emission from atmosphere has been neglected. This will not be the case if there is strong turbidity in ocean water or the observations were being made near 4  $\mu$ m where solar input starts becoming important. Using Mean value theorem, then we can rewrite above as

$$I(\nu) = B(\nu, T_s) \tau(\nu, p_0, \theta) + B_a(\nu) [1 - \tau(\nu, p_0, \theta)]$$

where  $B_a$  is the mean radiance of the atmosphere for the given  $\tau$  and  $\theta$ . It is clear from above equation that SST estimate (i.e.  $B(\nu, T_s)$ ) involves elimination of terms,  $B_a(\nu)$ .

## 3.1 MULTIPLE WAVELENGTHS:

If measurements at different wavelengths are used, the dependence of  $B$  and  $I$  on wavelength must be determined. This is needed because in multiwavelength mode, elimination of  $B_a$  and estimate for  $B(\nu, T_s)$  have to be performed at a reference frequency for ease of interpretation. For two wavelengths in the 10-12  $\mu$ m window this can be achieved by expanding the Planck function about  $\nu_r$  to give

$$B(\nu_r, T) = B(\nu, T) + [\delta B(\nu, T)/\delta \nu] [\nu_r - \nu]$$

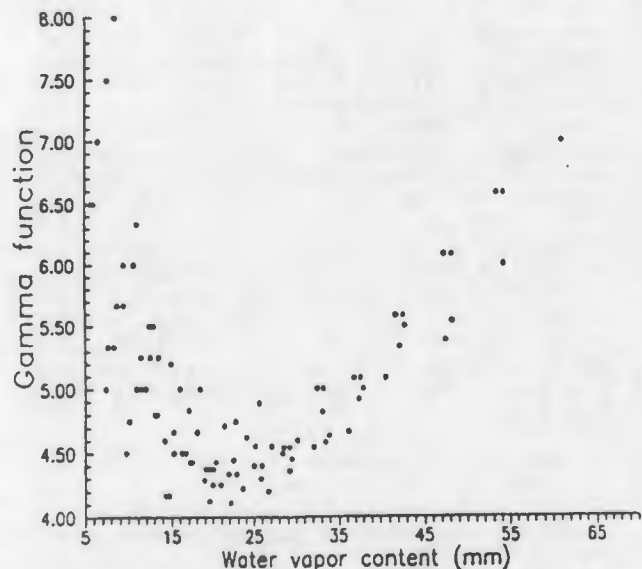
In the atmospheric window region,  $\delta B(\nu, T)/\delta \nu$  is very weakly dependent on the temperature. So if values of  $\nu$  and  $\nu_r$  are sufficiently close, it is possible to neglect the dependence of  $\delta B(\nu, T)/\delta \nu$  on temperature and then the SST retrieval equation for two channels can be written as

$$B(\nu_r, T_s) = I_1(\nu_r) + r [I_1(\nu_r) - I_2(\nu_r)]$$

where

$$r = \frac{[1 - \tau(\nu_1, p_0, \theta)]}{[\tau(\nu_1, p_0, \theta) - \tau(\nu_2, p_0, \theta)]}$$

If we plot gamma function vs water vapor content for different types of atmospheres, we can see from figure(1) that in all cases gamma decreases with WVC for lower WVC i.e. <15 mm and then increases for higher WVC (>30 mm), thus functional form of gamma can be determined with respect to WVC. But in region where WVC is between 15 and 30 mm, gamma can not be represented by a particular function in terms of WVC and so the usual relationship between gamma and WVC breaks down in this region.



r VS WVC (multichannel case)

figure1

### 3.2 MULTIPLE ANGLES

When the observations are made in optically related different view angles at same wave length, selection of a reference frequency is not required and  $\tau$  is given by

$$r = \frac{[1-\tau(v, p_0, \theta_1)]}{[\tau(v, p_0, \theta_1) - \tau(v, p_0, \theta_2)]}$$

The plot (figure 2) of  $\tau$  against the term  $[I_1(v_r) - I_2(v_r)]$  suggests that  $\tau$  is a linear function of the difference term. This means that for dual angle measurements,  $T$  is dependent on WVC alone in a simpler form. Once we know the value of  $\tau$  in terms of  $[I_1(v) - I_2(v)]$ , we can very well write the above equation as

$$B(v, T_s) = I_1(v) + \tau[I_1(v) - I_2(v)]$$

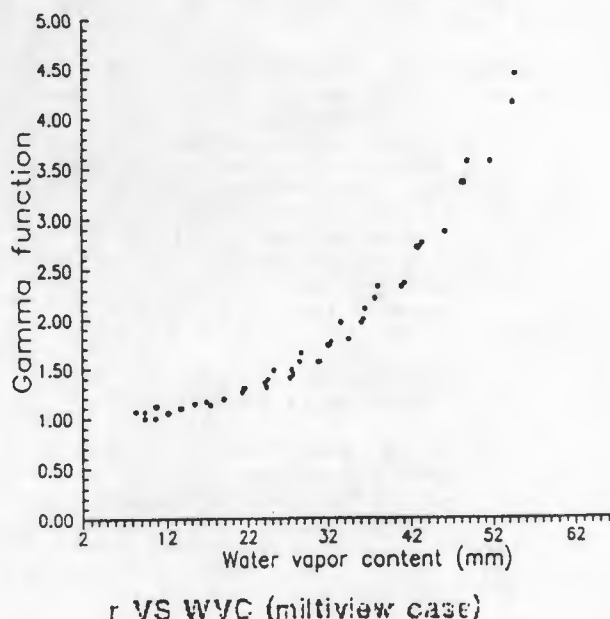


figure2

### 3.3 COMBINATION OF MULTIANGLE AND MULTI-WAVELENGTH OBSERVATIONS:

The split window observations can retrieve SST with an accuracy of 0.5 K in the low humidity regions but are unable to retrieve SST with the same accuracy in the regions of high humidity and stratifications unless we have more information to determine behavior of the function  $\tau$ . A part of the uncertainty is removed by using the multiple angle observations. Therefore, an alternative approach then can be put forward where we combine the multichannel with multiview observations. Such retrievals are possible from ERS-1/ATSR. A direct measurement of WVC is also possible using MWS.

Following this rationale, we have simulated the radiances and equivalent blackbody brightness temperatures for ATSR IR channels for forward scan as well as nadir scan and then we have regressed the input surface temperature taking the following relation:

$$SST = a + b (T(840, \emptyset)) + c (T(925, \emptyset)) + d (T(925, \emptyset) - T(925, 55)) + e (T(840, \emptyset) - T(840, 55))$$

and if we include MWS water vapor estimates

$$SST = a + b (T(840, \emptyset)) + c (T(925, \emptyset)) + d (T(925, \emptyset) - T(925, 55)) + e (T(840, \emptyset) - T(840, 55)) + W*(T(925, \emptyset) - T(925, 55)) + W*(T(840, \emptyset) - T(840, 55))$$

where  $T(840, \emptyset)$  is the equivalent blackbody brightness temperature of the channel wavenumber  $840 \text{ cm}^{-1}$  for nadir scan and  $W$  is water vapor retrieved by MWS. The regression coefficients alongwith the RMS error, correlation coefficients and goodness test coefficient are given in Table-1.

### 4.0 Boundary layer fluxes:

Next, we look at the responses of the channel spectral radiance to the structures in the planetary boundary layer. As we mentioned earlier, (Agarwal and Ashajayanthi 1982), the  $15 \mu\text{m}$   $\text{CO}_2$  band has spectral channels quite sensitive to the lower 1-2 Km of the atmosphere. A similar expectation has been raised in the "nadir" looks and the "oblique" looks of the ATSR though operating only in the "window-channel". The reason for such a speculation is that the oblique view specially at large angles (as the case in ATSR,  $\pm 55^\circ$ ) will have more serious dependence on the boundary layer distribution of the water vapor and temperature compared to the nadir looks due to the increase in the optical path of the radiance. Therefore, a simple linear difference of the spectral radiances will not be able to completely cancel out the water vapor absorption effects in the SST retrieval, a view point already expressed in the ongoing efforts for the SST retrievals from ATSR (Mathur and Agarwal 1992). At the same time, this strong dependence on the boundary layer water vapor distribution renders this combination quite useful for inferences of the evaporative/and or sensible heat fluxes from the surface.

We construct, these fluxes using empirical relations:

$$e = C_d \rho |v| (q_s - q_a)$$

$$s = C_d C_p \rho |v| (T_s - T_a)$$

where  $q_{s,a}$  are the water vapor mixing ratios for the surface and the air and  $T_{s,a}$  are the temperatures at the surface and the air respectively.  $|v|$  is the surface wind speed. The empirical coefficients  $C_d$  are called drag coefficients and are normally determined using the tower based observations of the vertical profiles of temperature and humidity and

TABLE-1

a	b	c	d	e	Correlation coeffs	RMS	Goodness
-7.81	-3.62	4.66	-2.73	2.52	0.93, 0.96, 0.56, 0.63	0.06	0.9

a	b	c	d	e	f	g	Corr coeffs	RMS	Goodness
11.66	1.16	-0.2	-1.17	-0.06	3.30	0.06	.93, .96, .56, .57, .63	0.03	0.9

the fluxes in the first 100m of the interfacial layer. The information about  $T_a$  is now expected to be available from the NOAA/HIRS 15  $\mu$ m and 4.3  $\mu$ m CO<sub>2</sub> observations while the  $q_a$  construction will be possible using NOAA/HIRS and ERS-1/ATSR combination. The surface wind speed  $|v|$  will be available from ERS-1/Scatterometer data.

#### 4.1 Evaporative fluxes:

We consider construction of an index:

$$\sigma = (WVC_{ex} - WVC_{ac}) / (WVC_{ex} + WVC_{ac})$$

as a measure of the dryness or wetness of the boundary layer where WVC<sub>ex</sub> is the water vapor content of the atmosphere extrapolated through the WVC for the atmosphere above 700 hpa and the retrieved SST values using the climatological relationships. WVC<sub>ac</sub> is actual water content as retrieved from the remote sensing data. The index  $\sigma$  will be -ve if the boundary layer has inversions and +ve if there is some convective activity. This index will be further reinforced due to changes in the boundary layer temperatures (Agarwal and Ashajayanthi 1983).

The requirement that the SST is retrieved quite accurately free from the boundary layer temperature and humidity perturbations, are no hindrances to the estimates of the index  $\sigma$ . The main problem encountered is in the estimates of WVC<sub>ac</sub>. The microwave sounders of the ATSR or SMMR type produce WVC retrievals accurate to  $\pm 4$  mm, while the atmospheric stratification in water vapor distribution for some of the cases can be weaker than this (even when the temperature stratifications is quite pronounced, as normally happens on the ground due to the industrial aerosols or in the big cities). The retrieval of the ground (non-oceanic regions) temperature raises some doubts about inferences on the land parts, since the thermal emissivity of the ground is not very adequately known for use in the retrieval of the ground temperatures. Therefore, presently all the analysis efforts are so far confined to the oceanic regions only.

The empirical adjustment of the drag coefficients are, however, left as open

question because the existing coefficients, these are presently calculated over the near coastal or island regions where a tower could be mounted easily, and that too mostly in Pacific and Atlantic regions. These drag coefficients are known to have dependence over the temperature and the wind speed (North 1990).

For simulation purpose, we took the basic meteorological observations from the ship measurements in the deep as well as coastal oceans reinforced with data from atolls and islands. The bulk aerodynamical calculations using the usual drag coefficients were performed to estimate fluxes. The radiances for the relevant channels in ERS-1/ATSR and NOAA/HIRS were generated using standard radiative transfer calculations for this data set.

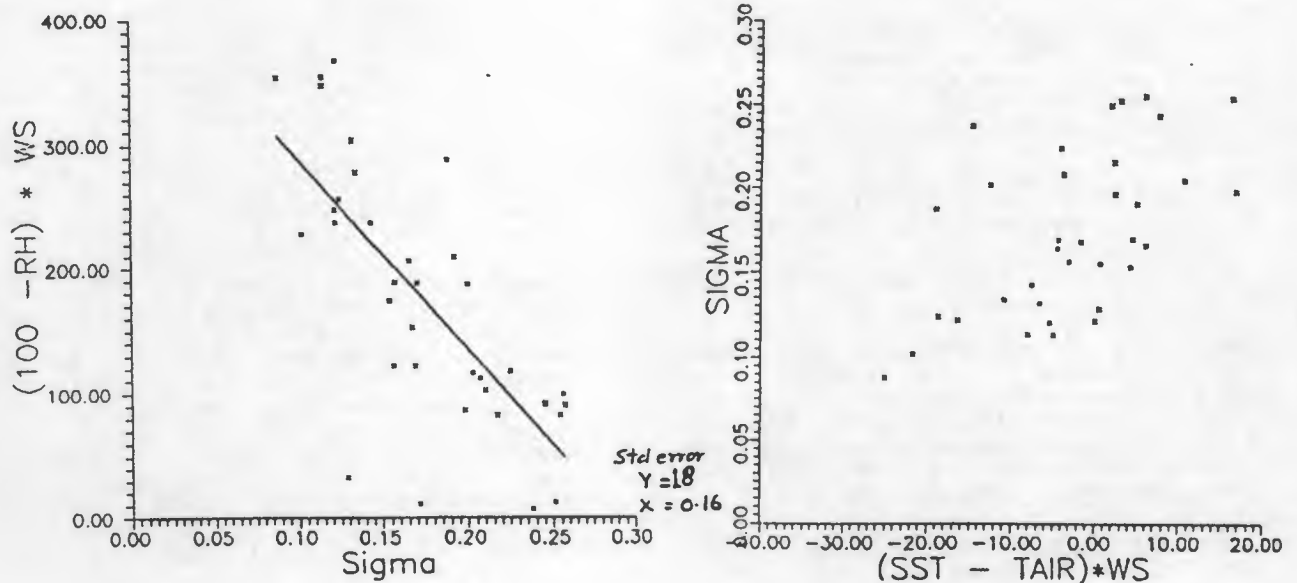
An index of the type:

$$\sigma = (\text{rad at } 55^\circ - \text{rad at } t0^\circ) / \text{mean}$$

has been constructed which signifies departure due to perturbations caused by the increase in the optical lengths in the lower troposphere. The index  $\sigma$ , then, can be studied in relation to the calculated fluxes. Apart from the tuning required due to the possibility of "unrealistic" drag coefficients, the relation does show very smooth behavior as shown in the accompanying graphs (figure 3 and 4). The rms deviation for a linear regression for  $\sigma$  vs  $(100-H)*W_s$  where H is relative humidity in the interfacial layer and  $W_s$  the wind speed, is less than 10% which is quite remarkable and indicates that the starting hypothesis has a reasonably valid base and hence, points to the possibility that the evaporative fluxes can be calculated from the ERS-1/ATSR + Scatterometer data. Detailed investigation of this hypothesis are possible only when actual ERS-1/ATSR data is available

#### 4.2 Sensible Heat fluxes:

Regarding the sensible heat fluxes, the SST retrieved from ERS-1/ATSR or NOAA/AVHRR+HIRS combination, alongwith the  $|v|$  measurements from ERS-1/Scatterometer can be used. The air-temperature estimations are some what tricky and will require an extrapolations of the



• vs latent heat

figure3

temperature profile retrievals from NOAA/HIRS. Therefore, the index for this purpose will be constructed as follows:

$$\beta = (T_{HIRS-8} - T_{HIRS-7}) / (T_{HIRS-7} + T_{HIRS-6})$$

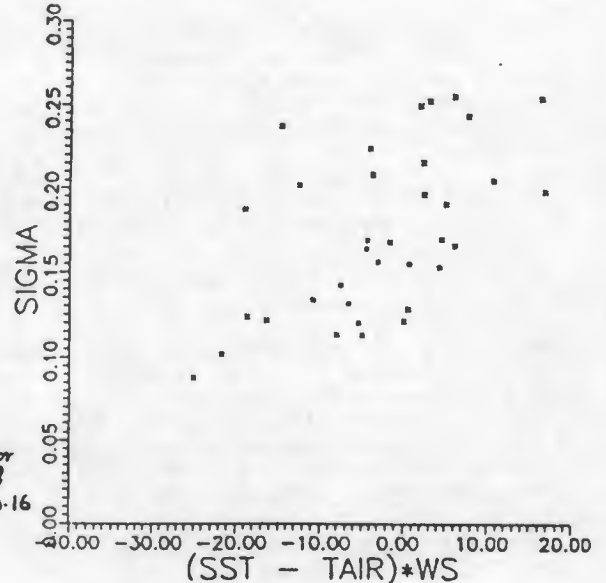
which has very strong correlation with  $(T^S - T^a)$  occurring in the sensible heat equation.

#### 5. Conclusions:

The above discussion, though based mainly upon the simulations and radiative transfer calculations, demonstrate that the estimates for the thermodynamic fluxes across the surface-atmosphere interfacial boundary are possible on synoptic scale using the satellite data. The expected accuracies from the existing satellite systems are relatively quite high (of the order of or better than 20%). The need for the use of the multi-satellite system, as at present, can be easily dispensed with when more sophisticated satellites and sensors (e.g. those planned for EOS platforms) are available. The need for the multi-sensor system is indispensable since it will require all varieties of spectral observations (microwave, thermal, near thermal, and multi-angle).

A model based calculation of the turbulent mixing in the boundary layer now seems to be possible through these stability analysis. The turbulent fluxes from the surface in terms of these mixings and the atmospheric drag effect on the surface are calculable in terms of the SST, surface wind, stability index, the air temperature and the moisture.

The calculations, presently with NOAA+ship data and later on to be ap-



• vs sensible heat

figure4

plied to ERS-1 data, have been compared with the classical bulk aerodynamic calculations based on the ship data in test areas. Though, the spot values do not agree very well, the synoptic pattern of the distribution matches quite well. This shows the basic idea is tenable and with some refinements can be used for the study of air-sea interaction processes.

#### 5. REFERENCES

- Agarwal V.K. and A.V. Ashajayanthi (1983) 'Boundary Layer Structure over Tropical Oceans from TIROS-N Infrared Sounder Observations.' *Journal of Climate and Applied Meteorology*, 22, pp 1305-1311.
- (1982) "Simulations study of multi-spectral estimation of SST from infrared observations" *Int.Jour.environ.* 12, 371-380
- (1981) " Simulatin studies of satellite spectral radiances for 11.1, 8.3, 7.3 and 6.7  $\mu$ m IR bands" *Proc. Ind.Acad.Sciences (EPS)* 90, 327-336
- Agarwal Vijay K and Aloke Mathur (1985) "Multichannel Estimate of SST - An experiment with NOAA data", pp 120-131, *Proc. US-India symposium cum workshop on remote sensing fundamentals and applications*, March 11-15, SAC, Ahmedabad (India).
- Anding D., R.Kauth (1970)' Estimation of Sea Surface temperature from space', *Remote Sensing of Environment* 1, pp 217-220.
- Barton I.J.(1983), ' Dual channel satellite measurements of Sea Surface Temperature.' *Quarterly Journal of Royal Meteorological Society*, 109 pp 365-378.

Dalu G.C. and R. Prabhakara, C. Lo and M.J. Mack (1979) 'An improved scheme for the remote sensing of sea surface temperature.' NASA Tech. Mem 80332 Goddard Space Flight Centre, Greenbelt, Maryland.

Delderfield J. et al. (1986), 'The Along-Track Scanning Radiometer (ATSR) for ERS-1,' in Instrumentation for optical remote sensing from space, Proc. SPIE vol. 589, pp 114-120.

Kneizys F.X., J.H. Chetwind, R.W. Fenn, E.P. Shettle, L.W. Abreu, R.A. McClatchey, W.O. Gallery and J.E.A. Selby (1980). 'Atmospheric Transmittance/Radiance computer code- LOWTRAN-5. Report no. AFGL TR 80-0067, Air Force Geophysics Lab. Massachusetts.

Mathur Aloke and Vijay K Agarwal (1992) (to appear) " Simulations of SST retrieval from ATSR and Microwave sounder on ERS-1 satellite", ESA Journal.

McClain E.P. (1980) 'Multiple atmospheric Window techniques for satellite derived sea surface temperatures.' in Oceanography from space (J.F.R. Gower, Editor), Plenum Press.

McMillin L. (1975) 'Estimation of sea surface temperature from two IR window measurements with different absorptions'. Journal of Geophysical Research Vol. 80 No. 36. pp 5133-5117.

Narayanan M S and B.M. Rao (1989) "Stratification and convection over Arabian Sea during monsoon 1979 from satellite data", Proc. Ind. Acad. Sciences (EPS), 96, 339-352.

-- (1981) "Detection of monsoon inversions by TIROS-N satellite", Nature, 294, 546-548.

Niemann R.A. (1977) 'A comparison of radiosonde temperature and humidity profile data base' CSC/TM-77/6133 Contract NAS-5-11999, NASA(USA).

O'Brien D.M. and A.J. Prata (1990) 'Navigation of ERS-1 Along-Track Scanning Radiometer (ATSR) images', ESA Journal, vol. 14 no. 4 pp 447-465.

Piexoto J.P. and A.H. Oort (1983) 'The Atmospheric Branch of hydrological cycle and climate, in variation of the global water budget (Riedel, London) p 5.13. Ramage C.S. (1971), 'Monsoon meteorology' pp 192. (Academic Press-New York).

Schuessal P., H.Y. Shin, W.J. Emery and H. Grassl (1987). 'Computation of satellite derived sea surface temperature with insitu skin measurements'. Journal of Geophysical Research vol. 92 no. c2 pp 2859-2874.

Smith W.L., P.K. Rao, R. Koffler and W.R. Curtis 'The determination of sea surface temperature from satellite high resolution infrared window measurements' Monthly weather review, 98 p 64.

WMO (1986) " Satellite-derived SST for global climate applications" Report of the COSPAR International Workshop, Camp Springs, Maryland, USA May 28-31 1985. pp 50

# ATSR CORRELATIVE SKIN MEASUREMENTS OF SEA SURFACE TEMPERATURE

Peter Schlüssel and Jens Meywerk

Meteorologisches Institut, Universität Hamburg, Bundesstraße 55, D-W-2000 Hamburg 13, Germany

## ABSTRACT

The Along Track Scanning Radiometer (ATSR) measures surface leaving radiation in four spectral bands and with a dual view at the same surfaces that enables an advanced atmospheric correction for an improved retrieval of sea surface temperatures (SST). Retrieval schemes are developed which take into account the instrument parameters and are tested together with those of other authors. The validation of the ATSR-derived SSTs which has been designed to reach accuracies of better than  $0.5 K$  requires in-situ skin measurements that also have a high accuracy. An experiment that meets this requirement has been carried out at the research platform *Nordsee* in the North Sea from May 1991 to January 1992. An infrared radiometer has been operated with a special on-line calibration to achieve a continuous high performance of the in-situ measurements. Case studies show that the ATSR-derived SSTs match the in-situ skin measurements within few tenths of a degree.

Keywords: ATSR, remote sensing, sea surface temperature, skin effect, validation.

## 1. INTRODUCTION

A new type of an infrared radiometer, the Along Track Scanning Radiometer (ATSR), is flown on the ERS-1 spacecraft in order to measure sea surface temperature (SST) with a higher accuracy than ever measured from space before. The expected accuracy of the ATSR-derived SSTs is better than  $0.3 K$  which should meet the scientific requirements of climate researchers. This achievement immediately requires to think about the definition of sea surface temperature. While infrared radiometers only receive information about the radiation that leaves the uppermost micrometres of the ocean, namely the skin of the ocean, the SST was formerly mostly considered to be a bulk temperature that is representative for the upper decimetres or metres of the water. The temperature of this bulk water is normally several tenths of a degree higher than the skin temperature. The difference between bulk and skin temperature might even reach values of more than  $1 K$  in extreme cases but also negative ones in the case of strong diurnal heating (Refs. 1, 2). Therefore it is no longer possible to use the satellite-derived SST as a proxy for the bulk temperature as it is done with other space-borne SST measurements (Refs. 3, 4) which have a lower accuracy.

First ATSR data have been made available by the

Rutherford Appleton Laboratory (RAL) for validation purposes. The ATSR products which are used here are already pre-processed by RAL using the so-called SADIST (Synthesis of ATSR Data Into Sea-surface Temperatures) Version-400 scheme. The Level-1.5 processed products contain calibrated and geolocated brightness-temperature images while those of Level-2.0 processed ones contain cloud-cleared images of sea surface temperatures. Both products are mapped to  $1 - km$ -resolution images of  $512 \times 512 km^2$ .

## 2. ATSR CHARACTERISTICS

The ATSR, operating in three infrared channels at  $3.7$ ,  $11$ , and  $12 \mu m$  and at a fourth channel at  $1.6 \mu m$  has four important characteristics that are new when compared to previous space-borne imaging infrared radiometers. The utilization of two internal black bodies with temperatures in a similar range which is covered by sea surface temperatures allows an absolute calibration of the instrument that is superior to previous approaches. The noise level is reduced by an active detector cooling to equivalent brightness-temperature differences well below  $0.1 K$  in all infrared channels. This is demonstrated in a brightness-temperature section retrieved from the image shown in figure 1 which has been scanned on 26 October 1991, 21:08 UT over the North Sea and adjacent land areas. Figure 2 shows the brightness temperatures measured in the infrared channels along a transect through waters with low temperature gradients not exceeding  $1 K$ . The noise levels which can be found are of the order of  $0.08$ ,  $0.02$ , and  $0.04 K$  for the channels centered around  $3.7$ ,  $11$ , and  $12 \mu m$ , respectively. A second image of the same scene is shown in figure 1 where only brightness temperatures of the North Sea are enhanced to get an insight into the SST variability. Clearly visible are frontal features in the temperature pattern which occur in the upper part of the image and the cold plume extending from the Elbe river to the middle of the image.

The third innovative property of ATSR is the inclusion of a channel at  $1.6 \mu m$  that allows a better cloud detection than with infrared channels only and which allows for an enhanced correction for attenuation by atmospheric aerosols in the infrared channels. Finally, the ATSR operates in a dual-view mode that enables the measurement of brightness temperatures of the same scene at two different viewing angles within about 2.5 minutes. This capability allows a more accurate atmospheric correction of the brightness temperatures for the retrieval of sea surface temperatures.

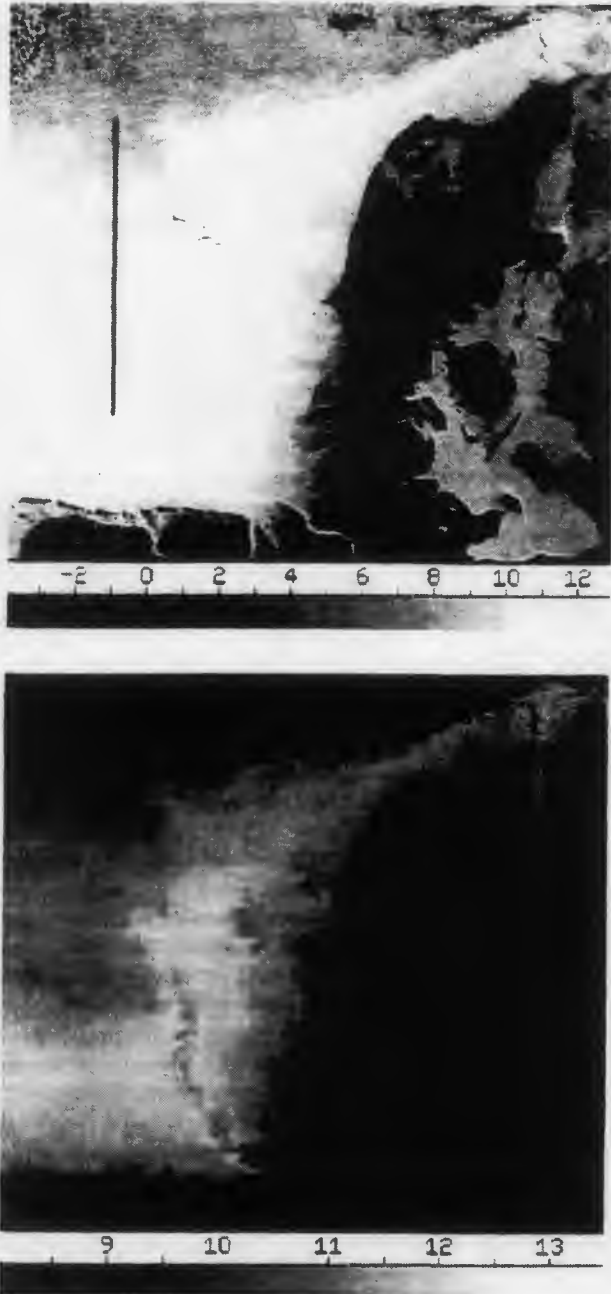


Figure 1. Brightness temperatures at  $11 \mu\text{m}$  in  $^{\circ}\text{C}$  over the North Sea and adjacent land areas as measured by ATSR on 26 October 1991, 21:08 UT. The lower image shows details of the temperature distribution in the North Sea.

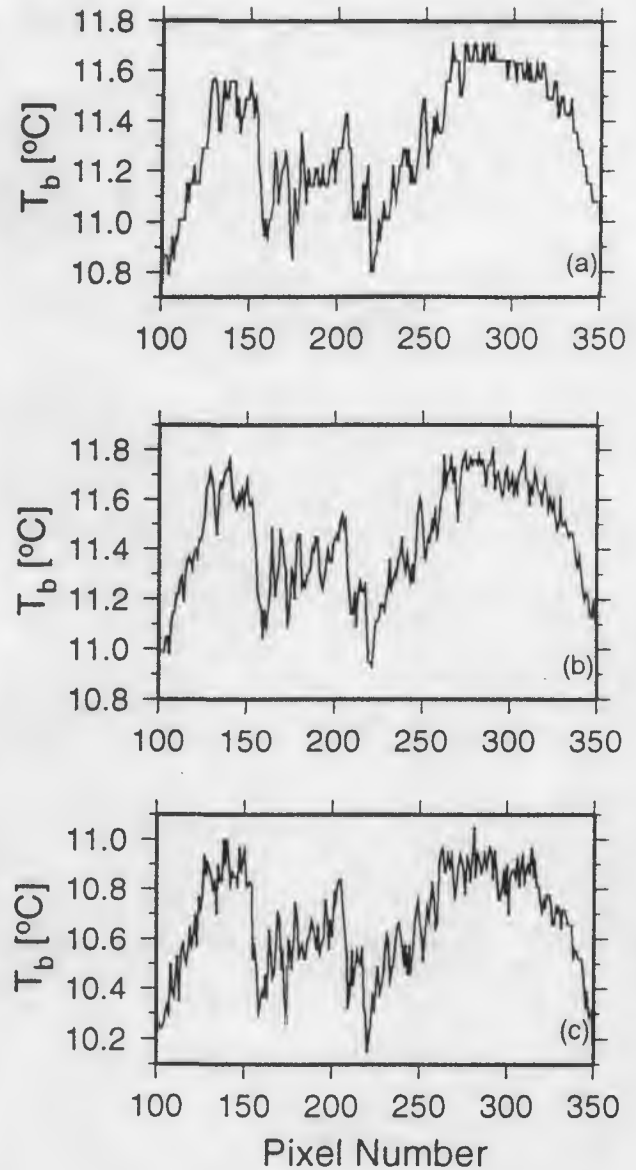


Figure 2. Brightness temperature distribution along the section shown in figure 1, (a) at  $3.7 \mu\text{m}$ , (b) at  $11 \mu\text{m}$ , and (c) at  $12 \mu\text{m}$ .

### 3. SST RETRIEVAL SCHEMES

The brightness temperatures as shown in figure 1 only represent relative distributions of brightness temperatures which are similar but not equal to the surface temperatures. An atmospheric correction has to be applied to the brightnesses in order to retrieve absolute sea surface temperatures. This can be done in several ways and many approaches exist using multi-spectral measurements to fulfil this task (Refs. 3-8). A new possibility that allows a more sophisticated correction is the dual-view capability of ATSR. Several retrieval algorithms have been proposed already for the use with multi-channel and dual-view SST retrievals (Ref. 6).

We have chosen to develop further retrieval schemes by

means of radiative transfer calculations in order to learn about the transmission of the ocean-leaving radiation to the satellite and its modification by the atmosphere. Four different retrieval algorithms have been developed. Three of them make use of the dual-angle capability. For daytime applications only the channels at 11 and 12  $\mu\text{m}$  are useful while during night also the 3.7  $\mu\text{m}$  channel can be incorporated. During daytime the sea surface temperature  $T_S$  is obtained by

$$T_{S1} = a_0 + a_1 T_{11} + a_2 (T_{11} - T_{12}) \quad (1)$$

$$T_{S2} = a_0 + a_1 T_{11} + a_2 (T_{11} - T_{12}) + a_3 (T_{11} - T'_{11}) \quad (2)$$

At night the 3.7  $\mu\text{m}$  channel is included and the retrieval schemes read

$$T_{S3} = a_0 + a_1 T_{3.7} + a_2 (T_{3.7} - T_{11}) + a_3 (T_{3.7} - T_{12}) + a_4 (T_{3.7} - T'_{3.7}) + a_5 (T_{3.7} - T'_{11}) + a_6 (T_{3.7} - T'_{12}) \quad (3)$$

$$T_{S4} = a_0 + a_1 T_{3.7} + a_2 (T_{3.7} - T_{11}) + a_3 (T_{3.7} - T_{12}) + a_4 (T_{3.7} - T'_{12}) \quad (4)$$

where  $T_{3.7}$ ,  $T_{11}$  and  $T_{12}$  are the measured brightness temperatures at 3.7, 11 and 12  $\mu\text{m}$ , respectively,  $a_i$ ,  $i = 1, 6$ , are coefficients which are optimized by regression using simulated brightness temperatures for a globally distributed set of atmospheric situations and corresponding sea surface temperatures. These coefficients are different for each of the given algorithms; their values are tabulated in table 1 together with estimated standard errors  $\epsilon$ . The primes indicate brightness temperatures at forward view while the plain quantities represent nadir view brightness temperatures. The input and output temperatures of equations (1) through (4) are measured in Kelvin.

As seen in table 1 the inclusion of a dual-view measurement is not far superior to a simple "split-window" estimate. The reason for this is the very low noise level of the 11  $\mu\text{m}$  measurements. The night-time measurements, however, benefit from both the inclusion of the 3.7  $\mu\text{m}$  channel as well as of the forward-view measurement. A similar behaviour has been found by Barton et al. (Ref. 7). The 1.6  $\mu\text{m}$  channel is not yet directly included. While it is used for cloud clearing it might be of value for further corrections accounting for extinction of the surface-leaving radiation due to aerosol particles.

#### 4. SURFACE SKIN MEASUREMENTS

From 31 May 1991 through 31 January 1992 surface skin-temperature measurements were taken at the German research platform *Nordsee* which is situated in the North Sea at  $54^{\circ}42'N$ ,  $7^{\circ}10'E$ . The skin temperatures were measured with a Heimann KT-4 radiation thermometer mounted at a height of about 23 m above the surface looking on to the surface at an angle of  $50^{\circ}$ . The KT-4 is equipped with a 10 - 12  $\mu\text{m}$  bandpass filter. Because of the non-blackness of the sea surface at these wavelengths,  $\lambda$ , which is represented in figure 3 as surface emissivity,  $\epsilon$ , at varying viewing angles,  $\Theta$ , a correction has to be applied to the measured brightness temperatures in order

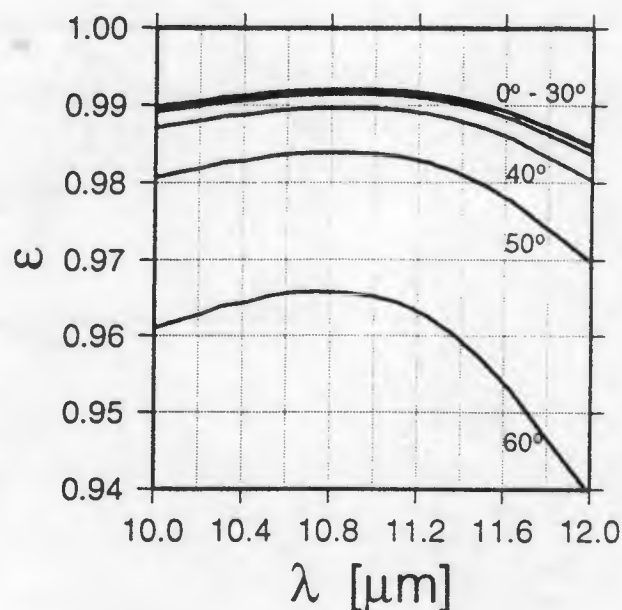


Figure 3: Surface emissivity of a flat sea surface at different viewing angles as computed with the Fresnel formulae and complex indices of refraction from Ref. 9.

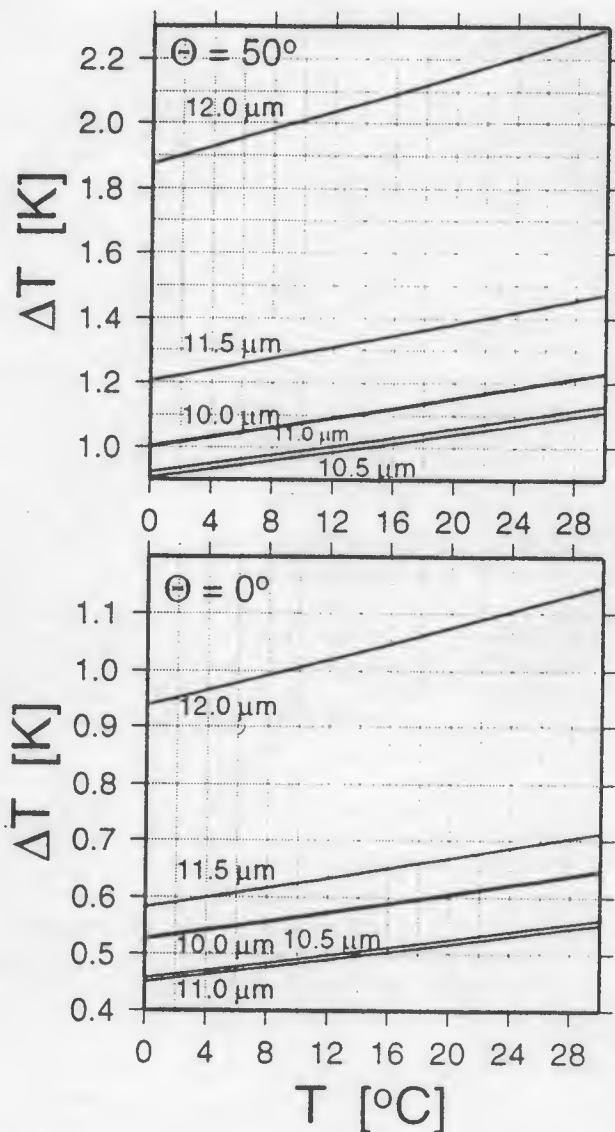
to get real skin temperatures. The temperature deficits caused by the non-blackness are shown in figure 4 as function of surface temperature for two viewing angles. The temperature deficits are diminished by a small amount only when accounting for the reflected downwelling radiation of the clear sky. Other effects that have an influence on the radiometric temperature measurements are drifts of the instrument electronics and the contamination of the entrance optics with sea spray. Therefore the radiometer is calibrated with a reference bath which is moved into the radiometer's field of view every other minute. This allows an accurate absolute calibration of the radiometer which accounts for all of the above mentioned effects and thus gives the surface skin temperature with an accuracy of 0.05 K. Further details of the calibration method are given in Ref. 1.

#### 5. VALIDATION OF SPACE-BORNE SST RETRIEVALS

The processing of ATSR brightness temperatures first requires a cloud detection with isolation of cloud contaminated pixels and, in a further step, the application of retrieval coefficients that combine the measurements at different wavelengths and viewing angles to give the surface temperature. Therefore only parts of the images can be filled with temperature values as seen in figure 5. A cloud mask as shown in figure 6 results from several cloud tests that have been applied within the frame of SADIST. Comparing the temperature image with the brightness temperatures from figure 1 sheds some light on the difficulties that are inherent to the cloud-detection schemes. Obviously clear areas have been flagged cloudy and excluded from the further processing. These are areas with strong temperature gradients which have probably been

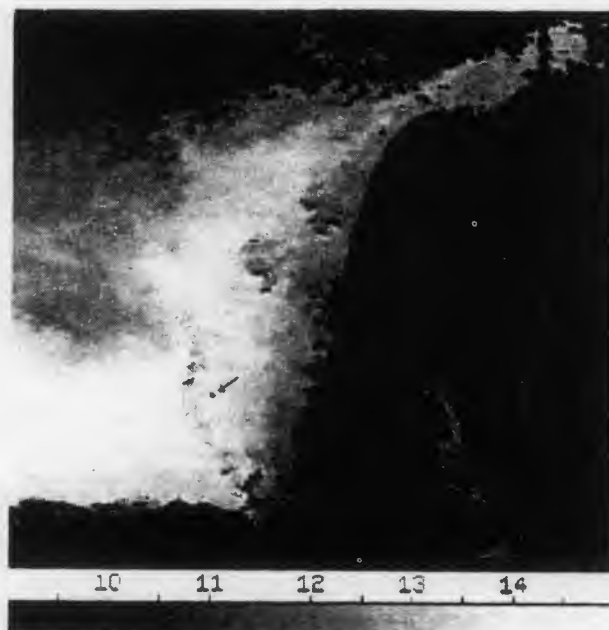
Table 1: Retrieval coefficients and estimated standard errors for equations (1) through (4)

Eq.	$a_0$	$a_1$	$a_2$	$a_3$	$a_4$	$a_5$	$a_6$	$\epsilon$
(1)	-0.053	1.015	2.475	-	-	-	-	0.39 K
(2)	-0.14	1.014	2.320	0.159	-	-	-	0.38 K
(3)	1.22	1.013	-0.530	0.281	-0.034	-0.121	0.278	0.18 K
(4)	1.20	1.011	-0.955	0.646	0.1715	-	-	0.19 K

Figure 4: Temperature deficits caused by the non-blackness of the sea surface at nadir view and  $\Theta = 50^\circ$ .

trapped in a spatial coherence test that is used to identify clouds.

Comparisons of ATSR-derived surface temperatures with those measured at the surface on 26 October 1991 and on 21 January 1992 are shown in figure 7. The two hour time series cover ERS-1 overpasses near 2100 UT. The bars demonstrate the range of ATSR-retrieved surface temperatures within boxes of  $3 \times 3$  pixels surrounding

Figure 5: Sea surface temperatures in  $^\circ\text{C}$  as derived from SADIST for the same scene as in figure 1. The position of the research platform *Nordsee* is indicated by the arrow.

the platform. The symbols indicate results from different retrieval schemes. It is clearly seen that results from those algorithms which are designed for the use with ATSR data match the surface skin measurements within few tenths of a degree while the application of retrieval schemes which were derived for the use with the Advanced Very High Resolution Radiometer (AVHRR), taken from Ref. 4, fail to match the in-situ means of comparison. The reason for this is mainly due to the different spectral locations of the  $12 \mu\text{m}$  channels of both instruments. The ATSR  $12 \mu\text{m}$  channel is shifted to higher wavelengths when compared to the corresponding AVHRR channel.

Further comparisons of the same type show similar results, however, a statistically significant conclusion cannot be drawn from the low number of match-ups yet. The use of ATSR measurements which are cloud covered to a small extent still contain information about the surface temperature as shown in figure 8 for an overpass on 6 January 1992 at 21:16 UT. A SADIST retrieved surface temperature is not available in this case because of the cloud influence which has been detected properly. The variability of the derived surface temperature as de-



Figure 6: SADIST cloud mask which has been applied to the image shown in figure 5. Bright areas have been assigned to be cloud covered.

rived with the remaining algorithms increases and certainly only the warmest retrievals represent a measure of the true surface temperature. For such cases a special retrieval scheme would be required that allows for partly cloud-contaminated measurements and that accounts for a supplemented error budget depending on the actual cloud impact.

## 6. CONCLUSIONS

Case studies have shown that sea surface temperatures as derived from ATSR with different retrieval algorithms match the surface skin temperatures which have been measured with a precisely calibrated radiation thermometer within few tenths of a degree. Partly cloudy ATSR data have been used too and show to be of value for SST retrievals within 0.5 to 1 K accuracy. Retrieval coefficients that are designed for the use with AVHRR data are inadequate for the use with ATSR measurements. The cloud detection scheme of SADIST properly rejects cloudy pixels but also cloud-free measurements in areas with strong SST gradients. The co-location of nadir and forward view measurements as given from the SADIST processing needs a further improvement for a better match-up. A further validation of ATSR derived sea surface temperatures is essential in order to get statistically significant conclusions about the accuracy of the derived products.

## ACKNOWLEDGEMENTS

We are grateful to Peter Kent and Albin Zavody both at Rutherford Appleton Laboratory for supplying the ATSR data and for fruitful discussions concerning the use of

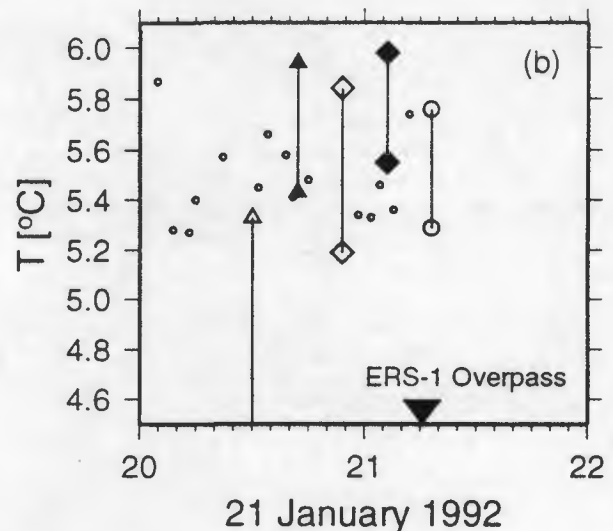
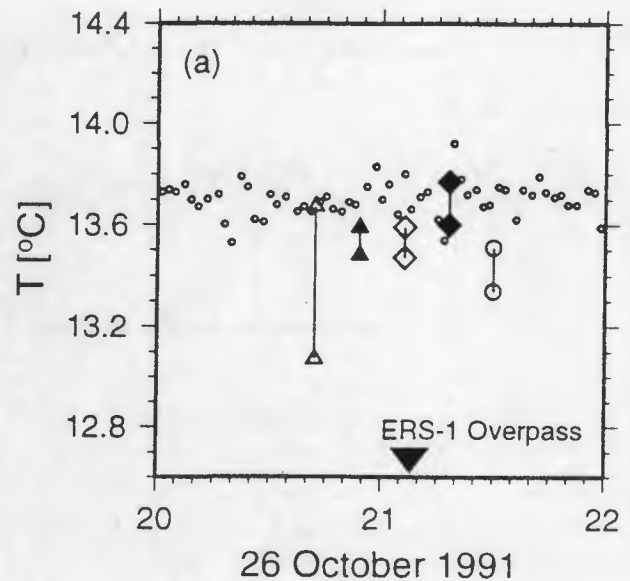


Figure 7: Time series of surface skin temperatures as measured with a KT-4 radiometer at the research tower *Nordsee* and SSTs derived from ATSR measurements (a) on 26 October 1991, 21:09 UT and (b) on 21 January 1992, 21:16 UT with different retrieval algorithms for a box of  $3 \times 3 \text{ km}^2$  using coefficients from ( $\Delta$ ) Ref. 3, ( $\blacktriangle$ ) Ref. 6, ( $\diamond$ ) equation (3), ( $\blacklozenge$ ) equation (4), and ( $\circ$ ) SADIST.

ATSR data. Thanks are due to Werner Biselli and to Michael Offermann as well as to the crew of the research tower *Nordsee* for their technical support in taking the surface skin measurements. This study has been supported by the Deutsche Forschungsgemeinschaft (DFG) and the Bundesministerium für Forschung und Technologie (BMFT).

## REFERENCES

1. Schlüssel P, Emery WJ, Grassl H, Mammen T 1990: On the bulk-skin temperature difference and its impact

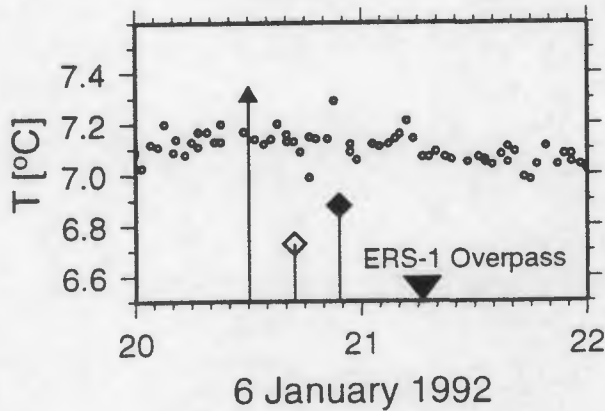


Figure 8: Same as in figure 7 but for 6 January 1992, 21:16 UT, considering a box of  $5 \times 5 \text{ km}^2$ .

on satellite remote sensing of sea surface temperature, Journal of Geophysical Research, 95, 13341-13356.

2. Schluessel P, Wick GA, Emery WJ 1992: A comprehensive comparison between skin and multi-channel sea surface temperatures as derived from AVHRR, Proceedings of the Central Symposium of the 'International Space Year' Conference, Munich, Germany, 30 March - 4 April 1992, 341-346.

3. McClain EP 1981, Multiple atmospheric-window techniques for satellite-derived sea surface temperatures, in Oceanography from Space, edited by J Gower, 73-85, Plenum, New York.

4. McClain EP, Pichel WG, Walton CC 1985, Comparative performance of ABHRR-based multichannel sea surface temperatures, Journal of Geophysical Research, 90, 11587-11601.

5. Walton CC 1988, Nonlinear multichannel algorithms for estimating sea surface temperature with AVHRR satellite data, Journal of Applied Meteorology, 27, 115-124.

6. Schluessel P, Shin HY, Emery WJ, Grassl H 1987: Comparison of satellite-derived sea surface temperatures with in situ skin measurements, Journal of Geophysical Research, 92, 2859-2874.

7. Barton IJ, Závody AM, O'Brien DM, Cutten DR, Saunders RW, Llewellyn-Jones DT 1989: Theoretical algorithms for satellite-derived sea surface temperatures, Journal of Geophysical Research, 94, 3365-3375.

8. Wick GA, Emery WJ, Schluessel P 1992: A comprehensive comparison between satellite-measured skin and multi-channel sea surface temperature, Journal of Geophysical Research, 97, 5569-5595.

9. Downing HD, Williams D 1975: Optical constants of water in the infrared, Journal of Geophysical Research, 80, 1656-1661.

## VALIDATION OF ATSR-1 USING AIRCRAFT RADIOMETER MEASUREMENTS OVER THE SOUTH ATLANTIC

A.H. Smith and R.W. Saunders

UK Met Office, Remote Sensing Instrumentation, Farnborough, UK

### ABSTRACT/RESUME

In November 1991, the First ATSR Tropical Experiment was carried out to validate the ATSR measurements of sea-surface temperature (SST) in the tropics. A multi-channel radiometer which had channels spectrally matched to those at  $11\mu\text{m}$  and  $12\mu\text{m}$  on the ATSR was flown around the tropics ( $8^{\circ}\text{S}, 14^{\circ}\text{W}$ ) on a C-130 aircraft and used to make radiance and brightness temperature measurements at a number of different altitudes. It was attempted to quantify the absorption/emission effect of any stratospheric aerosol due to the eruption of Mount Pinatubo in June 1991. ATSR sea surface temperature retrievals (using both nadir and forward instrument views) were compared with low level measurements of radiative sea surface temperature. Brightness temperature profiles of the atmosphere were obtained for comparison with those obtained from the Rutherford Appleton Laboratory radiative transfer model which was used to generate the ATSR SST retrieval coefficients.

Keywords: Sea surface temperature, ATSR, tropics, stratospheric aerosol

### 1 Introduction

The Along Track Scanning Radiometer (ATSR), an infrared radiometer designed for the measurement of sea surface temperature (SST), was launched on ERS-1, a sun synchronous polar orbiter, on 17th July 1991. Sea surface temperature measurements are made by measuring upwelling radiances in the atmospheric windows centred around  $3.7\mu\text{m}$ ,  $11\mu\text{m}$  and  $12\mu\text{m}$  through two different atmospheric paths, at nadir and  $55^{\circ}$  forward, within  $2\frac{1}{2}$  minutes of each other. This gives ATSR a better correction for the absorption and emission effects of the intervening atmosphere than any other existing radiometers used for SST retrievals. The atmospheric absorption around the wavelengths of the ATSR channels is highest in the tropics which means that tropical SSTs are more difficult to measure.

The First ATSR Tropical Experiment (FATE) was carried out in November 1991 by the UK Met Office in order to validate the ATSR measurements of SST in the tropics. A multi-channel radiometer (MCR) was flown on board a C-130 aircraft over an area of the Atlantic around Ascension Island ( $8^{\circ}\text{S}, 14^{\circ}\text{W}$ ) in order to measure radiances at a number of different altitudes. The MCR recorded radiances at a number of different views (nadir, nadir  $60^{\circ}$  and zenith) using narrow-band channels centred at  $11\mu\text{m}$  and  $12\mu\text{m}$  which were spectrally well matched to those on ATSR.

MCR radiances measured at 6.5km altitude were compared with those measured by ATSR in order to establish whether high concentrations of stratospheric aerosol (ie due to the eruption of Mount Pinatubo in June 1991) had affected the ATSR radiances.

At low flight levels a PRT-4 radiometer measured the radiative SST. This was then compared with the values of SST retrieved from ATSR using coefficients derived from the Rutherford Appleton Laboratory (RAL) radiative transfer model. Finally MCR nadir and zenith radiance measurements were made at several different levels in the atmosphere in order to validate the RAL radiative transfer model.

### 2 The Along Track Scanning Radiometer

The ATSR has three infrared channels centred at wavelengths of  $3.7\mu\text{m}$ ,  $11\mu\text{m}$  and  $12\mu\text{m}$  which are in atmospheric window regions for sensing the surface. An additional channel centred at  $1.6\mu\text{m}$ , in the near infrared, is used for the detection of cloud during the daytime. The ATSR achieves a high radiometric accuracy by having precise on-board calibration blackbody targets which are regularly viewed as part of the instrument's scan. In order to increase the ATSR's signal to noise ratio, the detectors are cooled to around 85K using a long life Stirling cycle cooler.

One advantage of using infrared radiation to estimate the SST is that the emissivity of the sea surface at these wavelengths is very close to unity: however the emission and absorption of longwave infrared radiation by the atmosphere is a process which is difficult to model accurately. In order to improve on SST measurements from space, the ATSR was designed to obtain a correction for the intervening atmosphere by observing a given area of the sea surface through two different atmospheric paths. The ATSR has a nadir view and a second view  $47^{\circ}$  forward of nadir which is equivalent to approximately  $55^{\circ}$  to local zenith for the ERS-1 orbit. As the brightness temperature measured in a given channel provides information on the SST and the intervening atmosphere, it follows that a second measurement of the brightness temperature through a longer path length will provide more knowledge of the intervening atmosphere. For more details on the ATSR instrument see Ref 1 and for ATSR instrument calibration see Ref 2.

Given an accurate calibration system and a knowledge of the ATSR spectral response, the measured signal can be converted to an equivalent blackbody brightness temperature. The SST in degrees K is obtained by combining the  $11\mu\text{m}$  and  $12\mu\text{m}$  brightness temperatures at nadir view only according to:

$$SST = \alpha T_{11} + \beta T_{12} + \gamma \quad (1)$$

This is the conventional 'split window' equation which is used for AVHRR SST retrievals. As  $\beta$  is negative, it is effectively the difference between the  $11\mu\text{m}$  and  $12\mu\text{m}$  brightness temperatures

which is used to calculate the SST. This brightness temperature difference gives a measure of how much infrared radiation is absorbed by the atmosphere. To make use of both the nadir and forward view ATSR brightness temperatures equation 1 is expanded to:-

$$SST = \alpha_N T_{11N} + \alpha_F T_{11F} + \beta_N T_{12N} + \beta_F T_{12F} + \gamma \quad (2)$$

where N and F denote nadir and forward views. The coefficients used in equations (1) and (2) have been derived theoretically to give the optimum performance in a given set of atmospheric conditions (eg. for this case tropical atmosphere coefficients are required). The coefficients used for equations (1) and (2) for the three clear air flights performed in FATE are listed in table 1. For a review of empirical and theoretical algorithms used to retrieve SST see Ref 3.

$\alpha_N$	$\alpha_F$	$\beta_N$	$\beta_F$	$\gamma$
3.9383	—	-2.8983	—	-12.128
6.5606	-3.3948	-4.8402	2.6567	4.978

$\alpha_N$	$\alpha_F$	$\beta_N$	$\beta_F$	$\gamma$
3.9454	—	-2.9052	—	-12.223
6.6196	-3.4706	-4.8657	2.6990	4.982

Table 1: The RAL coefficients used to calculate SST for nadir only (top row) and nadir and forward (bottom row) views. These are the values substituted into equations (1) and (2). The first set of coefficients applies for flights A139 and A144 whose flightpaths lay within  $\pm 25$ km of the sub-satellite track. The second set of coefficients applies for flight A143 which has a flightpath between 25 and 75km from the sub-satellite track.

### 3 C-130 Aircraft Radiometers

As well as having the capability to measure standard meteorological parameters such as static pressure, humidity and air temperature, the C-130 has two infrared radiometers which can be used to measure atmospheric and surface radiances.

#### 3.1 The Barnes PRT-4 Radiometer

This radiometer, which has a wide spectral response in the atmospheric window region of 8 - 14 $\mu$ m, is mounted directly beneath the aircraft fuselage so that it views downwards with a field of view of 2°. Calibration of the PRT-4 is carried out by moving a blackbody, whose temperature is normally kept within  $\pm 3$ K of the SST, in front of the radiometer. For the purpose of FATE this radiometer was used to measure the radiative SST from a height of about 70m. It has been shown (Ref 4) that the atmospheric absorption between the sea surface and the aircraft at this height is negligible when integrated over the PRT-4 spectral response. The measurement of radiative SST by the Barnes PRT-4 radiometer, which has an absolute accuracy of  $\pm 0.3$ K, is taken as the value against which the ATSR SST is validated.

#### 3.2 The Multi-Channel Radiometer (MCR)

The second infrared radiometer on board the C-130 aircraft is the Multi-Channel Radiometer (MCR). This is a narrowband radiometer which can view the sea surface at both nadir and a variety of oblique nadir views up to 60°. The radiometer can also view the zenith. During FATE regular measurements were made at the nadir, zenith and 60° forward view (as this is the closest view to the ATSR forward view at 55°). For FATE, two of the

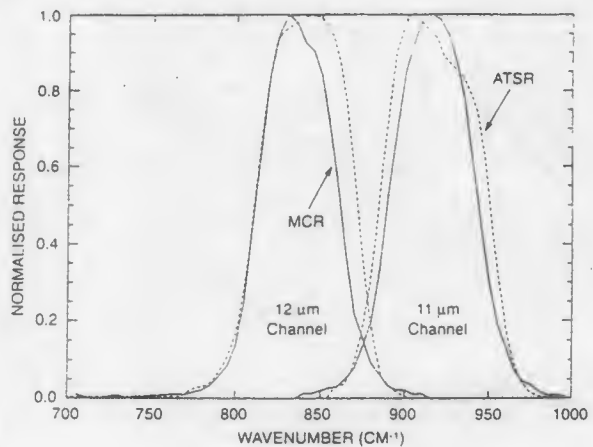


Figure 1: The spectral responses of the 11 $\mu$ m and 12 $\mu$ m channels of ATSR compared with similar channels on the Multi-Channel Radiometer

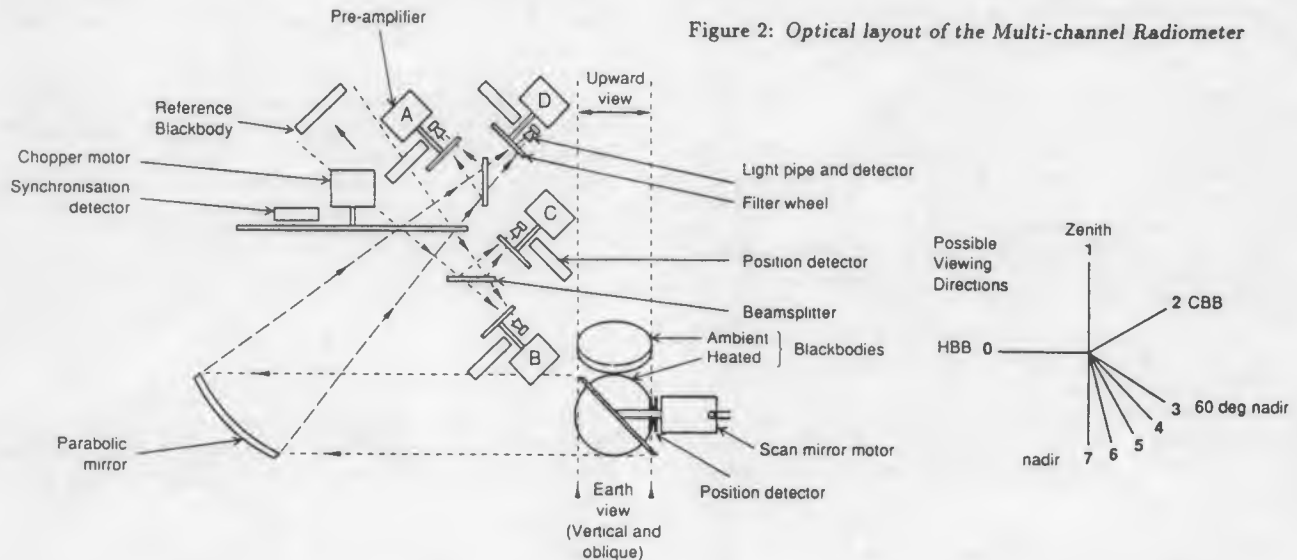


Figure 2: Optical layout of the Multi-channel Radiometer

narrow pass filters were rotated in front of pyroelectric triglycine sulphate (TGS) detectors. Figure 2 shows the layout of the MCR.

During each flight a blackbody is viewed for several minutes between the atmospheric measurements in order to obtain a continuous record of the gain of the longwave channels. In cloudfree conditions at high levels ( $> 6\text{km}$ ) the zenith view is also used to estimate the detector gain. The absolute accuracy of the MCR is  $\pm 0.3\text{K}$  (Ref 5)

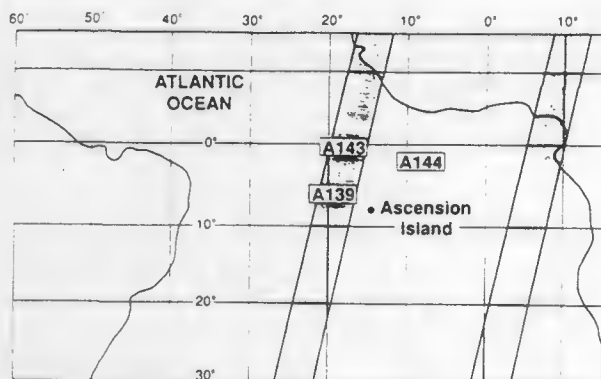


Figure 3: Locations of clear air flights A139, A143 and A144. The shaded area is the ATSR swath for flights A139 and A143.

#### 4 First ATSR Tropical Experiment

The UK Meteorological Office Research Flight mounted the First ATSR Tropical Experiment, (FATE), with the primary objective of validating ATSR top of atmosphere radiances and retrieved SSTs in tropical atmospheres. In addition MCR brightness temperatures were measured at a number of levels between 70m and 8km altitude to provide a brightness temperature profile which could be compared with that predicted by the RAL radiative transfer model which was used to derive the SST retrieval coefficients.

Figure 3 shows the region around Ascension Island ( $8^{\circ}\text{S}, 14^{\circ}\text{W}$ ) where FATE was carried out. This figure highlights the areas flown for three clear air flights A139, A143 and A144 (1/11/91, 7/11/91 and 8/11/91 respectively) with the ATSR sub-satellite track for flights A139 and A143 superimposed. Each flight is split into a number of runs corresponding to different C-130 altitudes. During each of the three clear air flights the aircraft was flying over a cloud-free region as shown in Figures 4(a),(b) and (c).

Top of the atmosphere brightness temperatures (ie. at 6.5km) were measured within ten minutes of the ERS-1 overpass. Approximately one hour later the aircraft was at the lowest level (70m) over the same area measuring the radiative SST using the  $11\mu\text{m}$  channel of the MCR and the PRT-4 radiometer. These measurements of radiative SST were taken as the 'ground truth' values to be compared with ATSR retrieved SSTs.

### 5 Results

#### 5.1 Top of Atmosphere Measurements

During each of the three clear air flights, the MCR was recording brightness temperatures at a height of approximately 6.5km within ten minutes of an ERS-1 overpass of the area. Brightness temperatures were also measured about five hours later at a height of 8km. For the purpose of this comparison the MCR measurements of brightness temperature taken at 6.5km will be used as these are closest in time to the ATSR overpass.

The ATSR data used for this validation were produced retrospectively by RAL using their in-house processing scheme which is called SADIST (Synthesis of ATSR Data Into Sea-Surface Temperature). This product contains 512 x 512 km collocated nadir and forward view brightness temperatures at 1km pixel resolution for the  $11\mu\text{m}$ ,  $12\mu\text{m}$  and the  $1.6\mu\text{m}$  channels of ATSR. Also supplied is a location grid containing 23 x 23 latitude/longitude pairs at 25km separation. This allows the location of any aircraft position to be calculated in terms of an along and across-track coordinate in the image. The estimated collocation error between the ATSR and C-130 aircraft positions is less than 2km at the earth's surface in the latitude and longitude directions. Figures 4(a),(b) and (c) show that the areas flown over at the time of the ERS-1 overpass were mainly cloudfree. Where it was suspected that a small amount of cloud was present those brightness temperatures which were colder and noisier than the surrounding values were removed from the average. Although these clouds do not show up in the MCR data, the aircraft scientist's log does refer to stratus being present outside the field of view of the MCR which may affect the ATSR average.

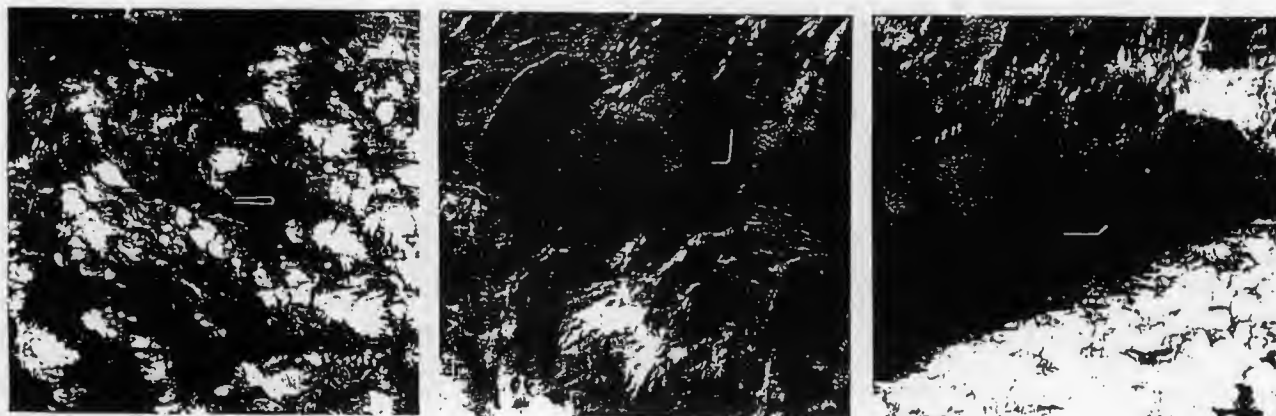


Figure 4: ATSR  $1.6\mu\text{m}$  reflectance images over a 512 x 512km area. The bold white lines represent the path of the C-130 aircraft at an altitude of 6.5km within ten minutes of the ERS-1 overpass. (a) A139, (b) A143 and (c) A144

Table 2 shows the averaged nadir and forward MCR and coincident ATSR 11 $\mu$ m and 12 $\mu$ m brightness temperatures for the three clear air flights. Each average is taken over one run of approximately 5 minutes close to midday. The table shows that MCR brightness temperatures are typically 0.8K warmer at 11 $\mu$ m and

Nadir View				
Flight	ATSR		MCR	
	11 $\mu$ m	12 $\mu$ m	11 $\mu$ m	12 $\mu$ m
A139	294.0K SD 0.1K	293.2K SD 0.1K	295.0K SD 0.5K	293.9K SD 0.6K
A143	293.3K SD 0.1K	292.0K SD 0.1K	293.9K SD 0.2K	292.4K SD 0.3K
A144	292.0K SD 0.1K	290.8K SD 0.1K	292.7K SD 0.3K	291.3K SD 0.3K

Forward View				
Flight	ATSR		MCR	
	11 $\mu$ m	12 $\mu$ m	11 $\mu$ m	12 $\mu$ m
A139	291.5K SD 0.1K	290.7K SD 0.2K	292.6K SD 0.7K	291.3K SD 0.6K
A143	290.3K SD 0.2K	289.0K SD 0.2K	290.7K SD 0.3K	289.0K SD 0.4K
A144	289.0K SD 0.05K	287.8K SD 0.1K	289.5K SD 0.3K	287.6K SD 0.4K

Table 2: Comparison of ATSR 11 $\mu$ m and 12 $\mu$ m brightness temperatures with coincident MCR brightness temperatures measured at approximately 6.5km altitude.

0.5K warmer at 12 $\mu$ m than the corresponding ATSR nadir view brightness temperatures. Absorption by the atmosphere between the MCR (at 6.5km) and the ATSR (777km) has been estimated as 0.4K at 11 $\mu$ m and 0.3K at 12 $\mu$ m by the RAL radiative transfer model. The remaining difference between MCR and ATSR brightness temperatures may be due to the presence of stratospheric aerosols as seen by other instruments on the C-130 (ref 6). Forward view MCR brightness temperatures are also warmer than those extracted for ATSR. Note that the ATSR forward view is at 55° to the local zenith compared with the MCR forward view of 60°. As the two paths to the surface are not identical, the MCR and ATSR forward view brightness temperatures cannot be so easily compared.

## 5.2 ATSR Sea Surface Temperature Retrievals

Approximately 100 minutes after the ERS-1 overpass, the C-130 aircraft flew down to a low level (70m) in order to measure the radiative SST using the MCR and the PRT-4 radiometer. Both of these radiometers have an absolute accuracy of  $\pm 0.3$  K. The measured radiative SSTs were averaged over a period of approximately five minutes. As the sea surface is not a pure blackbody at infrared wavelengths, a correction was made to the MCR and PRT-4 brightness temperatures for the downward reflected radiance which would apply for each flight and each spectral bandpass. The flightpath for this low level run was carried out close to, but not necessarily coincident with, the flightpath for the top of atmosphere brightness temperatures given in the previous section. When the ATSR brightness temperatures were extracted for this low level flightpath and compared with those corresponding to the top of atmosphere flightpath in table 2, both sets of brightness

Flight No	ATSR nadir view	ATSR nadir + forward views	MCR 11 $\mu$ m B Temp	PRT-4 8 - 14 $\mu$ m B Temp
A139	296.0K	297.4K	298.0K	298.0K
A143	296.6K	298.2K	299.0K	299.0K
A144	295.0K	296.6K	296.9K	297.3K

Table 3: Comparison of ATSR retrieved SSTs and brightness temperatures measured at 70m above the sea surface by the MCR 11 $\mu$ m channel and the PRT-4 radiometer (8-14 $\mu$ m). Each value is an average of a 5 minute, straight and level run. The reflected sky component in the MCR/PRT-4 measurement has been removed.

Flight No	MCR nadir view	MCR nadir + forward views	MCR 11 $\mu$ m B Temp	PRT-4 8 - 14 $\mu$ m B Temp
A139	297.9K	298.4K	298.0K	298.0K
A143	297.8K	298.9K	299.0K	299.0K
A144	296.3K	296.6K	296.9K	297.3K

Table 4: Comparison of MCR retrieved SSTs and MCR 11 $\mu$ m and PRT-4 (8-14 $\mu$ m) nadir brightness temperatures measured at 70m above the sea surface. The nadir and forward view MCR brightness temperatures were obtained at an altitude of 6.5km. Each value is an average of a 5 minute, straight and level run. The reflected sky component in the MCR/PRT-4 measurement has been removed.

temperatures agreed to within 0.1K, which is the average standard deviation of the brightness temperatures given in table 2.

ATSR SSTs are calculated by substituting the coefficients in table 1 in equations 1 and 2. Table 3 shows SSTs calculated using nadir only and both nadir and forward view ATSR brightness temperatures. The results show that for all three flights, the SSTs which are derived using 11 $\mu$ m and 12 $\mu$ m nadir view only brightness temperatures are 2.0K to 2.4K cooler than the radiative SST as measured by either the MCR or the PRT-4. When the ATSR forward view brightness temperatures for the 11 $\mu$ m and 12 $\mu$ m channels are combined with the nadir views according to the coefficients in table 1, the ATSR derived SSTs are 0.6K to 0.8K cooler than the measured radiative SST. Thus it has been shown for this case that combining the nadir and forward view ATSR brightness temperatures allows for a better correction of the intervening atmosphere than is possible using only the nadir brightness temperatures.

As an additional check on the retrieval, the MCR top of atmosphere temperatures are used to estimate the radiative SST using the same coefficients given in table 1. The results given in table 4 show that the SSTs retrieved using the MCR brightness temperatures are closer to the measured SSTs than the ATSR retrieved SSTs. This could be because the MCR brightness temperatures were not affected by stratospheric aerosol. For two out of the three flights (namely A143 and A144) the SSTs which are retrieved using 11 $\mu$ m and 12 $\mu$ m nadir and forward MCR brightness temperatures are closer to the measured radiative SSTs than are those SSTs calculated using nadir only views. However for flight A139 the SST estimated using the nadir only brightness temperatures of the MCR 11 $\mu$ m and 12 $\mu$ m channels is within 0.1K of the measured SST compared with the MCR estimate using nadir and forward

views which is 0.4K too warm. There are several possible reasons why the nadir only brightness temperature gives a better result in this case. Firstly the MCR radiances were noisier for this flight. Secondly the total water column for flight A139 is 23mm which is actually closer to a mid-latitude atmosphere (compared with ~40mm water column for flights A143 & A144). Also it should be noted that the coefficients in table 1 have been estimated for the special case of ATSR which has a forward view of 55° to the local zenith compared with the MCR forward view of 60° to local zenith. The ATSR signal to noise ratio is also much better than for the MCR. It follows that the coefficients derived for ATSR may not necessarily be appropriate for use on MCR data.

### 5.3 Brightness Temperature Profiles

During each of the three clear air flights, the MCR was able to make measurements of radiances at several different altitudes. At each level a zenith view radiance was measured, followed by measurements of the nadir and 60° nadir brightness temperature and radiances. The resulting brightness temperature profiles and zenith view radiances were supplied to RAL to be compared with those output from the radiative transfer model which is used to generate the SST coefficients given in table 1.

Examples of the brightness temperature profiles obtained during FATE are given in Figure 5. Figure 5(a) shows the 11 $\mu$ m brightness temperature profile for flight A139. The accuracy of MCR brightness temperatures is  $\pm 0.3$ K. The temperature deficit between the 11 $\mu$ m brightness temperatures measured at 70m altitude and those measured at 8km altitude gives an indication of how much absorption or emission has occurred for nadir and 60° nadir paths through the atmosphere. For flight A139 the temperature deficit is 2.5K for the nadir 0° view and 4.5K for the nadir 60° view. Also shown in figure 5(a) are the broadband PRT-4 measurements of SST and the ATSR 11 $\mu$ m nadir and 55° forward brightness temperatures.

A similar profile for the MCR 12 $\mu$ m brightness temperatures measured in flight A144 is shown in figure 5(b). In this case the temperature deficit between the values measured at 70m and 8km is 6.3K in the nadir 0° view and 8.3K in the nadir 60° view due to the higher total column water amounts for A144 and higher absorption at 12 $\mu$ m.

## 6 Conclusions

The First ATSR Tropical Experiment was planned to coincide with the end of the commissioning phase of ERS-1 in order to validate the operational SST retrieval algorithm developed by RAL. The objective of FATE was to measure brightness temperatures through a tropical atmosphere at the time of the ERS-1 overpass in channels similar to the 11 $\mu$ m and 12 $\mu$ m channels on ATSR and to obtain vertical profiles of ATSR channel radiances to verify the RAL radiative transfer model (and hence the SST retrieval coefficients).

For the three FATE clear air flights, the 'top of atmosphere' brightness temperatures measured by the MCR at 6.5km are on average 0.6K warmer than the equivalent ATSR 11 $\mu$ m and 12 $\mu$ m brightness temperatures. Half of this temperature difference is probably due to the presence of stratospheric aerosol (ie between the aircraft and ATSR) from the eruption of Mount Pinatubo in June 1991 and gives a measure of the effect of this aerosol at IR wavelengths.

The ATSR SSTs estimated using the nadir only 11 $\mu$ m and 12 $\mu$ m brightness temperatures are 2K to 2.4K cooler than the measured radiative SSTs. When the nadir and forward ATSR 11 $\mu$ m and 12 $\mu$ m brightness temperatures are combined using the RAL derived coefficients for a tropical atmosphere, the ATSR SSTs are only 0.6–0.8K cooler than the measured SSTs. This demonstrates the value of having two views through the atmosphere at least in the tropics when stratospheric aerosol is present. Part of this remaining bias (~0.7K) is likely to be due to the high concentra-

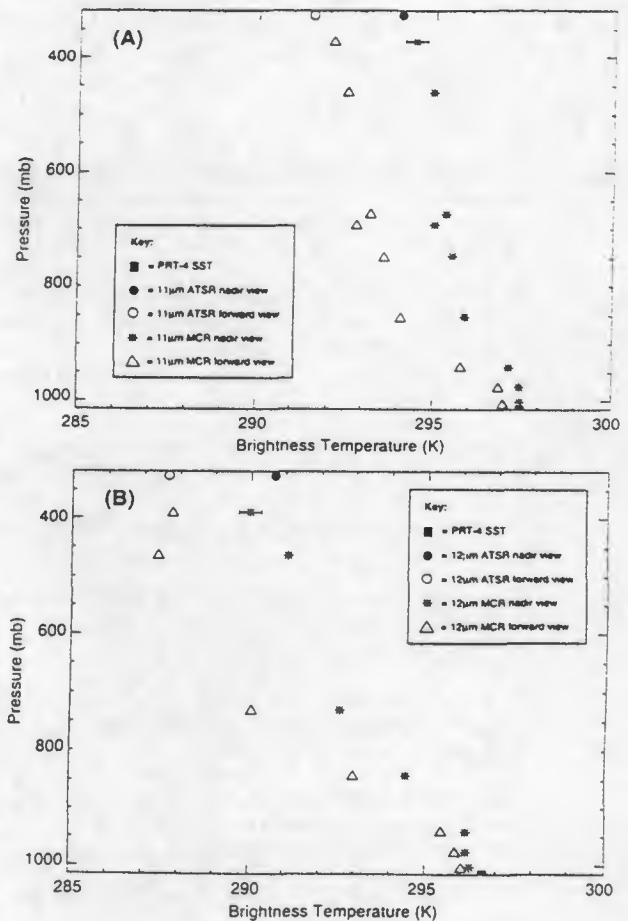


Figure 5: Brightness temperature profiles for (a) 11 $\mu$ m channel for flight A139 and (b) 12 $\mu$ m channel for flight A144.

tions of stratospheric aerosol present during this experiment. The aerosol effects are not included in the radiative transfer model used to generate the retrieval coefficients. This can be demonstrated using the high level nadir MCR brightness temperatures, unaffected by aerosol, which give SSTs much closer to those measured. Other biases in the radiative transfer model are now under investigation by comparison with the MCR nadir and zenith radiance profiles.

A recent comparison of ATSR SSTs with quality controlled drifting buoys reported in ref 7 also gives a cold bias but reduced to 0.4K. These data were not subject to high concentrations of stratospheric aerosol but would be expected to have a cold bias of several tenths of a degree due to the skin effect as in this case radiative SSTs are being compared with in-situ SSTs.

## 7 Acknowledgements

The ATSR was funded by the U.K. Science and Engineering Research Council with contributions from other institutes including the UK Met Office which provided the ATSR-1 focal plane assembly. Thanks are due to Wing Commander Blake for allowing the U.K. Meteorological Research Flight C-130 to operate out of Ascension Island and the RAF aircrew for their expert flying and continual guidance in planning and executing this campaign. The Met Research Flight of the UK Met Office carried out calibration of the MCR and PRT-4 data and supported the data analysis. Dr John Foot of the UK Met Office gave expert guidance at the early stages of this project. The Space Science Department of the

Rutherford Appleton Laboratory provided the FATE ATSR data and also gave helpful advice on analysing these data.

## 8 References

1. T. Edwards et al., 'The Along Track Scanning Radiometer - Measurement of Sea-surface Temperature from ERS-1' Journal of the British Interplanetary Society, Vol 43 pp160-180 (1990)
2. G. Mason, 'Test and calibration of the Along Track Scanning Radiometer, A satellite borne infrared radiometer designed to measure sea surface temperature.' D.Phil. Thesis Dept of Atmospheric, Oceanic and Planetary Physics, University of Oxford (1991)
3. I. Barton, 'Satellite-derived Sea Surface Temperatures - A comparison between Operational, Theoretical and Experimental Algorithms' Journal of Applied Meteorology May 1992, Vol 31, pp433-442 (1992)
4. R. W. Saunders and P. J. Minnett, 'The Measurement of Sea Surface Temperature from the C-130' MRF Internal Note 52 (1990)
5. R. W. Saunders and K. J. Dewey, 'The calibration of the longwave infrared channels of the Multi-channel radiometer' MRF Internal Note No 48 (1989)
6. R. W. Saunders, 'Radiative properties of the Mount Pinatubo volcanic aerosols over the Tropical Atlantic' submitted to Geophysics Research Letters (1992)
7. D.L. Harrison and C.P. Jones, 'A user appraisal of ATSR near real time products' in Report on First ERS-1 workshop Cannes Nov 1992.

## A USER APPRAISAL OF ATSR NEAR-REAL-TIME PRODUCTS

Dawn L. Harrison and Clive P. Jones

United Kingdom Meteorological Office  
London Road, Bracknell, Berkshire, England

### ABSTRACT

ATSR near-real-time (NRT) products consist of  $0.5^\circ \times 0.5^\circ$  averaged sea surface temperatures (ASSTs) plus ancillary data. Data are processed at Tromsø Satellite Station (TSS) and are transmitted to the United Kingdom Meteorological Office (UKMO), the end user, within 24 hours of their acquisition. The major task performed by the UKMO is to assess the quality of the NRT products with a view to incorporating the data in the operational SST analysis scheme. Comparison of NRT ASSTs with drifting buoys indicates that a bias of around  $-0.4\text{K}$  exists. This can largely be attributed to the genuine difference between the temperature of the ocean's radiative skin, as measured by ATSR, and the sub-surface bulk temperature measured by buoy sensors.

Keywords: ATSR, sea surface temperature, drifting buoys, skin-bulk temperature difference.

### 1. INTRODUCTION

The ATSR NRT demonstration project was established in order to address the needs of meteorological centres for fast-delivery (FD) data (ref. 1). It is a joint venture between Rutherford Appleton Laboratory (RAL), TSS and the UKMO, who are the pilot users of the data. ATSR NRT products consist of  $0.5^\circ \times 0.5^\circ$  ASSTs plus ancillary data.

The aim of the NRT demonstration project is to show that the data processing and transmission system devised can provide data, of high quality and in near real time, to an end user. If this can be achieved then it is hoped that the system will eventually be adopted by ESA as part of the ERS-1 FD service, which currently includes products from the scatterometer and radar altimeter. This will allow distribution of ATSR NRT products to other users.

The NRT ASSTs are assessed by comparison with coincident SSTs derived from the UKMO's operational global SST analysis and with collocated, high quality drifting buoy observations. The evaluation has been further subdivided into day and nighttime observations and those resulting from the use of single and dual view data because different algorithms are used for the SST retrieval under these conditions.

### 2. NRT PRODUCT RECEPTION

NRT products from the ATSR have been received by the UKMO since November 1991. The raw data are processed at TSS to form the ASSTs and the products are quality assured using data from the satellite's engineering reports. The quality assured products are then transmitted to the UKMO within 24 hours of their acquisition. On average, approximately 13000 ASSTs are received per day (see figure 2.1). The gaps in reception are the result of several different factors: orbit manoeuvres, payload power shut-downs and instrument operations have all caused data to be lost. Problems with the main antenna at TSS and with the communication links to the UKMO have also resulted in loss of data products on a number of occasions.

Reasonable coverage for latitudes between  $55^\circ\text{N}$  and  $55^\circ\text{S}$  is generated in several days, as indicated by figure 2.2 which shows data coverage for a 10 day period. At present, only sparse quantities of data are obtained for higher latitudes. This is due to imperfections in the cloud screening procedure causing an overestimation of the number of measurements contaminated by cloud. Optimisation of the cloud detection thresholds is still ongoing at RAL and has proved a complex task. Future modifications should go some way to improving the coverage obtained at mid/high latitudes.

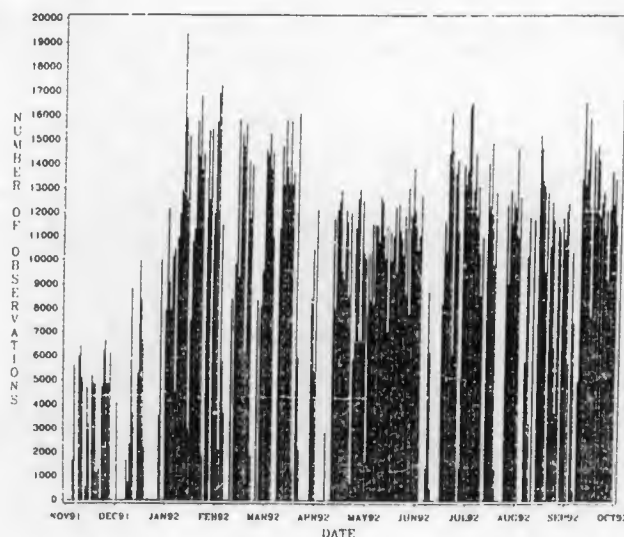


Figure 2.1: The total number of ATSR NRT products received by the UKMO per day, 01/11/91 to 01/10/92.

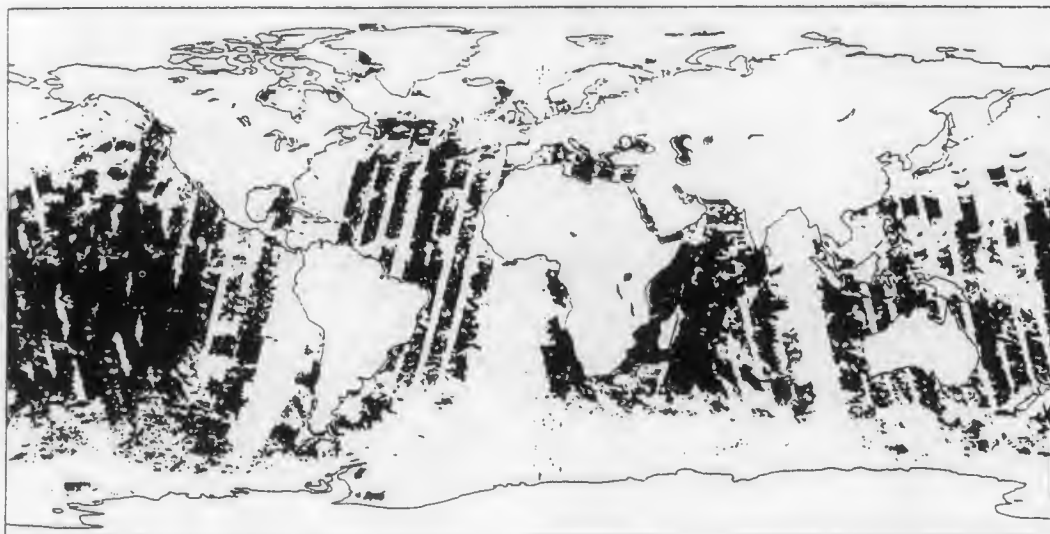


Figure 2.2: The distribution of ATSR NRT products for the period 08/08/92 to 17/08/92.

The processing of ATSR NRT products at TSS is limited to a maximum of 10 ERS-1 orbits per day. This results in some missing orbits, which can be identified in figure 2.2, and prevents global data coverage.

### 3. NRT PRODUCT EVALUATION

#### 3.1. Comparison against an *in situ* analysis

The quality of the NRT products is assessed primarily by comparison with coincident SSTs from the UKMO's operational analysis. This analysis is performed once per day and incorporates observations from surface marine sources (ships, buoys and bathythermographs) received, via the global telecommunications system, in a 24 hour period. The observations undergo quality control and then a background field, simply the previous analysis, is updated by incorporating the new observations using an iterative assimilation scheme. A detailed description of the UKMO operational SST analysis scheme is given by ref. 2.

The comparison of this analysis of *in situ* data and the NRT products has been useful in several respects: during the initial period of operation anomalies in the NRT processing system were rapidly identified and corrected and the impact of subsequent changes to the data processing system could be easily evaluated.

A global mean bias, for dual view data, of approximately -1 K with respect to the SST analysis (see table 3.1) has been persistent throughout the lifetime of the project. Part of this negative bias can be attributed to the genuine difference between the temperature of the oceans radiative skin, as measured by the ATSR, and the sub-surface bulk temperature measurements from ships and buoys. The skin temperature is generally of the order of several tenths of a degree K cooler than the bulk temperature but the difference is dependent on variations of a number of elements including surface wind stress, solar insolation and cloud cover (ref. 7). Other factors which may contribute to the detected bias are diurnal effects and the incomplete screening of cloud. The use of SST measurements made via the engine intake of ships in the SST analysis scheme may also be influential. This method of observing has been shown, in many cases, to produce temperatures with a warm bias of around 0.3 K (ref. 3).

#### 3.2. Single and dual view differences

The main feature of the ATSR which facilitates the retrieval of SSTs with an accuracy better than previously attainable is the availability of data from two views. This is made possible by the conical scanning technique employed by the instrument. The difference between ASSTs calculated from single and those derived from dual view data has been examined. ASSTs based on single view data are returned where both views are not cloud free. Table 3.1 shows the bias with respect to the bulk analysis for both single and dual view data and demonstrates the increased agreement achievable using the dual view algorithm. This is not surprising: the single view algorithm is intrinsically less successful in correcting for atmospheric attenuation and the single views tend to originate from more cloudy areas and are hence more prone to error (ref. 4).

Further evidence of the improvement in performance possible using the dual view technique is obtained by looking at the difference between dual view ASST and the corresponding ASST derived from the nadir view only. The differences, for 10 latitude bands, are plotted in figure 3.1. The largest discrepancies are found at tropical latitudes which coincides with the location of the greatest concentration of water vapour and the area where single view retrieval algorithms perform least well. Although the improved performance demonstrated by the dual view technique is very encouraging the results are by no means conclusive: the improved performance may simply be a reflection of errors in the single view retrieval algorithm.

Latitude	N		Mean O-A		S.D. O-A		Dual-single
	Single	Dual	Single	Dual	Single	Dual	
60-90 N	186	N/A	-1.70	N/A	0.88	N/A	N/A
30-60 N	15150	12176	-1.07	-1.06	0.74	0.80	0.23
0-30 N	25078	61389	-1.85	-1.13	0.65	0.62	0.46
0-30 S	28779	82544	-1.53	-1.00	0.55	0.56	0.38
30-60 S	32826	25452	-1.66	-1.35	0.75	0.80	0.30
60-90 S	1996	44	-1.57	-1.87	0.61	0.51	0.04
All	109703	15	-1.58	-1.10	0.67	0.63	0.38

Table 3.1: Observation minus analysis statistics for single and dual view ATSR NRT products, September 1992.

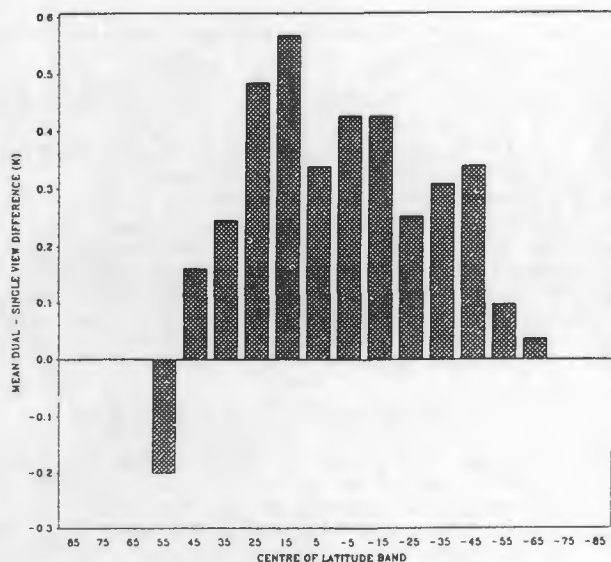


Figure 3.1: The mean difference between ATSR dual and nadir only view SSTs for 10° latitude bands, September 1992.

### 3.3. Comparison against drifting buoys

An additional study comparing ATSR NRT products with collocated, quality controlled, drifting buoy measurements has been carried out. Drifting buoy measurements are generally considered to give reliable SST measurements and have been used extensively to calibrate SSTs derived using other satellite instruments such as AVHRR (ref. 5).

Spatial and temporal limits for coincident ATSR and drifting buoy observations were set at 0.5° latitude/longitude and  $\pm 3$  hours. Figure 3.2 shows ATSR-drifting buoy observations, for day and nighttime observations made during August 1992. A mean bias for day and nighttime data is plotted using linear regression. The distribution of the drifting buoys used in this study is illustrated by figure 3.3: the Pacific and North Atlantic Oceans are well represented but few drifting buoys producing collocations are found in the South Atlantic or Indian Oceans. The daytime data show an overall bias of -0.4K; the nighttime bias is approximately 0.5 K larger. The

regression lines are approximately horizontal indicating a consistent bias over a range of sea temperatures. The daytime results are very encouraging since the remaining bias can largely be explained by the skin-bulk temperature difference. The poorer performance of night time ASSTs is probably the result of the loss of the 3.7  $\mu\text{m}$  channel (from 27/05/1992) and the consequent problems in identifying low level cloud. These results are significantly different from those obtained using the operational analysis and further highlight the limitations of using ship SSTs, a large proportion of which are now derived from engine intake temperature readings.

## 4. THE OPERATIONAL APPLICATION OF NRT PRODUCTS

One reason for the evaluation of ATSR NRT data is to deduce whether the data are of sufficient quality to be used in the operational SST analysis scheme. Other sources of satellite data have been used in the past: AVHRR and Meteosat data were used until shortly after the eruption of Mount Pinatubo, in June 1991. It became

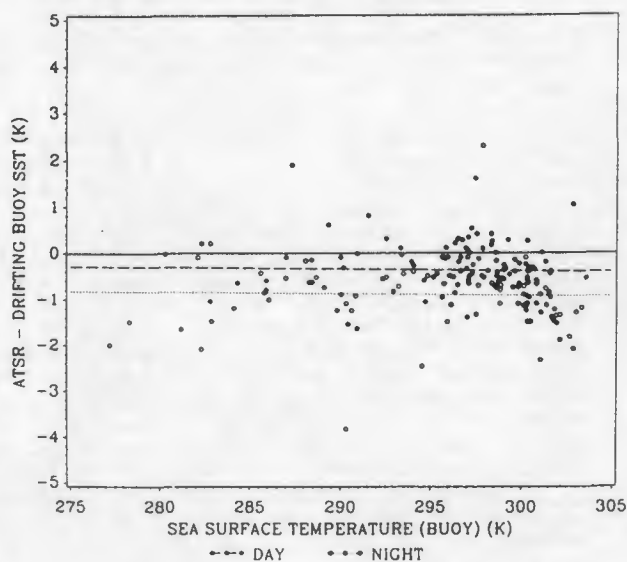


Figure 3.2: An illustration of the difference between collocated drifting buoy and ATSR dual view ASSTs, August 1992.

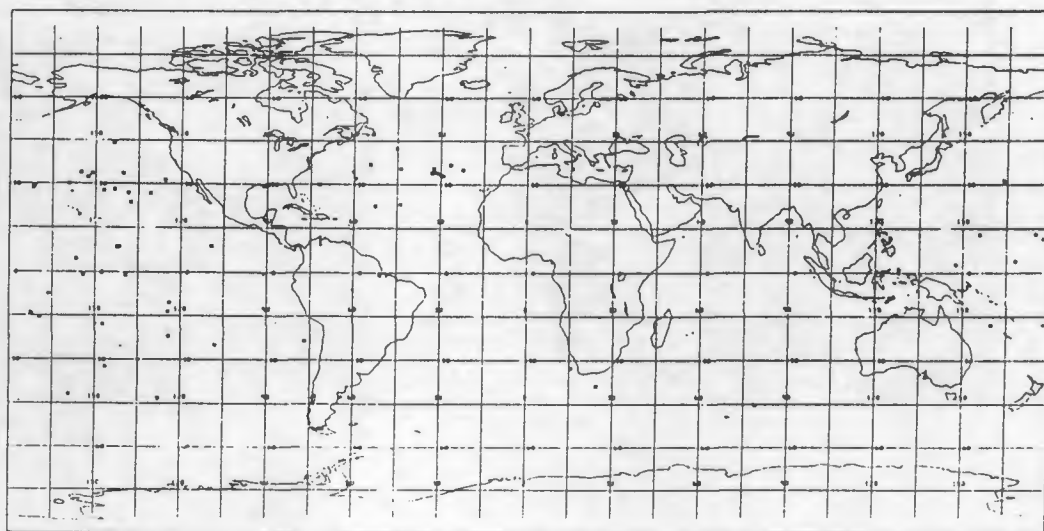


Figure 3.3: The distribution of drifting buoys used in the collocation study.

evident that aerosols forced into the stratosphere as a result of the eruption were having a detrimental effect on the quality of the SST retrievals (ref. 6). The dual view technique of the ATSR should mean that accurate SST retrievals are possible even under conditions of high aerosol concentrations.

Validation statistics for ATSR NRT data and other sources of SST observations are shown in table 4.1. The other satellite derived SSTs (from the NOAA polar orbiting satellites with AVHRR and the European

Observation type	N	Mean		Std. deviation	
		O-A	O-C	O-A	O-C
Ships	55127	0.06	0.24	1.05	1.17
Moored buoys	43978	-0.02	0.19	0.52	0.68
Drifting buoys	35182	-0.04	-0.09	0.36	0.56
Bathythermospheres	1186	0.18	0.44	0.41	0.53
Meteosat	30998	-0.47	-0.49	0.75	0.72
GMS	15884	-0.97	-1.90	1.12	1.16
AVHRR (NOAA-11)	90987	-0.13	-0.08	0.68	0.70
ATSR (ERS-1)	181605	-1.10	-1.01	0.63	0.65

Table 4.1: Observation minus analysis and observation minus climatology statistics for all SST observation types, September 1992.

(Meteosat) and Japanese (GMS) geostationary platforms) are derived using algorithms that are tuned empirically using *in situ* data. They are therefore estimates of bulk SST and have smaller biases than obtained from ATSR dual view data but comparable standard deviations. The standard deviation for ship data is considerably larger. These figures indicate the potential value of ATSR data once a suitable method for eliminating the bias problem has been established. One approach is to devise an empirical bias correction scheme based on selected high quality surface based observations. The other possible approach is to parameterize the skin effect using surface wind stress and heat flux fields from a numerical weather prediction model. This will take some time to develop.

Trial analyses using ATSR data only have been performed and the differences between these and the operational scheme have been examined (see figure 4.1). In general differences are negative and lie in the range -0.5 to -1.5 K. However, where data are missing

due to data processing constraints (see section 2) the pattern changes because the analysis reverts to climatology, which is based on ship (bulk) SST observations. The analysis is therefore inconsistent in its representation of SST. These anomalies would not occur if a correction was applied to the ATSR data to convert between skin and bulk temperatures.

AVHRR and ATSR data will be introduced into the operational analysis in the near future with a bias correction based on *in situ* data applied. This will greatly improve the global coverage provided by the various SST data sources, particularly in the southern hemisphere where coverage is sparse in the absence of satellite data, and should therefore lead to a better analysis.

## 5. SUMMARY AND CONCLUSIONS

ATSR NRT products have been evaluated over a period of one year. After the initial elimination of several errors in the processing system the data products are now of a quality which makes them suitable for operational application. Daytime ASSTs derived using the dual view algorithm give the best agreement with surface based observations. These data show a bias of approximately -0.4 K compared with drifting buoy observations. This can largely be attributed to the genuine difference between the oceans radiative skin and the sub-surface bulk temperature. ATSR data will therefore be introduced into the UKMO's operational SST analysis scheme in 1993 along with a bias correction scheme to eliminate the skin effect.

The improved agreement with *in situ* observations achieved by dual view SSTs suggests that the conical scanning technique used by the ATSR does produce improved results. The differences may, however, be simply be a reflection of errors in the single view retrieval algorithm.

## 6. ACKNOWLEDGEMENTS

The success of the ATSR NRT demonstration project has been possible only with inputs from a number of organisations: the funding provided by ESA and the Science and Engineering Research Council and the efforts of staff at RAL and TSS are greatly appreciated.

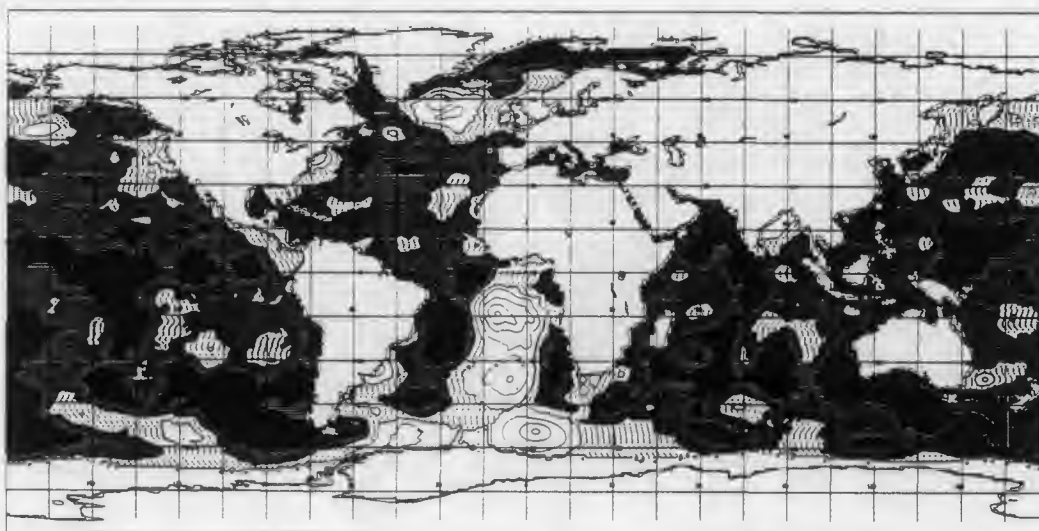
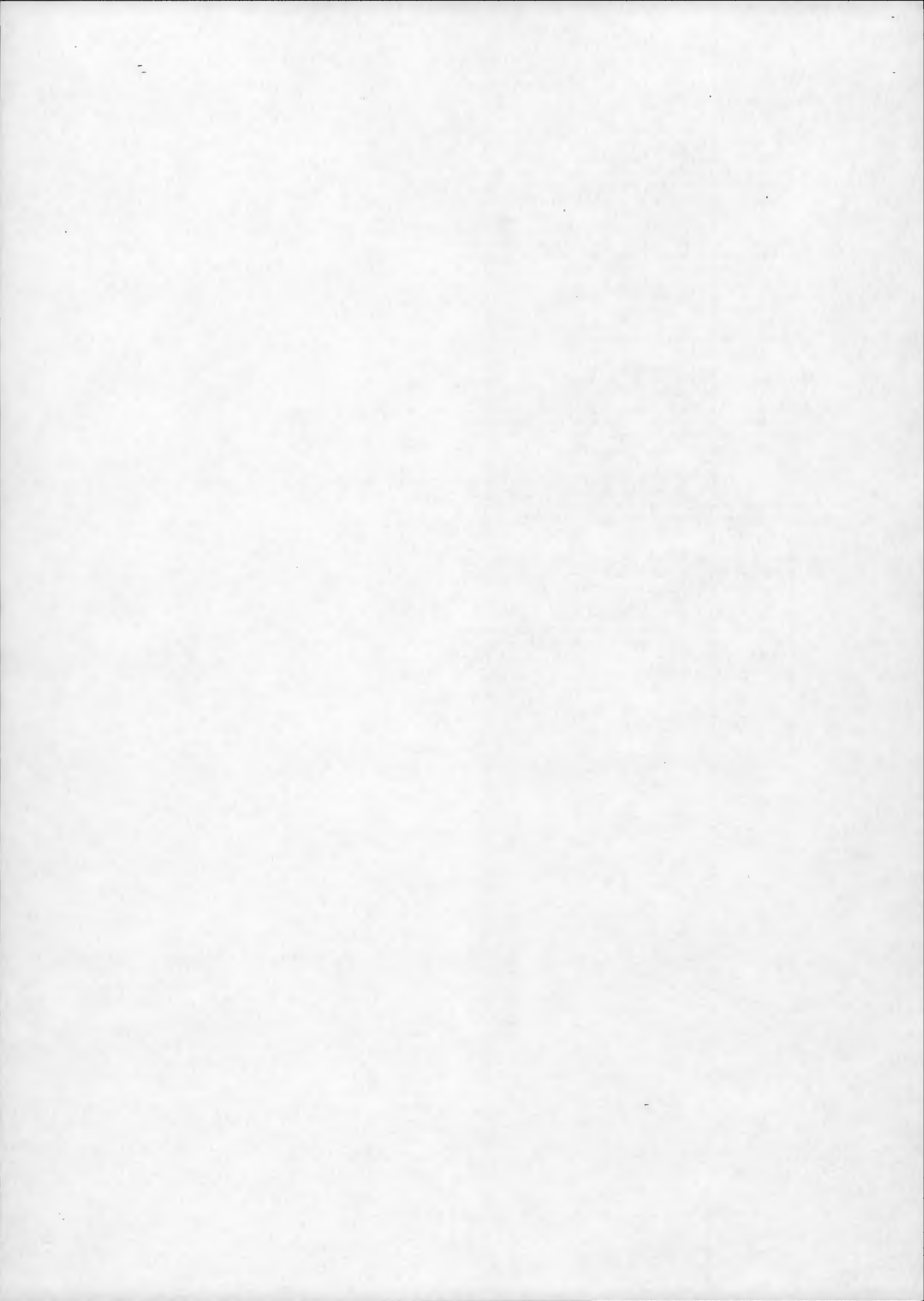


Figure 4.1: The difference between an ATSR only and the *in situ* analysis. The analyses are valid for 18/08/92: a 'spin up' period of 10 days was allowed for the ATSR analysis. Shading: light (0 to -0.5 K), intermediate (-0.5 to -1 K), dark (<-1 K).

## 7. REFERENCES

1. Eccles, D., Minde, S., Lee, D. and Harrison, D. L. (1992). The ATSR near-real-time demonstration project preliminary evaluation report. (Report compiled under ESA/ESRIN contract 9617/91/HGE-1).
2. Jones, C. P. (1991). The operational sea surface temperature analysis scheme. *Short range forecasting research technical note*, 67, Met. Office, Bracknell, Berkshire (unpublished document).
3. Kent, E. C., Truscott, B. S., Taylor, P. K. and Hopkins, J. S. (1991). The accuracy of Ships' Meteorological observations: Results of the VSOP-NA. *Marine Meteorology and related Oceanographic Activities*, 26, W.M.O.
4. Lorenc, A. C., Bell, R. S., Foreman, S. J., Holt, M. W., Offiler, D., Hall, C. D., Harrison, D. L. and Smith, S. G. (1992). The use of ERS-1 products in operational meteorology. *Short Range Forecasting Research Scientific Paper*, 9, Met. Office, Bracknell, Berkshire (unpublished paper).
5. Minnett, P. J., (1987). Satellite infrared scanning radiometers - AVHRR and ATSR/M. In: Vaughan, R. A. (ed.), *Microwave Remote Sensing for Oceanographic and Marine Weather-Forecast Models*, Dordrecht, D. Reidel, 141-163.
6. Reynolds, R. W. (1991). Effects of Mt. Pinatubo on NMC/CAC SSTs. *World Climate Research Programme Publication*, 63, J1-8, W.M.O.
7. Schluessel, P., Emery, W. J., Graßl, H. and Mammen, T. (1990). On the bulk-skin temperature difference and its impact on satellite remote sensing of sea surface temperature. *Journal of Geophysical Research*, 95, 13341-13356.



## CLOUD STUDIES USING ATSR DATA

C. I. Rice and E. J. Williamson

Department of Atmospheric, Oceanic and Planetary Physics  
University of Oxford, UK

### ABSTRACT

The two angle measurement technique of ATSR provides the opportunity of determining cloud characteristics. A simple one-layer model of a cloud can be used to determine the cloud top temperature and cloud optical depth from ATSR radiances in the nadir and forward views. Results are presented in which optically thick and optically thin clouds are identified using an interactive image display system.

**Keywords** ATSR, Cloud, Optical depth, Retrieval

### 1. The cloud model

A simple one layer model of a cloud is shown in figure 1. According to this model, the radiance received by ATSR when observing this cloud is given by

$$R_i(\theta) = B_i(T_\theta) - f(1 - e^{-\delta_i(\theta)}) [B_i(T_\theta) - B_i(T_c)]$$

where

$R_i(\theta)$  is the radiance measured by ATSR in channel  $i$  at zenith angle  $\theta$

$B_i(T)$  is the Planck function corresponding to measured brightness temperature  $T$  in channel  $i$

$T_\theta$  is the brightness temperature corresponding to a radiance at zenith angle  $\theta$

$f$  is the fraction of the field of view covered by cloud

$\delta_i(\theta)$  is the optical depth of the cloud in channel  $i$  at zenith angle  $\theta$

$T_c$  is the cloud top temperature

This model ignores scattering of radiation by the cloud and atmospheric absorption and emission above the cloud.

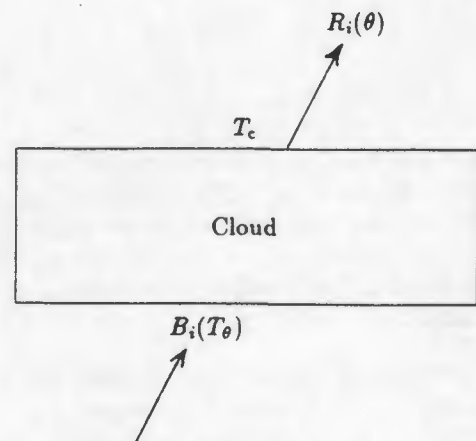


Figure 1. The cloud model

The optical depth is related to the cloud's spectral and geometric properties through

$$\delta_i(\theta) = \frac{z\beta_i}{\cos \theta}$$

where

$z$  is the geometric thickness of the cloud

$\beta_i$  is the volume extinction coefficient in channel  $i$

$\theta$  is the zenith angle

We will restrict ourselves to situations in which the cloud fills the field of view of ATSR ( $f = 1$ ). In this case the radiance can be written

$$R_i(\theta) = B_i(T_\theta)e^{-\delta_i(\theta)} + (1 - e^{-\delta_i(\theta)})B_i(T_c)$$

In the case of an optically thick cloud,  $\delta_i(\theta) \rightarrow \infty$  so  $R_i(\theta) = B_i(T_c)$  and the measured radiance is independent of zenith angle.

In the case of optically thin clouds, however, the ATSR measured radiance will be different in each of the nadir and forward views corresponding to the same cloud pixel.

If the zenith angles in the nadir and forward views are  $\theta_N$  and  $\theta_F$  respectively then the optical depths of the cloud in the two views will be given by

$$\delta_i(\theta_N) = \frac{z\beta_i}{\cos\theta_N} \quad \text{and} \quad \delta_i(\theta_F) = \frac{z\beta_i}{\cos\theta_F}$$

where  $z\beta_i = \delta_i(0)$  is the optical depth in the vertical direction.

The measured radiances in the two views will be given by

$$R_i(\theta_N) = B_i(T_{\theta_N})e^{-\frac{\delta_i(0)}{\cos\theta_N}} + (1 - e^{-\frac{\delta_i(0)}{\cos\theta_N}})B_i(T_c)$$

and

$$R_i(\theta_F) = B_i(T_{\theta_F})e^{-\frac{\delta_i(0)}{\cos\theta_F}} + (1 - e^{-\frac{\delta_i(0)}{\cos\theta_F}})B_i(T_c)$$

Here we have two equations in three unknowns. However the values of  $B_i(T_{\theta_N})$  and  $B_i(T_{\theta_F})$  can be estimated from measurements made in nearby clear pixels on the assumption that the radiance will be the same. This allows us to solve the equations for  $\delta_i(0)$  and  $T_c$ .

If we look at the difference between the forward and nadir views we obtain the relation

$$R_i(\theta_N) - R_i(\theta_F) = B_i(T_{\theta_N})e^{-\frac{\delta_i(0)}{\cos\theta_N}} - B_i(T_{\theta_F})e^{-\frac{\delta_i(0)}{\cos\theta_F}} - B_i(T_c) \left( e^{-\frac{\delta_i(0)}{\cos\theta_N}} - e^{-\frac{\delta_i(0)}{\cos\theta_F}} \right)$$

In the case of optically thick cloud, the difference is zero and if there is no cloud ( $\delta_i(0) = 0$ ) the difference is

$$B_i(T_{\theta_N}) - B_i(T_{\theta_F})$$

as we would expect. This difference is small unless the atmospheric correction is large. In the case of optically thin cloud, the difference can become much larger. This is illustrated in figures 2 - 4 which show images in the forward and nadir views and the difference image. An area of thin cloud which is not evident in the separate views shows up clearly as a dark area in the difference image.

Co-locating the forward and nadir views is not always easy and an interactive program has been written that allows this to be done manually. A cloud usually appears different in the two views. This is illustrated in figure 5.

The cloud appears displaced, mainly due to the stereoscopic effect which is proportional to cloud height. It may also have moved due to winds in the time between the forward and nadir views although this effect is usually small. It also changes shape becoming larger in the forward view. This effect increases with the thickness of the cloud.



Figure 2. Siberia (nadir view)

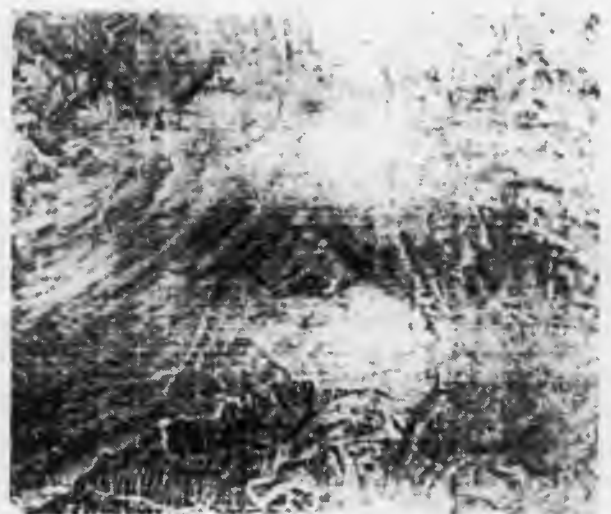


Figure 3. Siberia (forward view)

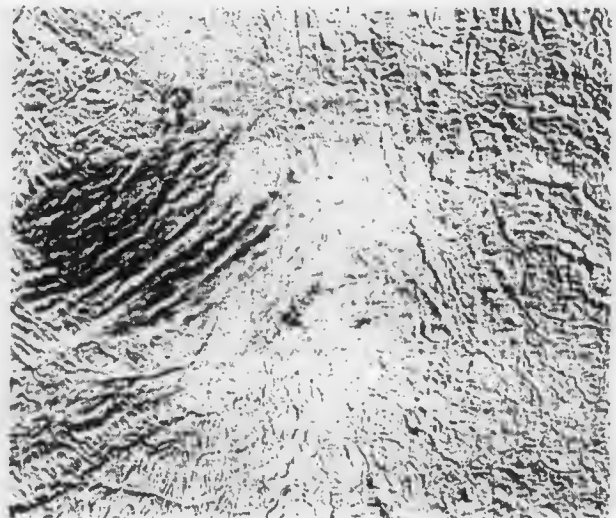


Figure 4. Siberia (difference image)

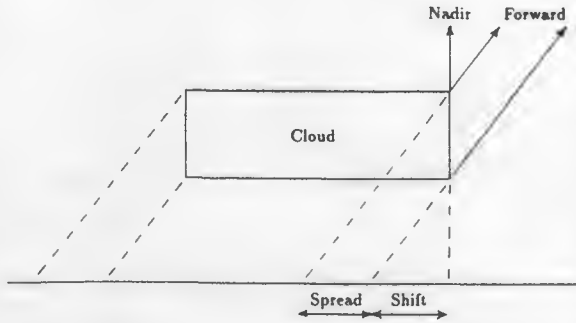


Figure 5. Cloud displacement and distortion

A second example illustrates the effect of optically thick and optically thin clouds. Figure 6 shows a nadir image with two areas of cloud identified as A and B. The clouds look much the same. In the difference image, figure 7, cloud A has virtually disappeared showing it to be an optically thick cloud whereas cloud B has turned black identifying it as an optically thin cloud.

We are hoping to automate the cloud registration process so that data can be processed to produce global cloud statistics.

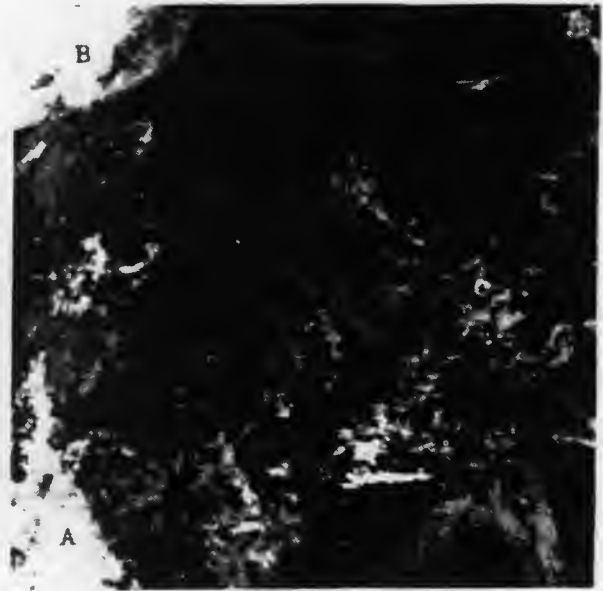


Figure 6. Lake Victoria (nadir view)

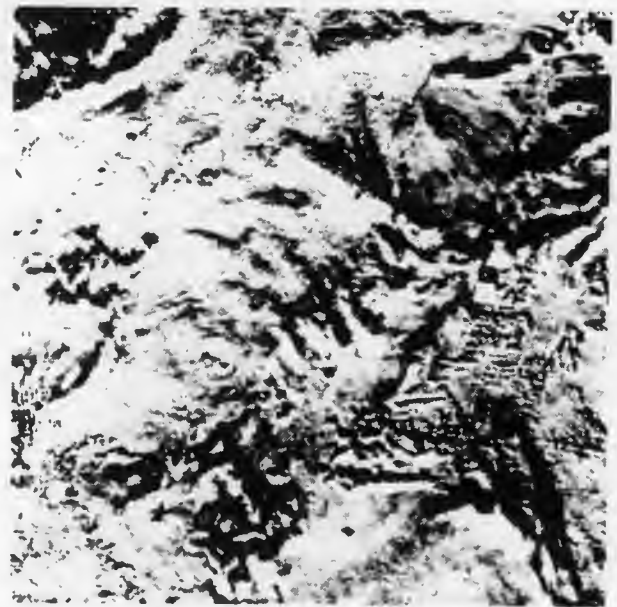
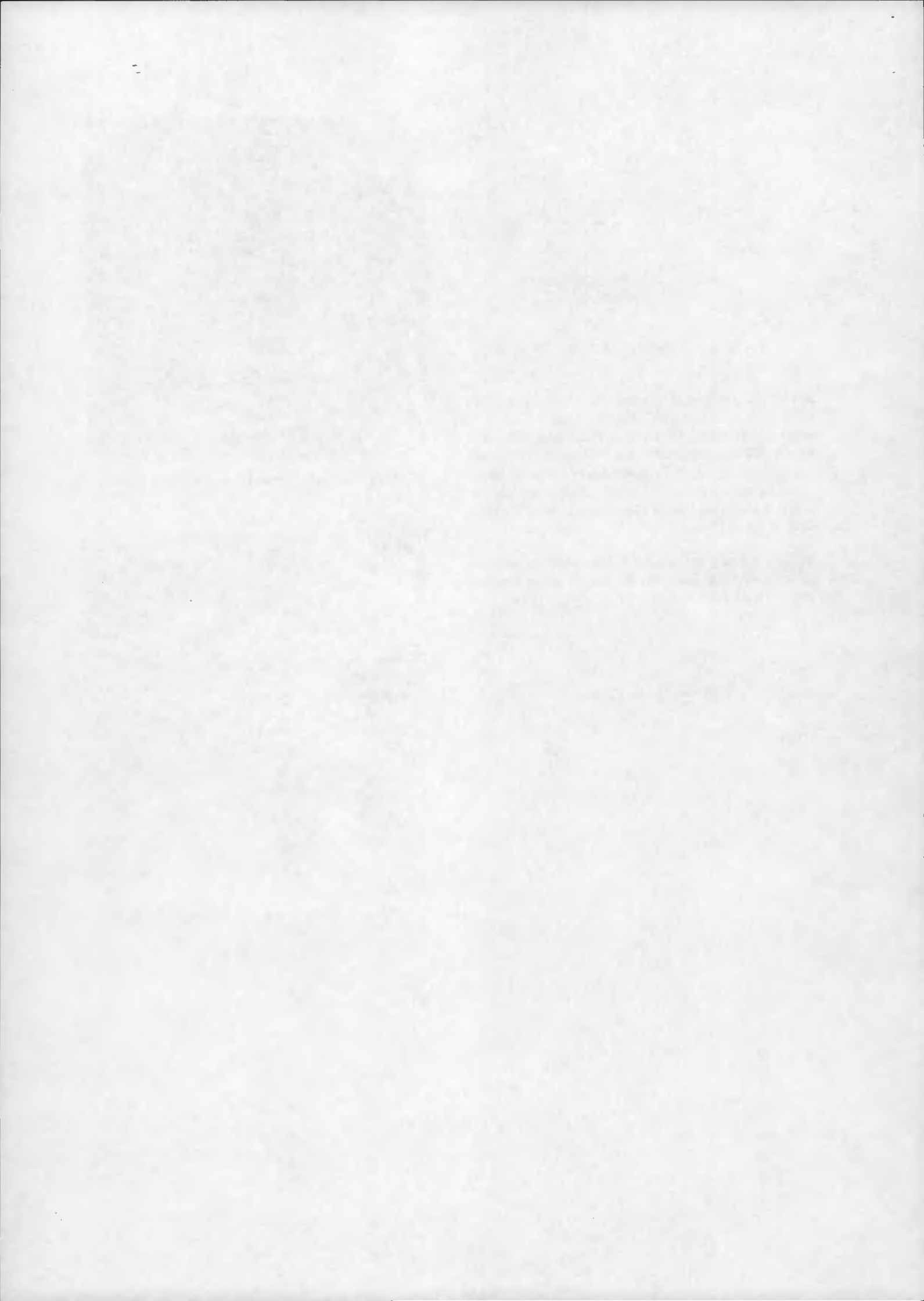


Figure 7. Lake Victoria (difference image)



**A COMPARISON OF ATSR AND SHIPBOARD RADIOMETER SST MEASUREMENTS  
ALONG TRANSECTS BETWEEN THE U.K. AND THE ANTARCTIC**

J.P.Thomas, J.Turner and C.J.Symon

British Antarctic Survey, Madingley Road, Cambridge, CB3 0ET,  
U.K.

**ABSTRACT**

Between October 1991 and May 1992 a campaign to make in-situ SST measurements to validate the ATSR SST product was carried out from the RRS Bransfield as it sailed from the UK to Antarctica and back. The ship carried an infra-red radiometer, a temperature sensor trailed from the side and a hull thermistor. The results show that the present ATSR SST product gives results cooler than the in-situ measurements. In the tropics the difference was  $\geq 1\text{K}$  except in the one case where the forward view was used in the retrieval, when agreement was within  $0.1\text{K}$ .

Keywords: ATSR, SST, Infra-red radiometer

**1. SHIPBOARD MEASUREMENTS**

**1.1 Ship/satellite co-location**

The British Antarctic Survey's ship RRS Bransfield makes an annual voyage from the U.K. to the Antarctic research stations, departing in October and returning the following May. It therefore passes through most of the major climatic zones of the Atlantic Ocean and crosses the Southern Ocean several times during the voyage. During the 1991/92 voyage the ship carried instrumentation to measure the sea surface skin temperature and atmospheric temperature and humidity profiles. ERS-1 overpass times were computed from orbit elements supplied weekly by the Royal Greenwich Observatory and wherever possible the ship's Master and the Navigation Officer worked out a course which followed an ERS-1 ground track to maximise the probability of obtaining co-located ATSR and in-situ data. ATSR has such a narrow swath that the zenith angle from the surface location to ERS-1 must be greater than  $75^\circ$  to be within the swath. It was therefore much more difficult to obtain collocated data than for a wide beam instrument such



Fig. 1. Location of SST datasets obtained simultaneously from RRS Bransfield and ATSR between October 1991 and May 1992 (+ = southbound; x = northbound; \* = ATSR data not yet processed)

as AVHRR, especially as the ship had to keep to a tight schedule and could not go to specific locations and wait for overpasses.

The map in Figure 1 shows the positions at which co-located measurements were successfully obtained from the ship and from ATSR. Most of the points lie in mid-latitudes and the tropics where weather conditions were more favourable, with less cloud cover, calmer seas and no sea-ice. A long in-situ time series was obtained in early December in excellent conditions in the southern Weddell Sea, but ERS-1

was being manoeuvred into the ice phase orbit so that it was difficult to predict overpasses. ATSR data for this period have recently become available, but have not been processed yet. If co-located data can be found from this period they will be extremely interesting as the Weddell Sea area was affected by volcanic dust from the Mount Hudson eruption at the time and very colourful sunsets were observed from the ship. The concentration of measurements in the tropics and sub-tropics is however very useful as this region provides the toughest test for ATSR due to the large amounts of atmospheric water vapour and also of volcanic dust from recent eruptions.

## 1.2 Shipboard Instruments

### 1.2.1 Infra-red radiometer

An infra-red radiometer was mounted on RRS Bransfield so that the temperature of the sea surface skin layer could be measured accurately. The radiometer was very similar in design to the one used in a previous campaign to validate AVHRR SST measurements from the same ship (Ref.1) but this time it was purchased from a commercial manufacturer, Satellites International Limited of Newbury, Berkshire, UK. The instrument was self-calibrating as it could periodically measure the signal from two internal black bodies at known temperatures, one at the internal instrument temperature and one heated to several degrees above this. The signal was limited to a narrow waveband centred at  $11\mu\text{m}$  or  $12\mu\text{m}$  by moving an appropriate filter into the field of view.

The radiometer was mounted on a boom which could be swung out over the bow of the ship so that it could view undisturbed water almost vertically below the aperture. This did however make the instrument vulnerable to waves and limit its use in rough conditions. The radiometer could also be swung inboard to view a well stirred tank of sea water at known temperature on the deck of the ship. These measurements were used to validate the algorithm relating the internal calibration measurements to external target temperature over a wide variety of climatic conditions. An example of one set of water tank measurements carried out in the tropics is shown in Fig.2. The sea water in the tank was cooled below its normal temperature by inserting bags of ice into the tank. It was then allowed to warm up again to produce a timeseries of increasing target temperatures. It can be seen from Fig.2 that the function relating the internal calibration measurements to the external target temperature must include a small quadratic component. The results from 15 sets of measurements made over a range of latitudes from polar to tropical show that the standard deviation of the difference between thermometric and

radiometric water tank temperature was 0.2K. The radiometer used is therefore capable of measuring the sea surface skin temperature with the accuracy required for ATSR validation.

### 1.2.2 Upper air profiles

A Vaisala radiosonde system was installed on the ship for obtaining the profile of atmospheric temperature and humidity during an ERS-1 overpass. The profiles were then processed at Rutherford Appleton Laboratories using a radiative transfer model (Ref.2) to calculate the brightness temperature of the sky. A correction for reflection of the sky could then be applied to the radiometer measurement of skin temperature.

### 1.2.3 Bulk sea water temperature

The bulk sea water temperature was measured by a TetraCon 96A-4 Temperature/Conductivity probe which was trailed from the ship and suitably weighted to keep it in the water and close to the surface. The ship has been fitted with a hull thermistor by the UK Met. Office so the temperature at 5m depth was also available.

## 2. ATSR SST DATA

All ATSR data used have been received directly from the Rutherford Appleton Laboratories (RAL). Initially an attempt was made to obtain near real time data at BAS in Cambridge while a team from RAL were working at Kiruna, but it was not usually possible to get information on the ship's position to them in time. Once the opportunity was missed the ATSR data disappeared into the system for several months.

Eventually the data discussed later were received, having been processed at RAL using the SADIST Version 400 software. Only the SST products as supplied by RAL were compared to the in-situ data and no alternative SST retrieval algorithms were tested. The SST products for the collocation times were extracted for pixels within a 5km radius around the ship's position so that the temperature variability in the vicinity could be assessed. If the area was cloud free then a sub-sample of pixels was taken within 1.5km of the ship, to account for errors in its position, and the mean SST for these 5 or 6 points calculated. Where these pixels were all cloud contaminated then the mean SST within the 5km sample was calculated.

## 3. RESULTS

The results of comparing the nine collocated datasets obtained so far are illustrated in Fig.3 where in-situ bulk and radiometer SST measurements are compared against the values from the SADIST product. Compared to the straight line indicating perfect agreement, the ATSR SST values are overall cooler than the in-situ SST.

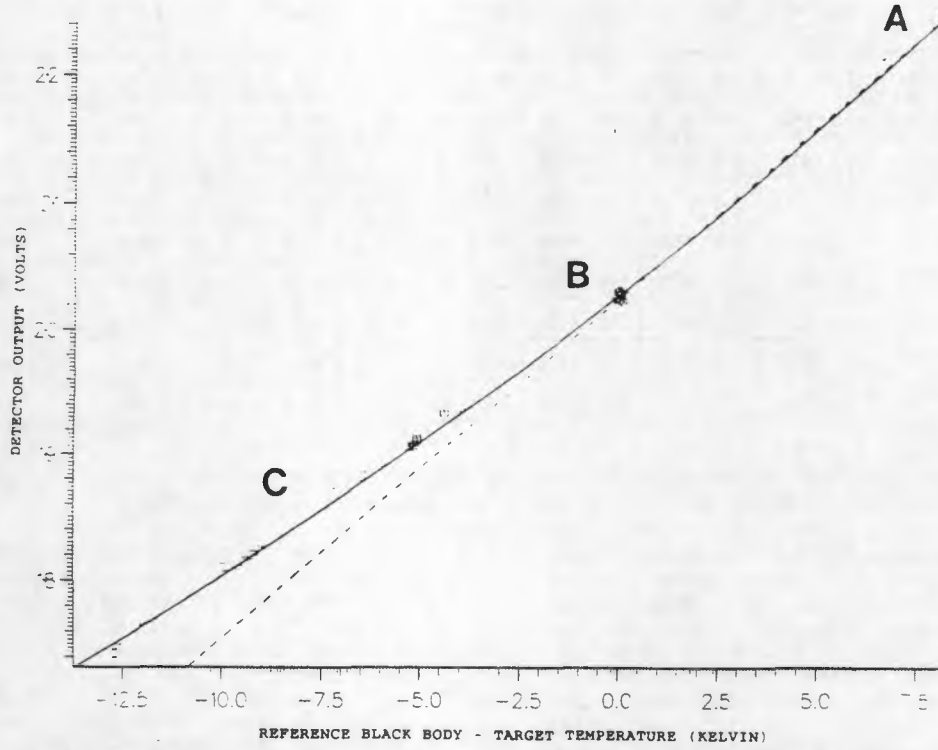


Fig. 2. SIL radiometer detector output signal vs. temperature for the calibrating hot black body (A), cold black body (B) and a well stirred water bath at known temperature (C). The solid line shows the quadratic calibration equation compared to the straight, dashed line.

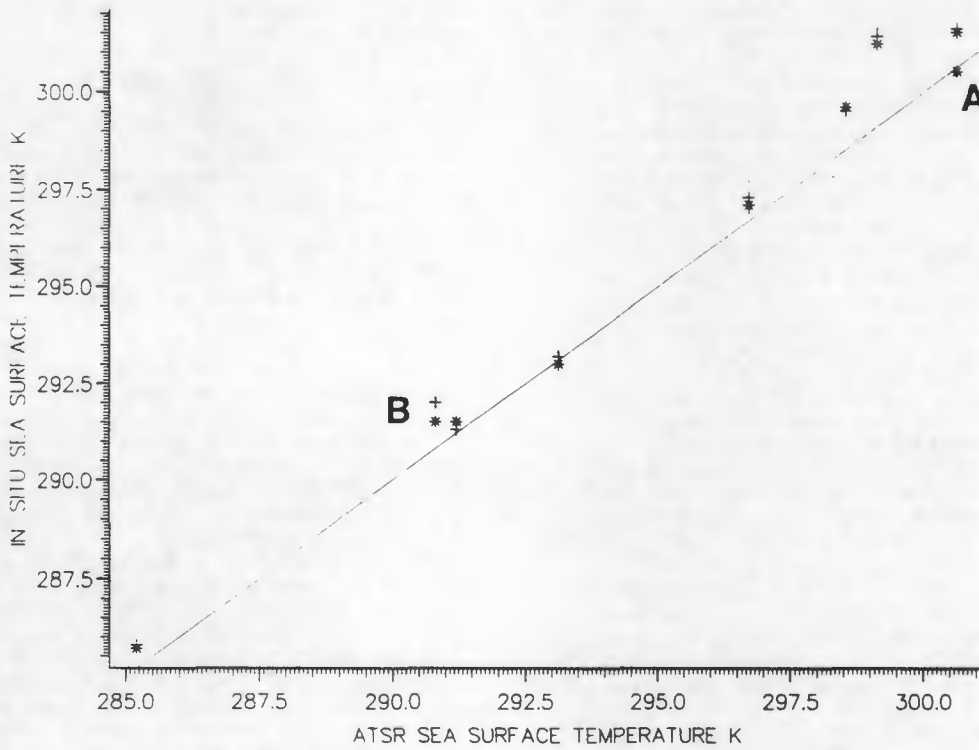


Fig. 3. ATSR vs. in-situ SST for 9 colocated cases. (+ = radiometer ; \* = bulk ; + = standard deviation)

DATE	TIME (GMT)	LAT.	Lon.	ATSR SST K	$\Delta$ BR	$\Delta$ BA	$\Delta$ RA	FORWARD VIEW	DAY/NIGHT
16/10/91	12:03	38.75N	14.25W	293.1	-0.2	-0.1	0.1	NO	DAY
19/10/91	12:06	27.65N	19.10W	296.7	-0.2	0.4	0.6	NO	DAY
21/10/91	23:45	17.20N	23.30W	298.5	0.1	1.1	1.0	NO	NIGHT
22/10/91	12:09	14.80N	24.29W	299.1	-0.2	2.1	2.3	NO	DAY
26/04/92	03:07	44.73S	57.47W	285.2	-0.1	0.5	0.6	NO	NIGHT
27/04/92	13:52	36.87S	56.39W	290.8	-0.5	0.8	1.3	YES	DAY
05/05/92	12:55	18.49S	38.76W	300.6	0.0	-0.1	-0.1	YES	DAY
06/05/92	01:20	16.50S	37.76W	300.6	-0.1	0.9	1.0	NO	NIGHT
19/05/92	12:00	36.78N	16.04W	291.2	0.2	0.3	0.1	NO	DAY

Table 1. Results of intercomparison of SADIST 400 ATSR SST with in-situ SST. ( $\Delta$ BR = Bulk-Radiometer;  $\Delta$ BA = Bulk-ATSR;  $\Delta$ RA = Radiometer-ATSR)

The disagreement is worst at the higher temperatures experienced in the tropics, except for one case (A in Fig.3) where there is perfect agreement. This is the only case out of the four above 298K where the forward view as well as the nadir view data were used in the SST retrieval algorithm. The magnitude of the disagreement in the other cases is too large to be explained by the skin effect, which is small in the tropics (Ref.1).

In only one out of the five cases at higher latitudes (temperatures lower than 298K) was the forward view included in the retrieval (B in Fig.3). Again the ATSR SST is cooler than the in-situ values, but there is significant disagreement between the radiometer and bulk measurements. These data were however collected as the ship entered the outflow from the River Plate, an area with high SST variability. Examination of the radiometer data shows variations of up to 3K in a few minutes as the continuous measurements could resolve much smaller, warm, surface features than either the hull thermistor record or the 1km ATSR pixel.

Table 1 gives more details of the SST differences between ATSR and in-situ measurements and between the two sets of in-situ data. It also shows whether the forward view was used in the ATSR retrieval algorithm and whether it was local day or night at the overpass time. Ignoring 27/4/92, the River Plate case discussed earlier, all the radiometer measurements lie within 0.2K of the bulk SST, with a bias towards being warmer. It would therefore seem that large skin temperatures did not occur during any of these overpasses. Radiometer data were collected as often as possible during the voyage, not just during overpasses, so the skin effect variability during the entire period can be assessed and compared to previous work (Refs.1,3) for consistency. This will give added confidence in the radiometer SST algorithm being used.

The in-situ minus ATSR SST values show that unacceptably large differences occur in the tropics, except for the one case where the forward view was used. At the higher latitudes two cases with quite large differences of 0.6K occur on the 19/10/91 and 26/04/92. The forward view was not used in either case, but there is no proof yet that this would make a difference. If cloud free forward view data exist for all the cases in Table 1, then it will be possible to include them in a new SST retrieval and so prove more conclusively whether they improve the results.

#### 4. CONCLUSIONS

Some results have been presented of comparisons of in-situ skin and bulk SST measurements with the SADIST SST product produced at RAL. The number of successful comparisons is quite small considering the time and effort involved which illustrates the difficulty of validating such a narrow swath instrument by an opportunistic rather than dedicated campaign. However, the campaign has been continued in late 1992 from the RRS James Clark Ross, so more data may soon be available. There is also one important Antarctic dataset from December 1991 which hasn't yet been analysed as the ATSR data only became available recently.

The results presented here show that the SADIST SST product has a cold bias compared to in-situ measurements, but the magnitude of this is unacceptably large only in the tropics. There is some evidence to show that including the forward view brightness temperatures in the retrieval improves the results considerably. Some further work is required to prove this conclusively.

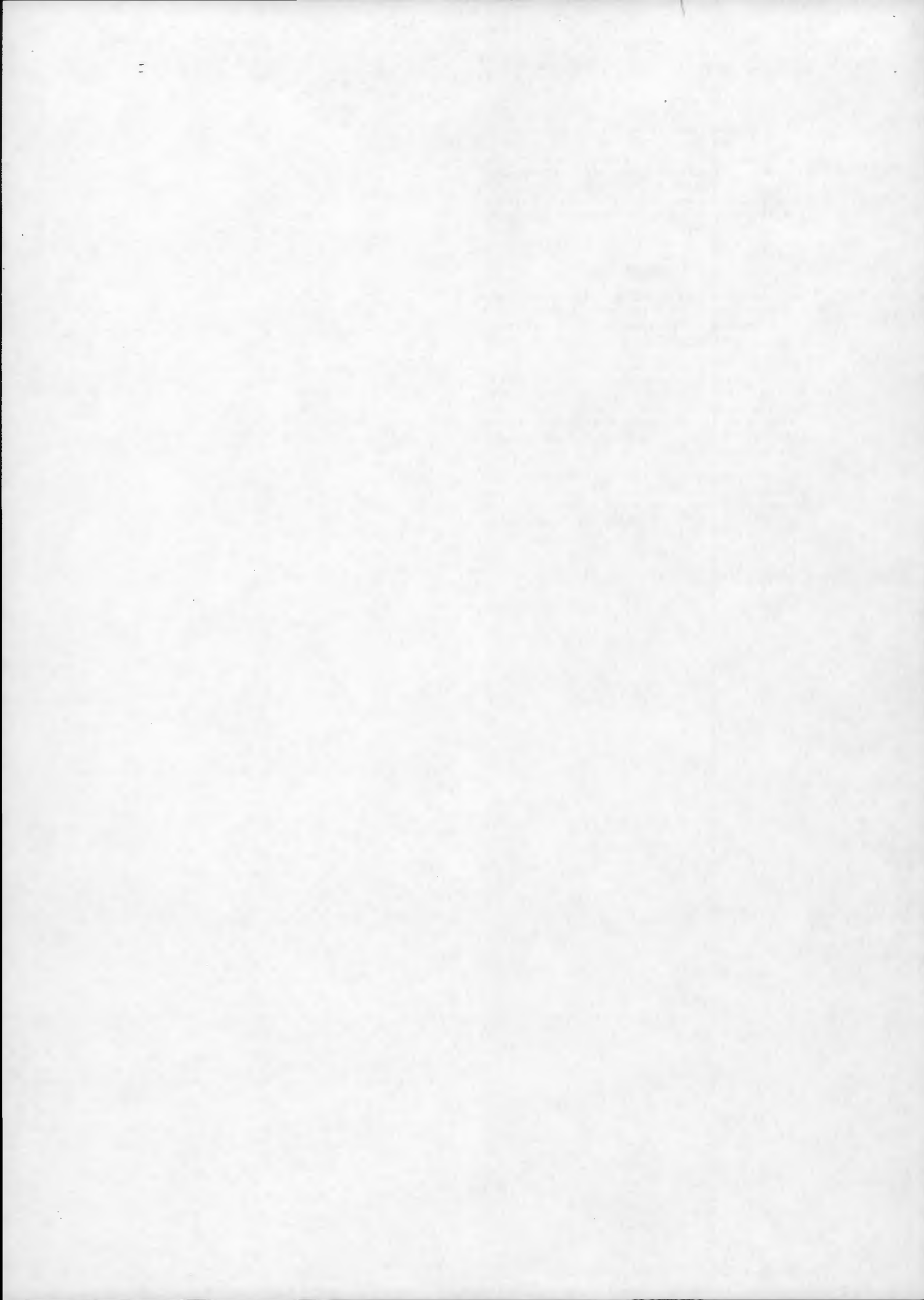
#### 5. ACKNOWLEDGEMENTS

The authors would like to acknowledge the invaluable assistance of the following:

The Masters, Officers and Crew of  
RRS Bransfield; S.Morrison,  
J.Shanklin, H.Roscoe, B.Aldhouse,  
British Antarctic Survey; G.Appleby,  
Royal Greenwich Observatory;  
Capt.G.Mackie, Met.Office; A.Zavody,  
P.Kent, R.Knight, Rutherford Appleton  
Laboratories.

#### 6. REFERENCES

1. Hepplewhite, C.L. 1989, Remote observation of the sea surface and atmosphere. The ocean skin effect, Int.J.Remote Sensing, 10, 4+5, 801-810.
2. Llewellyn-Jones, D.T. & al 1984, Satellite multichannel infrared measurements of sea surface temperature of the N.E.Atlantic Ocean using AVHRR/2, Quart. J.R.Met.Soc., 110, 613-631.
3. Schluessel P. & al 1990, On the bulk-skin temperature difference and its impact on satellite remote sensing of sea surface temperature, J.G.Res., 95, C8, 13 341-13 356.



## PRELIMINARY VALIDATION OF ATSR SEA SURFACE TEMPERATURES NEAR THE FAEROES

T.N. Forrester, T.H. Guymer, and P.G. Challenor

James Rennell Centre for Ocean Circulation,  
Chilworth Research Centre, Chilworth, Southampton SO1 7NS, U.K.

### ABSTRACT

Measurements of sea surface temperature made with a thermosalinograph on the *RRS Charles Darwin* on a cruise near the Faeroes have been compared with those derived from the Along Track Scanning Radiometer on ERS-1. Qualitatively, the temperature fields are very similar and show that the area was under the influence of the Iceland-Faeroes Front. Although the presence of significant horizontal gradients and of appreciable amounts of cloud has complicated the analysis it has been demonstrated that the accuracy of the ERS-1 temperatures is within their design specification of 0.5K. The ERS-1 values are a few tenths of a Kelvin colder than the *in situ* data, this being consistent with the skin effect.

Keywords: Sea surface temperature, front, ATSR, ERS-1, thermosalinograph

### 1. INTRODUCTION

The Along-Track Scanning Radiometer (ATSR) has been designed to measure sea surface temperature (SST) with an absolute accuracy of  $\pm 0.5\text{K}$  and, as a further scientific goal, to achieve  $\pm 0.3\text{K}$ . This represents a significant improvement over the performance of the Advanced Very High Resolution Radiometer (AVHRR) but requires careful comparison with in-water measurements if such accuracies are to be validated. The James Rennell Centre is contributing to the ATSR validation programme through measurements on research cruises. To date four have been held: near the Faeroes (September 1991), Tyrrhenian Sea (October/November 1991) and two in the North Atlantic (August 1991, June 1992). From November 1992 to April 1993 SST will also be measured on several cruises in the Southern Ocean, extending from the SE Pacific, across the Atlantic to the SW Indian Ocean, as part of the World Ocean Circulation Experiment. In this paper, preliminary results from the Faeroes experiment are presented.

During 8-24 September 1991 *RRS Charles Darwin* occupied a triangle to the northeast of the Faeroes with the main objective of obtaining an independent high quality dataset for the validation of radar altimeter significant waveheight, wind speed and sea level; scatterometer wind velocities; and ATSR SST and water vapour content. A detailed description of the measurement programme and first results was provided by Cotton et al.

(1992). Radiosonde determinations of atmospheric temperature and water vapour content were presented in Forrester & Guymer (1992) (Ref. 2) Here, we consider only those aspects relevant to the validation of SST.

Most of the measurements taken on the cruise were made in a triangle to the east and north of the Faeroes, two sides of which coincided with the subsatellite track of ERS-1, and hence with the middle of the ATSR swath (Fig.1). At this time ERS-1 was in its 3-day repeat. The ship was equipped with two systems for measuring SST, a thermosalinograph (TSG) recording temperature (and salt content) of water pumped on board from an intake at 5m depth and a thermistor trailed at a depth of 2 or 3 cm from a boom on the starboard bow. The latter suffered from large drifts with time probably due to leakage of the sensor. Only the TSG data have been used in this paper.

During the cruise two surveys round the triangle were made, coinciding with ERS-1 overpasses, so that spatial variations within the ocean could be measured. The SST data to be discussed are from the second of these surveys. The triangle was situated near an interesting oceanographic feature (the Iceland Faeroes Front) which is a climatological feature running approximately NW/SE through the area. Fig. 1 shows its mean position determined from several cruises in the 1970s. Its surface expression is often seen on IR images although cloud coverage is a problem. An AVHRR image acquired just before the cruise in cloud-free conditions showed an apparent surface front running approximately NNW/SSE through the western edge of the triangle with the coldest water at the northwest corner and the warmest at the southern corner.

### 2. PROCESSING

Before attempting comparisons with the satellite data the accuracy of the TSG has been investigated. During the cruise 26 Conductivity-Temperature-Depth (CTD) casts were made from the surface to cover most of the water column as part of a programme to determine sub-surface structure. (The CTDs had been calibrated to very high accuracy in the laboratory.) Values of temperature corresponding to 5m depth were extracted and compared with TSG values at the same location. The agreement was within 0.03K, showing that errors in the TSG data are negligible in the ATSR comparison. Although the comparisons are, of necessity, restricted to times when the ship was stationary there is no reason to suppose that the TSG accuracy deteriorated when underway.

During the survey ATSR passes occurred at 1156 and 2144GMT on 22 September. ATSR data were provided by Rutherford Appleton Laboratory in the form of 1km resolution SSTs (SADIST Version 3.10) (both passes) and the 0.5 degree spatially-averaged product (for the first pass only). The latter provides a mean SST for the 0.5<sup>0</sup> box even when the box is partially cloudy and has been designed for global climate applications. Both products have been atmospherically-corrected using a dual viewing angle and the split-window technique. We have chosen to validate the products separately.

### 2.1 Method for validating 1km product

One method of validating satellite data is to take ship data at the exact time of overpass and to compare them with values given by the satellite for the pixel in which the ship is located. (Some averaging of *in situ* data may be needed to obtain a value representative of that pixel as will be discussed later). The maximum number of comparisons thus obtained is equal to the number of satellite overpasses, which in our case was 10. However, for most of these occasions the pixel containing the ship was cloudy (see Fig. 2 for an example). Many more intercomparisons can be made if the requirement for exact coincidence is relaxed. SSTs for cloud-free pixels sampled at some other time by the ship can then be used. Clearly, there is a price to be paid for relaxing the time constraint in that the SST may change during the time interval due to diurnal warming or advection. On the other hand reducing the time tolerance limits the number of comparisons. A time lag of ~10 hours lapsed between the morning and night passes and a comparison of the two images showed a mean rms difference of 0.2K. Also, Minnett (1991) (Ref. 3) found that from buoy SSTs in a nearby region of the Norwegian Sea a time lag of between approximately 1 and 12 hours was associated with an r.m.s. difference of 0.2K. Given these facts, and after finding no correlation between increasing time lag and a larger ATSR/*in situ* difference, a time window of ±10 hours was adopted. Ship SSTs within this time window and a spatial tolerance of ±0.5km centred on the middle of each ATSR pixel were averaged to provide a single *in situ* comparison for each ATSR value. The number of cases satisfying these criteria for the two ATSR passes was 51.

### 2.2 Method for validating half-degree product

SSTs were extracted from the ATSR product for all half-degree boxes through which the ship track passed and in which a valid satellite value was obtained. Only those pairs of values for which the time difference was <2 days were retained in the analysis. The TSG data, having been sampled at 150m spacing were further averaged over 50km segments (equivalent to 0.5<sup>0</sup>) of ship track to produce data comparable with the satellite sampling. This neglects the effects of any cross-track SST gradients. Where the ship had crossed a half-degree box more than once an average of the ship values was taken. As a result ten comparisons were achieved.

## 3. RESULTS

The SST distribution given by the ATSR 1km product is shown in Fig. 2, the night-time pass on 22 September. Cold water (<8<sup>0</sup>C) lay to the north of the triangle with warm water (>10<sup>0</sup>C) to the south. At the NE corner the temperature was 9.5<sup>0</sup>C. This pattern was similar to that of the AVHRR image on 5 September. Fig. 3 shows the variation of SST measured by the ship as it surveyed the area and is consistent with the satellite data. In Fig. 4 comparisons have been plotted between the ATSR and

TSG data, processed as described in 2.1. The range of values was 8.9 - 10.3<sup>0</sup>C measured by the TSG but 8.3 - 10.2<sup>0</sup>C according to the ATSR. An indication of the spread of TSG values within each ATSR pixel is shown by the error bars, which correspond to one standard deviation; mostly these are <0.05K but two locations exhibit ~0.2K. An attempt to fit a straight line to the data has been made, but the range of SSTs is too small for this to be done satisfactorily.

Overall, the ATSR was found to be biased low compared with the TSG as given by the following relationship:

$$\text{ATSR-TSG} = -0.25 \pm 0.35\text{K} \quad (1)$$

Rather different results emerge, however, if the comparisons are carried out separately for the two passes. For the morning pass a straight line fit is a good approximation. No such behaviour is evident on the later pass where there is a wide spread of ATSR values for a restricted range of TSG temperatures. Possible reasons for this are discussed in Section 4.

Comparisons between the half-degree ATSR product and the 50km TSG averages have been plotted as differences in Fig. 5. (A scatter plot showed similar features to Fig. 4.) From these results the following relationship has been derived:

$$\text{ATSR-TSG} = -0.20 \pm 0.23\text{K} \quad (2)$$

For all but one of the squares the ATSR showed negative or zero bias, the largest value being 0.6K.

## 4. DISCUSSION

Both sets of comparisons revealed that the ATSR temperatures were low compared with the *in situ* data, sometimes by more than 0.5K, and by ~0.2K in the mean. There is a physical justification for such a bias since the ATSR measures the temperature of the surface skin (top micron), whereas the TSG sampled water from 5m below the surface. Evaporative and radiational cooling at the surface can lead to a temperature difference of several tenths of a degree between skin and bulk temperatures. Using the meteorological measurements that were also carried out on the cruise it may be possible to quantify the skin effect in terms of these surface fluxes. Near surface deployments of IR radiometers offer a more direct means of validating the ATSR SSTs but this option was not available to us on this particular cruise. For the rest of this discussion it is assumed that the bias is due to the skin effect and not to a bias in the ATSR.

The residual scatter about the mean is ±0.35K for the 1km comparisons and ±0.23K for the 0.5<sup>0</sup> comparisons, well within the accuracy specified for the ATSR. Some of this scatter is undoubtedly due to the real SST changes occurring in the time interval between the satellite measurement and the ship measurement. A cursory examination of the data shows that there is no obvious dependence of the size of the temperature difference on the time separation of the observations, as would be expected if diurnal heating were involved. (This effect was probably negligible given the strong mixing conditions and the large cloud amounts.) A more likely problem is that horizontal advection has occurred. Large temperature changes can take place if the observation point is located near a strong, mobile SST feature such as a meandering front. From Fig. 3 it can be seen that abrupt changes were

encountered by the ship in the southern portion of the triangle which were associated with the Iceland-Faeroes Front.

Several of the points in Fig. 4 refer to measurements taken very close to these regions of strong SST gradient and this may explain some of the scatter. In particular, the comparisons with the evening ATSR pass were obtained when the ship was passing through strong SST gradients near 62.7°N and 5°W. This raises a key issue for accurate validation of satellite SST. In regions of high oceanic variability adopting a time window of a few hours implies that the satellite and ship may be observing different patches of water with significantly different temperatures. If the variability is known to be small then a larger window can be used. However, completely homogeneous water (SST variability < 0.2K over 50km) is uncommon. Even if such 'calibration zones' can be found they are probably of much less oceanographic interest and it may be difficult to justify cruises in these areas. A further issue is that some SST gradient across the cruise area is desirable so that the validation can span a range of SST. It should be noted that the effects of spatial variability are much less severe for the 0.5° product comparison because the movement of SST features is typically very much less than the averaging scale used so it hardly affects the calculated mean.

These considerations also suggest that geolocation errors in satellite data can be of considerable importance in the validation of SST when near fronts. It is possible that errors of a few kilometres were present in the version of ATSR data used for this study and this aspect is being investigated further.

## 5. CONCLUSIONS

Using a thermosalinograph to measure bulk sea surface temperature it has been possible to validate ATSR skin temperature. Although the number of comparisons and range of SST are very limited these preliminary comparisons are very encouraging. They suggest that the ATSR has an absolute accuracy of better than 0.5K but that values are biased low by a few tenths of a Kelvin with respect to bulk temperatures. This result is consistent with the skin effect. The good agreement also indicates that the improved atmospheric correction scheme performed well.

## 6. REFERENCES

1. Cotton P D, Srokosz M A, Guymer T H, and Tokmakian R T 1992 Validation of ERS-1 in the Iceland-Faeroes region of the North Atlantic, *Prelim. Proc. of ERS-1 Geophysical Validation Workshop*, Penhors, France, ESA WPP-36, 151-156.
2. Forrester T N & Guymer T H 1992 Radiosonde data collected on the ERS-1 validation cruise *RRS Charles Darwin* Cruise 62A, Iceland Faeroes region, *Institute of Oceanographic Sciences Deacon Laboratory*, Report No. 297, 83pp.
3. Minnett P J 1991 Consequences of sea surface temperature variability on the validation and applications of satellite measurements, *J. Geophys. Res.*, 96, 18475-18489.
4. Gotthard G A 1974 Observed variations of the UK-Iceland Gap Front, *NAVOCEANO* TN-6150-20-74, Washington D.C., US Naval Oceanographic Office.

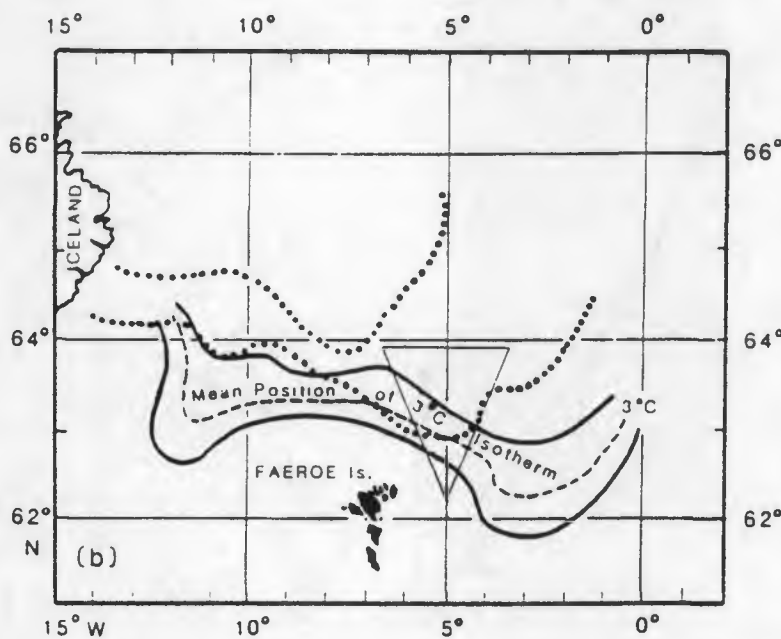


Fig. 1 The triangle occupied by *RRS Charles Darwin* during the ERS-1 validation cruise in relation to the mean position of the Iceland-Faeroes Front. Frontal positions were determined from 5 cruises in the early 1970s (Ref. 4) Dashed line: mean position of 3°C isotherm at 300m depth. Solid lines: envelope of frontal positions at 300m. Dotted line: envelope of frontal positions at 100m.

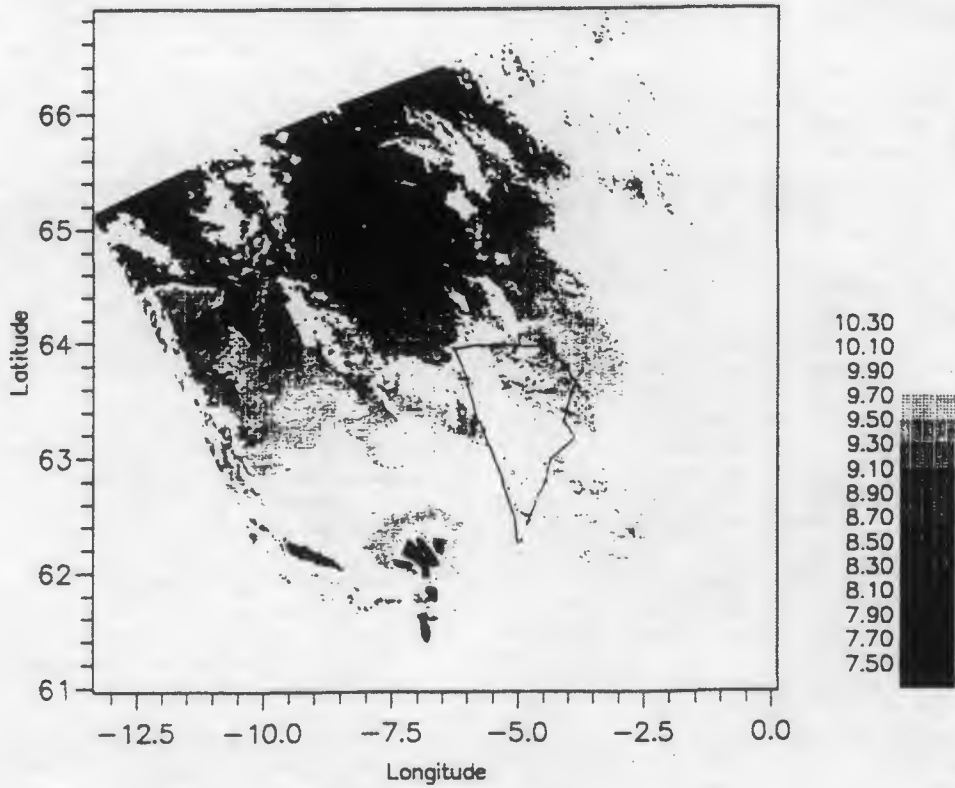


Fig. 2 ATSR sea surface temperatures to the north of the Faeroes at 2144GMT, 22 September 1991. The scale shows temperatures in °C. The track of RRS Charles Darwin during a ±10 hour window centred on the overpass time is also shown. Departures from the nominal triangle of Fig. 1 were due to weather conditions.

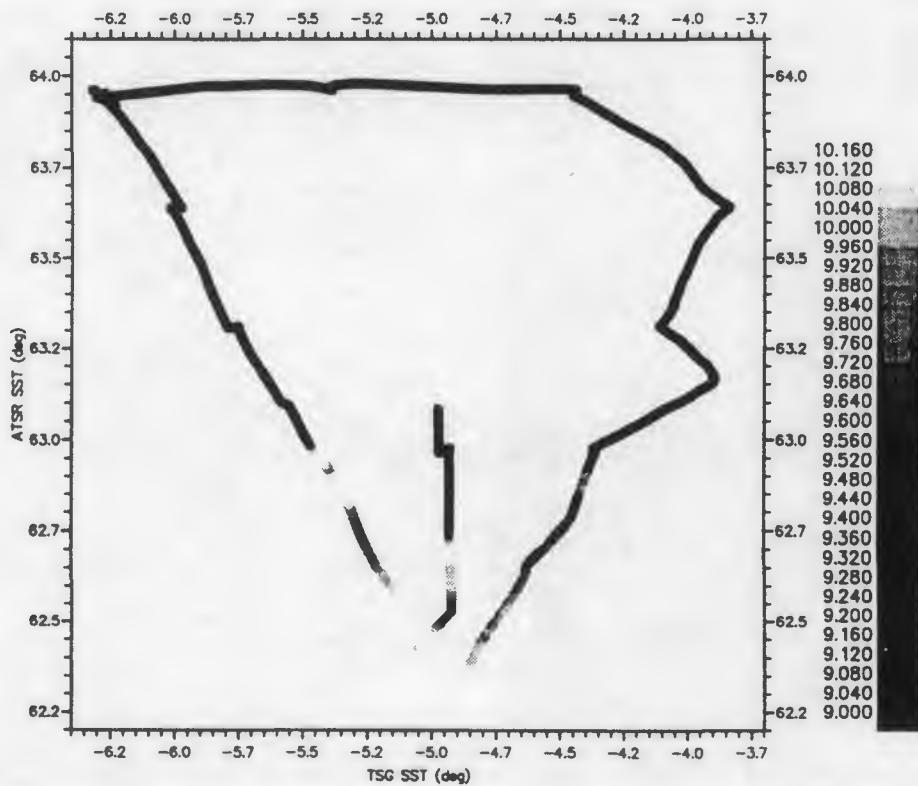


Fig. 3 Distribution of sea surface temperature along the ship's track as obtained from thermosalinograph data.

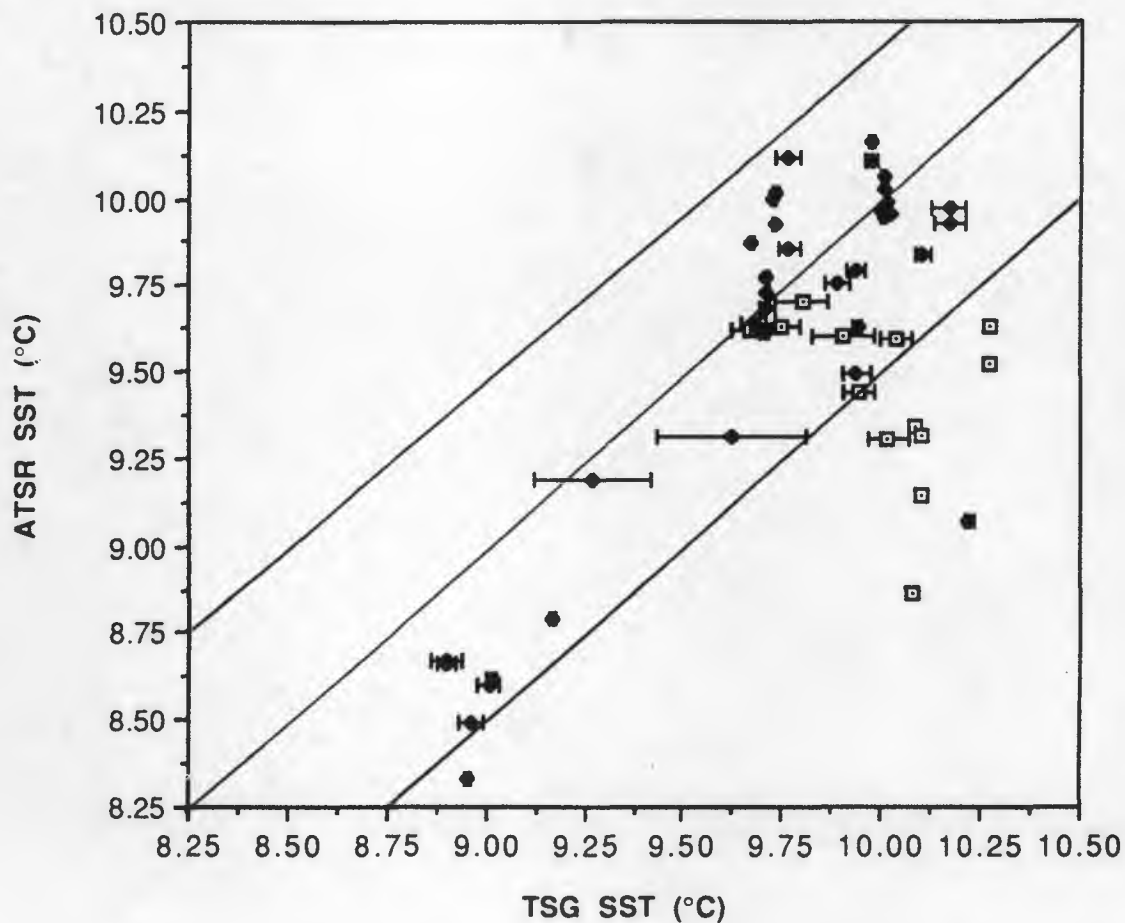


Fig. 4 A comparison of ATSR 1km sea surface temperatures with ship thermosalinograph sea temperatures (diamonds: morning pass on 22 September 1991; squares: evening pass on 22 September 1991). Lines of perfect agreement and  $\pm 0.5\text{K}$  accuracy specifications are also shown. The significance of the error bars is given in the text, section 3.

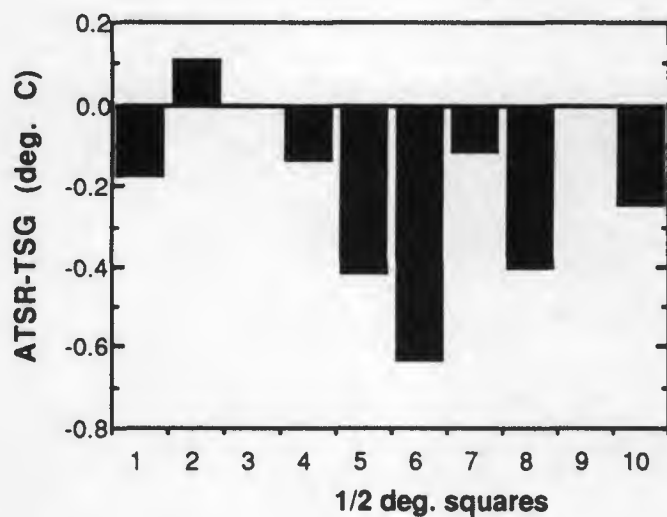
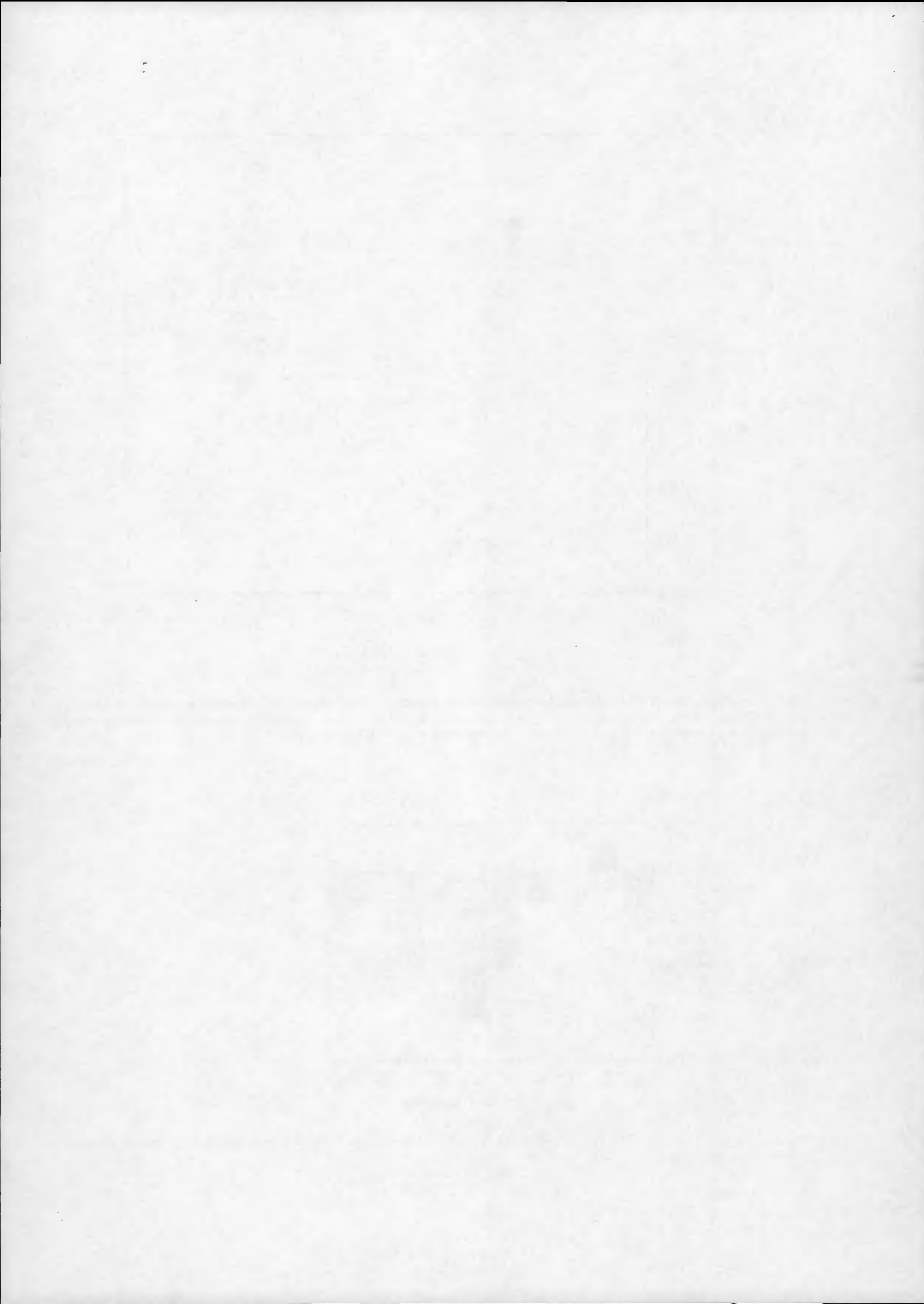


Fig. 5 Differences between ATSR spatially-averaged sea surface temperatures ( $0.50 \times 0.50$ ) and 50km along-track averages of thermosalinograph data.



## An investigation of intraseasonal variability in sea-surface temperature in the tropical Pacific using data from the Along-Track Scanning Radiometer

J. Murray<sup>1</sup>, M. R. Allen<sup>1,2</sup>, S. P. Lawrence<sup>2</sup>, C. T. Mutlow<sup>1</sup> and D. T. Llewellyn-Jones<sup>1</sup>

1) Rutherford Appleton Laboratory, Chilton, Didcot, UK

2) Atmospheric, Oceanic and Planetary Physics, Clarendon Laboratory, University of Oxford

### Abstract

Precision,  $0.5^\circ \times 0.5^\circ$  resolution, sea-surface temperature observations of the equatorial Pacific region from the Along-Track Scanning Radiometer are presented for the period August 1991 to March 1993. In addition to the annual cycle and 1991-2 and 1992-3 El Niño events, there is clear evidence of 30-50-day period wave activity  $2.25^\circ\text{N}$  of the equator in the central Pacific during the period August-December 1992. Such waves have been detected before, and have in the past been attributed to shear instabilities ("Legeckis waves"). Detailed comparison with data generated by an ocean model forced with daily wind-stress data, however, described in Lawrence *et al.* in this volume (Ref. 1), shows a remarkably-close correspondence of phase and phase-propagation velocity, indicating more may be involved in the generation of these waves than a simple instability.

Keywords: ATSR, Legeckis waves.

### 1 Introduction

The existence of seasonally-modulated, westward-travelling waves in the equatorial Pacific has been established by satellite and buoy measurements of sea-surface temperature in recent years, (Legeckis, Ref. 2; Halpern, Ref. 3). These *Legeckis* waves typically have periods in the range 14-43 days and occur during the May to December period (Legeckis, Ref. 4).

ATSR observations provide a data set of sufficiently good time and temperature-resolution to investigate the nature of these waves. Although ATSR covers about 90% of the Earth every three days, cloud coverage reduces the SST data-set to less than 50% of this coverage. A further problem is due to the nature of the orbit repeat cycle; the periodicity of the gaps

due to the 35-day repeat cycle poses difficulties in establishing the periodicity and significance of signals which appear in the sea-surface temperature signature.

### 2 The ATSR precision ASST product

ATSR appears to be measuring ocean skin temperature in the tropical Pacific to within the instrument's design specification of  $2\sigma < 0.5\text{K}$ , (Barton *et al.*, Ref. 5). The ATSR instrument is described in Delderfield (Ref. 6), and the details of the production of the precision Averaged Sea-Surface Temperature (ASST) product are given by Bailey, (Ref. 7).

The ASST product considered in this analysis consists of  $0.5^\circ \times 0.5^\circ$  spatially-averaged, sea-surface temperatures. The ATSR data set used here covers the period August 1991 to March 1993. Those data which fell outside the range of  $\pm 6\text{K}$  from climatological values have been omitted; this resulted in the exclusion of less than 0.5% of the temperature values. The remaining data were then averaged to a resolution of  $1.5^\circ \times 1.5^\circ$ , for direct comparison with the ocean model described in Lawrence *et al.*, (Ref. 1).

### 3 Results

The ATSR data are here presented in the form of Høvmøller diagrams, that is, plots of time versus longitude for a particular latitudinal cross-section. The latitude  $2.25^\circ$  North of the equator is chosen for initial consideration as it is this region of the Pacific in which the dynamical processes under investigation

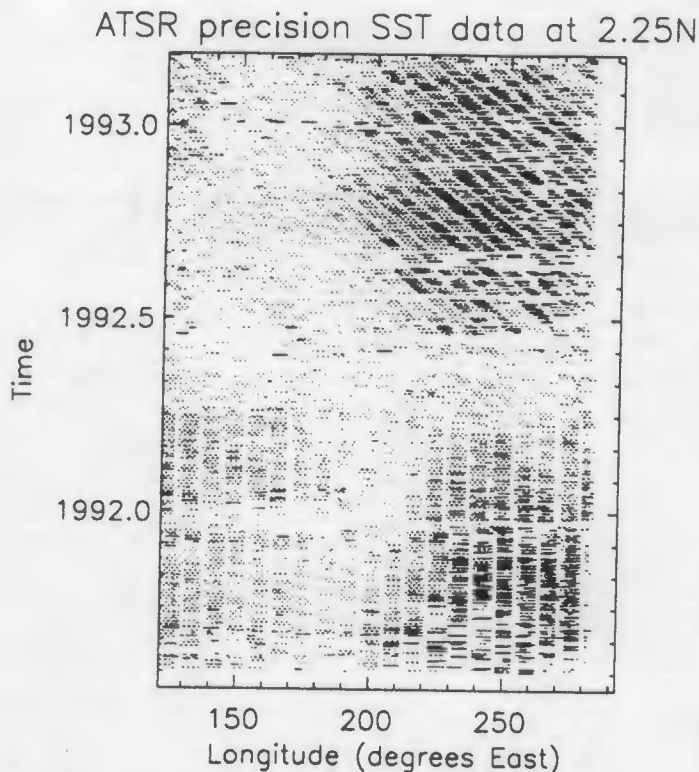


Figure 1: *Time-longitude section of ATSR precision SST data across the equatorial Pacific at 2.25° N. Dark corresponds to cold SST, light to warm. Missing observations shown white. Note pattern of gaps in data due to orbit repeat cycle, and westward-propagating waves (darker stripes, indicating colder temperatures) between 200 and 250° E.*

are expected to occur, being the northern boundary of the equatorial cold tongue.

Figure 1 shows the ATSR data at this latitude over the longitude range 120–290° East for the first 600 days of the mission. The regular pattern of the missing data is due to the orbit repeat cycle. From the initiation of data acquisition in July 1991 until March 1992, the ERS-1 satellite operated in a 3-day repeat cycle. In this mode, equatorial regions were observed once every three days, or not at all, hence the full or absent coverage at a particular longitude. Subsequent to this phase, a 35-day repeat was employed in order to achieve full global coverage. The transition is apparent as the change between the straight columns of gaps to the shifting coverage indicated by the diagonal columns in March 1992.

Clearly apparent in the figure is the seasonal cycle. Comparison with climatological data (not shown) clearly indicates anomalously warm conditions during these two El Niño years. However the most interesting aspect of the figure is the appearance of westward-propagating waves (dark stripes propagating lower-right to upper-left in the figure) during the August–December period in 1992.

The period of these propagating waves appears to closely match that of the orbit repeat cycle leading to suspicion these are not unconnected. Furthermore, there is little evidence of such significant wave activity during the corresponding season in 1991 when the 3-day repeat cycle was in use. (A method of establishing the significance of periodic signals detected using sparse and periodic sampling techniques is under development. This uses the technique of data-adaptive time-domain spectral filtering and will be the subject of a forthcoming publication.)

Figure 2 shows an expanded region of the first figure, that is the region from 200–270° East for the period January 1992 to March 1993.

#### 4 Model-ATSR data comparison

The suspicion that the wave activity apparent in Figures 1 and 2 might indicate an orbit-cycle-dependent bias in the ATSR data motivated a detailed comparison of this data with SSTs generated by an ocean model. SST data generated using the Oxford model of the tropical Pacific are described in Lawrence *et al.*, this volume. This is a medium-resolution Cox-based general circulation model forced with daily wind stresses obtained from the European Centre for Medium Range Weather Forecasting (ECMWF) analyses.

As discussed above, it is possible that the ATSR 35-day repeat cycle is implicated in the appearance of the 35-day signal; therefore it is important to note that no ERS-1 data was included in the ECMWF analyses used (scatterometer data are to be used in the operational analysis only from January 1994 onwards).

Figures 3 and 4 show the analogous plots as the first two figures for the model data, and it is apparent that the same waves appear at the same time of year. More interesting still, it is apparent that the most prominent wave appears to be coherent in both model and data, and with a remarkably similar phase-propagation velocity. This is surprising, since

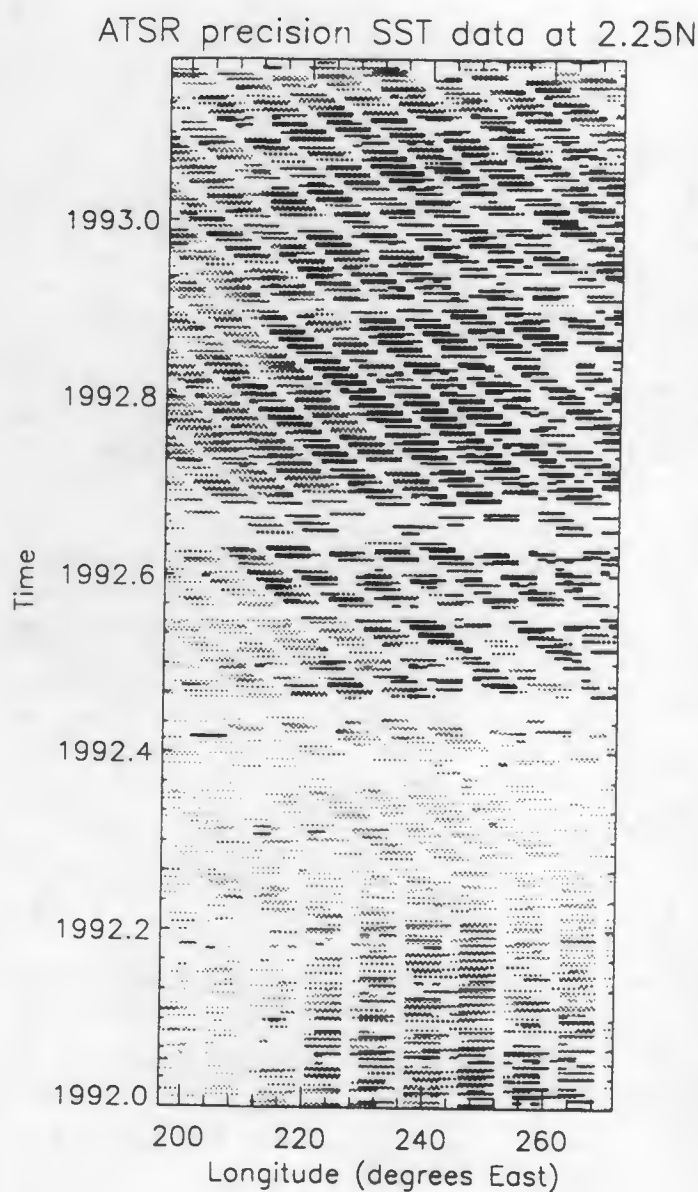


Figure 2: As previous figure but expanded to show wave activity more clearly.

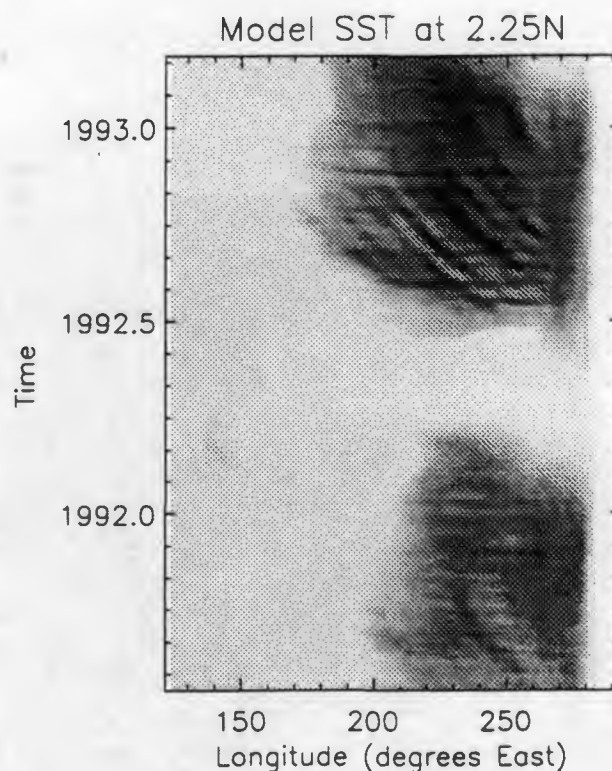


Figure 3: Time-longitude section of model SST data across the equatorial Pacific at 2.25°N. Dark corresponds to cold SST, light to warm. Note westward-propagating waves (darker stripes, indicating colder temperatures) between 200 and 250°E.

these waves are generally attributed to instabilities, and suggests there may be aspects of their generation mechanism which are still ill-understood.

Time series of model and ATSR SST data at 224.25°E and 233.25°E are shown in Figures 5 and 6. It must be emphasized that these two data-sets contain nothing in common other than the (real-world) data used in the ECMWF operational analysis. Note the additional noise at the beginning of the ATSR dataset, the origin of which is the subject of a separate publication. The relationship between the phases of the 30-40 day waves between model and data is clearly not a simple one. In the wave-generation region, to the east of 224°E, the first waves appear in phase, but propagate slightly slower in the model to the data, and so have moved almost exactly out of phase by 224°E. The strongest wave, however, appearing as a minimum in the ATSR data

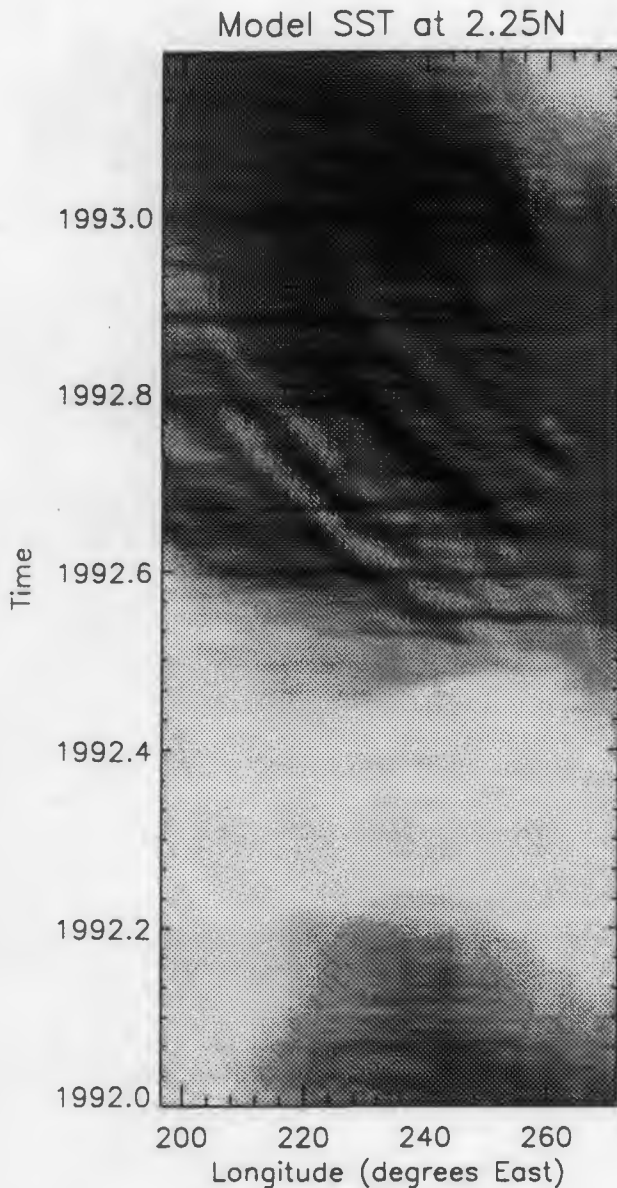


Figure 4: *Zoomed version of previous figure, expanded to show wave activity more clearly.*

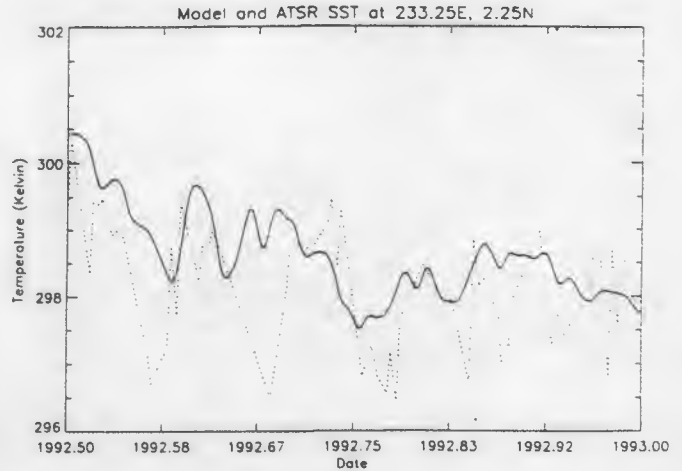


Figure 5: *Time-series of model (solid line) and ATSR (dotted) SST data at 233.25E, 2.25N.*

in the middle of October (Figure 5) and at the beginning of November 1992 (Figure 6), appears to remain in phase in model and data throughout its evolution. The appearance of these waves in a model of this resolution is in itself quite surprising. Further investigation of their generation and propagation characteristics using precision satellite SST data, supported by *in situ* observations, may shed more light on the details of their origin.

## 5 Future Work

Future plans include:

- the use of signal-reconstruction techniques to interpolate over missing data;
- the use of sophisticated signal processing to explore the significance of features which appear;
- the use of a longer ATSR SST data set as it becomes available.
- the investigation of sea temperature data from the TOGA/TAO buoy array.

## 6 References

1. Lawrence, S.P *et al.*, 1993, Tropical Pacific sea-surface temperature in an ocean general circulation model and as measured by the Along-Track Scanning Radiometer, *this volume*.

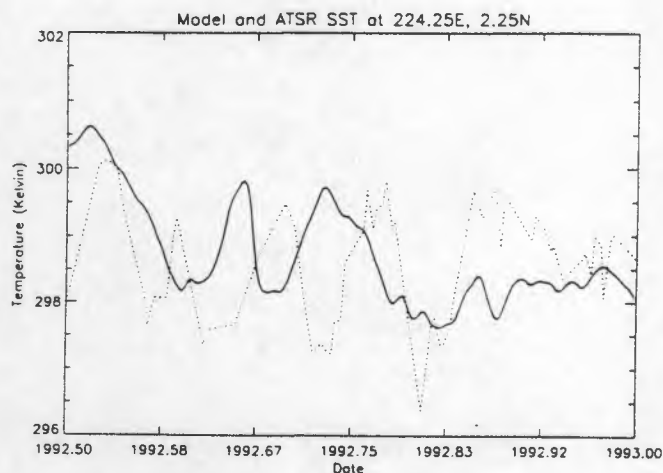
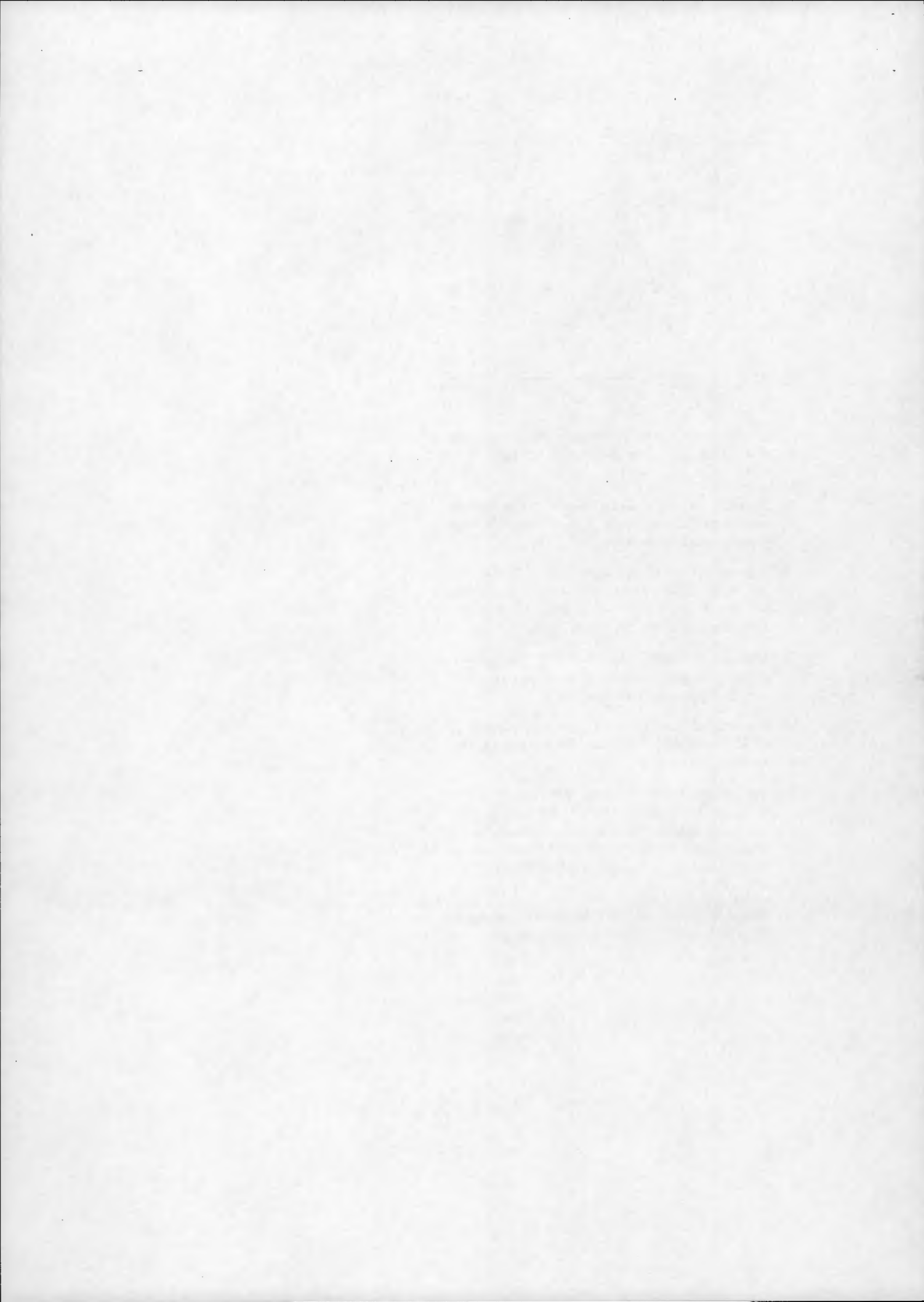


Figure 6: *Time-series of model (solid line) and ATSR (dotted) SST data at 224.25E, 2.25N.*

2. Legeckis, R. 1977, Long waves in the eastern equatorial Pacific Ocean: A view from a geostationary satellite. *Science* 197, 1179-1181.
3. Halpern, D. *et al.* Observations of 20-day period meridional current oscillations in the upper ocean along the Pacific Equator, *J. Phys. Oceanography*, 18, 1514-1533
4. Legeckis, R. 1986, Long waves in the equatorial Pacific and Atlantic Oceans during 1983. *Ocean-Air interactions* 1, 1-10.
5. Barton, I.J. *et al.* 1993, Intercomparison of AVHRR and ATSR data and data products, *this volume*.
6. Delderfield J. *et al* 1986, The Along Track Scanning Radiometer (ATSR) for ERS-1, "Instrumentation for optical remote sensing from space", John S. Seeley, John W. Lear, Andre Monfils, Sidney L. Russak, Editors, Proc. SPIE, 589, 114.
7. Bailey, P. 1993, SADIST Products, (available from Rutherford Appleton Laboratory).



LAND SURFACE TEMPERATURE RETRIEVAL FROM ATSR DATA OVER THE  
NIAMEY (NIGER) AREA

J. Labed, Z.L. Li, and M.P. Stoll

Laboratoire des Sciences de l'Image et de la Télédétection  
Groupe Scientifique de Télédétection Spatiale - Strasbourg, France

ABSTRACT

Five ATSR images (day-time and night-time) acquired over Niger, in the framework of the HAPEX-Sahel experiment, have been analysed. The objective was to compare different algorithms for surface temperature retrieval, combining spectral channels and/or view angles, along with atmospheric correction based on radiosoundings. For night-time images, with dry atmosphere, all algorithms behave very well within 0.2 K. For general situations, the work tends to indicate that, when using non nadir data, account should be made of emissivity angular effects. Large "apparent" emissivity angular variation has been extracted, especially for day-time images, the origine of which is not yet understood. High radiometric resolution allows observing faint thermal contrasts related to geological features and hydric soil properties.

Keywords: surface temperature, infrared emissivity, atmospheric corrections.

1. INTRODUCTION

The HAPEX-Sahel [Hydrology Atmosphere Pilot Experiment] campaign, that took place between mid-August and mid-October 92, was focussed on surface fluxes in relation to hydrology, at the scale of the [2-3° E], [13-14° N] square. Remote sensing is the only means to address the question of the spatial extension of the local measurements. Land surface temperature (LST) is a key parameter for mapping energy fluxes and soil hydric properties. Thus, it was expected that the ATSR thermal infrared radiometer on board ERS-1 could provide superior results because of its high radiometric resolution and accurate calibration. Five ATSR scenes, and for each one both nadir and forward images, have been made available, for the dates 08/19, 09/17, 09/23, (daytime) and 09/25, 09/28 (night-time). The data are available in thermal channels 1 (12 μm) and 2 (11 μm) only, since the 3.7 μm channel 3 was no longer in operation. The main objective of the present work is to check different algorithms developed for correcting satellite data for atmospheric effects, and the potential of this new generation of instrument for land surface studies.

2. METHODS

2.1 LST retrieval

Because of geographical location and season of acquisition of the images, changing atmospheric conditions, relative to water vapor

content and aerosols can be expected, making the atmospheric correction step more demanding. Atmospheric corrections are best made by solving the radiative transfer (RT) equation with the help of a RT code and atmospheric profiles derived from coincident radiosoundings. Otherwise, the easily implemented Split-Window (SW) method has been widely used with dual channels instruments such as AVHRR/2 (Ref.1). Similarly, methods combining different channels and / or viewing angles can also be applied, the latter being a specificity of ATSR having both nadir and forward views.

In the present work, radiosoundings exist for images 1, 2, 4 and 5. They were made at location [13°33' N, 2°06 or 2°24' E ], within less than 50 minutes of the satellite time of pass<sup>(a)</sup>. These soundings will allow comparing RT corrections with SW or DA (dual angle) methods and observing their areal validity.

SW algorithms developed for AVHRR/2 channels 4 and 5 can be transposed to ATSR's channels 1 and 2 since the channel spectral filter functions are comparable. These algorithms are of the general form:

$$T_s = a_1 T_1 + a_2 T_2 + a_0 \quad (1)$$

where  $T_1, T_2$  are the brightness temperatures at the satellite. From theory, the coefficients  $a_i$  depend on atmospheric state, surface emissivities and view angle. Their dependence is minimized through a regression method that relies on the use of a RT code, here LOWTRAN-7 (Ref. 2), with a wide set of surface conditions (temperatures and emissivities) and atmospheric conditions (temperature and humidity profiles, total water vapor content W, plus minor gaseous constituents, and, as much as possible, aerosols). With respect to view angle effect, the situation with ATSR is simpler than with AVHRR since the view angle does not change much accross an image, either nadir or forward, the latter corresponding to a view angle of approximately 53° at the surface. With ATSR, similar regression methods can be applied to built (dual angle) DA-LST algorithm with one spectral channel.

The algorithms that have been used in this work are the following:

- SW (nadir or forward):

$$T_{SW}(\theta) = a_0(\theta) + (1 + a(\theta)) \frac{1 - \epsilon_\theta}{\epsilon_\theta} + b(\theta) \frac{\Delta \epsilon_\theta}{\epsilon_\theta} \frac{T_i + T_j}{2} + (c(\theta) + d(\theta)) \frac{1 - \epsilon_\theta}{\epsilon_\theta} + e(\theta) \frac{\Delta \epsilon_\theta}{\epsilon_\theta} \frac{T_i - T_j}{2} \quad (2)$$

<sup>(a)</sup> We are indebted to Météo-France for providing the radiosounding of image n°2, and to Météorologie Nationale du Niger for providing the other soundings.

where the subscripts  $i$  and  $j$  refer to channels 1 and 2, and  $\Delta\epsilon_\theta = \epsilon_{\theta_i} - \epsilon_{\theta_j} = \Delta\epsilon_\theta(i, j)$ .

- DA (channel  $i$ ,  $i = 1, 2$ ):

$$T_{DA}(i) = T_{0i} [\beta_{0i} + \beta_{1i}(1 - \epsilon_{0i}) + \beta_{2i} \Delta\epsilon_{\theta i}] + (T_{0i} - T_{\theta i}) [\alpha_{0i} + \alpha_{1i}(1 - \epsilon_{0i}) + \alpha_{2i} \Delta\epsilon_{\theta i}] \quad (3)$$

where  $\Delta\epsilon_{\theta i} = \epsilon_{0i} - \epsilon_{\theta i} = \Delta\epsilon_\theta(0, F)$ .

The coefficients appearing in equations (2) and (3) take different numerical values depending on atmospheric water content. These values will not be given here for shortness.

It has been demonstrated theoretically (Refs. 3, 4) that precise LST determination requires the knowledge of the channel emissivities, with emphasis on the spectral difference between the two SW channels. This information is presently not available for the area of interest and at the scale of the ATSR pixels. However, field measurements that we conducted during the HAPEX experiment of averaged emissivity  $\epsilon$  [10.5-12.5 $\mu$ m], and associated spectral investigations, have given, for a variety of soils,  $\epsilon = 0.974 \pm 1\%$  and little spectral variation. The emissivities at the pixel size are likely to be of the same order of magnitude or higher because of sparse vegetation and humidity. For the present analysis, a guess value of  $\epsilon(11\mu\text{m}) = 0.975$  and a difference  $\epsilon(12\mu\text{m}) - \epsilon(11\mu\text{m})$  equal to zero were adopted.

With ATSR's forward view, the question of an angular variation of the surface emissivity arises. No information exist on such an angular effect at the proper scale. Angular variation of emissivity does exist for smooth surfaces (water) as a consequence of Fresnel coefficients. Laboratory work on soils (Ref. 5) also showed angular effects, a few % for the angular range and spectral domain of interest, that are difficult to assign, probably a combination of Fresnel and roughness effects. Nevertheless, for ATSR data, an angular dependence cannot be ruled out. Angular effects on emissivity have been reported (Ref. 6) for AVHRR data under different view angles. The work hypothesis was made that the effect is the same in both 11 and 12  $\mu$ m channels.

Actually, SW, or similar algorithms, cannot correctly operate with one set of constant coefficients for all atmospheric situations, because of the non linearity of the RT equation. One way to overcome the difficulty is to make the coefficients dependant on atmospheric total water vapor content  $W$ . Several methods, not relying on actual radiosoundings, have recently been proposed and developed for different instruments (Refs. 7-9). The "R" method used in this work is similar to the SW Variance Ratio (SWVR) of Jedlovec (Ref. 8) and is based on a statistical procedure applied to the satellite data. It can be shown (Ref. 10) that the ratio  $R$  of the atmospheric transmittances (here  $R = \tau_1/\tau_2$ ) is related to the variability of the brightness satellite temperatures in the SW channels, provided that the channel emissivities are very similar and that the LST exhibits sufficient spatial heterogeneity:

$$R = \tau_1/\tau_2 = \frac{\sum_{j=1}^N (T_{1j} - \bar{T}_1) (T_{2j} - \bar{T}_2)}{\sum_{j=1}^N (T_{2j} - \bar{T}_2)^2} \quad (4)$$

From regression analysis, a non linear relationship can be found between  $W$  and  $R$ .

This "R" method is however very sensitive to the noise (radiometric resolution) of the instrument and is more likely to correctly work with ATSR, contrarily of AVHRR. It also needs enough temperature heterogeneity of the ground surface to be applied.

## 2.2 Cloud filtering

With two thermal channels, cloud filtering of ATSR images relies

on thresholds on  $T_1$  and difference  $(T_2 - T_1)$ . These thresholds are different for day-time and night-time images, and for nadir and forward views. Two other contributions were found usefull for detecting clouds: i) comparison between forward and nadir images (a specificity of ATSR) due to the parallax effect on clouds relative to ground; ii) sensitivity of the "R" method to thin clouds (see next §).

## 3. ANALYSIS OF DATA

### 3.1 Atmospheric water content

The "R" method was applied after the first step of cloud filtering. The size of the box used to calculate  $R$  was chosen to be 30x30 pixels, a compromise between stability and representativeness of result and fine mesh grid to eventually investigate the variability of the atmosphere. Cloudy pixels tend to give  $R \geq 1$ , a value which is not physically acceptable for the ratio  $\tau_1/\tau_2$ . Thus, the method can be used to complement cloud filtering, and values very close to unity were attributed to contamination by thin clouds.  $R$  (or  $W$ ) values were used to segment the image into classes of water vapor content, and appropriate SW coefficients accordingly chosen.

Consistency of the "R" method was checked against the  $W$  figures obtained from the soundings (Table 1): the first column gives the  $W$  values obtained from the radiosoundings; the second shows the  $W$  values for a 4x4 boxes area around the location of the sounding; the third is  $W$  averaged over all boxes in the image.

Table 1: Atmospheric water content  $W$  ( $\text{gcm}^{-2}$ )

im. n°	W(sdg)	W(R)	<W(R)>
1	3.14	2.71	2.56
2	2.05	-	1.44
3	-	2.31	1.87
4	2.26	2.04	1.40
5	1.53	1.24	0.96

Image n°2 has the smallest number of pixels available for applying the method because of extensive cloud contamination and a number of pixels with high surface temperature leading to a saturation of the instrument. Although not identical, the  $R$ -extracted values (column n°2) are comparable in magnitude with  $W(\text{sdg})$  and exhibit the same behavior. The relative error between the two determinations is 10-15%. This, however, would represent a still rather large error, were the technique used for meteorological problems. It should be noted that, in the present case, the method is used for adapting the SW coefficients, for which purpose, an estimate of  $W$  is enough. The  $W$  averaged over the image systematically exhibit lower values; more detailed analysis is needed before we can decide on an explanation.

### 3.2 LST results

Three LST products were extracted from each image in the following manner: i) use SW(nadir) to obtain  $T_{SW}(0)$ ; ii) extract the angular variation of emissivity  $\Delta\epsilon(0,F)$  between nadir and forward views, in channel (2) from inversion of DA(2) algorithm using  $T_{SW}(0)$ ; iii) obtain  $T_{SW}(F)$  using  $\epsilon_i(F)$  as determined in the previous step, with the assumption that the angular effect is the same in both channels; iv) obtain  $T_{DA}(1)$  using the angular variation of  $\epsilon_1$ . With images n°1, 2, 4 and 5, the surface temperature was also determined by solving the RT equation in one channel (1 or 2), with LOWTRAN-7 to calculate the atmospheric transmittances and radiances. Strictly speaking, only the apparent (i.e. including the reflection of the downward atmospheric radiation) ground brightness temperature could be obtained. The surface temperature is only at the cost of assigning an arbitrary value to the channel emissivities. The same figures as above were used.

Table 2 presents the three LST products, along with the temperatures obtained from RT correction for the nadir images in the 11  $\mu\text{m}$  channel, and variance associated with temperature in column 1.

Table 2: Surface temperature from SW, DA methods and RT correction ( $^{\circ}\text{C}$ )

im. n <sup>o</sup>	T <sub>SW</sub> (0)	T <sub>SW</sub> (F)	T <sub>DA</sub> (11 $\mu\text{m}$ )	T <sub>RT</sub> (0) (11 $\mu\text{m}$ )	$\sigma$
1	39.10	38.38	38.90	39.93	11.55
2	37.71	38.51	38.39	36.68	12.47
3	37.55	38.51	39.13	-	7.73
4	26.91	28.81	27.90	26.59	3.44
5	25.14	25.14	25.30	25.11	3.70

Taking T<sub>SW</sub>(0) as the reference, it is observed that the difference with respect to T<sub>RT</sub>(0) is on the average less than 1 $^{\circ}\text{K}$  and less than 0.3 $^{\circ}\text{K}$  for night-time images with little heterogeneity, indicating that the adapted SW performs well, especially regarding the lack of spectral information. With image n<sup>o</sup>5, which corresponds to the driest atmosphere, the agreement is excellent between all types of algorithms. This, however, is not true with the other images where, on the average, the LST products disagree by 1-2 $^{\circ}\text{K}$ . There is a tendency for the T<sub>DA</sub> algorithm to give better agreement with T<sub>SW</sub>(0) than for the T<sub>SW</sub>(F). This might indicate that, apart from the emissivity spectral effect, the regression coefficients have not been correctly worked out with respect to the dynamical range of emissivity angular effect (see next  $\S$ ). With regard to the spatial variability of the atmospheric water content, it was not possible to draw any reliable conclusion, although, for image n<sup>o</sup>1, looking at the difference [T<sub>SW</sub>(0)-T<sub>RT</sub>(0)] shows a tendency for this figure to have larger values farther from the location of the sounding.

### 3.3 Emissivity angular behavior

The emissivity at 53 $^{\circ}$  can be obtained, as seen above, either by means of the DA method or from RT correction in the forward image. It is thus the consequence of setting the surface temperature equal to the temperature given in the nadir image. The histograms of  $\epsilon(F)$  are presented on figure 1a (DA method) and 1b (RT correction). It is found that  $\epsilon(F)$  is, on the average,

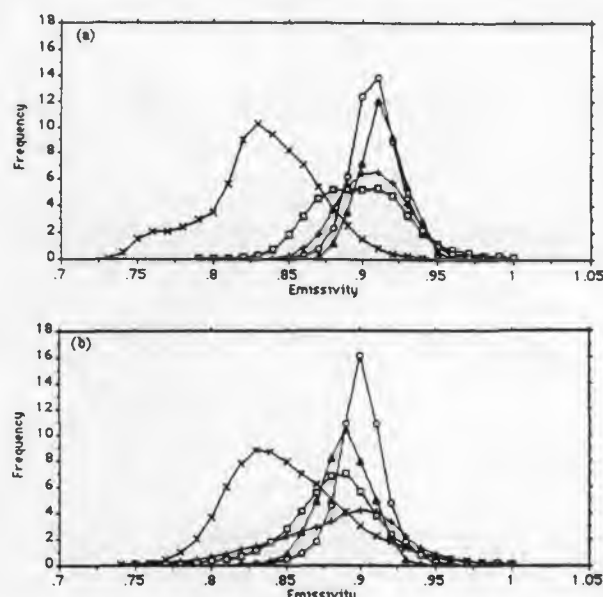


Figure 1. Histograms of  $\epsilon(F)$ : a) DA method; b) RT correction  
 $\blacklozenge$  Im. n<sup>o</sup>1  $\square$  Im. n<sup>o</sup>2  $\times$  Im. n<sup>o</sup>3  $\circ$  Im. n<sup>o</sup>4  $\blacktriangle$  Im. n<sup>o</sup>5

statistically lower than  $\epsilon(0)$  by 6-7%, for night-time images (half-maximum spread of 3%). For day-time data, we observe the same tendency, although with a wider spread particularly towards lower values. There is a trend to spreading and lowering the  $\epsilon(F)$  values from one image (day) to the other. Image n<sup>o</sup>3 exhibits the strongest effect, with an average of 0.83 (15% decrease) and values as low as 0.75. Closer inspection show that these very low values come from pixels imbedded in a cloudy region, and thus not quite reliable. When  $\epsilon(F)$  is extracted on the basis of RT correction, the result is not much different, although for day-time data, the spreading tends to develop towards lower values and the trend is more clearly observed for images 1, 2 and 3 (this one was tentatively corrected for atmospheric effects using a standard atmosphere). Looking at  $\epsilon(F)$  for image n<sup>o</sup>1 (Figure 2), it is observed that the pixels located on the river Niger have the smallest effect ( $\epsilon \approx 0.95$ ). This is consistent with an emissivity decrease with observation angle of the order of 1.5% measured for water surfaces (Ref. 11). As a consequence, day-time  $\epsilon(F)$  images make quite apparent the river and a number of segments of the hydrological network (see figure 2). The origin of the large emissivity decrease observed is extremely difficult to understand. Part of it might be an artefact of the atmospheric correction procedure, although image n<sup>o</sup>5 would contradict. Since the decrease and spreading tend to develop with increasing thermal heterogeneity, part of the effect is likely to arise from a brightness temperature anisotropy, associated with vertical structure in sparsely covered areas (for instance: tiger bush plateaus), rather than from an actual angular emissivity effect. It must be emphasized that residual atmospheric effects, from aerosols for instance, cannot be ruled out. This is particularly the case with image n<sup>o</sup>3 (09/23) for which the aerosol optical thickness  $\tau(0.45 \mu\text{m}) = 1^{(b)}$ , and which has the most pronounced effect.

**Note:** different values for the emissivity  $\epsilon(2)$  in channel 2, and for the spectral variation were used, too. This results in a shift of the LST, but the general features are not significantly altered.



Figure 2.  $\epsilon(F)$  cartography for image n<sup>o</sup>1 (08/19/92; DA method)

### 3.4 Surface temperature images

Figure 3 is the surface temperature (RT correction) for August 19, 92 (day-time). Figure 4 is the surface temperature image for September 25, 92 (night). Although the surface temperature is quite homogeneous (see Table 2) the high radiometric resolution of ATSR make it possible to observe the detailed, and in some

(b) Artemio Fattori, Laboratoire d'Optique Atmosphérique - Private communication.

respect, very subtle thermal structure: indeed, a series of thermal "filaments" hardly discernable on day-time images, running across the image, can easily be seen, representing a temperature modulation of less than  $\pm 0.5$  K. A preliminary inspection shows that this is in relation to paleo-dunes system that reveals in ground thermal and hydric properties. Similarly, dark elongated areas correspond to moist soils. Thus, ATSR images appear to be very powerful for surface hydrology.

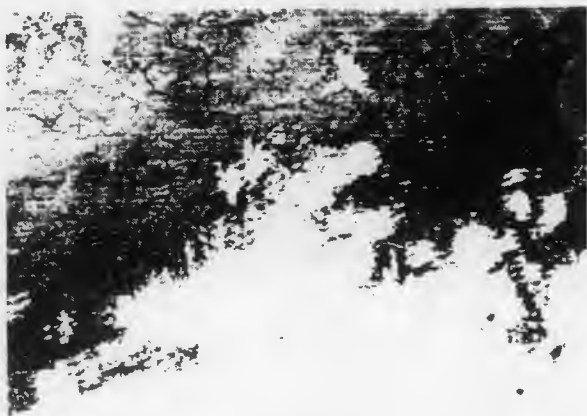


Figure 3. Surface temperature cartography for image n°1 (08/19/92; RT correction)

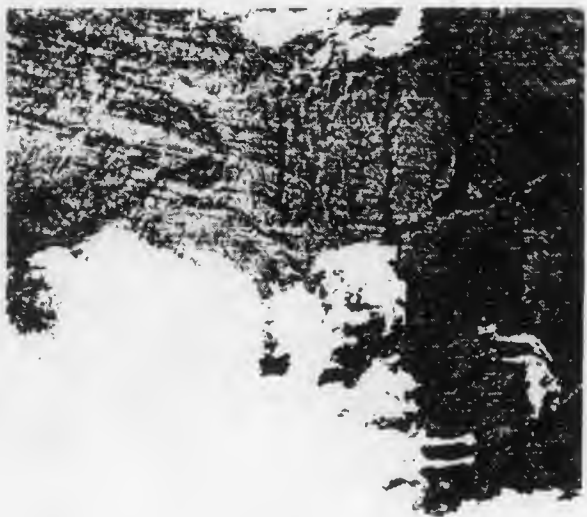


Figure 4. Surface temperature cartography for image n°4 (09/25/92; RT correction)

#### 4. CONCLUSION

The analysis of a series of ATSR images (day and night-time) over the Niamey (Niger) area indicates that the different algorithms developed for the different combinations of channels and/or view angles perform correctly, provided that the actual atmospheric situation (total precipitable water) is taken into account. It is crucial, particularly when using the forward view, to account for large emissivity angular effects along with emissivity spectral effects. Indeed, large "apparent" emissivity angular effects have been extracted, the interpretation of which being still an open question and leading to new lines of research

in the field of land surface processes. Beside this, the high radiometric resolution of the instrument allows observing very faint thermal contrasts that might be of great significance for geological and soil studies.

#### 5. ACKNOWLEDGEMENTS

The authors are indebted to Centre National de la Recherche Scientifique for financial support through a contract from Programme National de Télédétection Spatiale, 1990, and thank Dr. J.C. Pion for constructive discussions and comments.

#### 6. REFERENCES

1. McMillin L.M. (1975): Estimation of sea surface temperature from two infrared window measurements with different absorption. *J. of Geophys. Res.* 80: p 5113-5117
2. Kneizys F.X., Shettle E.P., Abreu L.W., Anderson G.P., Chetwynd J.H., Gallery W.O., Selby JEA, Clough SA (1988): *Users guide to LOWTRAN-7. Technical Report AFGL-TR-88-0177*, Optical/Infrared Technology Division, U.S Air Force Geophysics Laboratory, Hanscom Air Force Base, Mass.
3. Becker F. (1987): The impact of spectral emissivity on the measurement of land surface temperature from a satellite. *Int. J. Remote Sensing* 8:1509-1522
4. Becker F. and Li Z.L. (1990): Towards a local split-window method over land surface. *Int. J. of Remote Sensing* 3: 369-393
5. Labed J. and Stoll M.P. (1990): Angular variation of land surface spectral emissivity in the thermal infrared: laboratory investigation on bare soils. *Int. J. of Remote Sensing* 12:2299-2310
6. Prata A.J. and C.M.R. Platt (1991): Land surface temperature measurements from the AVHRR. *Proceedings of the 5th AVHRR user's meeting*, Trömsøe, Norway, 25-28 June EUM-P09: p433
7. Guillory A.R., Jedlovec G.J. and Fuelberg H.E. (1993): A technique for deriving column-integrated water content using VAS split-window data. *J. Appl. Meteor.* 32:1226-1241
8. Jedlovec G.J. (1990): Precipitable water estimation from high resolution split-window radiance measurements. *J. Appl. Meteor.* 29:851-865
9. Kleespies T.J. and McMillin L.M (1990) Retrieval of precipitable water from observation in the split-window over varying surface temperature. *J. Appl. Meteor.* 11: 1326-1333
10. Sobrino J.A., Li Z.L. and Stoll M.P. (1992): Determination of the atmospheric transmittance from AVHRR/2 data: implications on the split-window algorithms. *2nd Intern. Conf. on Modelling of Global Climate Change and Variability*, Max Planck Inst. for Meteor. - Hanover, sept. 1992
11. Rees W.G. (1992): Angular variation of the infrared emissivity of ice and water surfaces. *Intern. J. of Remote Sensing* 13: 2873-2886

## TROPICAL PACIFIC SEA-SURFACE TEMPERATURE IN AN OCEAN GENERAL CIRCULATION MODEL AND AS MEASURED BY THE ALONG-TRACK SCANNING RADIOMETER

S. P. Lawrence<sup>1</sup>, M. R. Allen<sup>1,2</sup>, T. N. Stockdale<sup>3</sup>, C. T. Mutlow<sup>2</sup> and D. T. Llewellyn-Jones<sup>2</sup>

<sup>1</sup>Atmospheric, Oceanic and Planetary Physics, University of Oxford, Parks Road, Oxford OX1 3PU, U.K.

<sup>2</sup>Rutherford Appleton Laboratory, Chilton, Didcot, Oxon OX11 0QX, U.K.

<sup>3</sup>European Centre for Medium-Range Weather Forecasting, Reading, Berks., U.K.

### ABSTRACT

The Oxford model of the tropical Pacific (a medium-resolution Cox-based general circulation model) is forced with wind data from the European Centre for Medium Range Weather Forecasting analyses and a simple parameterisation of other surface fluxes for the period covered by the ERS-1 mission (August 1991 to present). One aim of this work is to compare model results with data from the Along-track Scanning Radiometer, although this comparison will not be made here. Results of a simulation of the decline and re-occurrence of the 1991-92 El Niño event will be discussed. The re-warming of the tropical Pacific ocean in 1993 was not consistently forecast by the modelling community, indicating that there are important processes involved in the decline of ENSO events which are still poorly understood. A propagating signal of about 35 day period was discovered in the model results which is considered to be a Legeckis-wave type instability. Such waves are unusual in a model which uses a medium resolution grid, and the results will be considered in some detail.

Keywords: ATSR, El Niño, GCM.

### 1. INTRODUCTION

In order to model and predict ocean dynamics more precisely, it is essential to have accurate knowledge of observed wind stress, heat fluxes and sea-surface temperature (SST). The Along-track Scanning Radiometer (ATSR) provides SST accurate to better than 0.5° C in tropical regions (see Barton et al., this volume). It will greatly benefit the modelling community as a long, consistent SST data-set becomes available.

Large-scale (~ 10<sup>3</sup> Km) oceanic processes were simulated using a Cox-based ocean general circulation model (GCM) of the tropical Pacific ocean for the period January, 1991 to September, 1993. Whilst emphasis during this work was placed on a comparison between the model data and that obtained from ATSR, we will mainly discuss the model results here. Readers are referred to Allen et al., in this volume, for more details of the ATSR/model comparison.

The essential difference between this study and other model simulations in Oxford (Ref. 1, Ref. 2) is that this model was forced with daily varying wind stresses obtained from the European Center for Medium Range Weather Forecasting (ECMWF) analyses. Previously, the forcing consisted of linearly interpolated monthly values, using the stresses produced by O'Brien et al. (Ref. 3). The ECMWF analysis winds for the period considered here do not contain ERS-1 or ATSR data. This is an important point if we are to make an objective comparison with ATSR data, since we want to be sure that the model results are not corrupted by the inclusion of these satellite data, however implicit that may be.

Section 2 outlines the GCM (described more fully in Stockdale, Ref. 1), while section 3 describes the wind and heat flux forcing fields used. Section 4 discusses the results and finally, in section 5, a summary and conclusions are provided, together with our suggestions for further work in this area.

### 2. THE MODEL

The Oxford GCM which was used in this study is due to Stockdale (Ref. 1). It is closely based on the Cox code (Ref. 4), with a regular 1.5 degree tropical Pacific grid spanning the region 30°N to 30°S. There are 16 levels in the vertical with high resolution (10m) near the surface. The boundaries are closed, no-slip and insulating East and West, but heat transport is allowed through the North-South boundaries. The vertical mixing scheme is due to Paconowski and Philander (Ref. 5).

### 3. FORCING FIELDS.

The forcing fields occur in the equations which represent the transport of heat and momentum. The heating term used in the model is a parametrisation in which the SST always adjusts towards a model seasonal cycle (i.e. a model climatology computed *before* this simulation). Equation (1) below illustrates the method, and has the following effect. If the SST is larger than the climatological value, then the heat flux will act to decrease the SST in subsequent calculations. On the other hand, if the SST is less than the climatological value, the heat flux will act to increase it.

$$Q = Q_c - \gamma \left. \frac{\partial Q}{\partial T} \right|_o (T_m - T_c) \quad (1)$$

Here,  $Q_c$  represents the heat flux obtained from the model climatology and  $T_c$  the corresponding SST.  $\partial Q/\partial T$  is an empirical quantity obtained from Oberhuber (1988).  $T_m$  is the model SST calculated during the simulation and  $\gamma$  determines how strongly the SST relaxes towards the model climatology.  $Q_c$  is calculated from an analogue of equation (1), replacing model climatological values with observed (Oberhuber, Ref. 6) values.

The forcing of momentum is a wind stress  $\tau = (\tau_x, \tau_y)$ , obtained as daily averages from the ECMWF analysis and interpolated linearly onto the model grid. In this work, we are using a prescribed  $\tau$ , thus allowing the simulation of the actual ocean state through the direct response of the model to a wind stress. This allows a more realistic comparison with ATSR data than forcing with monthly winds. The problem is that the O'Brien winds have been averaged over a month and are temporally smoother than the daily ECMWF winds. Forcing with the monthly winds therefore results in a model response which will be smoother than reality.

### 4. RESULTS

In this section, the results of the model simulation are discussed. These take the form of plots of time versus longitude, for a particular latitudinal cross-section (Høvmøller diagrams). The latitude used in all of these plots is 2.25° North of the equator. The cross-sections thus encompass the equatorial waveguide, a region of the Pacific in which many of the important dynamical processes occur which are of interest in this study.

Figures 1 and 2 show the zonal and meridional components of the wind stress. The important features are illustrated in figure 1, where we note that the zonal stress is largely Easterly (black end of the spectrum). This is, of course, a characteristic of winds over the tropical Pacific ocean close to the equator (see, for example, Ref. 7). Other features of interest

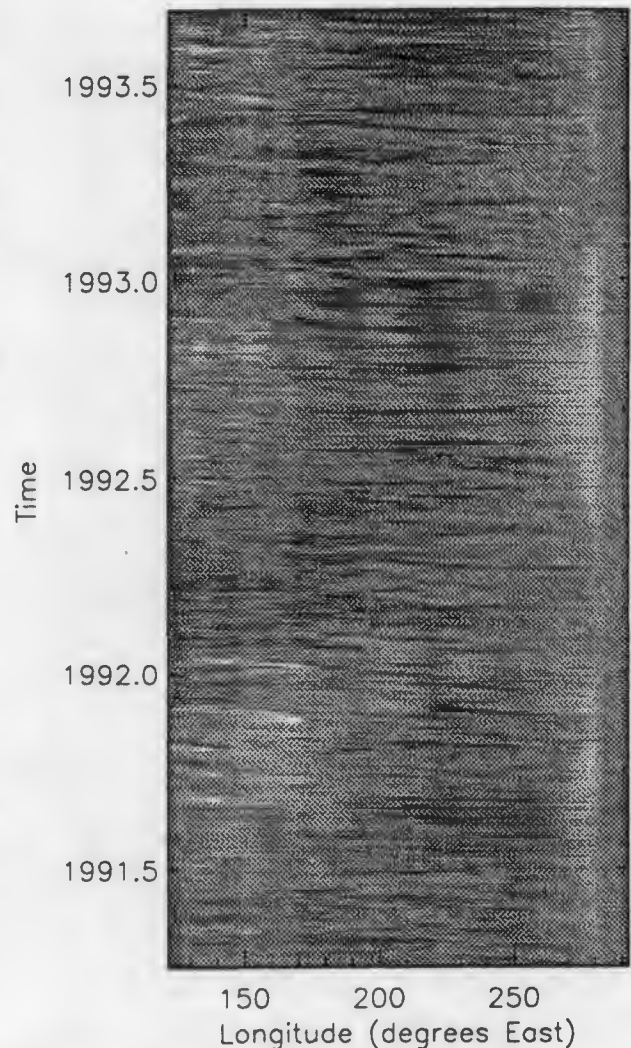


Figure 1. The zonal wind stress

in figure 1 are the Westerly wind bursts, evident at the times marked with an arrow, and occurring right over in the West Pacific. Although these bursts are relatively short lived (lasting for only a few days) they are high amplitude ( $\sim 0.15 \text{ N m}^{-2}$ ). These bursts have a significant effect on the ocean as we will now discuss.

Figure 3 shows the average temperature of the first 360 m. There are several features of interest. Firstly, one notices the seasonal cycle, in which the temperature rises during Northern summer months (white represents 32° C, black 24° C), particularly in the Eastern Pacific. This rise in temperature is modulated in 1992 by the 1991-92 El Niño event, in which the temperature is higher than that found in the other two summers. Secondly, one notices the fast ( $\sim 2 \text{ m s}^{-1}$ ) Eastward propagating signals, whose starting time is labelled by arrows. These are equatorially trapped Kelvin waves and are excited by the high-amplitude wind bursts discussed above. As the Kelvin waves strike the eastern coast, they reflect to form Westward propagating Rossby waves, and these are just visible in figure 3, where the time at which

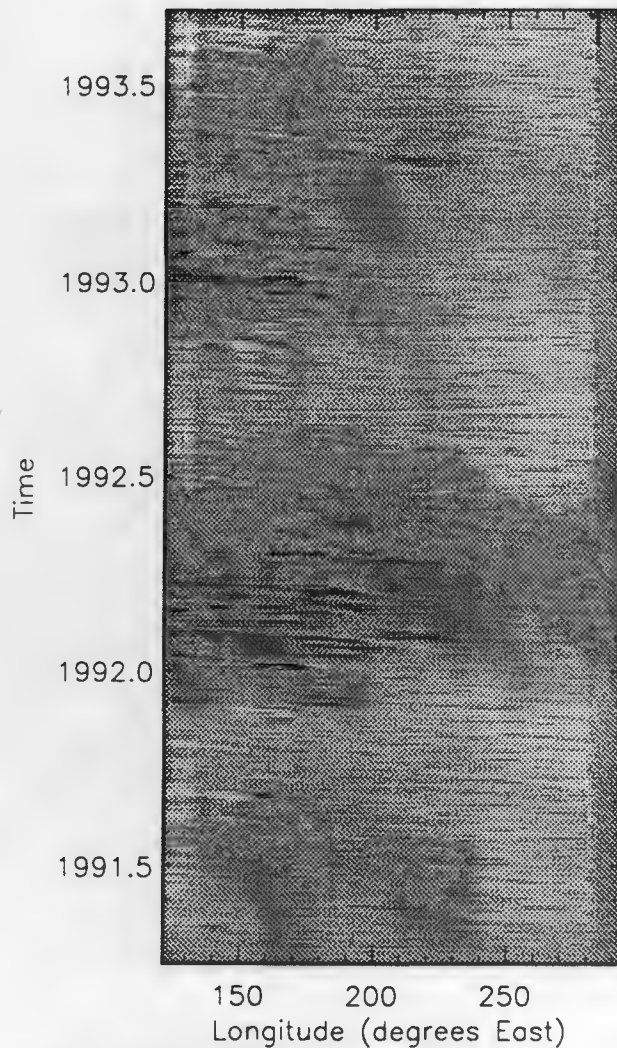


Figure 2. The meridional wind stress

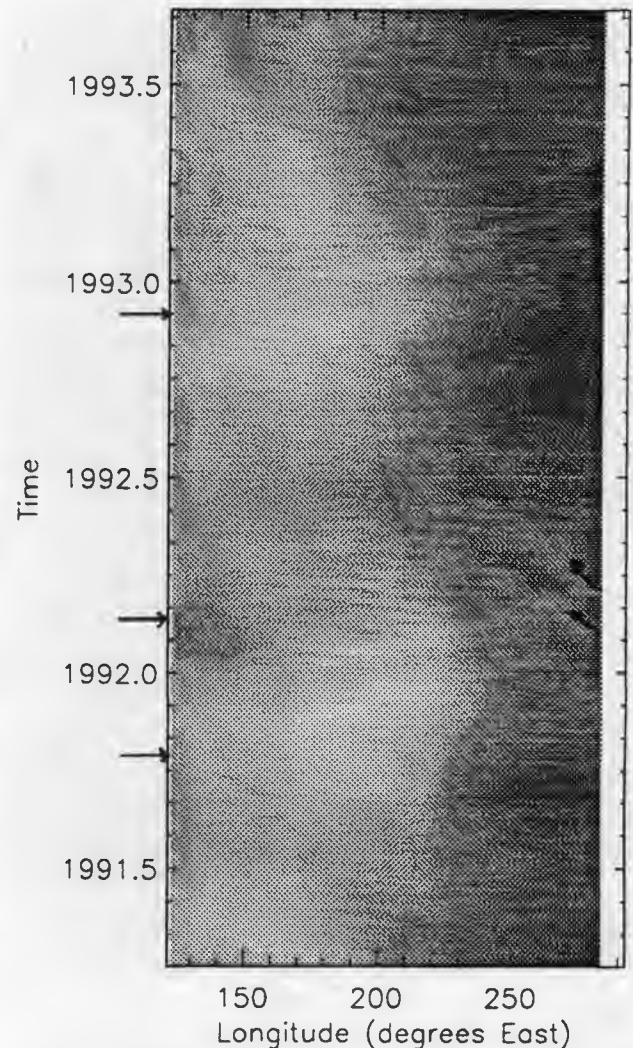


Figure 3. Vertically averaged temperature of the first 360 m (ten levels).

they reflect off the Eastern coast and their initial speed is denoted by arrows (these waves are more prominent when a colour scale is used). Note that the first of these propagates faster than the second, indicating that they are two different Rossby modes, possibly with different vertical structure corresponding to first and second vertical modes.

In figure 4, the bulk sea surface temperature (i.e. at 5m depth) is plotted for comparison with ATSR data (see Allen et al. in this volume). Again one notes the seasonal cycle, and the 1992 warming due to the El Niño. Figure 5 shows the corresponding results using the O'Brien (Ref. 3) winds for the years 1991 and 1992 and one finds that the temperatures in the Eastern Pacific are generally higher than those of figure 4. The reason for this is that the model has been tuned towards the use of the O'Brien winds, which are generally stronger than the ECMWF stresses and hence induce more upwelling of colder, sub-surface water in the East. Furthermore, the Kelvin and Rossby waves described above are not evident in either of these plots, since they are largely due to sub-surface dynamics, and one would not expect them to be so prominent in a plot of SST.

Finally, we point out the propagating features in figure 4. These appear to begin in the Eastern Pacific during August, 1992 and propagate Westward until about January 1993. The important point to note here is that these features are also present in the ATSR data (see Allen et al. in this volume), occurring at the same time and place. It is not obvious why these model waves should match so favourably with ATSR, since we are comparing two independent data sets. As stated earlier, the model contains no forcing fields which are common with ATSR. The data-sets are not completely identical, however, since the ATSR waves quickly become out of phase with the model waves. We conjecture here that these waves are Legeckis waves, or shear instabilities, (Ref. 9) excited by a particular frequency component in the ECMWF wind stresses. Note that the forcing of this model with O'Brien stresses do not show such features, possibly because there is not enough power in those winds at the relevant forcing frequencies. A more complete statistical study of these waves can be found in the article by Allen et al. , in this volume.

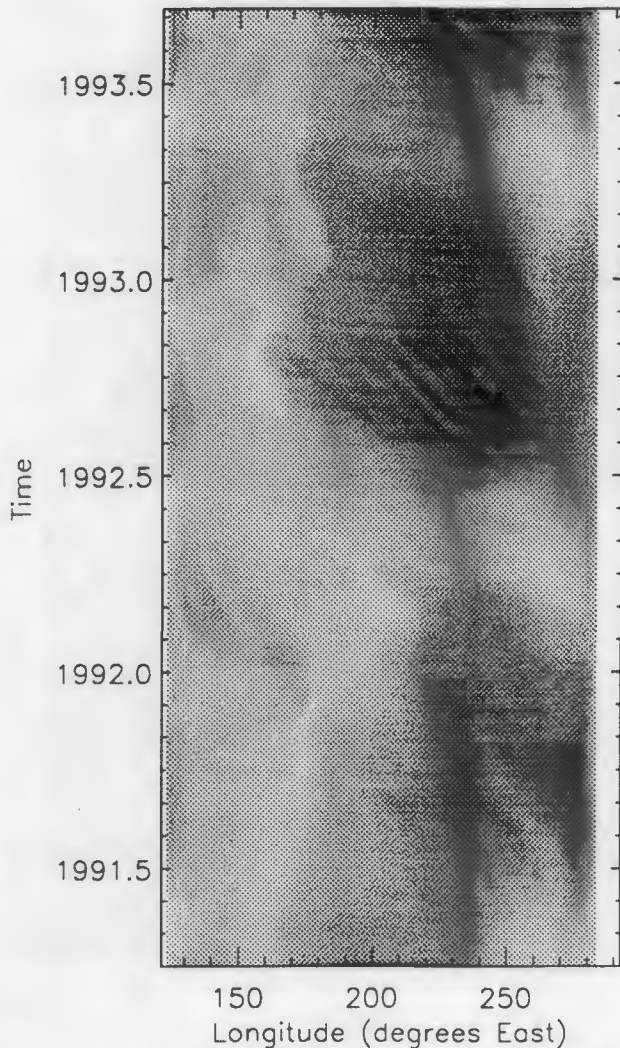


Figure 4. Temperature in the first layer of the model when forced with the ECMWF winds.

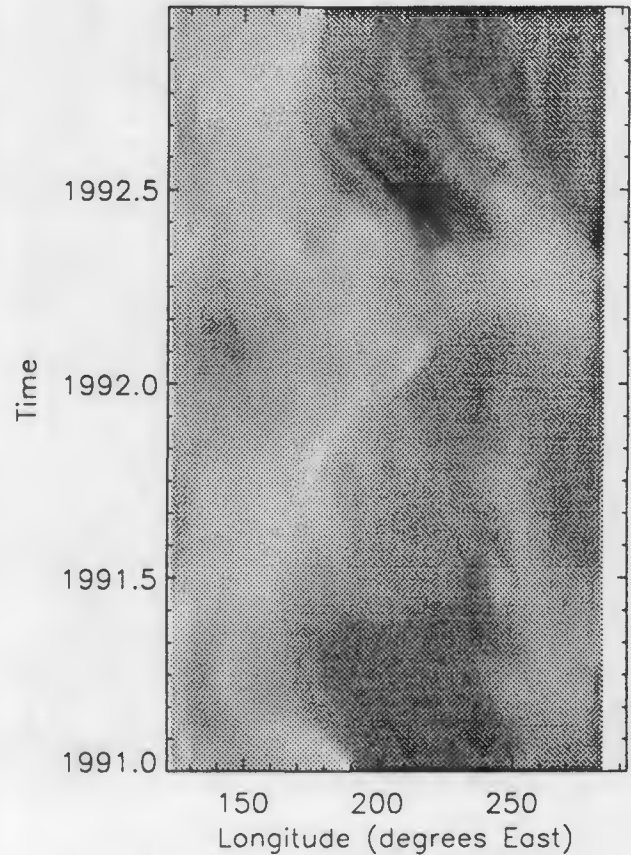


Figure 5. Temperature in the first layer of the model when forced with the O'Brien winds.

## 5. DISCUSSION

In this paper, we have summarised results obtained from an ocean GCM forced with daily winds. Many of the results are consistent with previous work (e.g. Ref. 1,10). The seasonal cycle is well determined, although generally warmer than expected. Kelvin and Rossby waves are produced by the model, consistent with the Westerly wind bursts in the ECMWF wind stress data. The important result, however, is that Legeckis waves occur and this is very unusual in a model whose grid resolution is so low as to be below the threshold for spontaneous instability to occur. With regard to further work, the primary aim will be to determine the cause of the 35-day waves. In order to pin-point the source more precisely, we have forced the model with the ECMWF wind's climatology plus red-noise with power at frequencies of interest (i.e. greater than  $0.0083 \text{ cycles day}^{-1}$ ). The point is that if the waves are due to model dynamics as well as direct wind forcing, then they will also appear in this analysis. That is, an ocean instability may be produced because the ECMWF wind cli-

matology establishes an ocean state from which the waves can be initiated, and then forces the ocean at the 'correct' frequency. That is, the ocean acts as a kind of filter to the winds. The results indicate that the waves do appear when forced with a climatology plus red-noise, but are almost absent when forced with the climatology alone.

Figure 6 shows the resulting SST when forced with climatology plus noise, whilst figure 7 shows the result when forced with the climatology alone. These results could explain why the Legeckis waves can be seen in higher-resolution models forced with the monthly winds (e.g. Ref. 2): the instabilities presumably depend upon the model and its parametrisations, such as grid size or mixing, and so the question as to whether they will be excited by different forcing fields will depend upon the model. This question is currently under investigation by studying the behaviour of the waves as the resolution of the grid is increased.

There are several other approaches which will aid the study of the waves. For example, are the waves produced by the forcing of the model with different wind

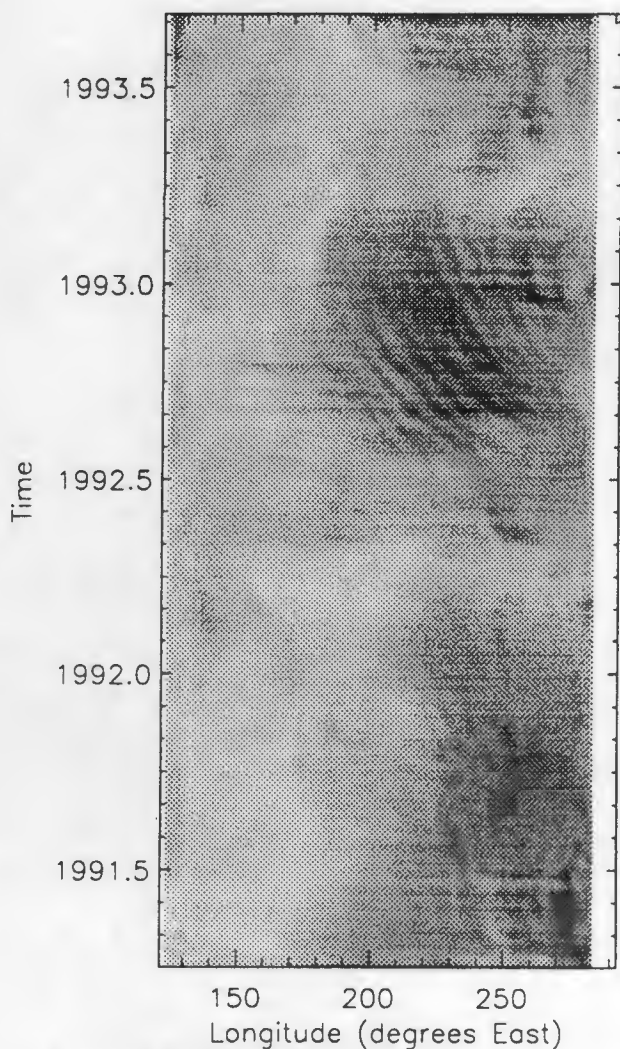


Figure 6. Temperature in the first layer of the model when forced with the ECMWF wind climatology plus red noise.

fields (e.g. U.K. Met. Office; ECMWF interactive wave model)? Do the waves appear in other data? We have already alluded to the fact that the waves do occur in the ATSR data. It would be interesting to determine if they are also present in data from an independent source, for example the TOGA/TAO buoy array.

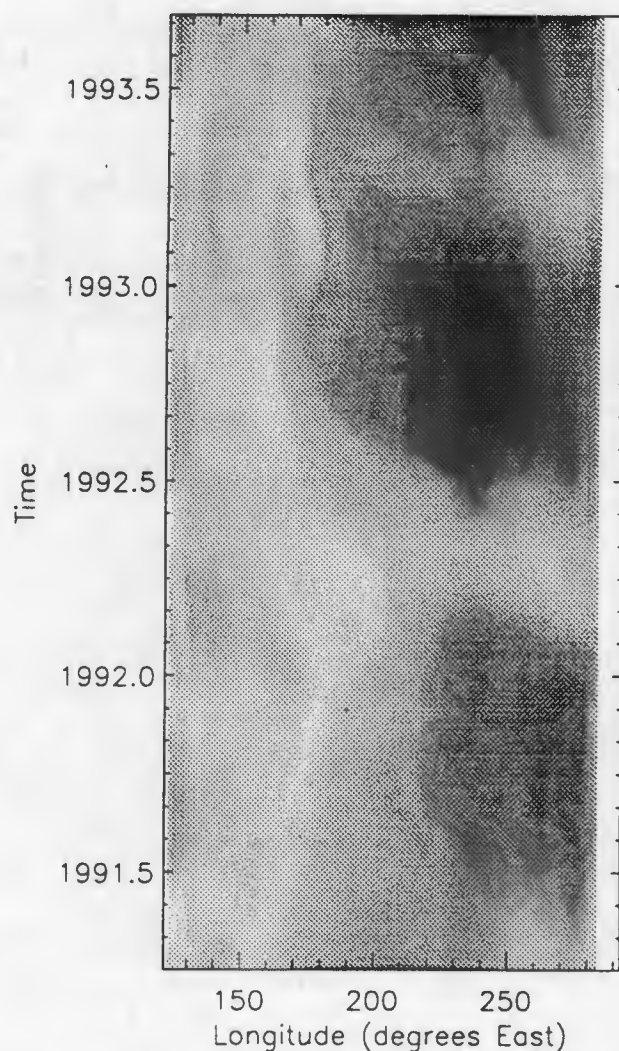


Figure 7. Temperature in the first layer of the model when forced with the ECMWF wind climatology.

#### REFERENCES

1. Stockdale, T.N 1992, Simulation and prediction of tropical SST with a coupled ocean-atmosphere model, *D.Phil. Thesis*, University of Oxford, U.K.
2. Stockdale et al. 1993, *Intercomparison of tropical ocean GCMs*, World Climate Programme, report number 79.
3. Goldenburg, S.B. and O'Brien, J.J. 1981, Time and space variability of the tropical Pacific wind stress, *Mon. Weath. Rev.*, 109, 1190-1207.
4. Cox, M.D., 1984, *A primitive equation, 3-dimensional model of the ocean*, GFDL Ocean Group Technical Report No. 1, GFDL/NOAA, Princeton University, Princeton NJ 08452.
5. Pacanowski, R.C. and Philander, S.G.H. 1981, Parametrizations of vertical mixing in numerical models of tropical oceans, *J. Phys. Oceanogr.*, 11, 1443-1451.

6. Oberhuber, J.M. 1988, *An atlas based on the COADS data set: the budgets of heat, buoyancy and turbulent kinetic energy at the surface of global oceans*, Max-Planck Institut für Meteorologie, Report No. 15.
7. Gill, A.E. 1982, *Atmosphere-Ocean Dynamics*, Chapter 11, Academic Press, London.
9. Legeckis, R. 1978, A survey of worldwide sea surface temperatures fronts detected by environmental satellites, *J. Geophys. Res.*, 83, 4501-4522
10. Davey, M.K. et al 1991, *Coupled tropical ocean global atmosphere models at the UKMO*, CRTN 21, Hadley Centre for Climate Research and Prediction, Bracknell, UK.

## Water Surface Temperature

Chairman: D T Llewellyn-Jones, Rutherford Appleton laboratory, UK  
Present Address: University of Leicester, UK

### Introduction

This session was devoted to the use of data from one ERS-1 sensor, the Along-Track Scanning Radiometer, which, unlike the other ERS-1 instruments is a nationally provided experimental instrument developed by a consortium of research institutes in the UK, with additional contributions from France and Australia. The consortium is led by the Rutherford Appleton Laboratory in the UK.

### The ATSR Instrument - In-flight Performance

The in-flight performance of ATSR was reviewed by the ATSR Principal Investigator (Llewellyn-Jones, Rutherford Appleton Laboratory, UK). The instrument, is one of the most available (better than 97%) of the ERS-1 sensors and it continues to perform with great stability, with almost negligible degradation of the main sub-systems including the closed cycle cooler, the first of its kind in space and arguably the most technically adventurous feature of the satellite payload.

However, there are two aspects of ATSR which have not reached expectations. One these is the 3.7 micron wavelength channel, which failed very suddenly in May 1992, despite producing extremely high quality data almost continuously prior to that time. The other negative aspect of the data concerns the presence of low levels of EM interference, internal to the instrument, which primarily affects the 12 micron channel and can be seen in some SST images as "grooving" of the image scene. although this disfigures some of the image data, it does not detract from ATSR's overall objective of measuring SST with an accuracy better than .5C, which, according to recent validation results is being properly met.

### SST in the Indian Ocean

The Indian Ocean is a particularly important area for ATSR. Not only is it extremely important from the point of view of air/sea interaction, but also, on account of the high water vapour burdens and gradients, it is a particularly difficult region in which to measure SST from space. An initial assessment of ATSR data over the Indian Ocean (Agarwal et al, ISRO India) showed that ATSR's data was consistent with the .5C accuracy objective.

### Filamentary Structures in Turbulent Mixing

This was one of the most remarkable discoveries from ATSR data. Robinson et al (University of Southampton, UK) showed examples (first seen in public in the 1993 ATSR Calendar - February Image!) of fine structure in SST patterns. which can be seen from ATSR on account of its particularly high radiometric resolution.

This turbulence can be very clearly seen over scales ranging from 2 Km to 200 Km. Two distinct characteristic types of turbulence could be seen, and it is possible that there are two

mechanisms at work - one the traditional fluid mixing, which can now be very effectively represented in dynamical models; while the other is possibly a surface (or near-surface) effect, possibly related to roughness effects which are not properly understood. This result showed quite clearly that ATSR, with its exceptionally high radiometric sensitivity and good optical definition, is capable of opening up new opportunities in dynamical oceanography.

### **Tropical Validation in the Presence of Aerosol; and Global Validation**

Results were given of ship-borne measurements from the tropical Atlantic (Thomas et al, British Antarctic Survey, UK) confirmed the very important result that ATSR, with its two-angle view is in fact able to provide useful and accurate SST measurements in the presence of aerosol contamination which, at the time, was making SST measurements from other satellite instruments extremely difficult.

Other validation results presented in a poster (Mutlow et al, Rutherford Appleton laboratory, UK) showed that, in comparison to drifting buoy measurements the ATSR dual-view night-time data agrees with the buoys to within  $.1 \pm 0.35$  deg C.

### **Comparison with AVHRR**

Detailed comparisons with AVHRR data (Barton et al, CSIRO Australia) showed the very significant advantages to be gained from ATSR's superior digitisation, signal-to-noise ratios and two-target on-board calibration system.

### **The Detection of Climate Change**

An analysis based on ocean-atmosphere coupled model results (M Allen, Rutherford Appleton laboratory, UK) indicated that results from short time-series need to be treated with extreme caution. The need for continuity of observations over periods of ten years or more is imperative.

### **Conclusions**

The excellent SST data coming from the ERS-1 ATSR is opening up new possibilities for the study of dynamical oceanography. The good SST measurements that the satellite was able to make in the presence of severe aerosol contamination is of exceptional interest to those considering future operational observing systems, and to those who require continuity of data-quality.

## WATER VAPOUR RETRIEVALS USING COMBINED ATSR INFRARED AND MICROWAVE DATA

I.J. Barton<sup>1</sup>, A.M. Zavody<sup>2</sup>, C.T. Mutlow<sup>2</sup> and D.T. Llewellyn-Jones<sup>2</sup>

<sup>1</sup>CSIRO Division of Atmospheric Research, Aspendale, Victoria 3195, Australia

<sup>2</sup>Rutherford Appleton Laboratory, Chilton, Didcot, Oxon OX11 0QX, U.K.

### ABSTRACT

The ATSR instrument provides six infrared measurements of the upwelling radiance from the earth's surface and atmosphere. In clear conditions the atmospheric transmittances are largely determined by the water vapour and temperature profiles in the lower atmosphere. By combining the six infrared measurements with the total water vapour amount derived from the microwave channels, it may be possible to determine low level structure in the water vapour and temperature profiles. This possibility is explored using data from coincident radiosonde and satellite measurements.

### 1. INTRODUCTION

Water vapour, because of its strong absorption in the infrared spectrum, is the major atmospheric constituent that contributes to the greenhouse effect. However water vapour is also the most highly variable constituent in the atmosphere, and thus it is important that its distribution and transport be accurately monitored if we ever expect to monitor climate changes using numerical models.

Water vapour has strong absorption features throughout the infrared spectrum from the near infrared bands at 1.1, 1.4, 1.9 and 2.7 microns, through the middle infrared at 6.3 microns, to the rotational absorption bands that make the atmosphere virtually opaque between 20 microns and the millimetre wave-band. Superimposed on the absorption lines in the middle infrared is a continuum absorption whose origin is still open to debate. This absorption is important for the energy balance of the earth's system as the longwave radiation that must be emitted to space to balance the absorbed solar shortwave radiative energy occurs at these wavelengths. To enable numerical models of climate to accurately simulate the radiative energy balance detailed information on

the water vapour content of the atmosphere will be required. This information must include the vertical structure of water vapour as the temperature and concentration of water vapour determines the radiant energy loss to space. The effect of water vapour near the surface, which is at a temperature close to that of the surface, is relatively easy to parametrise, but water vapour at elevated levels, which has a temperature less than the surface, has a profound effect on the atmospheric radiative balance.

Passive microwave and infrared radiometers have been developed and flown on spacecraft to give a remote measurement of total water vapour content, and these instruments perform reasonably well. The HIRS instruments that are carried on the NOAA operational meteorological satellites have infrared sounding channels for both temperature and water vapour and the data from these instruments are used operationally. The channels giving water vapour profiles use the wings of the 6.3 micron absorption band to determine a water vapour profile at several levels in the upper atmosphere. However, the bulk of the water vapour is below 5km altitude and the HIRS channels have an extremely poor vertical resolution and give little useful information on the water vapour distribution below a height of 5 km.

The ATSR has been developed specifically to provide an accurate measure of sea surface temperature (SST) from space. One of the design features incorporated in this instrument is the provision of six infrared measurements in highly transmissive spectral regions to assist in the determination of the atmospheric absorption which constrains the accurate determination of the SST. (The ATSR makes measurements at 3.7, 11 and 12  $\mu\text{m}$  at two different view angles.) Further details of the ATSR are given by Delderfield et al (Ref. 1). In each of these measurements the main atmospheric absorber is water vapour, and in each "channel" the amount of absorption is different. Because of this feature it should be possible to use the ATSR as a sounding instrument for low level atmospheric water vapour. An analysis procedure is explored in this paper by studying

the water vapour absorption in the lower atmosphere and using a band model of absorption in the atmosphere to produce simulated ATSR data for testing the procedure. Many simplifications are made in this work: the two view angles of ATSR are fixed at 0 and 55 degrees, surface emissivity is assumed to be unity, and the ATSR data are assumed to have no measurement error. Before an operational procedure is developed a more thorough investigation using an accurate line-by-line model with global ATSR data will be required. Alternatively an empirical technique could be developed in the same manner as that used for the analysis of sounding data from the HIRS instrument.

## 2. ATSR WEIGHTING FUNCTIONS

The radiance received by a satellite instrument can be expressed as

$$I_\nu(z, T) = B_\nu(T_s)\tau_\nu + \int_0^z B_\nu(T)K(z, T)dz \quad (1)$$

where  $I_\nu(z, T)$  is the radiance received at the satellite,  $B_\nu(T)$  is the Planck radiance at temperature  $T$  and frequency  $\nu$ ,  $(T_s)$  is the temperature of the earth's surface and  $z$  is the height above the surface. The term  $K(z, t)$  is often referred to as the weighting function and is given by

$$K(z, T) = \frac{\partial \tau_\nu}{\partial z} \quad (2)$$

Here a band model of transmission in the atmosphere is used that has been described by Barton (Ref. 2). The temperature dependence of the continuum absorption in the 10 to 12 micron band has been changed to agree with the values determined by Barton (Ref. 3). This increases the continuum absorption coefficients at the temperatures of the mid and upper troposphere while leaving those near the surface at their accepted values. Using the mid latitude summer standard atmosphere of McClatchey et al (Ref. 4) the model has been used to determine weighting functions for the ATSR infrared channels. These are shown in Figure 1. The figure clearly shows the different absorption in the six "channels"; a feature that is required if they are to be used for vertical profile determination (as well as SST).

The figure also indicates how the ATSR data can be used to provide information on the vertical structure of water vapour. The signal in the 3.7N (3.7 $\mu$ m, nadir view) channel is more dependent on the water vapour near the surface while the 12F (12 $\mu$ m, forward view) signal is more dependent on the water vapour above a height of 2 km. By examining the difference between the signals in the six ATSR channels an estimate of water vapour distribution should thus be possible. This hypothesis is investigated in the next sections using simulated ATSR data.

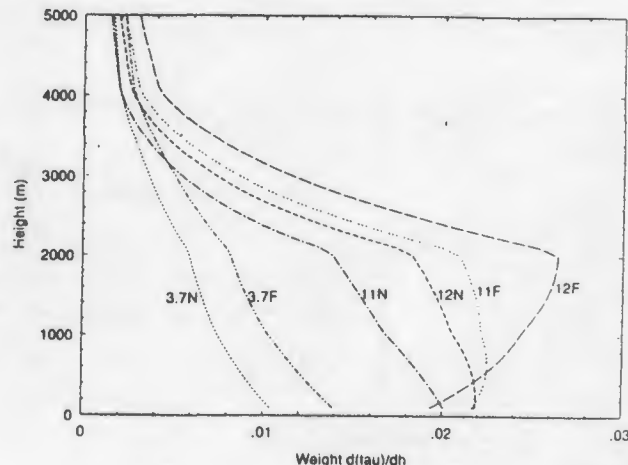


Figure 1. The ATSR weighting functions for water vapour retrieval.

## 3. A SUB-TROPICAL CASE STUDY

During the five months following the launch of ERS-1 several validation cruises were undertaken in Australian sub-tropical waters. On occasions when the research vessel was in the swath of the ATSR, radiosondes were launched from the vessel as part of the ground truth data collection for ATSR validation. A selection of these data has been used to explore the hypothesis that ATSR data can give water vapour profile details in the lower atmosphere.

When the ATSR brightness temperatures for the validation cruises were studied it was evident that there was considerable variation in the differences between pairs of channels for different locations. These differences must be due to variation in the structure of the atmosphere, or the difference between the air and sea temperatures. Therefore, in this analysis, the differences between pairs of ATSR brightness temperatures were compared with the structure of the atmosphere as measured by the radiosondes.

First a selection of validation data was used to derive an average difference between pairs of ATSR channels. The pairs selected, and their average values are given in Table 1. From these data a subset was selected that had clear skies, had all six ATSR brightness temperatures available (night data only due to solar contamination at 3.7  $\mu$ m), and for which radiosonde data were available. From over thirty SST validation coincidences these criteria restricted the analysis to only three cases. For each case the brightness temperature differences were determined and then the ratio of the differences to the average values, as given in Table 1, were calculated. The results are given in Table 2. For comparison the water vapour profiles for each case are given in Figure 2.

TABLE 1. ATSR data analysis for selected radiosonde profiles.

Channels	3.7N-11N	11N-12N	12N-3.7F	3.7F-11F	11F-12F
Averages (K)	0.41	1.01	0.31	0.63	1.35

TABLE 2. Ratios of differences to average differences for the ATSR brightness temperatures.

Date (1991)	Time(Z)	3.7N-11N	11N-12N	12N-3.7F	3.7F-11F	11F-12F
13 Sept.	1100	0.17	0.85	1.08	0.40	0.82
22 Sept.	1215	1.30	1.01	0.68	1.08	0.96
19 Nov.	1305	0.12	0.70	1.86	0.37	0.64

The water vapour profiles shown in Figure 2 indicate almost identical profiles for the 13 September and the 19 November, while the profile for September 22 shows a similar structure, but has much more water vapour between 2 and 5 km above the surface and a moister lower layer. The ratio of the differences in Table 2 also show similar values for the first two dates but give markedly different values for the latter date. The lack of water vapour in the upper levels appears to be correlated with the ratio values for the 3.7N-11N, 12N-3.7F and 3.7F-12F differences. This suggests that the differences between the ATSR brightness temperatures may be used to derive a water vapour profile. This possibility is explored in the next sections.

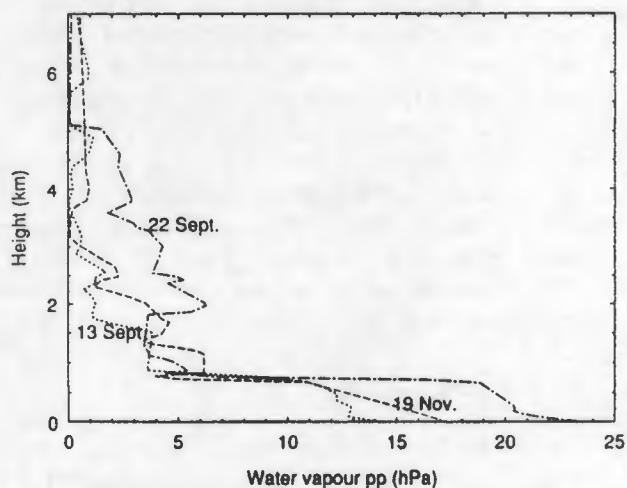


Figure 2. The radiosonde water vapour profiles.

#### 4. SIMULATED DATA ANALYSES

The band model of transmission is used to provide a standard data set to test the retrieval of vertical water vapour profiles. Again the standard mid-latitude atmospheric model of McClatchey et al (Ref. 4) is used as a basis. To enable a wide range of different atmospheres to be included in the simulation study the following alterations to the standard atmospheric profile were made.

1. The SST was set at 280K, 285K, 290K, 295K and 300K.

2. The surface air temperature (SAT) was set at SST-3K, SST and SST+3K.

3. For an SST of 290K the following values of water vapour were assumed -

Height (km)	WV partial pressure (hPa)
0-1	5, 10, 15, 20
1-2	10, 6, 2
2-4	4, 1
4-6	2, 0
above 6	0

4. The water vapour values at 290K were multiplied by factors of 0.5, 0.75, 1.25 and 1.5 to obtain the values for SST values of 280K, 285K, 295K and 300K respectively.

5. The temperature profile was set as follows -

Height (km)	Temperature (K)
Surface	SAT
1	SAT-6
2	SAT-12
4	SAT-22
6	254
8	244
10	232
15	210
20	220

These parameters give 720 profiles with a wide range of surface temperatures, air-sea temperature differences and water vapour vertical distributions. While doing this they also maintain realistic values of water vapour amounts and atmospheric structure. One phenomenon not included is the temperature inversion that often occurs at heights where there is a strong discontinuity in the water vapour profile. However, the range of profiles should be sufficient for a preliminary investigation of the feasibility of retrieving water vapour structure.

#### 4.1. Method 1.

Examination of the weighting functions in the above section indicate that the water vapour profile information is intrinsically held in the relative values of the six ATSR brightness temperatures. However the air-sea temperature difference also has a strong effect on these values. If the air-sea temperature difference and the SST are known, and an accurate transmission model is available, then brightness temperatures can be calculated for a known total atmospheric water vapour amount and a standard shape of the water vapour profile. If this is done then the water vapour profile details should be obtainable from the six differences between the measured and calculated brightness temperatures in each channel. This is the basis of the technique developed here and described below.

First the ATSR data are used to determine the SST using a standard retrieval algorithm. In our simulation study a standard regression algorithm is determined using the simulated data set. The algorithm for the data set is -

$$SST = a_0 + \sum_{i=1,6} a_i T_i \quad (3)$$

where the coefficients  $a_i$  are determined by a standard multiple regression technique. If the input brightness temperatures are assumed to be measured with no errors or noise then the SST is retrieved with a standard error of 0.03K and the algorithm has a correlation coefficient of 0.999.

To enable the calculation of the brightness temperatures for the standard shape of the water vapour profile the total water vapour amount is required. Here there are two possible sources of this parameter. The ATSR includes a dual channel microwave radiometer that can be used to derive the total water vapour amount. Eymard (1992) has shown a retrieval accuracy of 0.4 cm in total precipitable water for clear sky retrievals. Alternatively the simulated data set (or the measured ATSR brightness temperatures) can be used to derive a total water vapour algorithm in the same manner as for the SST: i.e.

$$WV = b_0 + \sum_{i=1,6} b_i T_i \quad (4)$$

For the simulated data set the total water vapour retrieval has a standard error of 0.23 cm and a correlation coefficient of 0.966.

The main inhibitor to an accurate retrieval of total water vapour is the air-sea temperature difference. In cases where the sea and surface air temperatures are equal the water vapour retrieval in the simulated data set, using the infrared channels only, can be achieved with a standard error of 0.11 cm.

If measurement errors or noise are included in the brightness temperatures the standard errors, of course, become larger. If the errors in each temperature is assumed to be 0.04K (a realistic estimate for the ATSR) then the standard errors increase from 0.03 to 0.11K, and from 0.23 to 0.28 cm.

Having obtained estimates of the SST and the total water vapour amount it is only necessary to now specify the shape of the standard water vapour profile before calculating the expected ATSR brightness temperatures. For this an exponential decrease in water vapour with a scale height of 2 km is assumed. This is equivalent to a forty percent decrease in water vapour amount for each kilometre rise in height. Again, as in the original profiles, a constant water vapour amount in each of the four lower levels of the atmosphere is used. The differences between the measured (simulated) values and those derived from the standard profile are then determined.

When this data set of the differences is examined it becomes obvious that they are dominated by the air-sea temperature difference. Also it is evident that a change in the shape of the water vapour profile (e.g. an increase in water vapour near the surface with a decrease at levels above 2 km) has a similar effect on the values of the differences. This means that a relatively accurate measure of the air-sea temperature difference is required if the profile details are to be determined in this manner. If the air temperature is constrained to be equal to the water temperature then a linear multiple regression analysis can determine the 0-1 and 4-6 water vapour ratios with correlation coefficients of 0.90 and 0.85. The water vapour ratio is the amount of water vapour in a defined layer divided by the total water vapour amount. When the noise on the ATSR brightness temperatures is included the errors in deriving the water vapour ratios become rather large and it may be necessary to derive separate coefficients for a range of total water vapour amounts and surface temperatures.

#### 4.2. Method 2.

The ATSR infrared data can be used in a variety of ways to derive the SST. For any algorithm the error in the SST determination is due to abnormalities in the temperature and water vapour profiles. If the profiles are "standard" then the algorithm should deliver an exact value for the SST. This feature of SST derivation may lead to a technique for determining the water vapour profile that does not have the same dependence on the air-sea temperature difference as found in the first method.

The simulated data set was used to produce five different SST algorithms - each using a different pair of channels. The hypothesis here is that the errors in the five derived SST values will be dependent on the

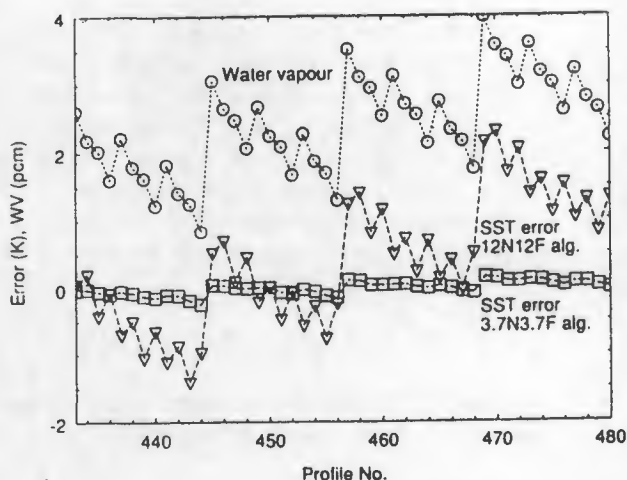


Figure 3. The total water vapour content and the errors in derived SST using the (3.7N 3.7F) and (12N 12F) algorithms for the profiles with the sea and air temperatures set at 290 and 287K respectively.

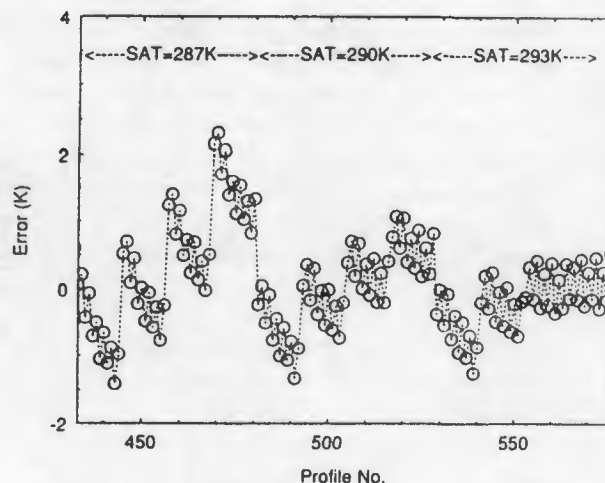


Figure 5. The error in derived SST using the (12N 12F) algorithm for the profiles with sea temperature set at 290K and air temperature set at 287, 290 and 293K.

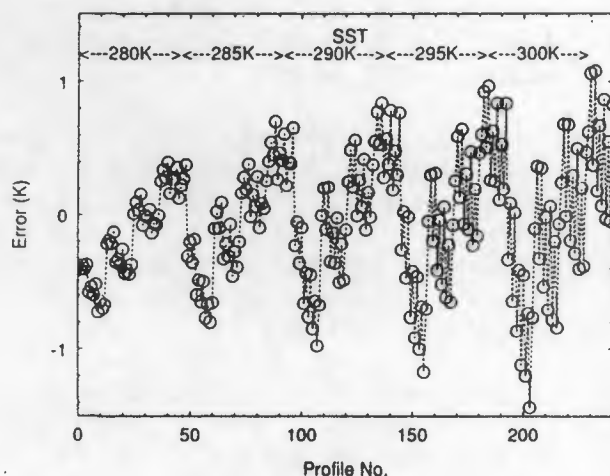


Figure 4. The errors in derived SST using the (12N,12F) algorithm for the profiles with sea and air temperatures set at 280, 285, 290, 295, and 300K.

shape of the water vapour profile. All algorithms had the form  $SST = aT_1 + bT_2 + c$  and were derived for the following pairs of channels: (3.7N 3.7F), (3.7N 11N), (11N 12N), (11N 12F) and (12N 12F). To determine the errors in these simple algorithms a full six-channel algorithm could be considered to give the true value, but in this analysis the value was assumed to be that input to the model.

The errors in the derived SST show some interesting features. For example, Figure 3 shows the total water vapour content and the errors in derived SST using the (3.7N 3.7F) and (12N 12F) algorithms for those

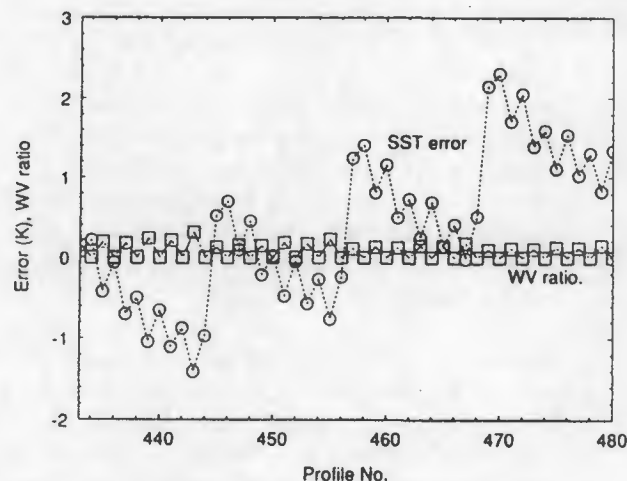


Figure 6. The water vapour ratio in the 4-6 km layer and the errors in derived SST using the (12N 12F) algorithm for the profiles with sea and air temperatures set at 290 and 287K respectively.

profiles which have the sea and air temperatures set at 290 and 287K respectively. The two algorithms shown in the figure are the extremes of the errors given by the selected algorithms. There is an obvious strong correlation between the water vapour and the SST errors.

The errors in the (12N,12F) algorithm for a range of equal sea and air temperatures are shown in Figure 4. Here, again, there is a strong correlation between the errors and the SST value. Finally, Figure 5 shows the errors for an SST of 290K and air temperatures of 287, 290 and 293K. These three figures show clearly that the errors are dependent on the total water vapour content, the actual sea surface temperature and the air-sea temperature difference.

When the well-defined dependencies on the surface temperatures and the total water vapour amount are accounted for the remaining variations in the SST errors are due to the anomalies in the water vapour profile. Figure 6 shows the SST error for the (12N 12F) algorithm along with the water vapour ratio in the 4-6 km atmospheric layer. The correlation between the error and the water vapour ratio is clearly shown.

Analysis of this second possible method shows that the water vapour retrieval may be possible using a careful analysis of ATSR data.

### 5. DISCUSSION

The two methods explored for water vapour profile determination give similar conclusions. For a useful retrieval it will first be necessary to derive the sea surface temperature, the total water vapour amount and the air-sea temperature difference. The first two parameters are those for which ATSR was designed and should be available on an operational basis. The third parameter, the air-sea temperature difference should be available from the ATSR data. The air-sea temperature difference in itself is a valuable climate parameter as it affects the latent heat flux at the air-sea interface and thus exerts a major control on the surface energy balance.

The effect of variation in the atmospheric aerosol content is not taken into account in this analysis. Variations in the differences between the ATSR brightness temperatures will occur with changes in aerosol content, but will have a different "signature" to the water vapour effects. Whether the ATSR data are sufficiently accurate to determine both aerosol and water vapour anomalies will require further careful investigation.

Finally, the coarse determination of the shape of the water vapour profile should be extremely valuable in refining the algorithms used for the accurate determination of the SST. Currently the operational algorithms do not account for anomalies in the water vapour profile and some improvement in SST accuracy may be achieved with careful analysis of both the infrared and microwave data from the ATSR.

### 6. ACKNOWLEDGEMENTS

The crew of the RV Franklin are acknowledged for their assistance in collecting the ground truth data.

### 7. REFERENCES

1. Delderfield J. et al 1986, The along track scanning radiometer (ATSR) for ERS-1, "Instrumentation for optical remote sensing from space", John S. Seeley, John W. Lear, Andre Monfils, Sidney L. Russak, Editors, Proc. SPIE 589, 114.
2. Barton I.J. 1985, Transmission model and ground-truth investigation of satellite-derived sea surface temperatures, *J. Clim. Appl. Meteor.*, 24, 508-516.
3. Barton I.J. 1991, Infrared continuum water vapor absorption coefficients derived from satellite data, *Appl. Opt.*, 30, 2929-2934.
4. McClatchey R.A. et al 1972, Optical properties of the atmosphere, *Rep. AFCRL-72-0497, Air Force Cambridge Res. Lab.*, Bedford, Mass., USA.
5. Eymard L. et al 1992, Validation of the ATSR/M microwave radiometer data, *Proc. First ERS-1 Symp., Cannes, France*, ESA SP-359, 763-766.

## QUANTITATIVE REMOTE SENSING IN THE 11 $\mu$ m WAVELENGTH REGION USING ATSR

A.M. Závody<sup>1</sup>, C.T. Mutlow<sup>1</sup>, D.T. Llewellyn-Jones<sup>1</sup> and I.J. Barton<sup>2</sup>

<sup>1</sup>Rutherford Appleton Laboratory, Chilton, Didcot, Oxon OX11 0QX, U.K.

<sup>2</sup>CSIRO Division of Atmospheric Research, Aspendale, Victoria 3195, Australia

### ABSTRACT

The Along Track Scanning Radiometer (ATSR) was designed to measure the sea surface temperature (SST) by using brightness temperatures obtained from two views of the surface and in two or three wavelength bands. Model results are used to investigate inconsistencies between SST values, derived from different combinations of the views and channels, when volcanic aerosols are present in the stratosphere. By using ATSR data it is found that similar inconsistencies arise over a real atmosphere which is likely to have aerosol contamination present, and it is shown that it may be possible to use the value of these inconsistencies to correct further the SST values derived by the two-view algorithm, without any additional in-situ measurements.

Keywords: Sea surface temperature, ATSR, aerosols

### 1. INTRODUCTION

The validation of data from any new instrument is always necessary for two reasons: firstly, to show that the theoretical basis of the instrument is right, and secondly, to demonstrate that the instrument is functioning correctly. ATSR – for a description of the instrument see Delderfield et al (Ref. 1) – is measuring the skin temperature of the sea hence its ultimate accuracy can only be checked by comparing the results with coincident radiometrically measured surface temperatures. The latter are usually obtained by using research vessels. A major problem, however, is the very low number of coincidences, caused by cloudiness and the long times it takes for the ships to reach areas within the instrument's swath.

It is not the purpose of this paper to study ATSR's performance by using in-situ validation data. The results obtained by Forrester et al, Thomas et al, Smith et al, Mutlow et al (Ref. 2 – 5) and others are all very promising and show that, in almost every case, the SST values retrieved by using both the nadir and forward views agree more closely with the

in-situ values than the SSTs derived by using the nadir-view brightness temperatures only. On some occasions, however, there are significant disagreements even in the former case and a possible cause is the presence of volcanic aerosols in the stratosphere.

There was a powerful volcanic eruption in June 1991 in the Phillipines (Mount Pinatubo). The aerosols in the stratosphere quickly formed a belt near the latitude of the eruption, which then spread slowly to neighbouring latitudes. The effect of the aerosol contamination was severe enough to trigger the standard AVHRR cloud-clearing algorithms and, even when SST values were retrieved, the AVHRR SSTs were in error by up to 2 K.

We are presenting results from an atmospheric model first, showing the predicted effect of the tropical atmosphere on ATSR-measured brightness temperatures, and the additional deficits arising when a realistic amount of volcanic aerosol is present in the stratosphere. The likely effect of the aerosol contamination on the retrieved SST is also computed. In the second half of the paper the results are compared with those from a case study, using ATSR data obtained in March 1992 and in an area likely to be contaminated by aerosols. The paper is concluded by proposing a tentative scheme for correcting for aerosol contamination in the SST retrieval scheme.

### 2. THE EFFECT OF VOLCANIC AEROSOLS – MODEL RESULTS

The RAL atmospheric model, substantially as described in Barton et al (Ref. 6), was used to compute the brightness temperatures that would be measured by ATSR over a tropical atmosphere. The atmospheric profiles of temperature and water vapour density were those given by McClatchey et al (Ref. 7) for the tropical atmosphere.

To start with, the atmosphere was assumed to contain no volcanic aerosols, and the brightness temperature deficits are given in the first line of figures in Table 1.

TABLE 1: Simulated temperature deficits (K) for the US Standard Tropical Atmosphere

view channel	nadir			forward		
	3.7 $\mu$ m	11 $\mu$ m	12 $\mu$ m	3.7 $\mu$ m	11 $\mu$ m	12 $\mu$ m
	3.01	4.73	6.53	4.79	7.19	9.31
	aerosol effect: increase in deficits (K)					
fresh	0.46	0.71	0.52	0.78	1.21	0.88
aged	0.36	0.71	0.55	0.61	1.21	0.93

The two channels in the 10 $\mu$ m window have a considerably higher temperature deficit than the 3.7 $\mu$ m channel, this is caused by the strong water vapour absorption.

The figures in the two lines following show the additional temperature deficits, caused by the presence of volcanic aerosols in the stratosphere. The terminology and cross-sections used were those given in McClatchey et al (Ref. 8). *Fresh* aerosols are aerosols with a size distribution corresponding to that found shortly after a volcanic eruption, and the *aged* aerosols refer to those about a year after the eruption. The aerosols were assumed to be distributed uniformly in a layer at a height between 20km and 25km, and with a concentration giving an optical depth of 0.011 at 11 $\mu$ m in the nadir view. Single scattering only was assumed.

By definition, the increase in the atmospheric deficits is the same at 11  $\mu$ m for both kinds of aerosols. It is also for this channel that the aerosol effect is the greatest, caused by the peak value in the absorption index near 10  $\mu$ m.

It should also be noted that although the increase in both water vapour and aerosol column amounts would increase the deficit in all the channels, the *difference* between the 11 $\mu$ m and the 12 $\mu$ m brightness temperatures are predicted to *decrease* with increasing aerosol densities.

### SST retrieval errors

In the ATSR processing scheme, the SSTs are retrieved by using the standard equation of

$$SST = a_0 + \sum_{i=1,n} a_i T_i \quad (1)$$

where  $n$  is the number of brightness temperature channels used. The coefficients  $a_i$  have been determined by a standard multiple regression technique using model-generated brightness temperatures for a collection of real atmospheric profiles of temperature and humidity, but without any contamination by volcanic aerosols. The coefficients used with data in this paper were generated by assuming that the

brightness temperatures  $T_i$  have negligible instrumental noise contamination, corresponding to the case where they have been averaged over an area large enough for this assumption to apply.

Table 2 shows the simulated error in retrieved SST when the brightness temperatures derived for the US Standard Tropical Atmosphere are used with the standard coefficients. The standard deviations in the error of the simulated SSTs are given in the last column, these were derived from the same collection of 83 tropical atmospheres as had been used in the derivation of the retrieval coefficients.

TABLE 2: Simulated SST errors (K) for the US Standard Tropical Atmosphere

Channels and views used						aerosol type			
nadir			forward			none	fresh	aged	sd
3.7	11	12	3.7	11	12				
	x	x				0.17	-1.14	-1.05	0.48
x	x	x				-0.07	-0.62	-0.49	0.11
	x	x		x	x	-0.07	-0.46	-0.46	0.13
x	x	x	x	x	x	-0.05	-0.30	-0.27	0.03
x				x		-0.08	0.23	0.17	0.11
	x			x		-0.19	0.37	0.36	0.42

The figures under the aerosol heading 'none' show the error in the absence of any volcanic aerosol contamination. The errors in this column are always less than 0.2K, even when only two channels are used in the retrieval.

The presence of aerosols reduces the retrieved SST when channels of more than one wavelength are used, and increases it in the two cases shown for single-channel retrievals. For the aerosol contamination assumed, the error is largest from the algorithm having the nadir-viewing 11 $\mu$ m and 12 $\mu$ m brightness temperatures only and, as expected, is smallest when the channel least effected by the atmosphere and aerosols (the 3.7 $\mu$ m channel) is used on its own.

For any combination of wavelength channels, the errors are always smaller when both views are used, compared with errors from the algorithms having the nadir-view brightness temperatures only. It should also be noted that even in the two-view retrievals the error caused by the aerosols can be significant and can approach a value equal to the aerosol effect on the nadir-view brightness temperatures.

### 3. SELF CONSISTENCY IN THE ATSR DATA

As mentioned in the the Introduction, the ultimate test of ATSR is the comparison of the ATSR-

measured SST with in-situ values. Checks on the self consistency of the brightness temperatures measured in the different channels, and of the SST values derived by using different channels, can also be useful for showing up possible errors in the atmospheric model used in the generation of the SST retrieval coefficients, or even in the performance of the ATSR instrument. As there are no reasons to believe that the brightness temperatures measured are not within specifications, the latter possibility will not be considered further.

The consistency checks should ideally use a large amount of data so that if there are any unexpected results, their dependence on geographical location, date, temperature, humidity, etc could be used for establishing their cause. The major problem with using global data from a surface-viewing infrared instrument is that the data must be known to be 100% cloud-free, otherwise cloud contamination can always be suspected as a possible cause of any discrepancies.

We have used data from just one standard-size ATSR image product (area 512km x 512km), after a routine histogram plot of the 11 $\mu$ m minus 12 $\mu$ m difference had revealed an unusually large range of atmospheric conditions above it. The data were obtained at night on 4 March 1992 over the Indian Ocean, and the centre of the image is at 2.3°N, 80.6°E. The cloud tests have flagged only small amounts of clouds, mostly in the lower right hand (SE) quadrant. The 12 $\mu$ m brightness temperature image (Figure 1) shows a strong North-South temperature gradient.

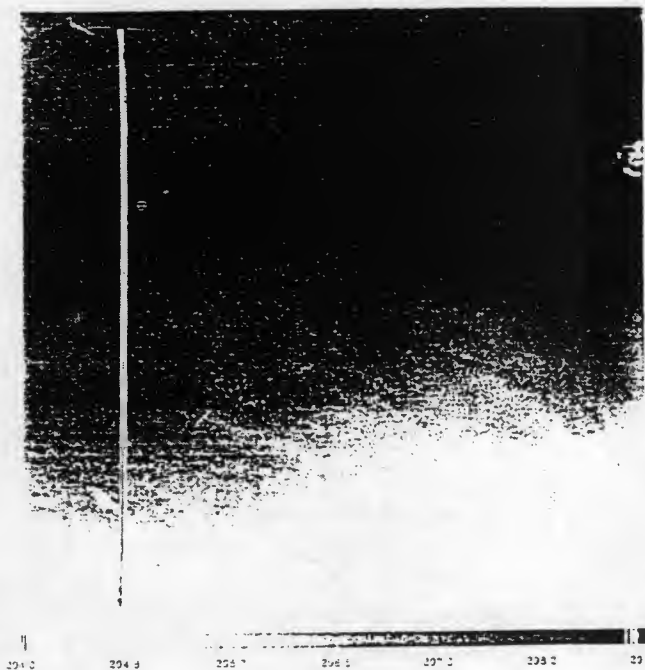


Figure 1. 12 $\mu$ m ATSR brightness temperature image

The behaviour of all three nadir-viewing infrared channels and of the SSTs, retrieved by using the data

in both views, is shown quantitatively in Figure 2 where the values plotted were taken along the vertical line drawn in Figure 1. It can be seen not only that the brightness temperatures in all the channels decrease southwards but also that the differences between the 11 $\mu$ m and 12 $\mu$ m channels also increase in the the same direction. A strong increase in column water vapour with along-track distance could produce both the decrease and the divergence in the brightness temperatures. The plot of the retrieved SST values shows that the sea temperature does not have the North-South slope found in the brightness temperatures.

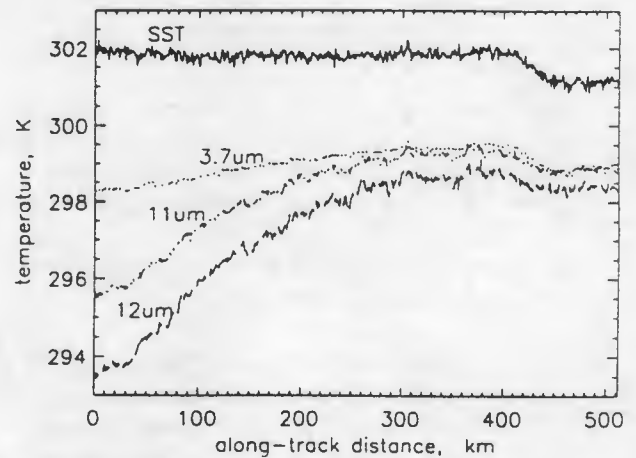


Figure 2 ATSR SST and nadir-view brightness temperature values along the line in Figure 1

The SSTs were also calculated for the whole of the image, using all the channel combinations shown in Table 2. In order to reduce the effect of instrumental noise, the brightness temperatures of up to 100 cloud-free pixels were first averaged over an area of 10km x 10km. Results are only presented for the area within 100km of the sub-satellite track so that the pixels used were all viewed at approximately the same angles.

The two-view 3-channel algorithm is normally the most accurate hence SST values generated by this algorithm are used as a reference in the SST difference plots shown in Figure 3. The  $x$  axis is the difference between the brightness temperatures from the 11 $\mu$ m and 12 $\mu$ m nadir-viewing channels: it is roughly proportional to the atmospheric water vapour content as well as to the distance measured southwards from the top of the image. It can be seen that, for 11 $\mu$ m minus 12 $\mu$ m brightness temperature differences larger than about 1K, there is no clear dependence of the errors on this difference. It follows that, unless the aerosol layer over the area is non-uniform and varies monotonically in the South-North direction, the discrepancies shown in the figures are not dominated by errors in the model water vapour absorption. Comparing the sign and value of these discrepancies with the calculated aerosol-induced errors, taken from ta-

ble 1 and shown as crosses (fresh aerosols) and circles (aged aerosols) indicates that the aerosol parameters used in Section 2 are approximately right to explain the discrepancies found in the higher water vapour areas. For points at  $11\mu\text{m}$  minus  $12\mu\text{m}$  differences less than about 1K the SST differences do seem to be a function of  $x$  but, as  $x$  is proportional not only to the column water vapour amount but to distance in the image as well, this may well be caused by the aerosol density itself varying in this region.

#### 4. CORRECTION FOR AEROSOLS USING ATSR DATA ONLY

In the existing routine SST retrieval scheme, no independent information is available on the amount or the optical depth of the stratospheric aerosols. The results from the section above show, however, that the differences found in SSTs retrieved by using different channel combinations are consistent with the presence of volcanic aerosols.

As the aerosol effect is small, the changes due to aerosols in the brightness temperatures and SSTs can all be approximated by a linear dependence on the total column amount. It follows that the discrepancies in SSTs could be used both for further correcting the retrieved SST values and for determining the aerosol loading of the atmosphere.

At night-time, and if the  $3.7\mu\text{m}$  channel is present, the two-view 3-channel SST could be corrected most accurately by using the difference between it and the single-view 3-channel SST. The results from table 1 show that the aerosol effect on the two-view SST was  $-0.25\text{K}$  for fresh volcanic aerosols ( $-0.22\text{K}$  for aged), and that the effect on the difference between the SSTs from the two algorithms was  $-0.30\text{K}$  for the fresh ( $-0.20\text{K}$  for aged) aerosols, for the aerosol amount used. The 'uncontaminated' SST could be retrieved by adding to the two-view 3-channel SST the difference between the two SSTs multiplied by a factor between 0.83 and 1.1. The value of this factor depends on the age of the aerosols and, as it is operating on a small quantity, the implied uncertainty would be acceptable.

If SSTs using the  $3.7\mu\text{m}$  channel data are not available, the 2-channel algorithms could be used in a similar way. Again using the data in Table 2, the multiplying factor would be about 0.41 and, in this case, it is almost the same for the two types of aerosols used in the model.

By using the differences between the two-view and single-view SSTs it may be erroneously assumed that the accuracy of the corrected SSTs would be degraded to a figure that is comparable or even worse

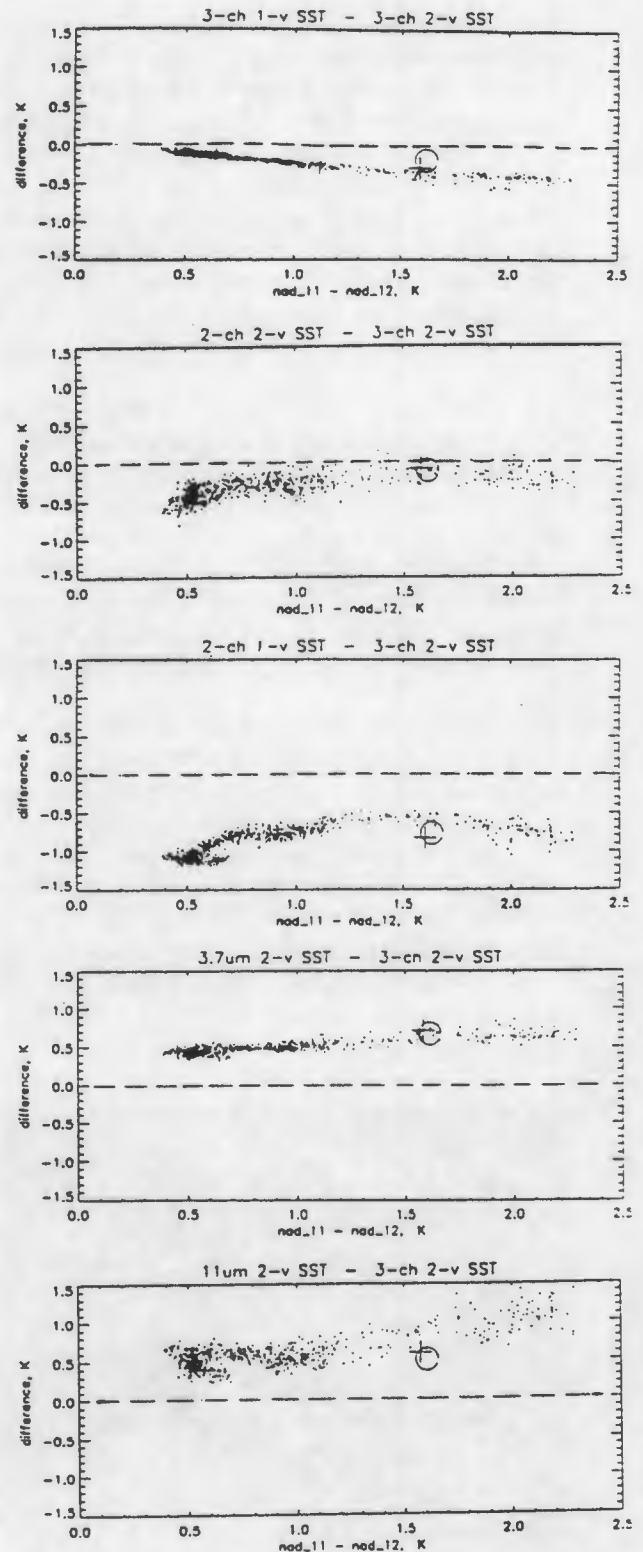


Figure 3. Differences between SSTs from algorithms using the channel and view combinations shown, and SSTs retrieved by the two-view 3-channel algorithm. Values taken from the image are shown as dots, and those from the model, deduced for conditions given in the text, as crosses (fresh aerosols) and circles (aged aerosols)

than that for the single-view retrieval. Owing to the high correlation of the SST errors in the two retrievals this, however, is not the case and the rms errors in the corrected SSTs are predicted to be in-

creased by less than 0.05K with respect to those from the two-view retrievals, with both the 2-channel and 3-channel algorithms.

## 5. CONCLUSIONS

The results from the atmospheric model have shown that if there is significant aerosol contamination, the SSTs retrieved by algorithms using different channel and view combinations are all biased and different. The value of the bias is normally negative and, as expected, is smallest when the two-view algorithms are used.

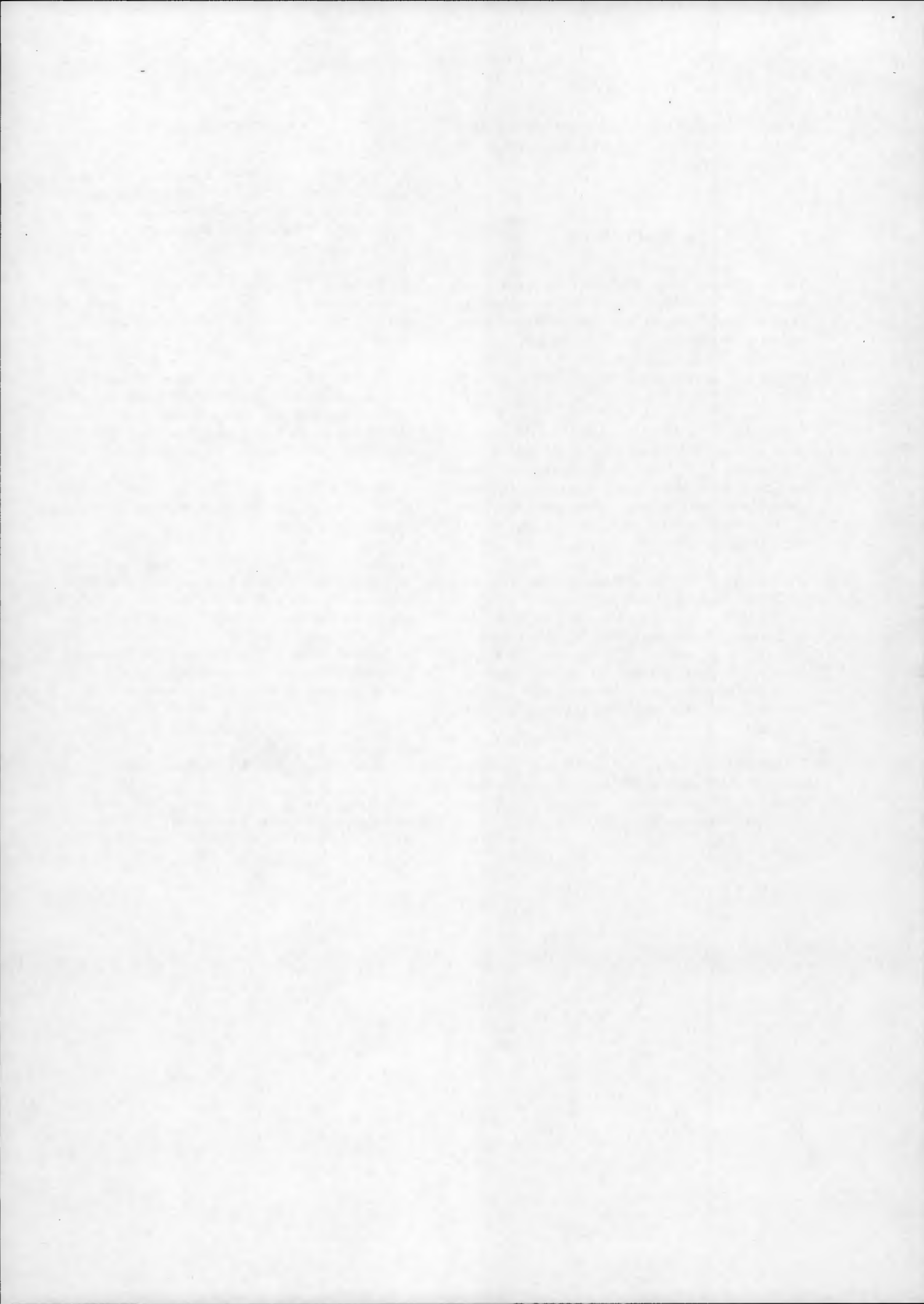
In the sample of ATSR data selected for analysis in this paper, the major part of the inconsistencies between SSTs from different algorithms could have been caused by an almost uniform stratospheric aerosol layer over the scene. The optical thickness of the aerosols, required to explain the results, was found to be about 0.01 at 11 $\mu$ m.

If it is assumed that the SST inconsistencies are primarily caused by volcanic aerosols, a correction is possible by using the values of the differences in a correction term, after scaling them by factors deduced from the model results. The random SST errors, caused by variability in the clear atmosphere, would inevitably increase owing to the use of SSTs from less accurate algorithms, but the increase is predicted to be small.

For the most accurate corrections, it is necessary to fully understand and model the standard atmosphere with negligible aerosol contamination, and further work is still required in this field.

## 6. REFERENCES

1. Delderfield, J et al. 1986, The Along Track Scanning Radiometer (ATSR) for ERS-1, "Instrumentation for optical remote sensing from space", John S Seeley, John W Lear, Andre Monfils, Sidney L Rusak, Editors, Proc. SPIE 589, 114.
2. Forrester, T N et al. 1993. Validation of ATSR sea surface temperatures near the faroes. *Proc. of 1st ERS-1 Symp., Cannes 4 - 6th Nov. 1992*, ESA SP-359, Vol. II, 807-811
3. Thomas, J P et al. 1993. A comparison of ATSR and shipboard SST measurements along transects between the UK and the Antarctic, *Proc. of 1st ERS-1 Symp., Cannes 4 - 6th Nov. 1992*, ESA SP-359, Vol. II, 801-805
4. Smith, A F et al. 1993. The validation of ATSR using aircraft radiometer data, In press *J. Atmos. Oceanic Technology*
5. Mutlow, C T et al. 1994. The Along Track Scanning Radiometer (ATSR) on ESA's ERS-1 Satellite: Early results and performance analysis, *Submitted for publication to Journal of Geophysical Research*
6. Barton, I J et al. 1989. Theoretical algorithms for satellite-derived sea-surface temperatures. *Journal of Geophysical Research*. 94, 3365-3375
7. McClatchey R.A. et al 1972. Optical properties of the atmosphere. *Rep. AFCRL-72-0497, Air Force Cambridge Res. Lab., Bedford, Mass., USA*
8. Kneizys et al 1980. Atmospheric transmission/radiance: Computer code LOWTRAN 5, *Rep. AFGL-TR-80-0067, Air Force Geophysics Laboratory, Hanscom AFB, Mass., USA*



## SEA SURFACE TEMPERATURE AND BOUNDARY LAYER

## FLUXES FROM ERS-1/ATSR DATA

A K Mathur, S Ilanthirayan and V K Agarwal  
 Meteorology and Oceanography Division  
 Space Applications Centre (ISRO)  
 Ahmedabad 380 053 INDIA

## ABSTRACT

The dual angle and multi-spectral observations from ERS-1 ATSR has been shown to be useful not only affecting corrections for sea surface temperature but also in helping to estimate the moisture and temperature structure of the lower boundary layer. In continuation of our earlier study to this effect, some sample data analysis has been presented here. The SST has been retrieved to a good level of satisfaction. The feasibility of estimating the surface-air exchanges over the oceans has also been confirmed even by analyzing the scanty data we could gather.

Keywords: SST, surface flux, ATSR, water vapour correction

## 1. INTRODUCTION

Sea Surface Temperature (SST) retrieval from satellite IR observations is always perturbed by the attenuation of the IR signal reaching the satellite sensor due to water vapor alongwith CO<sub>2</sub> and Ozone gases present in the intervening atmosphere. Therefore, the major efforts for retrieving the SST from satellite data is always concentrated towards a reasonable estimate of this perturbation. There have been several attempts to achieve this goal (McClain 1983, Barton 1983, Schluesal 1987, Mathur 1991) under different conditions of the atmosphere. The biggest bottleneck has been the conditions prevailing in the tropics where the atmosphere is extremely humid and there is possibilities of the boundary layer inversions being present (WMO 1986). Then, there is an associated problem of monitoring the atmosphere-ocean exchanges on the global basis. These exchanges, mainly require monitoring of the specific humidity, surface winds, and air temperature at the ocean-atmosphere interface alongwith the conditions of stability in the lower boundary layer.

With the launch of ERS-1 in July 1991,

new possibilities have opened up in this direction. ERS-1 carries onboard Along Track Scanning Radiometer (ATSR) which has a unique feature of viewing the earth's surface from two different angles i.e. 0° and 55° and in multispectral mode. As described in earlier simulation studies by the authors (Mathur and Agarwal 1992, Agarwal et al 1992), ATSR dual angle observations alongwith the water vapor observation by Microwave Sounder (MWS) can remove the ambiguities due to WV distribution and provide improved SST retrieval even in the tropics. Furthermore, due to the availability of the surface winds by Scatterometer on the same platform, there is now a strong possibility of monitoring of the surface fluxes in the oceanic regions as well. Our earlier study (Mathur et al 1992, Agarwal et al 1992) has demonstrated these possibilities through simulations.

In this paper, we present results from a few ATSR data sets obtained under ESA-AO. We have estimated SST with and without water vapour information. In the absence of Microwave sounder data, being not available for the sample data set we have received so far, we have attempted to retrieve climatic estimates of the total columnar water vapor content also by ATSR. This estimate is based on the fact that the differential nadir and forward observations will basically depend upon the moisture in the lowest layers. Under stable atmospheric conditions, the moisture in the lowest layers will have direct bearing on the total water vapour content. (cf with the method for determining the surface fluxes).

## 2. ATSR DATA

Sample ERS-1/ATSR data for 3rd March '92 (Descending pass) has been provided by Rutherford Appleton Laboratory, UK under an ESA project (Announcement for project proposal for ATSR utilization of ATSR data IND-4). The calibrated and collocated data is in the form of equivalent blackbody brightness temperature (EBBT)

of thermal channels centering around 11  $\mu\text{m}$  and 12  $\mu\text{m}$  and in the form of reflected radiance for 1.6  $\mu\text{m}$  channel. The data for the 3.5  $\mu\text{m}$  channel is not reported as it is still under suspicion. The whole pass is divided into 10 images each of 512 X 512 size extending from 30°S to 10°N and 90°E to 105°E.

### 3. SST COMPUTATION AND IMAGE REPRODUCTION

A software has been written to read the ATSR EBBT data and compute SST for cloud-free and landless regions. The cloud mask is obtained by analyzing the 1.6  $\mu\text{m}$  image. All the clouded pixels are forced to have minimum gray value while land is masked at the highest gray count.

SST is computed by applying two different retrieval schemes. The first scheme (called "implicit") is a single step retrieval where SST is directly estimated by using a chosen combination of ATSR nadir and forward thermal channels as discussed in an earlier paper by the authors (Mathur and Agarwal 1992). The retrieval equation for this scheme is:

$$\begin{aligned} \text{SST} = & - 2.2646 - 2.0498 * \text{CH4\_N} \\ & + 3.0589 * \text{CH3\_N} \\ & - 2.1865 * (\text{CH4\_N} - \text{CH4\_O}) \\ & + 2.8129 * (\text{CH3\_N} - \text{CH3\_O}) \end{aligned} \quad (1)$$

where CH3 and CH4 stand for the equivalent black body (EBBT) temperature for the channels 3 and 4 (at 11  $\mu\text{m}$  and 12  $\mu\text{m}$  respectively) and N and O stand for the Nadir and Off-nadir observations.

The second scheme is referred to "explicit" scheme which is a two step retrieval. First, the total water vapor content in the atmosphere is estimated by ATSR observations (assuming that the atmosphere may be stable and follow climatic behavior), then this water vapor content is kept as a forced independent parameter in the final step to compute SST. This procedure has the advantage of direct assimilation of the water vapor estimates from the ATSR microwave sounder. Our experience demonstrate that this scheme of retrieval is far more suited for the tropical atmospheres. The retrieval equations for this scheme are:

$$\begin{aligned} \text{WV} = & - 3.3955 \\ & - 7.6902 * (\text{CH4\_N} - \text{CH4\_O}) \\ & + 11.330 * (\text{CH3\_N} - \text{CH3\_O}) \\ & + 17.765 * (\text{CH3\_N} - \text{CH4\_N}) \end{aligned} \quad (2A)$$

$$\begin{aligned} \text{SST} = & 0.84831 - 0.5985 * \text{CH4\_N} \\ & + 1.6063 * \text{CH3\_N} \\ & + 0.01248 * (\text{CH3\_N} - \text{CH3\_O}) * \text{WV} \end{aligned} \quad (2B)$$

The retrieved SST values are transformed into image and contours for display.

### 4. Surface fluxes

As we have discussed in another earlier paper (Agarwal et al 1992), that the oblique viewing capability of the ATSR sensor can be exploited to get the estimates of the surface air specific humidity, the retrieving equation for this parameter (over the oceans) is:

$$\begin{aligned} \text{Qa} = & - 2.6902 - 6.9857 * \text{SIG1} \\ & + 10.916 * \text{SIG2} \end{aligned} \quad (3)$$

where

$$\begin{aligned} \text{SIG1} &= 100 * \frac{(\text{CH3\_N} - \text{CH3\_O})}{(\text{CH3\_N} + \text{CH3\_O})} \\ \text{SIG2} &= 100 * \frac{(\text{CH4\_N} - \text{CH4\_O})}{(\text{CH4\_N} + \text{CH4\_O})} \end{aligned}$$

The evaporative flux over the sea surface is then given by the bulk aerodynamic formula:

$$\text{LE} = \text{Cd} * |\text{V}| * (\text{Qs} - \text{Qa}) \quad (4)$$

where,

$$\begin{aligned} \text{Qs} &= 0.625 * \text{ess} / (1013 - \text{ess}) \\ \text{ess} &= 10 ** (23.55 - 2937 / \text{SST}) \\ & * (\text{SST} ** (-4.928)) \end{aligned} \quad (5)$$

Cd is the normalized bulk drag coefficient and |V| is the wind speed which is available from ERS-1 Scatterometer data.

The air-temperatures near the surface are not discussed here since the sample ATSR data falls outside the experimental box for this experiment and the NOAA-TOVS data required for this purpose could not be obtained for the longitudes beyond 95E from our station at Hyderabad. These results will be reported later when actual ATSR data over our experimental box is available.

## 5. RESULTS AND DISCUSSION

### 5.1 SST

Figure 1 shows a black & white image of ATSR channel 3 EBBT (nadir view) over the Thailand region. The lowest EBBT i.e. 288K is assumed to represent the thickest clouds. Figure 2 is the computed SST image with "implicit" retrieval scheme. It is obvious here that clouds are better distinguished in this image than figure 1 because of better thermal contrast of the cloud top temperature and the uniform ocean background. Most of the SST values lie between 299K and 300K, which matches with the climatological temperatures in the region. Bottom left is showing some warmer region of the order of 301 K. Figure 3 shows SST retrieval with "ex-

PLICIT" scheme. It is evident from the image that not only the clouds are distinguished better, the thermal structures are also enhanced in this SST image. For example in the top right corner (around 109.2E 11.4N), one can see a slight intrusion of the cold water into the warmer waters, a feature which is not seen in any of the previous images. This extra enhancement could have been due to the high water vapor correction required in this region. Such kind of features are possible (Ali, Private communication) when the current moves southwards.

This analysis leads to the possible conclusion that the water vapor correction is highly variable and the corrections for the SST images should not be undertaken in the same way as normally adopted for the grid-value estimates for the SST. As a by-product of this analysis we can have a mapping of total water vapor content, though only tentative estimates because corrections for the atmospheric stability are not incorporated in this scheme.

## 5.2 Surface Fluxes

The figures 4 and 5 show the calculations for the  $Q_s$  and  $Q_a$  terms in the evaporative flux estimate equation.  $Q_s$  calculation obviously follow the pattern for the SST distribution. The  $Q_s$  calculation which indicate the mixing ratio for the air layer in the immediate vicinity of the sea water (probably a few centimeters thick) while the  $Q_a$  calculations have been adjusted to the air observations at the "deck level (10 m)" or the "screen level" at the ground. The evaporative flux has been seen to have much larger value over the regions (109.2E 11.4N) where the SST contrast was not seen in the original thermal image. The conclusion is evident.

At other places, the evaporative flux are not large. This is supported by the SST image and the thermal image since the contrasts are quite well marked.

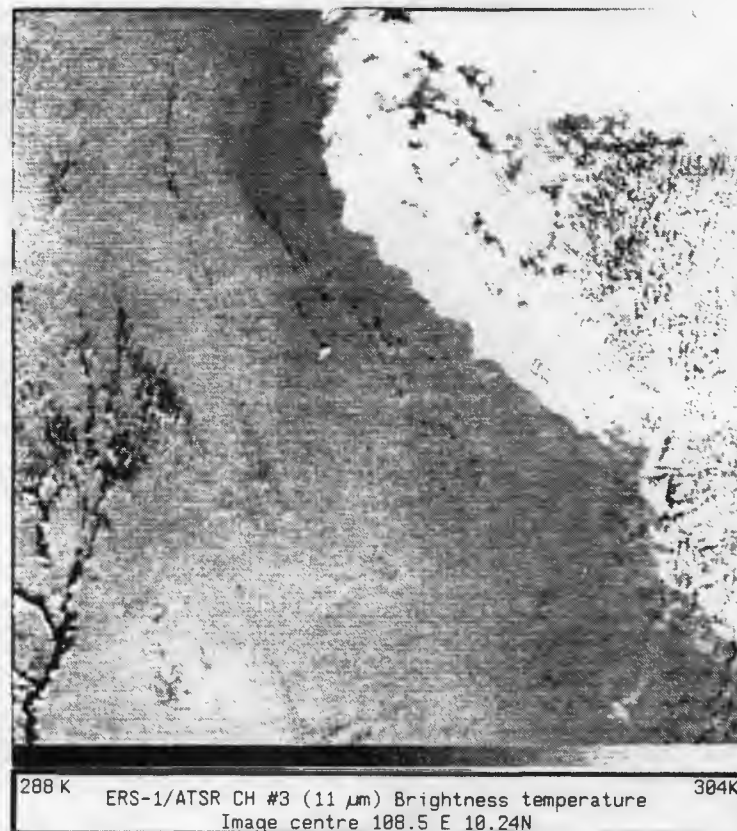
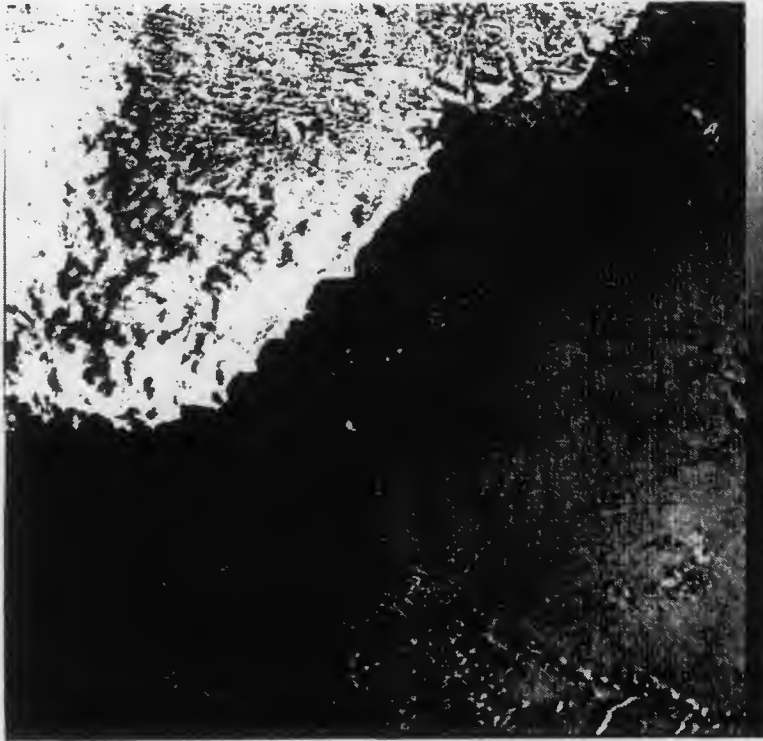
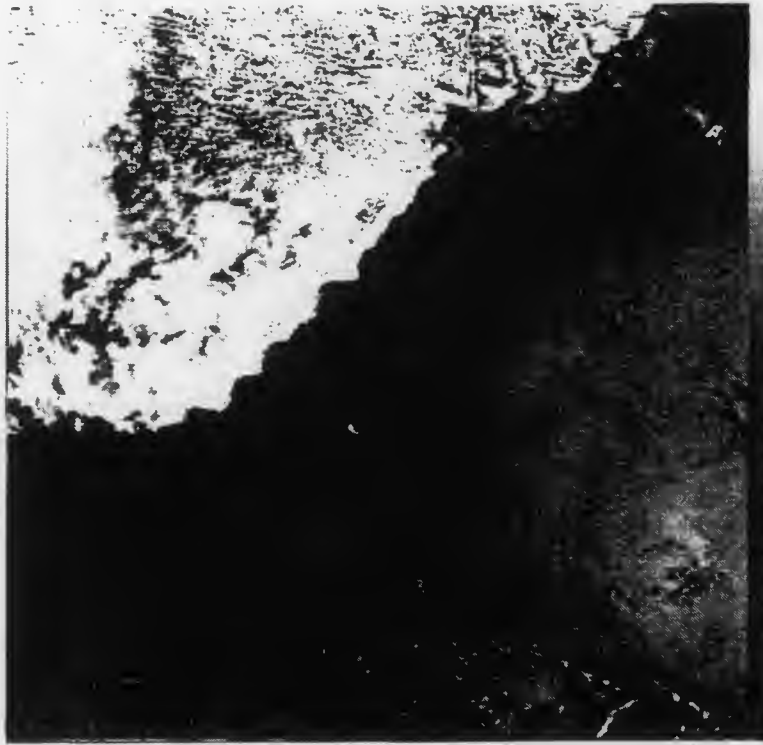


Figure 1: Brightness temperature image of ERS-1/ATSR channel 3 (11  $\mu\text{m}$ ) dated 03-03-1992.



296K Sea Surface Temperature from ERS-1/ATSR Data 304K  
 (Implied Water Vapour correction)  
 Image centre 108.5 E 10.24 N Date 03-03-1992

Figure 2(a): Sea Surface Temperature from ERS-1/ATSR data with "Implicit" water vapour correction dated 03-03-1992.



296K Sea Surface Temperature from ERS-1/ATSR Data 304K  
 (explicit Water Vapour correction)  
 Image centre 108.5 E 10.24 N Date 03-03-1992

Figure 3(a): Same as figure 2(a) except with "Explicit" water vapour correction.

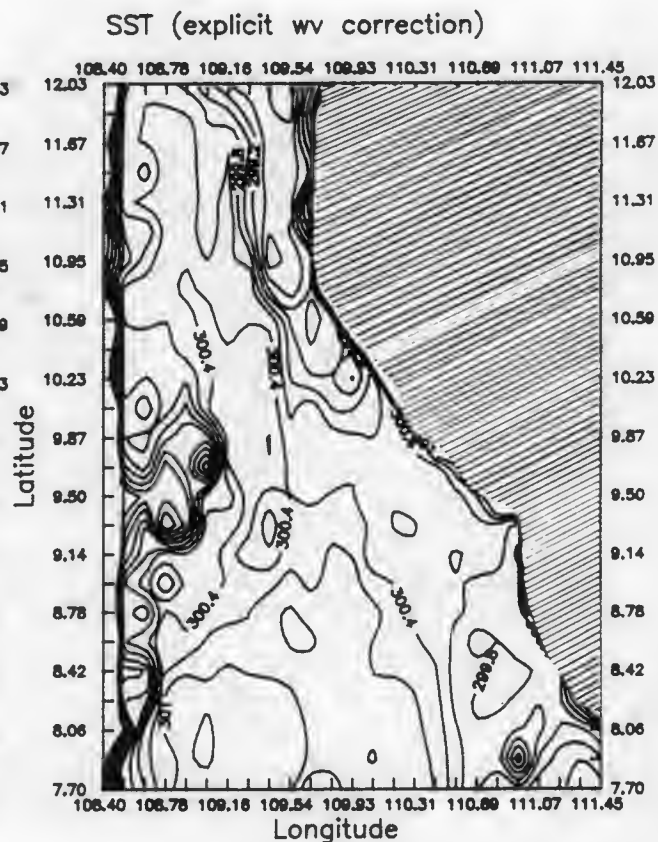
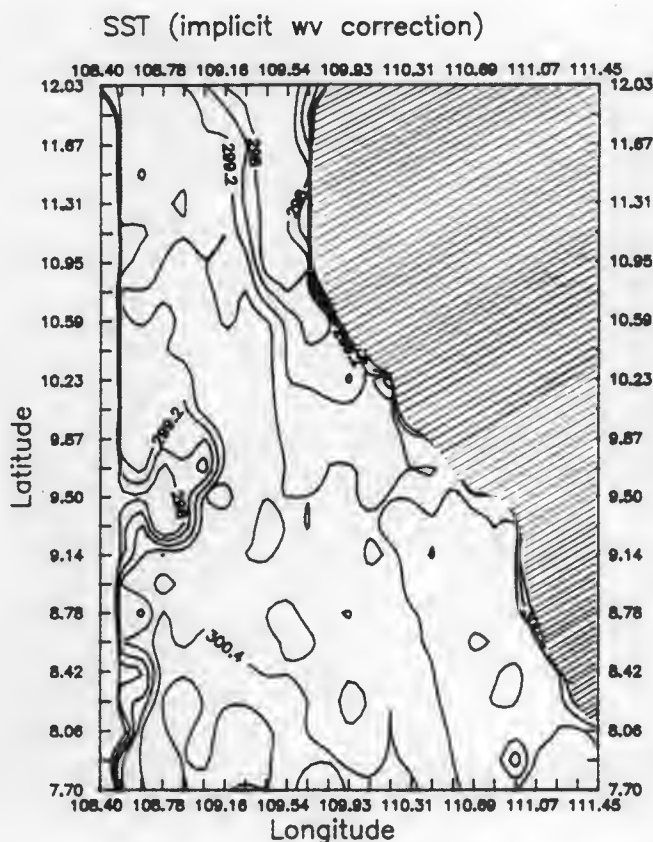


Figure 2(b): Sea Surface Temperature contours for figure 2(a) (contour interval 0.3K, shaded region is land)

Figure 3(b): Sea Surface Temperature contours for figure 3(a) (contour interval 0.3K, shaded region is land)

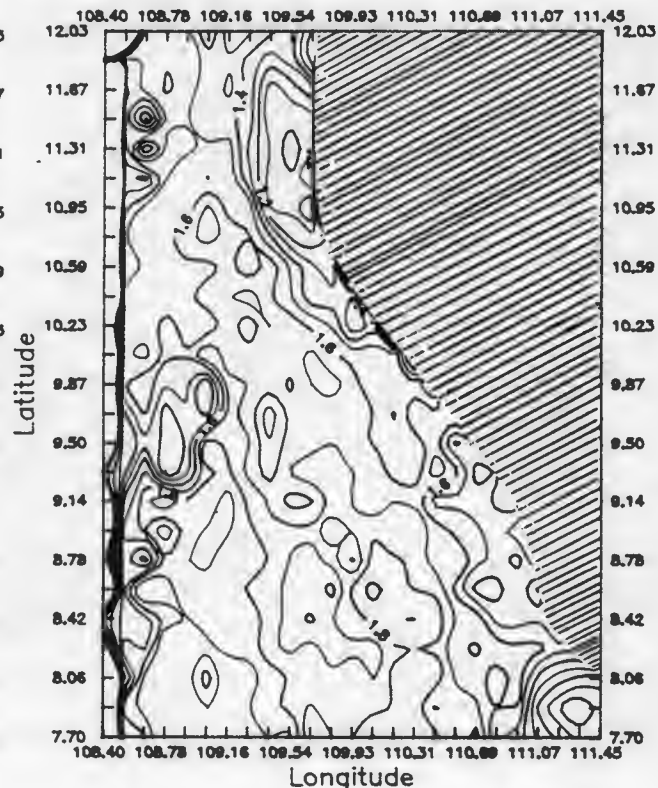
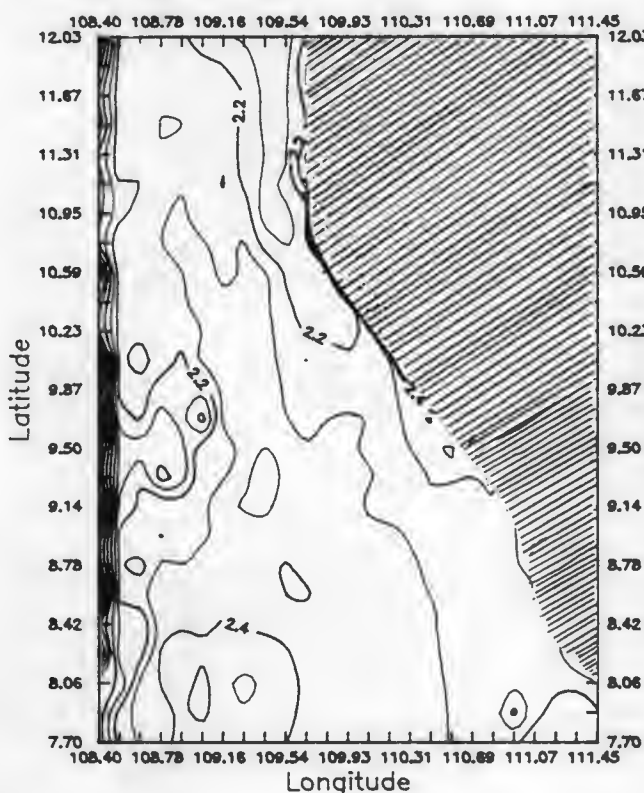


Figure 4: Contours of Specific humidity at surface ( $Q_s$ ) (contour interval 0.1)

Figure 5: Contours of Specific humidity near surface ( $Q_a$ ) (contour interval 0.1)

#### Acknowledgement

The authors thank Mr. Arun Chakravorty from Dept. of Physics, Indian Institute of Technology, Kharagpur, India for his help in computations. ATSR data from RAL/UK is gratefully acknowledged.

#### REFERENCES

Agarwal Vijay K, A.K.Mathur and S.Ilanthirayan (1992) 'Estimates of the surface fluxes from satellite observations of boundary layer and the surface' Proc. 1st ERS-1 symposium, 4-6 Nov.1992, Cannes, France, (published ESA SP 359, p 773)

Ali M M , private communication.

Barton I M (1983) 'Dual channel satellite measurements of Sea Surface Temperature', Q.J.R. Meteorol. Soc. 109 pp 365-378.

Mathur A K and V K Agarwal (1991) 'A quantitative study on the effect of water vapor on estimation of Sea Surface Temperature using satellite IR observations'. Oceanography of the Indian Ocean, edited by Dr.B N Desai, Oxford-IBH publication, N. Delhi.

Mathur A K and Vijay K Agarwal (1992) 'Multichannel dual angle approach to SST retrieval in ontext of ERS-1 scenerio', Proc. 1st ERS-1 symposium, 4-6 Nov.1992, Cannes, France, (published ESA SP 359, p 767)

Schluessal P., H.Y. Shin, W.J.Emery and H. Grassl (1987), 'Computation of satellite derived Sea Surface Temperature with insitu skin measurements'. Journal of Geophysical Research vol. 92 no.C2 pp 2859-2874.

## FILAMENTS AND FINE STRUCTURE OF SEA SURFACE TEMPERATURE IN ATSR IMAGE DATA

Ian S Robinson<sup>1</sup>, Craig Donlon<sup>1</sup>,

David Llewellyn-Jones<sup>2</sup> and Chris Mutlow<sup>2</sup>

<sup>1</sup>Department of Oceanography, University of Southampton, U.K.

<sup>2</sup>Rutherford Appleton Laboratory, Chilton, Didcot, Oxford, UK

### ABSTRACT

One of the benefits of the ATSR, in addition to its role in accurately monitoring global sea surface temperature, is the sensitivity and low noise of the detector, resulting in single channel brightness temperature images from the nadir view which have a high radiometric resolution. Single channel brightness temperature images of locations in the Mediterranean Sea and in the South Atlantic Ocean are examined and found to contain a richness of spatial detail not encountered previously in the data from other sensors. Of particular interest is the existence of filamentary structures, having an amplitude of a few tenths of a degree K, a width of 1-3km, coherent over lengths of 50-100km, and apparently drawn into patterns by the mesoscale geostrophic flow field. The oceanographic implications and possible causes of these features are discussed. The discovery of such finescale filaments raises a number of questions about the dynamics and physics of the ocean surface, and demonstrates the enhanced utility of mapping sea surface temperature from space with a high sensitivity radiometer.

### 1. INTRODUCTION

ERS-1 was launched on 17th July 1991 and since 15 September 1991 the Along Track Scanning Radiometer (ATSR) has been operating almost continuously. The ATSR was designed primarily to achieve very accurate measurements of sea-surface temperature (SST). What distinguishes it from previous infra-red scanning sensors such as the advanced very-high Resolution radiometer (AVHRR) flown on the NOAA satellites is its conical scanning mechanism (Ref. 1), and consequent ability for improved atmospheric correction using its two-look capability. The scanner operates with two wavebands in the 10-12.5 $\mu$ m window, and a 3.7  $\mu$ m waveband also measured thermal emission at night, although this channel has now ceased to function.

Whilst most analysis of ATSR data has so far concentrated on the accuracy of absolute SST recovery, this paper is concerned primarily with what can be observed on single channel nadir-view images of brightness temperature at maximum spatial resolution. One reason for the improved accuracy of SST retrieval by the ATSR is the sensitivity of the detectors themselves. Cooled by a Stirling-cycle cooler, and calibrated

on board by reference to two independent black-body reference targets, the 11  $\mu$ m brightness temperature should have a noise level less than 0.1 deg K.

High resolution SST maps derived from other infra-red satellite sensors, notably the AVHRR, are now accepted as a useful means for the study of ocean mesoscale dynamical features. To obtain surface temperature patterns at maximum resolution, brightness temperature images from a single band are used. Because no atmospheric correction is applied the images are less noisy and more sensitive for detecting temperature structure (Ref. 2), although the absolute values of temperature recorded may be several degrees in error. Compared with AVHRR, the use of ATSR single band images does not necessarily improve the absolute accuracy, but does promise significant improvement in radiometric sensitivity. Since virtually all our knowledge about the detailed distribution of SST is based on satellite infra-red measurements, an improvement in the technique may reveal features of surface temperature structure which hitherto have not been observed. The objective of the research described here was to discover whether ATSR does improve the resolution of SST and whether ATSR images reveal any novel features of the ocean surface which have previously escaped detection by other thermal infra-red scanning sensors.

### 2. IMAGE SELECTION AND PROCESSING

Single Channel (11 $\mu$ m waveband) brightness temperature images were obtained from the SADIST 410 and 500 processing systems for ATSR data at Rutherford Appleton Laboratory. The images have been geometrically corrected and resampled onto a 1 km rectangular grid aligned with the satellite azimuth. A full image is therefore 512  $\times$  512 km. Clear sky conditions were sought, but any cloud that is present, being much cooler than the sea, will appear black on the images. Data corresponding to day and night overpasses of the same area were sought, but because of the different orientation of ascending and descending overpasses they do not overlay each other exactly without further geometric manipulation. In the search for oceanic conditions which might demonstrate the resolution capabilities of the ATSR, attention was directed at regions already known to have strong

thermal dynamical signatures on AVHRR data.

The first set of images was selected from the South-West Atlantic Ocean in the region of the confluence of the Brazil and Malvinas (Falkland) Currents. The images had already been processed for a calibration-validation exercise in which a ship-borne radiometer was deployed on a transit cruise from the North to the South Atlantic. The specific region of interest is off the South American coast, between 30°S and 45°S and 50°W to 60°W (Fig. 1). The second set of images was selected from a set of cloud-free images of the Mediterranean Sea, all recorded in May 1992. The region of interest is the western basin, between 0° and 15°E (Fig. 2).

The data output from the SADIST processor has a resolution of 0.01 degC, but for ease of display the pixel temperature values were truncated to a resolution of 0.1 degC and manipulated as 8-bit unsigned binary integers. For this paper, the images are presented in greyscale form, with a contrast stretch applied to emphasise the variability. As will become apparent, such is the resolution of the temperature variability within some images that a single greyscale is inadequate to show the full dynamic range. The endpoints of the temperature range represented by the greyscale are noted on each figure. Temperatures outside this range are represented as black or white, darker tones being colder and lighter being hotter. In most cases the contrast stretch is linear.

### 3. SOUTH ATLANTIC ATSR IMAGES

Figure 3, although it contains some small cloud patches, illustrates the general pattern of SST in the region. The region of bright tone stretching from the top right of the image corresponds to the warm Brazil Current flowing from the north-east. The darkest tone to the left represents the coldest water, the Falkland Current, flowing from the south-west. The slightly warmer region at the top left may be the shelf water of intermediate temperature. To the bottom of the image is a confused region of intermediate temperature, resulting from the dynamical interaction of the two opposing currents. Cyclonic cold core eddies and anticyclonic warm core eddies are apparent. There are sharp frontal zones where the temperature changes by 5 degC in a few kilometres, and sinuous meandering intrusions of both warm and cold water. This part of the ocean is revealed as a region of great thermal complexity.

The overall structure revealed by Fig. 3 was already familiar from studies of AVHRR data. Indeed, with a less sensitive infra-red scanner, the VHRR, Legeckis and Gordon (Ref. 3) were able to describe in outline the dominant features in this region. However, from the ATSR there is a richness of detail which is new, and which reveals that the complexity of thermal structure is found at shorter scales, down to 1 - 2 km, as well as at the scales of tens to hundreds of kilometres. This is particularly evident in the region left of centre of the image where the two water masses oppose each other directly. The ATSR image is able to reveal that the intermediate water is not homogeneous as might have been concluded from a less sensitive detector, but is made up of interleaving bands of warm and cool water. This observation is significant in relation to understanding the balance between the advective processes (drawing out the gradients and producing streakiness) and the diffusive processes (smoothing the steep gradients and tending towards uniformity).

Figure 4 illustrates this even more vividly. This is about 600 km south three days later and we see to the top centre-left a tongue of warm water which originates from the Brazil Current. The dominant feature is a large cold core eddy, some 150 km in diameter. In the intermediate water, created from a mixing of the two main water masses, a richness of spatial detail is apparent with variability length scales as short as 1-2 km. What is remarkable, and has not been so clearly revealed previously, is the coherence of long filaments of water entrained into the eddy's periphery. These filaments differ in temperature from their immediate surroundings by between 0.2 and 0.5 degC and are only one or two kilometres wide, but extend as coherent entities for up to 200 km.

Fig. 5, expanding details of Fig. 4, reveals this further by applying steeper contrast stretches. The characteristic patterns are similar in the original and the zoomed images. There are small eddies and hammerhead shapes which, although their thermal amplitude is weaker, are otherwise identical to the patterns at the larger scale. This is evidence for the self-similarity of the geophysical fluid dynamical processes which control the water movements, although more rigorous analysis of the patterns will be needed before confident conclusions can be drawn. What this preliminary survey does confirm is that the ATSR is able clearly to reveal thermal structures which have an amplitude of 0.2 degC and a width of 2 km, as well as structures with a length scale of 20 km and 200 km. It is only in cases where a front is exceptionally steep that AVHRR can resolve patterns down to such short length scales. The power of the ATSR to resolve the smaller features is further demonstrated in fig. 6, where a different contrast stretch has been applied to the warm zone of fig. 4. Present in the data, but not capable of display at the same time as the rest of the image using a single grey scale, are patterns caused by filaments drawn from tiny cold core eddies, an order of magnitude smaller than, but otherwise indistinguishable in form from, the large eddy in fig. 4.

Fig. 7 is a southward continuation of fig. 3 and half its area (the bottom left) overlaps the top right of fig. 4 which was recorded three days later. Although fig. 7 is cloudier, the large cold core eddy is discernable, and the warm water mass is present to the north-west of it. Comparison between the two images shows many similarities but also significant deformations of the overall pattern. The enhanced resolution makes the task of correlating the movements of detailed patterns between the images easier.

### 4. MEDITERRANEAN ATSR IMAGES

Figure 8 is a morning image of the Western Mediterranean Sea. The Spanish coast is at the top left and the Algerian at the bottom right. The island of Majorca is located centrally. In order to reveal the texture of SST patterns in the greyscale image a histogram equalisation stretch has been used, resulting in an indistinct coastline although it is not ambiguous in the data. As for the South Atlantic images there is a wealth of detail in the image, including narrow filaments a few tenths of a degree warmer or cooler than their surroundings, stretched out coherently over more than 100 km.

The richness of the mesoscale patterns in this region is not unexpected, having been observed often in both ocean colour (CZCS) and temperature (AVHRR) images (Refs. 4 & 5). The complexity of the fine scale patterns is not necessarily

evidence of a similarly complex mesoscale velocity field but could result from the non-linearity of lagrangian advection by a relatively simple circulation. Font (Ref. 6) and La Violette (Ref. 7) have examined the circulation of the Catalan Sea, the north western part of this image. The latter of these papers made extensive use of AVHRR imagery in order to provide a regularly updated context in which to interpret individual *in situ* measurements. The AVHRR has clearly revealed the eddy and plume structures which characterise the region. However, the narrow, fine temperature filaments have not previously been seen so clearly because the temperature fluctuations defining them are too small to distinguish from the noise of sensors such as the AVHRR. Now that they are more precisely mapped by the ATSR, they provide additional information about the fluid dynamics of the area.

For example, the improved sensitivity to the fine scale texture of SST should facilitate the application of cross correlation analysis to sequences of images in order to estimate the surface circulation vectors. The persistence time for the fine structure to remain recognizably coherent may also contain information about the near-surface mixing, and air-sea interaction processes. Fig. 9 is an evening overpass, obtained 12 hours later than fig. 8. Note that after sunset the islands and mainland are now cooler than the sea, and that the orientation is rotated slightly clockwise compared with fig. 8. Although the greyscale loses some of the detail, a comparison of the originals confirms that both images contain the same spatial details, implying that the patterns are genuinely in the SST field and not an artefact of the atmosphere. Moreover, since they do not change in amplitude between day and night in this case, it appears that they are representative of the upper ocean rather than ephemeral patterns of the surface skin temperature decoupled from the bulk temperatures below.

## 5. BANDED TEMPERATURE PATTERNS

Figure 10 is an ATSR image from the sea around Sardinia and Corsica and fig. 11 is an enlargement of the region to the west of the islands. The dominant features west of Corsica are banded linear structures, a few tenths of a degree in amplitude and 2-4 km wide. As with the images discussed above, the SST patterns appear to be the result of deformation by the mesoscale eddy structures typical of this part of the sea, and again the resolution achieved by the ATSR is able to demonstrate that the structures are coherent over lengths of 50-100 km. However, close inspection shows that this phenomenon is not quite the same as the interleaving of water masses having contrasting temperatures evident in the Falklands Confluence, or further west in the Mediterranean.

What first appears different is the absence of distinctive regions which could be considered to be the warm and the cool pools from which the interleaving structures are being drawn by advection. The patterns here seem to be defined by filaments of warm water which are the highest temperatures within the image west of Corsica. It is possible that they have been advected in from a warm region outside the extent of the image, but in that case it is unlikely that they would remain so distinct and coherent for the several days which it would have taken for the patterns to evolve by Lagrangian advection. It therefore seems more likely that the warm bands are associated with local surface heating.

It should be remembered that only the skin temperature of the

ocean is observed by infra-red radiometers. This is likely to differ from the "bulk" sea surface temperature (i.e. at 1-2m depth such as is typically measured from a ship) by up to  $\pm 1$  deg C (Refs. 8-10). Such a difference may be caused by the effect of solar heating creating a diurnal thermocline within the topmost metre of the water column. Alternatively it may be the result of the thermal skin effect; the inhibition of turbulent heat transfer by the presence of the air-sea boundary permits a steep temperature gradient within 1 mm of the surface.

Given the dependence of the skin temperature deviation upon local meteorological factors (wind speed, air-sea temperature difference, humidity) and local surface ocean properties (surface slicks and surfactants, local wind-wave field) it might be expected that SST variability with a magnitude of a few tenths of a degree, now capable of being detected by the sensitivity of the ATSR, would either be completely random or controlled by local meteorological length scales. If that were the case, we would expect the skin temperature to be decoupled from the underlying upper ocean temperature in relation to variability at length scales of one to perhaps fifty kilometres.

However, this is not consistent with any of the images presented here in which even the most subtle fluctuations of SST appear to be controlled by the mesoscale patterns associated with the motion of the underlying ocean. This is not only counter-intuitive, but at variance with the evidence of Schluessel (Ref. 8) who demonstrated from field measurements a loss of correlation between the skin and the bulk temperature at length scales less than 60km. In the case of figs. 3-9 it appears that if there is a skin temperature deviation at all it does not vary enough horizontally to mask the underlying temperature structure. However, in fig. 11 this may not be the case.

Fig. 11 was obtained in the evening, when the effect of any diurnal warming might be expected to be greatest. It is therefore interesting to examine fig. 12 which was obtained 36 hours earlier in mid morning before appreciable diurnal warming could take place. While it is apparent that there is a general similarity in the overall mesoscale patterns, allowing for some deformation in the intervening period, nonetheless the sharply defined filamentary features of the evening image contrast with the weaker and less clearly defined patterns in the morning image. It is difficult to propose a mechanism other than very shallow heating which could effect the change between fig. 12 and fig. 11.

This is consistent with the patterns being related to solar heating, affecting both the diurnal thermocline and the thermal skin deviation. If this is the immediate cause of the raised temperatures, we must still find a mechanism by which the skin temperature variability is coupled to the underlying mesoscale field, which undoubtedly it is, as evidenced by its large scale coherence. One possibility is that material surface slicks are present in banded structures. These would be advected by the mesoscale velocity field, forming patterns which evolve over a time scale of several days. Given suitable meteorological conditions, the slicks would cause local changes in the near surface thermal structure which appear as the observed thermal patterns. Slicks could also affect the surface emissivity and hence the apparent radiative temperature (ref. 11) In this explanation the time scale of the surface temperature patterns could be very much shorter than

the advective time scale of the eddy field, which is consistent with the strengthening of the thermal signature in the evening image. In effect, the temperature patterns might be "painted" each day onto the surface by suitable solar heating conditions modulated by the surface slick which has been advected by the mesoscale eddies.

Another possibility is that the structure is associated with horizontal vortices in the upper ocean which, being conservative, are stretched and deformed by the mesoscale eddy field. Such vortices would generate lines of surface upwelling and downwelling. Given the right solar heating and wind cooling conditions, these would show up as zones of cooler and warmer water respectively.

Credence is given to the hypothesis that the phenomenon is a surface effect coupled to the underlying motion because the patterns are so similar in character to those of sun glitter in the visible waveband photographs taken from the Space Shuttle (Ref. 12). Although the length scale is shorter in the shuttle photographs by a factor of 2 to 5, apart from this the structures are almost indistinguishable in the two types of image. The sun glitter patterns are assumed to be the result of a coupling between the surface roughness and the underlying flow field. Surface roughness changes may be sufficient in themselves to produce apparent temperature patterns because the infra-red emissivity is sensitive to the surface slope distribution (ref. 13).

## 6. CONCLUSIONS

It is clear that the enhanced sensitivity of the ATSR has enabled high spatial resolution images (1 km pixel size) of brightness temperature to be obtained with very fine temperature resolution. Under suitable conditions these images reveal patterns of SST variation with greater detail than hitherto recorded by other sensors. Temperature fluctuations of order 0.2 to 0.4 deg C are clearly resolved when they would have been lost in the random noise fluctuations on single band images from other scanning radiometers. The degree of detail is exquisite in some images, revealing fine filamentary patterns embedded into the mesoscale structures which images from previous sensors had tended to show as apparently uniform.

This preliminary analysis of a few images points to the need for much further work. For example, it is important to perform seasonal surveys to determine whether the occurrence of the detailed patterns is persistent, seasonal, or an atypical situation which was fortuitously encountered. Unless it is the latter, it should be possible to develop analytical tools to exploit the sensitivity of the ATSR by using the subtle temperature structures as tracers of water movement, and as indicators from which to infer information about mixing processes in the upper ocean. It will also be worth examining areas of ocean previously assumed, on the evidence of less sensitive scanners, to be devoid of thermal structure, in case there are weak thermal signatures which reveal dynamical features. It may be necessary to revise assumptions about the uniformity of SST in certain areas, and consider what effect the subtle temperature variations detected here have on the calibration of global scale satellite SST datasets using buoy measurements. If ATSR has revealed fine structures of variability down to length scales of 1-2 km, there may be even finer structures present, as yet unresolved, which could compromise the claim of *in situ* measurements from buoy or

ship to be representative of a wider area of sea.

## 7. REFERENCES

1. Edwards T *et al.*, 1990. The along-track scanning radiometer - measurement of Sea-surface temperature from ERS-1, *J. British Interplanetary Society*, **43**, 160-180.
2. La Violette P E & Holyer R J, 1988. Noise and temperature gradients in multichannel sea surface temperature imagery of the ocean, *Remote sensing of environment*, **25**, 231-241.
3. Legeckis R & Gordon A L, 1982. Satellite observations of the Brazil and Falkland currents - 1975 to 1976 and 1978, *Deep-Sea Res.*, **29**, 375-401.
4. Arnone, R A & LaViolette P E, 1986. Satellite definition of the bio-optical and thermal variation of the coastal eddies associated with the African Current, *J Geophys Res.*, **91**, 2351-2364.
5. Tintore J, LaViolette P E, Blade I & Cruzado A, 1988. A study of an intense density front in the Eastern Alboran Sea: the Almeria-Oran front, *J.Phys. Oceanog.*, **18**, 1384-1397.
6. Font J, Salat J & Tintore J, 1988. Permanent features of the circulation in the Catalan Sea, *Oceanologia Acta*, **1988**, SP, Océanographie pélagique méditerranéenne, édité par H J Minas et P Nival, 51-57.
7. La Violette P E, Tintore J & Font J, 1990. The surface circulation of the Balearic Sea, *J Geophys Res.*, **95**, 1559-1568.
8. Schluessel P, Emery W J, Grassl H & Mammen T, 1990. On the bulk-skin temperature difference and its impact on satellite remote sensing of sea surface temperature, *J. Geophys. Res.*, **95**, 13341-13356.
9. Saunders P W, 1967. The temperature at the ocean-air interface, *J. Atmos. Sci.*, **24**, 269-273.
10. Robinson I S, Wells N C & Charnock H, 1984. The sea surface thermal boundary layer and its relevance to the measurement of sea surface temperature by airborne and spaceborne radiometers, *Int. J. remote Sensing*, **5**, 19-45.
11. Kropotkin M A, Verbitskiy V A, Shuveleva T Yu & Tarashkevich V N, 1978. Radiation temperature of a water surface with an oil slick, *Oceanology*, **18**, 730-731.
12. Scully-Power P, 1986. *Navy oceanographer shuttle observations; Mission report*, NUSC Technical Document 7611, 26 March 1986, Naval Underwater Systems Center, Newport, R.I., USA.
13. Masuda K, Takashima T & Takayama Y, 1988. Emissivity of pure and sea waters for the model sea surface in the infrared window regions, *Remote sensing of environment*, **24**, 313-329.

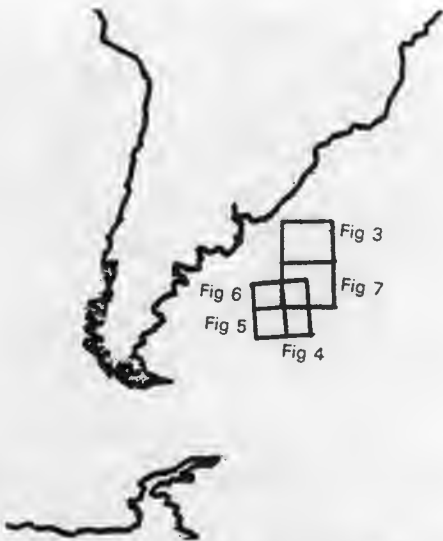


Figure 1. Location of South Atlantic ATSR images



Figure 4. South Atlantic ATSR 11 μm brightness temp. image with histogram equalisation stretch. 13 Oct, 1992, 02:25 UT.



Figure 2. Location of Mediterranean Sea ATSR images



Figure 5. Enlarged detail of Fig. 4, with linear stretch between 7.1 and 12.2 degC.

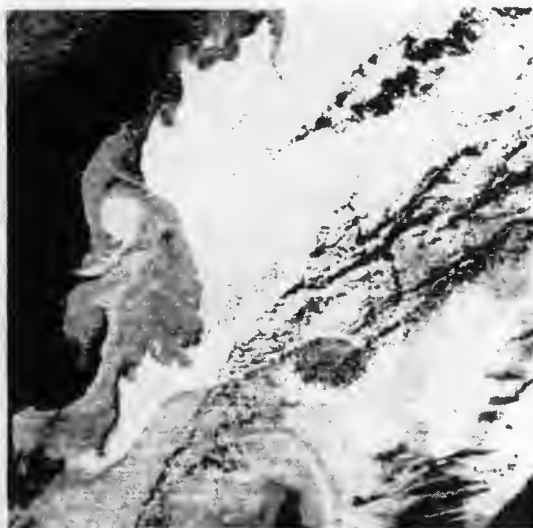


Figure 3. South Atlantic ATSR 11 μm brightness temp. image with histogram equalisation stretch. 10 Oct, 1992, 02:21 UT.



Figure 6. Detail of Fig. 4, with linear stretch between 12.6 and 14.3 degC.



Figure 7. South Atlantic ATSR 11  $\mu\text{m}$  brightness temp. image with histogram equalisation stretch. 10 Oct, 1992, 02:20 UT.

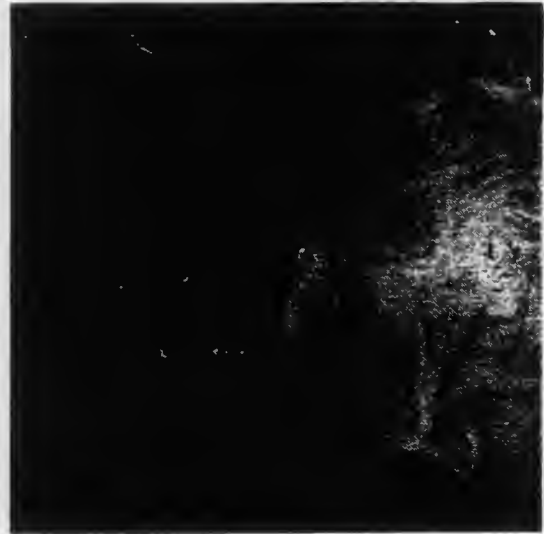


Figure 10. Mediterranean ATSR 11  $\mu\text{m}$  brightness temp. Linear stretch, 14.4 - 19.2 degC. 13 May 1992, 21:23 UT

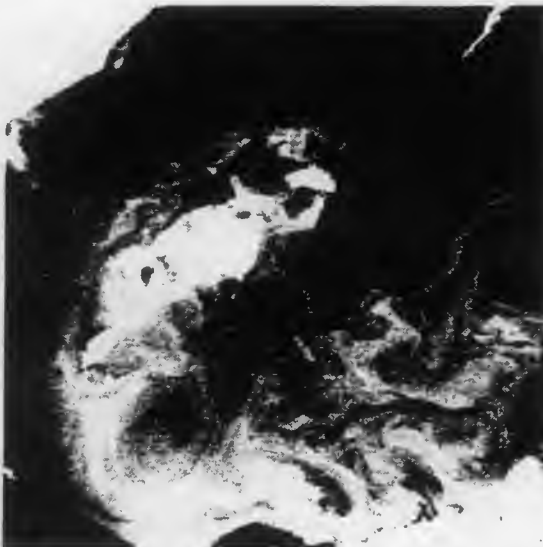


Figure 8. Mediterranean ATSR 11  $\mu\text{m}$  brightness temp. image with histogram equalisation stretch. 15 May 1992, 10:44 UT



Figure 11. Enlarged detail of Fig. 10, with linear stretch between 14.9 and 17.1 degC.

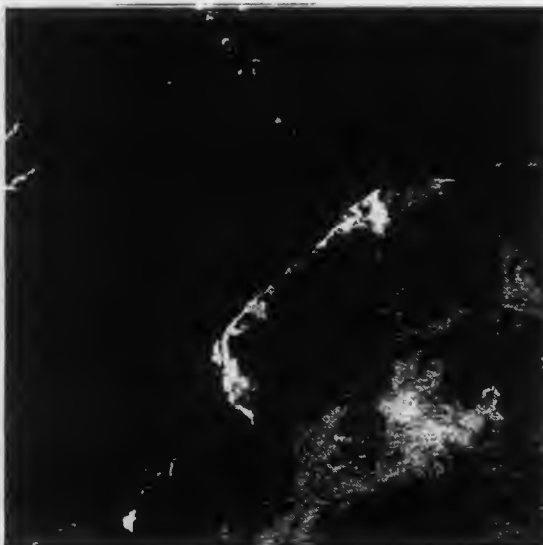


Figure 9. Mediterranean ATSR 11  $\mu\text{m}$  brightness temp. image with linear stretch, 15.4 - 17.7 degC. 15 May 1992, 22:01 UT



Figure 12. Enlarged detail of Mediterranean ATSR 11  $\mu\text{m}$  brightness temp. image, linear stretch 13.0 - 16.0 degC. 12 May 1992, 10:38 UT.

## AN ASSESSMENT OF THE ACCURACY OF ATSR DUAL VIEW SEA SURFACE TEMPERATURE ALGORITHMS

J.P.Thomas and J.Turner

British Antarctic Survey, Madingley Road, Cambridge, CB3 0ET, U.K.

### ABSTRACT

Between October 1991 and May 1992 *in-situ* skin and bulk SSTs were measured from the RRS Bransfield within the ATSR measurement swath as ERS-1 passed overhead. Intercomparison of the *in-situ* and ATSR SSTs shows that there was a 0.7K cold bias in the ATSR values due to the presence of stratospheric aerosol over the tropical North Atlantic. In the South Atlantic, at mid-latitudes, a 0.5K cold bias in ATSR SST could only be removed by including the 3.7 $\mu$ m brightness temperature measurement in the dual view SST algorithm. At several other locations there was good agreement between *in-situ* and ATSR SSTs.

Keywords: ATSR, SST, skin temperature, aerosol.

### 1. INTRODUCTION

The preliminary results of an intercomparison between ATSR sea surface temperatures (SST) and *in-situ* measurements from an infra-red radiometer and thermistors were described in Ref.1. The main conclusions were that the ATSR SSTs had a cold bias of between 1 and 2 K in the tropical Atlantic Ocean but that some of this offset could be due to the ATSR data processing scheme in use at that time. It was suggested that the magnitude of the cold bias was due to the fact that only the ATSR's nadir view brightness temperatures (BT) had been used in deriving the SST in most of the tropical cases.

The ATSR SST values were derived at the Rutherford Appleton Laboratories (RAL) where an automated processing scheme, called SADIST (Synthesis of ATSR Data Into SST), was applied to the ATSR BT measurements. This included steps to geolocate the measurements; application of cloud clearing algorithms and, finally, derivation of SSTs using a multi-channel algorithm in either dual-view or nadir-only configuration. The SADIST software has gone through several stages of development and improvement during its lifetime. The ATSR SST values given in Ref.1 were derived from version 400 of the software, which has since been replaced by version 500

due to several shortcomings in the earlier version (Ref.2), although the SST algorithms used have not been changed. The version 500 products for the cases discussed in Ref.1 have not yet been obtained. However, it was possible to re-derive values of SST directly from the version 400 BT measurements using the dual view algorithms. These new SST values were then compared again with the *in-situ* SSTs to see if the magnitude of the SST differences was reduced by the inclusion of the forward view BT measurements.

### 2. DATA PROCESSING METHODS

#### 2.1 *In-situ* measurements

The preliminary results discussed in Ref.1 were for 9 sets of co-located *in-situ* and ATSR SST measurements. Since then two more sets of ATSR data have been obtained, one in the tropical Atlantic and one in the Weddell Sea (see Figure 1). One of the cases, that for 16 October 1991, has been omitted from the present analysis due to difficulties with cloud clearing. The Weddell Sea case will be treated separately as there was a time lapse of 12 hours between the *in-situ* measurements and the satellite overpass. There are features of the SST variability for this case which are of qualitative interest. The 9 remaining sets of co-located measurements have been chosen as the best possible datasets for making intercomparisons of the *in-situ* and ATSR SSTs. Many other possible datasets were rejected because of extensive cloud or sea ice cover at the time or because of a time difference of several hours between the satellite overpass and the *in-situ* measurements. The radiometer was installed on the ship for a total of eight months but was not operated during all of this time either because it was undergoing repair or because no personnel were available to operate it. The total number of possible operational days was 100. The small number of good intercomparisons which were obtained was due to several factors:

- (i) the narrow ATSR swath and the large distance between sub-satellite tracks which sometimes led to long periods when the ship was not within an ATSR swath.
- (ii) bad sea conditions preventing use of the radiometer. This was a particular problem when crossing the Southern Ocean between South America and Antarctica.
- (iii) extensive cloud cover preventing ATSR from viewing the sea surface, particularly in the Weddell Sea

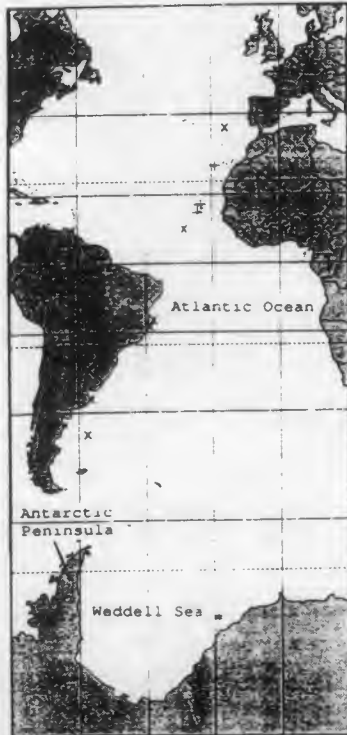


Fig. 1. Locations of simultaneous *in-situ* and ATSR measurements (+ = October 1991 ; \* = December 1991 ; x = April/May 1992)

and near to the Antarctic Peninsula, where sea ice was also extensive.

The intercomparison dataset is therefore biased towards measurements in the tropical and sub-tropical Atlantic Ocean. The *in-situ* SSTs were measured using an infra-red radiometer and thermistors attached to or towed from the ship. These are briefly described in Ref.1. A fuller description of the radiometer and the validation of its measurement accuracy is given in Ref. 3. It has been shown to be capable of measuring the sea surface skin temperature with an accuracy of  $\pm 0.1\text{K}$ . It was essential to measure the skin temperature as this was the parameter being measured by ATSR. The skin temperature can be significantly different to the bulk SST traditionally measured from ships (Ref.4).

## 2.2 ATSR Brightness Temperatures

The SADIST version 400 SSTs had a cold bias compared to the *in-situ* SSTs in most cases (Ref. 1). The bias was more than 1 K in several tropical cases with the largest value being 2.3 K. The SADIST 400 processing and confidence flags, provided with the SST data, indicated that only the nadir BT measurements were being used in deriving SST in 7 out of the 9 cases investigated. This was also true for the additional tropical case which has become available more recently. Visual inspection of the BT images indicated that in most cases the region around the ship's position was cloud free or only affected by scattered cloud which produced a speckled effect on the image. The rejection of forward view measurements due to cloud contamination in these cases was not justified therefore and it was actually possible to derive SST from the dual view algorithm. A crude cloud clearing scheme was applied to the SADIST 400 BT measurements before the dual view SST was derived. This was done by applying maximum and minimum limits to the BT

values for each channel so that only clear sea surface values were allowed. The limits were chosen from visual inspection of histograms of BT distribution for individual images.

In most of the cases only the  $11\mu\text{m}$  and  $12\mu\text{m}$  channel forward and nadir view data were used. Two of the tropical cases and one of the mid-latitude cases were at night and therefore the effects of the  $3.7\mu\text{m}$  channel could also be investigated as these cases predated the failure of this channel on 27 May 1992.

Another problem which occurred in the SADIST version 400 data was that forward and nadir view pixels were often incorrectly co-registered by the Earth coordinate location software (Ref.2). Before SSTs could be derived from the BTs therefore the forward and nadir views had to be correctly matched together so that the appropriate pixels from each view were used in the SST algorithm. A correlation matching technique was developed to do this. Only BTs from cloud free pixels were included in the correlation test. The success of the correlation matching scheme could easily be tested in images which showed part of a coastline or an ice edge. In open ocean areas features such as ocean fronts and eddies were used to check that correct co-registration was obtained. In most cases a shift of the forward image of up to 7 pixels, in the along track direction, relative to the nadir image was required. Having correctly matched the views in each channel, the SST could then be derived for chosen pixels and the intercomparison carried out.

## 3. RESULTS

### 3.1 Atlantic Ocean SST measurements

The results for all the intercomparisons where ATSR and *in-situ* measurements were made simultaneously are given in Table 1. Figure 2a shows the differences between ATSR nadir only SST and *in-situ* radiometer SST as a function of the total water column measured by radiosondes at each location. These results are similar to those given in Ref.1, with very large cold biases in the ATSR SST in tropical conditions where the water column was greater than 30mm. There was one exception to this, which was the 5 May 1992 case where the cold bias was only 0.3 K. The next smallest cold bias, of 1 K, was for 6 May 1992. These cases were in the tropical South Atlantic near the coast of Brazil. The tropical North Atlantic cases all had much larger cold biases although for the 21 October 1991 case the bias was reduced by approximately 0.6 K by including the  $3.7\mu\text{m}$  BT. The magnitude of the bias in the tropical Atlantic does not appear to be linked to the amount of atmospheric water vapour.

The higher latitude cases also showed that the ATSR SSTs had a cold bias if the nadir only BTs were used. The bias was smaller than for most of the tropical cases, with a maximum value of 0.7 K. In the one nighttime case where the  $3.7\mu\text{m}$  BT was available it made very little difference to the ATSR SST result, only changing it by 0.1 K.

Figure 2b shows the effect on the ATSR SSTs of using the dual view algorithm. This was not possible for the 6 May 1992 case as the forward view pixels were obstructed by cloud. In most cases the dual view SSTs lead to better agreement with the *in-situ* measurements. However, the ATSR SSTs still had a cold bias of approximately 0.7 K in the tropical North

DATE	TIME (GMT)	LAT.	LON.	RADIOMETER SST K	$\Delta_{RB}$	$\Delta_{RD}$	$\Delta_{RN}$	$\Delta_{RD37}$	$\Delta_{RD37}$
19/10/91	12:00	27.66N	19.09W	296.8	-0.4	-0.1	0.7	-	-
21/10/91	23:45	17.20N	23.30W	299.5	0.0	1.2	1.6	0.7	1.0
22/10/91	12:23	14.75N	24.28W	300.8	-0.4	0.7	1.6	-	-
26/04/92	03:07	44.73S	57.47W	285.8	0.1	0.7	0.5	0.2	0.6
27/04/92	13:52	36.87S	56.39W	292.1	-	0.6	0.5	-	-
05/05/92	12:55	18.49S	38.76W	300.5	0.0	0.1	0.3	-	-
06/05/92	01:20	16.50S	37.76W	301.6	0.1	-	1.1	-	1.0
12/05/92	12:27	10.13N	28.43W	299.0	0.0	0.8	1.7	-	-
19/05/92	12:00	36.78N	16.04W	291.3	-0.2	-0.3	0.7	-	-

Table 1. Results of the intercomparison of ATSR SST with in-situ SST measurements. ( $\Delta_{RB}$  = radiometer - bulk ;  $\Delta_{RD}$  = radiometer - ATSR dual view ;  $\Delta_{RN}$  = radiometer - ATSR nadir view ;  $\Delta_{RD37}$  = radiometer - ATSR dual view with 3.7 $\mu$ m ;  $\Delta_{RD37}$  = radiometer - ATSR nadir view with 3.7 $\mu$ m)

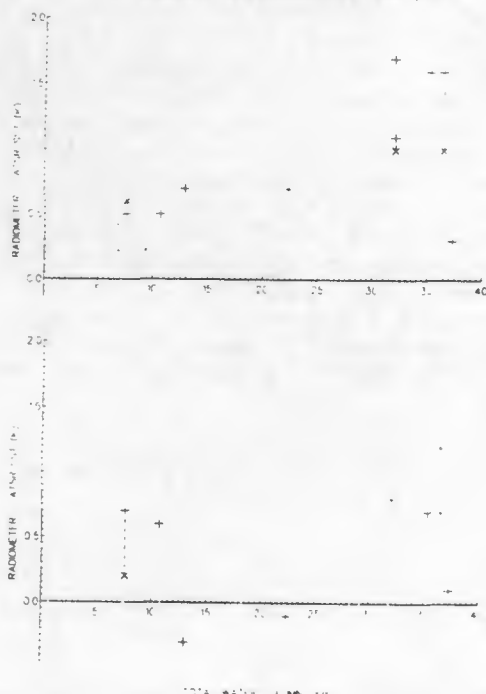


Fig. 2. Differences between in-situ skin temperature and ATSR SST versus total water column for the cases in Table 1. (a) Nadir-only ATSR SST algorithm. (b) Dual view ATSR SST algorithm. (+ = 11 $\mu$ m and 12 $\mu$ m channels used ; x = 11 $\mu$ m, 12 $\mu$ m and 3.7 $\mu$ m channels used).

Atlantic. The one remaining tropical South Atlantic case, 5 May 1992, was within 0.1 K of the *in-situ* SST. The cold bias of 0.7 K agrees well with the results presented in Ref.5 where radiometer measurements of SST were made from a low flying aircraft in the South Atlantic between the Equator and 8°S in November 1991. In Ref.5 the offset is attributed to the presence of stratospheric aerosols due to the eruption of Mt.Pinatubo in June 1991. Aerosol optical depth maps (Ref.6) show that values were high in the area where the airborne measurements were made. Similar values occurred in the region where the two tropical North Atlantic *in-situ* measurements were made on 21 and 22

October 1991. It therefore seems very likely that stratospheric aerosol was responsible for the 0.7 K cold bias shown in Figure 2b. By May 1992 the Mt.Pinatubo aerosol was more dispersed with a band of the highest concentrations centred on latitude 10°N (Ref.7). This was the latitude at which the *in-situ* and ATSR SSTs were measured on 12 May 1992. By that time the amount of stratospheric aerosol was much less than in October 1991 and the amount of atmospheric water vapour was still for this case. The cold bias in the ATSR SST was less as large as 0.8 K even when the dual view algorithm was used. The BT images on this occasion revealed that the area near the ship had a speckled appearance indicating varying amounts of sub-pixel scale cloud, typical of convection cells experienced over the tropical ocean in the early afternoon. This was confirmed by visual observations from the ship at the time which also indicated a complete cover of a haze due either to thin cirrus at high level or dust, possibly of Saharan origin. The cold bias in this case was therefore due to a combination of factors. This case could provide an interesting test for the cloud clearing scheme used in version 500 of SADIST. It might not allow an SST calculation due to the presence of the sub-pixel cloud if it is able to detect it. This might limit the sampling of tropical ocean areas where the satellite passes overhead near to local midday by which time convection cells are usually well developed. On the other hand, if an SST can be computed then it will have a cold bias if the cloud covers a significant portion of each pixel.

The effects of the dual view algorithm on the mid-latitude ATSR SSTs were beneficial in the two cases with the largest water column values of 22mm and 13mm. These were in the North Atlantic on 19 October 1991 and 19 May 1992 respectively. Both SST values were within 0.3 K of the *in-situ* value, with a warm bias. In the other two cases, which were in the South Atlantic near the coast of Argentina, there was very little effect. In fact, the dual view algorithm gave slightly worse agreement with the *in-situ* SSTs. The agreement was greatly improved for the case with the lowest water column value, 26 April 1992, when the 3.7 $\mu$ m BT was included, although this had little effect on the nadir only SST for the same case. These two cases were both in areas where there was a great deal

of variability in local SST due to the mixing of waters between the Brazil and Falkland Currents and also the outflow of the River Plate. Correct co-registration of forward and nadir pixels was therefore critical for these cases. The correlation matching scheme may not have been adequate for this purpose which explains why the dual view algorithm gives a slightly worse result. The water column values for the two cases were low so that little benefit was to be expected from the use of the dual view in this region. However the  $3.7\mu\text{m}$  measurement had a significant effect when included in the dual view algorithm. This suggests that another atmospheric constituent, which had little effect in the  $11\mu\text{m}$  and  $12\mu\text{m}$  channels, might be responsible for the cold bias in ATSR nadir-only SSTs in this area.

### 3.2 Weddell Sea

The one case available from high latitudes has been omitted from the intercomparison graphs shown in Figure 2. The reason for this was that the *in-situ* measurements were made approximately 12 hours before the area was within the ATSR swath. The case will still be discussed here as some useful observations can be made concerning changes in ocean skin temperature which can occur in a few hours. The ship entered the ice-free waters of the Weddell Sea shore polynya at about 13:00 GMT on 14 December 1991 and did not re-enter pack ice until nearly midday on 15 December. Radiometer and bulk SSTs were measured throughout this time and for most of the period the sky was completely clear of cloud. At this time ERS-1 was being manoeuvred into the first "ice phase" orbit and it was therefore difficult to predict when overpasses would occur. It transpired that only the first few hours of the ship's track coincided with the edge of an ATSR

overpass 12 hours later. The *in-situ* measurements were made during the period when the ship was under completely cloudy skies but the ATSR BT images show that this area was cloud free by the time they were acquired due to the eastward movement of a mesoscale depression clearly visible within the image. The radiative balance at the sea surface had therefore changed completely between the time of the *in-situ* and the ATSR measurements. This is illustrated in Figure 3 which shows the complete time series of *in-situ* radiometer and bulk SSTs.

At the beginning of the transect the bulk and radiometric SSTs are quite close together with the radiometric values being slightly higher. This is slightly puzzling as the skin effect usually results in radiometric temperatures being lower than the bulk temperature. The air temperature was about 2 K cooler than SST at the time, as cold, dry polar air was moving northwards over the sea and cloud was being formed towards the northern edge of the polynya. Sensible and latent heat loss would lead to a cool skin in these conditions and radiative heat loss would be very small due to the presence of the cloud layer. The reason for the warm radiometric SSTs is probably that an incorrect value was used for the BT of the sky above the ship during this part of the radiometer measurements. As water is not a perfect black body a small proportion of the radiance measured by the radiometer is the reflected downward radiance from the sky. The sky BT value was computed using RAL's radiative transfer model (Ref. 8) applied to the atmospheric temperature and humidity profile measured by a radiosonde launched from the ship. The effects of cloud were included in the model calculations by assuming that the cloud behaved as a black body at a height estimated from visual

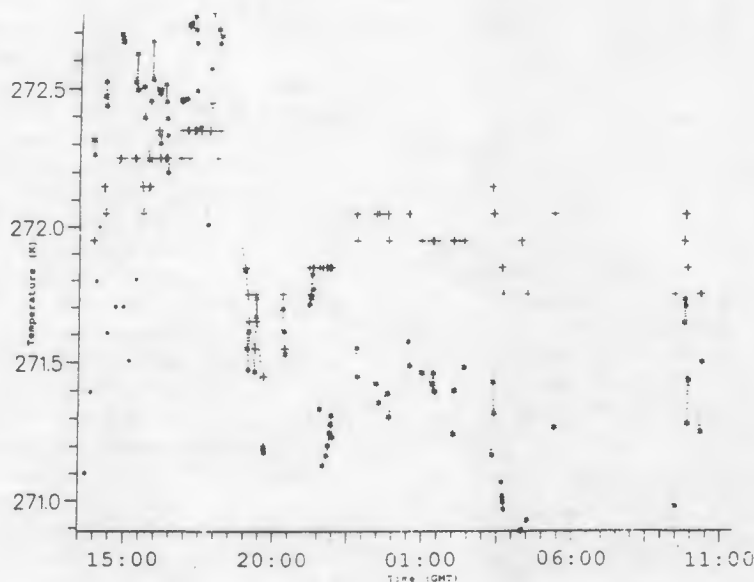


Fig. 3. SST measurements along a transect through part of the Weddell Sea on 14 and 15 December 1991. (\* = skin temperature ; + = bulk temperature ; o = ATSR dual view SST).

observations and inspection of the radiosonde profile. It is possible that an inaccurate value of the sky BT was responsible for the warm bias in the radiometer SSTs.

At approximately 19:30 GMT the ship altered course to move in towards the ice shelf which forms the southern coastline of the Weddell Sea in this region. Figure 3 shows that the SST then dropped by almost 1 K and that the bulk and skin SSTs diverged significantly at about 21:30 GMT which corresponded to the time when the sky became cloud-free. Radiative cooling from the skin would have increased as a result of the clear sky and also the air temperature was dropping as the solar zenith angle decreased - although complete darkness did not occur here at this time of year. The ATSR SSTs for the part of the transect which crossed the corner of the image have also been plotted on Figure 3. The values are about 1 K smaller than the *in-situ* values measured 12 hours previously and much nearer to the values measured later in the radiometer transect when skin temperatures were much cooler for the reasons discussed above. It is therefore impossible to intercompare measurements separated by this amount of time in this region due to the significant changes in radiative conditions which can occur as well as factors such as cooling due to sea ice melting and advection effects in the ocean. The behaviour of the skin effect at temperatures near to the freezing point of sea water is a problem which does not appear to have been investigated, although there are many studies of its behaviour at higher temperatures. As the skin is usually cooler than the bulk SST, particularly in polar conditions, the surface tension layer could reach the freezing point before the bulk of the water underneath. In ice-edge regions this might lead to incorrect conclusions on the extent of sea ice from satellite infra-red measurements if the theoretical minimum SST is used to define its limit. On the other hand the usual model of the skin effect (Ref.4) may not apply at these temperatures. This is a subject which might warrant further investigation if the relationship between skin and bulk SST is to be understood properly at low temperatures.

#### 4. CONCLUSIONS

An intercomparison of *in-situ* SSTs, measured using an infra-red radiometer, with SSTs derived from ATSR BT measurements has been carried out. One case, in the Weddell Sea, was only able to demonstrate qualitative agreement in the SSTs, but showed how critical it is to make simultaneous measurements in this area.

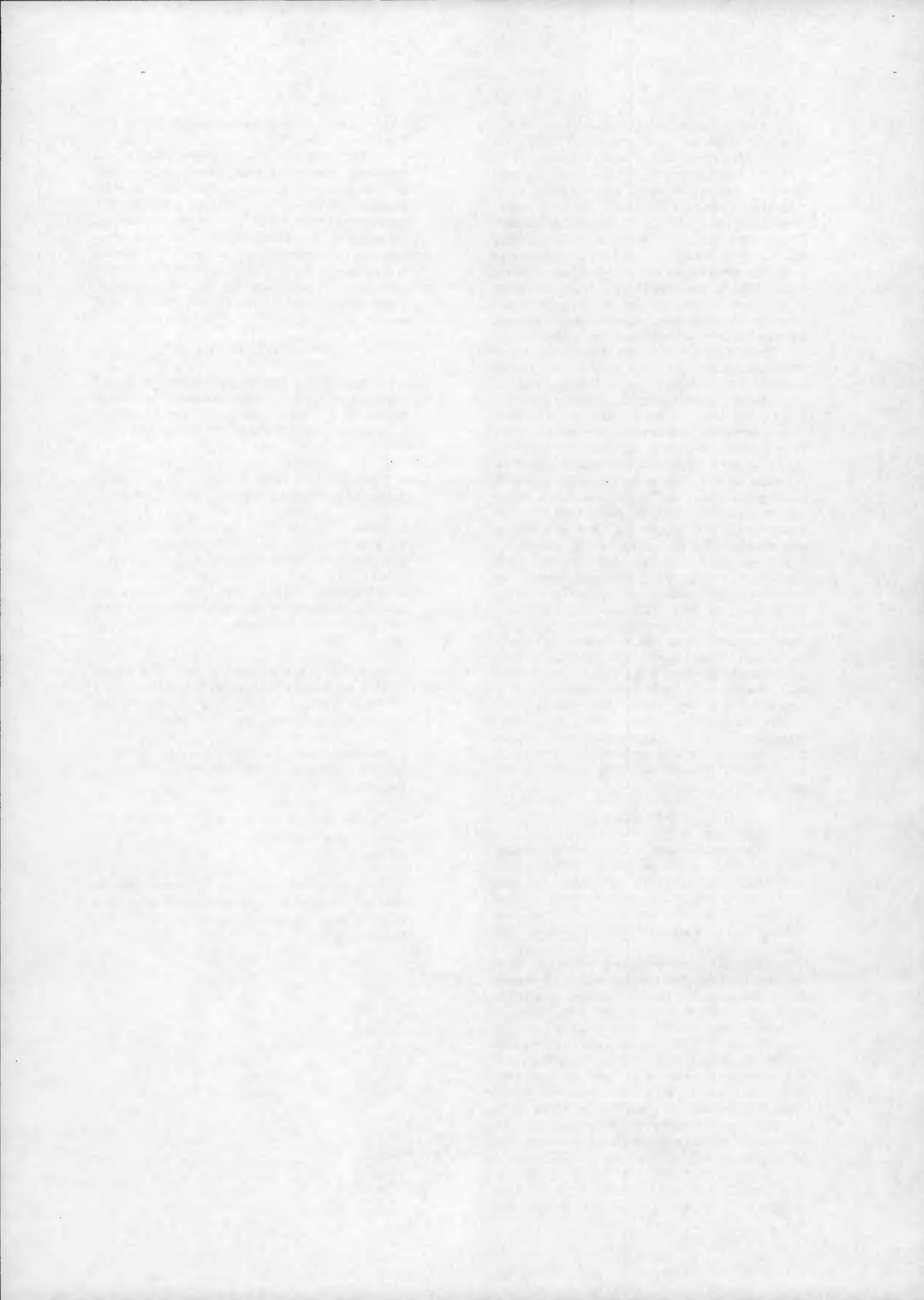
The other *in-situ* measurements were all made at the same time as ATSR measurements. They showed that it was essential to use the dual view algorithm to retrieve SST from BT measurements in the tropics. In the tropical North Atlantic there was a cold bias of approximately 0.7K in ATSR SSTs due to the presence of stratospheric aerosols from the Mt. Pinatubo eruption. In one case there was also some contribution from sub-pixel scale cloud over the tropical ocean. In a tropical South Atlantic case and two higher latitude North Atlantic cases good agreement was obtained with the *in-situ* SSTs. Two cases near 40°S showed a cold bias of 0.5K in the ATSR SSTs. The 3.7 $\mu$ m BT could be used in one of these cases. The dual view ATSR SST was then only 0.2K colder than the *in-situ* SST. This suggested that an atmospheric constituent other than

water vapour or aerosol was responsible for the cold bias in nadir only SST.

The dataset of *in-situ* radiometric measurements which were collected was small but very valuable. They have already yielded results which have provided insights into the factors affecting accurate SST measurements from ATSR. They have also confirmed the results of other authors (Ref. 5). The cases which have been discussed provide a variety of tests for various aspects of ATSR data processing and can be used again in the future to test the effects of improvements to the processing schemes and SST algorithms.

#### 5. REFERENCES

1. Thomas, J.P. et al 1993, A comparison of ATSR and shipboard radiometer SST measurements along transects between the UK and the Antarctic, in Proc. 1st ERS-1 Symposium, Cannes, France, 4-6 November 1992, ESA SP-359.
2. Bailey, P. 1993, SADIST Products (Version 500), Rutherford Appleton Laboratories, Chilton, U.K.
3. Thomas, J.P. et al 1994, The calibration of a shipborne infra-red radiometer for measuring sea surface temperatures, Submitted to J.Atmos.Ocean.Technol.
4. Schlüssel, P. et al 1990, On the bulk-skin temperature difference and its impact on satellite remote sensing of sea surface temperature, J.G.Res., 95, C8, 13 341 - 13 356.
5. Smith, A.H. and R.W.Saunders 1993, Validation of ATSR-1 using aircraft radiometer measurements over the South Atlantic, in Proc. 1st ERS-1 Symposium, Cannes, France, 4-6 November 1992, ESA SP-359.
6. Saunders, R. 1993, Radiative properties of Mount Pinatubo volcanic aerosols over the tropical Atlantic, G. Res. Lett., 20, 2, 137-140.
7. Halpert, M.S. et al 1993, 1992 brings return to moderate global temperatures, EOS, Trans. A.G.U., 74, 38, 443.
8. Llewellyn-Jones, D.T. et al 1984, Satellite multichannel infra-red measurements of sea surface temperature of the N.E.Atlantic using AVHRR/2, Quart.J.R.Met.Soc., 110, 613-631.



## INTERCOMPARISON OF AVHRR AND ATSR DATA AND DATA PRODUCTS

I.J. Barton<sup>1</sup>, C.T. Mutlow<sup>2</sup>, A.M. Zavody<sup>2</sup>, and D.T. Llewellyn-Jones<sup>2</sup>

<sup>1</sup>CSIRO Division of Atmospheric Research, Aspendale, Victoria 3195. Australia

<sup>2</sup>Rutherford Appleton Laboratory, Chilton, Didcot, Oxon OX11 0QX. U.K.

### ABSTRACT

The AVHRR instruments on the NOAA operational meteorological satellites have been supplying infrared images of the earth's surface for many years. The ATSR on the ERS-1 satellite is a similar instrument which has been specifically designed to provide accurate estimates of the sea surface temperature. A comparison between the data and data products from these two instruments highlights the design features of the ATSR which enables it to supply sea surface temperatures with an accuracy better than 0.3K. The intercomparison is supplemented by high quality ground based data obtained at the same time as the satellite images.

### 1. INTRODUCTION

In mid-July 1991 ESA launched the ERS-1 satellite which carries a suite of instruments aimed at studying the earth's oceans from space. Included in the payload is the Along Track Scanning Radiometer (ATSR) which has been designed as a highly accurate, low noise, infrared radiometer which is capable of supplying data from which the surface temperature of the ocean surface can be derived with an accuracy that is suitable for climate research. Before 1991 satellite measurements of SST were supplied regularly from the NOAA series of polar orbiting operational satellites. The AVHRR instrument has been most successful in supplying infrared and visible images of the earth's surface for over fourteen years and, for most applications, measurements of SST provided by this instrument have been quite adequate. However, with the increasing concern of climate modification due to man's activities, numerical models of the climate system are requiring basic data sets with an increased accuracy. ATSR has been developed to provide the SST accuracy defined by the international TOGA program.

In this paper a comparison between the data and data products of the AVHRR and ATSR is given.

### 2. THE SATELLITE RADIOMETERS

#### 2.1 The AVHRR

The Advanced Very High Resolution Radiometer (AVHRR) is one of the core instruments carried on the NOAA operational meteorological satellites. NOAA has maintained two of these satellites in orbit at all times over the last twelve years. The satellites are designed to serve the world's meteorological services and data are continually available through direct broadcast at no cost to the user. Because these data are so readily and cheaply available their use has extended well beyond the meteorological community and AVHRR data products are applied in a large variety of disciplines. Details of the AVHRR instrument, and the means for analysing and calibrating the data are given in the NOAA Technical Memorandum by Lauritson et al (Ref. 1).

The latest AVHRR instruments have five channels (wavelengths of 0.6, 0.9, 3.7, 10.8 and 11.9  $\mu\text{m}$ ) which view the surface with a spatial resolution of 1.1 km over a three thousand km swath. The two NOAA satellites thus give global coverage four times daily. Future AVHRR instruments will include a channel at 1.6  $\mu\text{m}$  for discrimination between ice, snow and water clouds.

#### 2.2 The ATSR

The Along Track Scanning Radiometer (ATSR) has been designed to give the same spatial resolution as the AVHRR and also has similar channels in the infrared bands at 3.7, 11 and 12  $\mu\text{m}$ . ATSR also includes a channel at 1.6  $\mu\text{m}$ . Several novel design features have been included in the ATSR to ensure that the demanding accuracy requirements can be met. Two highly precise on-board calibration targets, maintained at temperatures near 305K and

265K, give an accurate absolute calibration for the radiances received and measured by the instrument. A Stirling cycle cooler is used to cool the detectors well below 100K giving noise temperatures for each channel that are lower than 0.05K at 300K. Finally a conical scanning technique is used that enables the earth's surface beneath the satellite to be viewed from two different angles within the space of three minutes. This dual angle information at 55 degrees from nadir and close to nadir enable an extra correction for the absorption of the surface infrared signal by the atmosphere. ATSR thus gives six measurements of the earth's surface that enable an improved estimate of the SST. Unfortunately the conical scanning technique limits the measurement swath of the instrument to 250 km each side of the sub-satellite track. When this is combined with the basic three-day repeat cycle of ERS-1 the ATSR gives almost global coverage of the oceans twice every three days. Mid-latitude and polar regions are well covered while tropical areas may have data voids depending on the orbit configuration. Further details of the ATSR instrument are given by Delderfield et al (Ref. 2).

### 2.3 AVHRR and ATSR Instrument Comparison

Table 1 gives details of the two radiometers.

TABLE 1: ATSR and AVHRR specifications.

	ATSR	AVHRR/2
Infrared bands ( $\mu\text{m}$ )	3.7 10.8 11.9	3.7 10.8 11.9
Vis.NIR bands ( $\mu\text{m}$ )	1.6	0.6 0.9
Surface views	Double	Single
Calibration targets	2	1
Space views	0	1
Aperture (cm)	10	20
Integration time ( $\mu\text{sec}$ )	75	23
Detector temp. (K)	80	105
Digitisation (bits)	12	10
Detector NEDT (K)	0.025	0.10
Passive $\mu\text{wave}$ bands	Yes	No
Surface swath (km)	500	3000
Pixel size (km)	1.1	1.1

## 3. DATA SETS FOR COMPARISON

To enable a comparison of data from the two instruments one image from each has been obtained for an area over the north-east coast of Australia. The two data sets were obtained within four hours during the night of September 13, 1991. The area was free of cloud so that surface measurements could be used to support the satellite data. Comparisons between individual lines and pixels, as well as large areas have been made.

### 3.1 The ATSR image

The ATSR data were obtained from an ascending pass at 1300Z on September 13 and the image from the 11  $\mu\text{m}$  channel is shown in Figure 1. The image centre is at 19.25°S, 145.90°E. and is close to the city of Townsville. The ATSR processing system removes the effect of the conical scan and produces an image of 512 x 512 pixels centred along the subsatellite track. In the case shown the image is aligned so that north-north-west is to the top of the image. This scene shows the full swath of the ATSR instrument. The data also contain measurements from the 3.7  $\mu\text{m}$  channel that has subsequently failed (during May 1992). The ATSR image shows cold surface water near the coast in the south of the image and warmer water to the north and away from the coast. The image also shows much information over the land; e.g. the warmer land adjacent to rivers and in low lying areas. The land surface is considerably cooler than the ocean due to the radiative cooling that is active under the clear sky conditions.

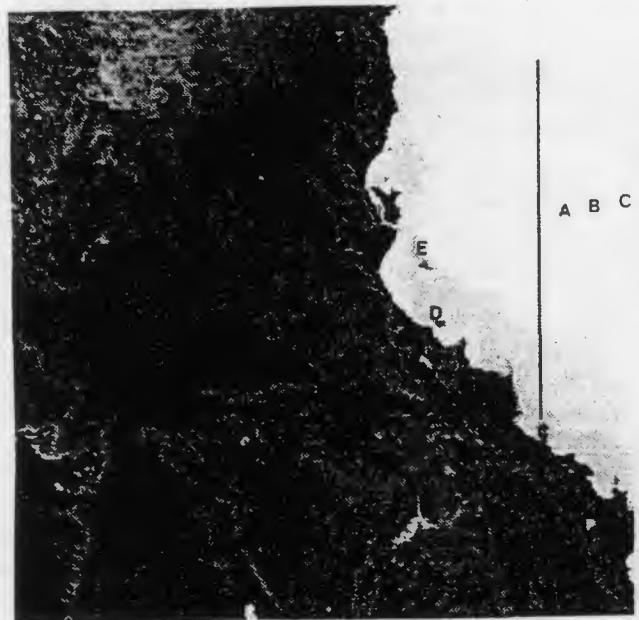


Fig. 1. The ATSR image for 1300Z, 13 September 1991.

### 3.2 The AVHRR image

The corresponding AVHRR image is that obtained from the NOAA-12 instrument at 0930Z on the same day (Orbit No. 01729). The satellite was also in an ascending orbit with the subsatellite track passing just to the east of the ATSR image. The AVHRR image has been sub-sampled to 512 x 512 pixels and provides a similar areal coverage as the ATSR. The AVHRR image from the 11  $\mu\text{m}$  channel is shown in Figure 2. As expected, the same broad features can

be seen in both the ATSR and AVHRR images. Over the land the brightness temperatures are warmer than in the ATSR image as the AVHRR data are obtained early in the evening.



Fig. 2. The ATSR image for 0930Z, 13 September 1991.

#### 4. COMPARISONS

To enable a comparison of data from the two instruments those obtained along the lines drawn in Figures 1 and 2 have been reproduced in Figures 3 and 4. There is less noise on the ATSR signals due to the lower noise temperatures in the instrument and the increased digitisation of the data (ATSR has 12-bit digitisation while AVHRR is only 10-bit). The noisy signal that plagues the AVHRR 3.7  $\mu\text{m}$  channel is evident in Figure 4. The data from the two instruments do not agree exactly due to the time difference in data collection and the non-coincidence of the lines in Figures 1 and 2. One interesting further comparison is of interest. In the ATSR data the 3.7  $\mu\text{m}$  and 11  $\mu\text{m}$  values have approximately the same value, while the 12  $\mu\text{m}$  temperature is about 1K less. This is to be expected as a radiosonde launched from a research vessel during the night showed the atmosphere to be quite dry (total water content of 1.22 cm, 15 hPa partial pressure of water vapour below 1 km and relatively dry above). In contrast the AVHRR 3.7  $\mu\text{m}$  data are similar to those in the 12  $\mu\text{m}$  channel. This suggests some absolute calibration error in the AVHRR data.

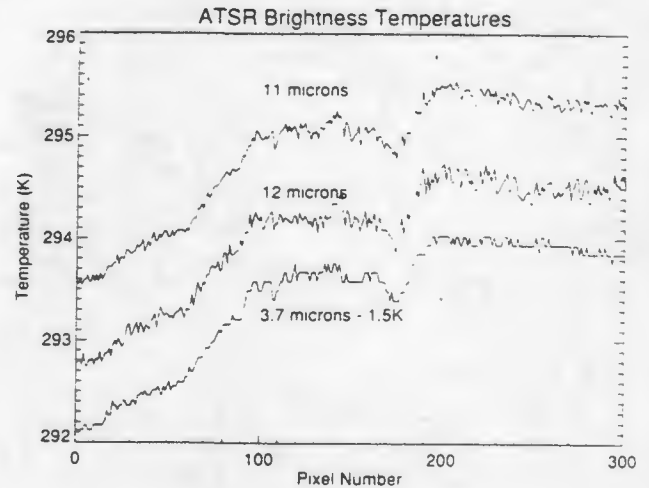


Fig. 3. ATSR brightness temperatures along the line in Figure 1.

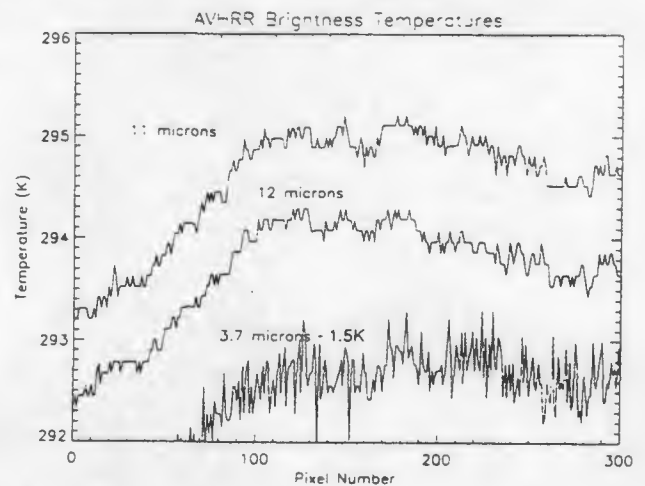


Fig. 4. AVHRR brightness temperatures along the line in Figure 2.

A comparison of the sea surface temperatures from each instrument shows good agreement (see Figure 5). The ATSR SST was derived using the pre-launch algorithm developed for the 11 and 12  $\mu\text{m}$  channels in the nadir view (see Ref. 3). This algorithm is used to be consistent with the MCSST product derived from the AVHRR data. The extra noise on the AVHRR product is evident and is mainly due to the effect of digitisation as discussed by Barton (Ref. 4). Fluctuations between one half and one degree are introduced by the 0.12K digitisation levels in the two channels used to derive the SST.

TABLE 2: Ship and satellite measurements.

Ship	Fig.1 code	Location °S °E	Time(Z) 13/9/1991	Bulk SST(K)	Skin SST(K)	ATSR SST(K)	MCSST (K)
<i>RV Franklin</i>							
	A	18.11 147.60	0930	298.05	-	297.86	297.1
	B	18.01 147.82	1300	297.85	297.70	297.70	297.4
	C	17.91 148.04	1600	297.85	-	297.20	297.4
<i>RV Lady Basten</i>							
	D	18.97 146.78	1300	296.55	296.01	296.10	296.0
	E	18.59 146.44	1600	296.75	-	296.80	296.6

## CONCLUSIONS

The comparison between the ATSR and AVHRR shows that both instruments can provide a good measurement of sea surface temperature. However the improvements in the design of the ATSR show the advantages of low noise detectors and increased digitisation levels for these type of data. Improvements in the absolute accuracy of the ATSR SST product are evident when the satellite products are compared to ground measurements. The dual view capability of the ATSR, and the improved on-board calibration, show that the SST can be retrieved from space with the accuracy required for climate studies. However, to gain full advantage from these accurate measurements a long data set is required, and the inclusion of ATSR-2 on ERS-2, and AATSR on ENVISAT, should ensure that such a data set will become available during the next decade.

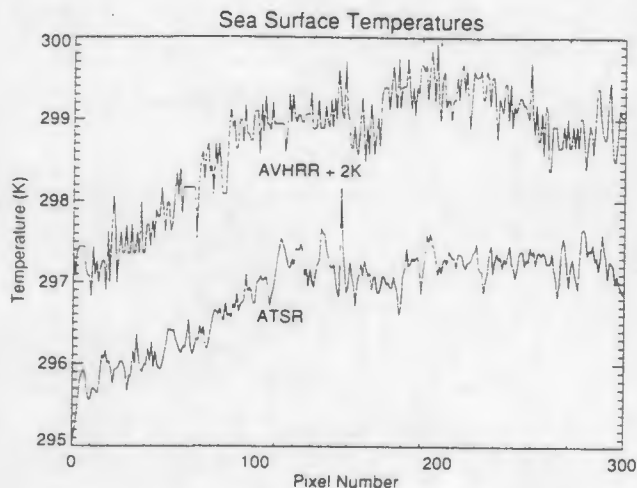


Fig. 5. Satellite-derived SSTs along the lines in Figures 1 and 2.

## 5. GROUND MEASUREMENTS

Two research vessels, fitted with infrared radiometers and in situ monitors of the bulk sea temperature, were in the area viewed by the ATSR during the night of September 13. The ship locations and their temperature measurements are given in Table 2. The ship locations are also shown in Figure 1. In this comparison the ATSR SST was derived using the full instrument capability (i.e. using all six "channels"). The ground data comparison shows one of the main differences between ATSR and AVHRR products. The ATSR algorithms have been derived theoretically and provide a measure of the skin temperature of the ocean. This is the radiative temperature that is measured using an infrared radiometer either from ship or from a space platform. In contrast the MCSST algorithm for the AVHRR data has been derived using a regression analysis between satellite and buoy data. The AVHRR thus supplies a measure of bulk temperature. Under normal conditions the skin temperature is 0.2 to 0.5K less than the bulk temperature and this effect can be seen in the ship data given in Table 2.

## ACKNOWLEDGEMENTS

The ATSR data are used by courtesy of the European Space Agency. The Rutherford Appleton Laboratory processed and provided the ATSR data products. The Australian Institute of Marine Science provided a berth on their research vessel, and the crews of both the FRANKLIN and the LADY BASTEN are thanked for their support.

## REFERENCES

1. Lauritson L. et al 1979, Data extraction and calibration of TIROS-N/NOAA radiometers, *NOAA Tech. Memo.*, 107, 73pp.
2. Delderfield J. et al 1986, The along track scanning radiometer (ATSR) for ERS-1. "Instrumentation for optical remote sensing from space", John S. Seeley, John W. Lear, Andre Monfils, Sidney L. Russak, Editors, Proc. SPIE, 589, 114.
3. Zavody A.M. 1993, The ATSR data processing scheme developed for the EODC, In Press *Int. J. Remote Sens.*
4. Barton I.J. 1989, Digitisation effects in AVHRR and MCSST data, *Remote Sens. Environ.*, 29, 87-89.

## PROSPECTS FOR GLOBAL CHANGE DETECTION WITH SATELLITE SST OBSERVATIONS

M. R. Allen<sup>1,2</sup>, M. J. Panter<sup>2</sup>, G. M. C. Blumberg<sup>3</sup>, C. T. Mutlow<sup>2</sup> and D. T. Llewellyn-Jones<sup>2</sup><sup>1</sup>Atmospheric, Oceanic and Planetary Physics, University of Oxford, Parks Road, Oxford OX1 3PU, U.K.<sup>2</sup>Rutherford Appleton Laboratory, Chilton, Didcot, OX11 0QX, U.K.<sup>3</sup>Dept. of Geography, Mansfield Rd., Oxford OX1 3TB, U.K.

## ABSTRACT

It is often claimed that precise, global observations of sea-surface temperature from satellite instruments such as the ATSR will assist in the detection of a possible anthropogenic global warming. But satellite data-sets are inevitably short (order 15 years), and the natural variability of the climate on these time-scales is high. This raises the question whether any ~15-year data-set may be directly relevant to the problem of global change detection. We use a detrended global mean SST from historical ship observations as a proxy for the natural interannual variability of the climate system, add linear trends to it, and test for the detectability of a trend in short segments of the artificial series so produced. With a warming rate of 0.025°C per year (the IPCC "best guess"), we find a >80% chance of detection after ~12.5 years, or ~11 years if the effect of El Niño can be removed. These figures assume complete confidence in observing system stability. Detection times depend critically on our ability to quantify, control and compensate for any drift in the observations.

Keywords: ATSR, Climate change, Trend detection.

## 1. INTRODUCTION.

If an anthropogenic change in the global climate is taking place, it is clearly important that it is detected and quantified as soon as possible. A key, although by no means the only, indicator of such a change would be to detect a significant rise in the global mean sea-surface temperature (SST). SST is a particularly attractive indicator because the thermal inertia of the oceans means they act to filter out high-frequency noise [17]. If we examine the historical record of global mean SST compiled primarily from ship-of-opportunity observations [2] (figure 1, dotted line), it does show a (statistically significant) warming trend. This warming is, however, far from

the approximately linear trend which most models indicate should result from the (approximately exponential) increase in carbon-dioxide concentrations observed over the past century. Moreover, quite elaborate *post hoc* quality controls must be applied to the historical database [6] to prevent longterm changes in observing methods from introducing spurious drifts. The sampling density on which the historical records are based also varies considerably, with large sections of the Southern Hemisphere virtually unobserved prior to around 1950.

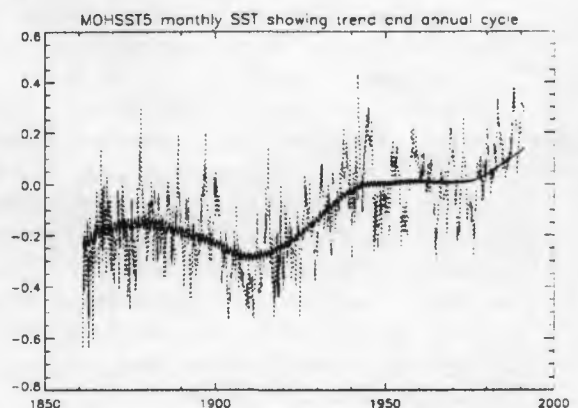


Figure 1: Dotted line: variations in global mean SST 1861-1992 from the MOHSST5 database of 5° × 5° monthly anomalies. Data provided by D. E. Parker and M. Jackson, UKMO. Averaging taken over all available grid-boxes, weighting by the cosine of latitude but not taking into account amount of land in a grid-box. Solid line: reconstructed >40-year variability and annual cycle. Anomalies have been expressed about the 1951-80 climatology: hence the small annual cycle near beginning of series.

While detailed studies of the effect of changes in sampling on historical records of the global mean temperature do not indicate any systematic bias [9], these problems inevitably reduce our confidence in attributing the warming trend in figure 1 to the enhanced greenhouse effect. Hence the interest in detecting trends in newly-available satellite-based

data-sets. These offer near-global coverage, with no significant hemispheric sampling bias. Comparison with accurate *in situ* observations also allows satellite data to be checked systematically for observing system drift. For example, *in situ* validation shows that an apparent warming trend in AVHRR data during the 1980s [15] can be attributed entirely to drifts in instrument characteristics and atmospheric effects [12]. Similar *in situ* validation is also possible to check recent ship-of-opportunity observations, but in this case global validation is complicated by the fact that different observations are not made by the same instrument, introducing possible systematic regional biases.

The ATSR has been developed specifically to measure SST with an accuracy of 0.5K ( $2\sigma$ ) on a  $0.5^\circ \times 0.5^\circ \times 1$ -day spatio-temporal resolution. The noise-reducing effect of averaging should mean that ATSR is capable of measuring a monthly global mean SST with an accuracy considerably better than 0.5K. The exact effect of averaging on confidence intervals depends, however, on the spatio-temporal structure of the fields under observation, making our absolute confidence in a monthly global mean SST measured by ATSR an important matter for further investigation. Two features of the ATSR facilitate effective validation against *in situ* observations. First, the retrieval algorithm [1] relies on a physical atmosphere model rather than on empirical, instrument-specific regression against *in situ* data, making ATSR-derived SSTs a genuinely independent data-set. Second, the instrument is relatively stable on short time-scales and (because of the dual view) much less sensitive than the AVHRR to regional variations in atmospheric composition, increasing our confidence that validation results based on a limited region may be applied globally.

Considerable interest has also arisen in the prospect of detecting a secular trend in data from the Microwave Sounding Units (MSUs) on the TIROS-n satellites. The MSUs may be stable enough for climate research [14], although they are measuring a parameter (tropospheric air temperature) which is inherently noisier (at a local level) than SST. The current length of the MSU dataset is almost 15 years, similar to the proposed length of the combined ATSR, ATSR-2 and AATSR datasets. Investigating evidence for trends in such datasets inevitably begs the question of whether we should *expect* to be able to detect a trend of the magnitude which models predict to be caused by greenhouse gases in this number of years of observations of the global temperature.

## 2. PREDICTED WARMING TRENDS AND NATURAL VARIABILITY.

The rates of warming which we may expect to be due to the enhanced greenhouse effect, assuming emis-

sions scenario A of IPCC 1992 [7], range from 0.015 to 0.04°C per year, with a "best guess" of 0.025°C per year, depending on the climate sensitivity (see figure Ax.2 in ref. [11]). Even with a perfectly stable and accurate observing system, two factors place a lower limit on the number of years required for such a trend to be detectable at a given significance level:

- Non-greenhouse-gas related century-time-scale variability, either natural or anthropogenic, may compensate for the warming due to greenhouse gases. Examples would include the cooling effect of sulphate aerosols (for which there is some evidence [3]) or any ultra-low-frequency climatic oscillation with a period of a century or more (for which there is little positive evidence, but cannot be excluded *a priori*).
- Natural sources of stationary climate variability, acting on time-scales of up to a few decades, introducing "noise" into the signal which may mask any warming trend.

The impact of century-time-scale variability can only be assessed through accurate modelling of all relevant climatic processes. The question amounts to whether the current generation of models take all relevant processes into account and have been adequately initialised. This is clearly a matter for climate modellers. The potential impact of shorter time-scale variability is also important, particularly for trend detection in relatively short datasets. This may be investigated empirically using past data on global temperatures.

The annual cycle and low-frequency (>40-year) component of the global mean SST, shown as a solid line in figure 1, have been reconstructed using a sliding-window data-adaptive filtering technique based on Singular Spectral Analysis [16]. We propose to use the residual stationary component (dotted minus solid lines) as a proxy for the natural <40-year time-scale climate variability which may be present in any satellite-derived time-series of global temperatures. An obvious objection to this approach is that this residual will also contain noise due to incomplete spatial sampling and observational errors in the historical database. Once data have been averaged to give a global monthly mean surface temperature, however, the magnitude of this type of noise may be quite small relative to natural sources of variability which would still be present even with a perfectly accurate observing system. In any case, we are not assuming that the historical record is completely reliable; simply that it adequately represents the statistics of <40-year climate variability. Supporting this hypothesis, simple statistics (variance and lag-1 autocorrelation) of the historical record do not change significantly from 1901 onwards, despite a considerable improvement in coverage and refinement of observational techniques. Prior to 1901 the data is

somewhat noisier, so we use only the most recent 90 years in this analysis.

Data based on remote sensing, moreover, contains its own sources of noise, such as atmospheric effects which have not been adequately characterised in the SST retrieval. The key advantage of satellite data is not so much in that it is less noisy than surface observations but that, compared with ship-of-opportunity data at least, it is much easier to quantify sources of error in satellite data, since all observations at a given time are taken with a single instrument.

### 3. TESTING FOR TRENDS WITH ADEQUATE NOISE MODELS.

Detecting a linear trend in a scalar series  $y_t$  amounts to testing (at a pre-defined confidence level) the null-hypothesis  $\mathcal{H}(b = 0)$  in the model:

$$y_t = a + bt + \epsilon_t \quad (1)$$

where  $\epsilon_t$  represents stationary processes contributing to  $y_t$ . If we confine attention to positive trends, then the null hypothesis becomes  $\mathcal{H}(b \leq 0)$ . If, rather than simply detecting *any* trend, we wish to use  $y_t$  to restrict the range of possible values of the climate sensitivity, then we test  $\mathcal{H}(b \leq b_1)$  and  $\mathcal{H}(b \geq b_2)$  to obtain lower and upper limits respectively for the rate of warming.

Crucial to any such tests are the properties of the  $\epsilon_t$  "noise" term, normally thought of as a stochastic forcing. In general, our model of the system is incomplete, and we have to use  $y_t$  itself to infer the properties of the noise term to use in the statistical test. If we have an adequate model of a stationary process contributing to  $\epsilon_t$  (such as the effect of El Niño on global temperatures, discussed below), the effect of that process can be removed, giving a new series,  $y'_t$ , to which we apply the trend-detection algorithms. If we have only partial knowledge of a component of  $\epsilon_t$ , this knowledge may be incorporated into the statistical test itself. It is very important to check, before concluding that a significant trend has been detected, that the assumptions regarding  $\epsilon_t$  used in the statistical test are actually satisfied by the residuals after the trend has been removed. An important example of how such assumptions can affect the power of statistical tests is the case of autocorrelation.

Consider the simplest form of autocorrelated noise, the AR(1) process:

$$u_t = \gamma u_{t-1} + \alpha z_t \quad (2)$$

where  $\gamma$  and  $\alpha$  are process coefficients, while  $z_t$  represents a unit-variance "white noise" (uncorrelated, gaussian distributed) forcing. The first term on the RHS represents the "memory" of the process. The lag-1 autocorrelation of an AR(1) process

( $\mathcal{E}(u_t u_{t-1})$ , where  $\mathcal{E}$  is the expectation operator) is equal to  $\gamma$ . This noise model is particularly relevant to the problem of trend-detection in SST and other large-scale climate parameters, because we do indeed have a situation where an effectively-white noise forcing (atmospheric weather) is applied to a system with inertia, and hence some memory (the ocean).

Failing to take autocorrelation into account can invalidate the results of statistical tests. For example, in an ensemble of 120-point segments of AR(1) noise (10 years of monthly data), with a lag-1 autocorrelation  $\gamma = 0.85$  (which is similar to that of the monthly global mean SST after the trend and annual cycle have been removed), ordinary least squares (OLS) regression indicates a warming trend, significant at the 97.5% level ( $\sim 2\sigma$  for a one-tailed t-test), in almost 30% of cases, even though this series is actually stationary. A similar proportion indicate a cooling trend. If the noise model were adequate, incorrect detection of the trend in such a series should, by definition, only occur in 2.5% of cases if we are testing at the 97.5% confidence level.

The Durbin-Watson test [5] allows us to check for the presence of autocorrelation in the residuals of a regression problem by calculating the following statistic

$$d = \frac{\sum_{t=2}^N (e_t - e_{t-1})^2}{\sum_{t=1}^N e_t^2} \quad (3)$$

where the  $e_t$  are the actual residuals after optimal regression parameters have been identified. In the analysis presented here,  $d$  was checked against a look-up table compiled from ref. [10]. Following standard procedure, the upper 5% critical value of  $d$  was used throughout as an indicator that OLS-based results were probably invalid. Unsurprisingly, the test indicates very clear evidence of autocorrelation in the detrended, deannualised monthly mean SST data, even after the El Niño signal has been removed (see below).

In data which contains AR(1)-type noise, almost unbiased estimates of the gradient  $b$  of a linear trend and confidence intervals for  $b$  can be obtained using estimated generalised least squares (EGLS) or maximum likelihood (ML) methods. Both are discussed in ref. [4]. Essentially, they involve fitting data to equation (1) with  $\epsilon_t$  replaced by  $u_t$  from equation (2) or, equivalently, finding the parameters  $a$ ,  $b$  and  $\gamma$  which minimise  $\sum_t e_t^2$  in

$$y_t - \gamma y_{t-1} = a(1 - \gamma) + b[t - \gamma(t - 1)] + e_t \quad (4)$$

In the ML case, the cost-function to be minimised is rather more complicated, but the principle is the same. If  $\gamma$  is known, the EGLS and ML estimates are exactly equivalent. If, as is generally the case,  $\gamma$  is unknown, then EGLS gives slightly less biased

estimates. EGLS is used here, although ML estimation was found to give very similar results in all that follows.

We then apply the Durbin-Watson test to the residuals  $e_t$  after optimal parameters have been found in equation (4). We find that, in general, the null hypothesis of no autocorrelation in these  $e_t$  cannot be rejected, indicating that the AR(1) model (unlike the white noise model assumed in OLS regression) is adequate to describe the detrended, deannualised, monthly SSTs both before and after the El Niño signal has been removed.

#### 4. RESULTS

Having decided on the estimation method to use, we generate artificial timeseries of global monthly mean SST which mimic that which might be observed by a satellite, as follows. We take the last 90 years of the detrended, deannualised monthly mean SSTs and add a linear trend with a specified background gradient,  $b_{true}$ . 11 values of  $b_{true}$  were tested, ranging from 0 to 0.05°C per year at 0.005°C per year intervals. We then extract as many  $n$ -month segments as possible from each 90-year (1080-month) artificial series, with the segment start points separated by an (arbitrarily chosen) 7 months. The segment length  $n$  ranged from 24 to 1080 months, in 3-month intervals. The fact that the segments overlap does not matter, because they are not assumed to be independent.

We test each  $n$ -month segment separately for the presence of a positive trend, using EGLS regression and a confidence level of 97.5% throughout. For each value of  $b_{true}$  and segment-length  $n$  tested, the proportion of  $n$ -month segments in which a significant positive trend is detected provides an estimate of the probability of detecting a trend in an  $n$ -month record if the actual trend in global SST really is  $b_{true}$ . For  $n \geq 360$  or so (30 years), the statistics become almost meaningless since the number of truly independent samples is so small. But the range we are interested in is 5–20 years ( $60 \leq n \leq 240$ ), where we do have a reasonable number of independent samples.

Figure 2 displays the results. For all background trend and segment-length combinations ( $[b_{true}, n]$  pairs) above the solid line, there is a  $\geq 50\%$  chance of detecting a significant positive trend at the 97.5% confidence level. Likewise, for all points above the dashed (dotted) line there is a 80% (95%) chance. Note that if  $b_{true}$  is 0.025°C per year (the IPCC "best guess"), we have an 80% chance of detection after 12.5 years with a perfectly stable observing system (point a). If the true trend is 0.015°C per year, we require 18 years for an 80% chance (point b).

If we have independent information on certain processes which are known to contribute to the global

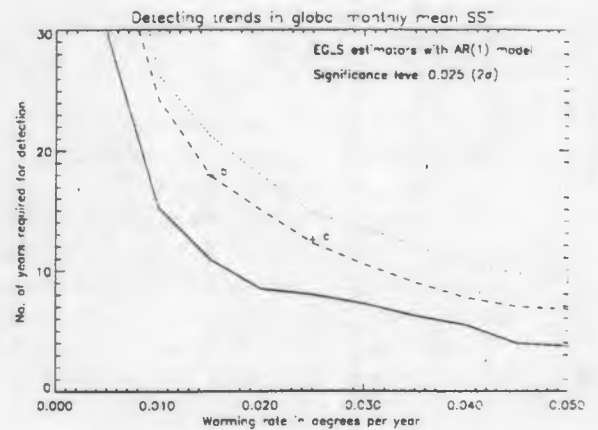


Figure 2: Probability of detecting a linear trend in detrended, deannualised monthly global mean SST with a linear background trend added to it, as a function of the true size of the background trend ( $b_{true}$ ) and the segment length available ( $n$ ). For all trend and segment-length combinations above the solid/dashed/dotted line, there is a  $\geq 50\%/80\%/95\%$  chance of detecting a significant positive trend at the 97.5% confidence level.

mean SST, the effect of these processes can be removed prior to analysis. An important influence on global temperatures on these timescales is the El Niño / Southern Oscillation phenomenon (ENSO). Following standard practice, we use the monthly mean Southern Oscillation Index (SOI) as a proxy for the state of ENSO. Jones [8] defines the SOI as the normalised difference in sea-level pressure between Tahiti and Darwin, with the individual station data themselves normalised and centered about their respective 1951–80 climatological annual cycles.

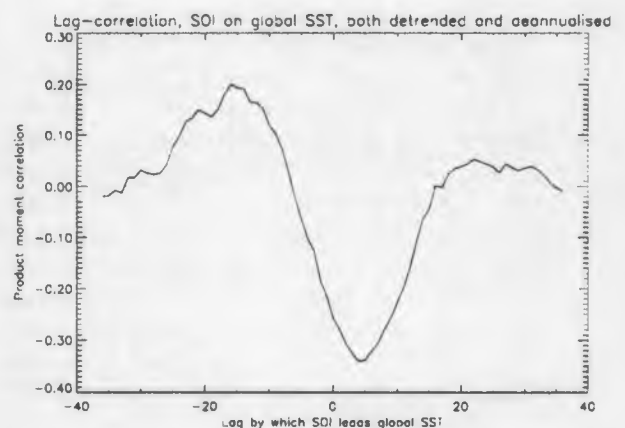


Figure 3: Product-moment correlation between detrended, deannualised global SST and monthly Southern Oscillation Index as a function of no. of months by which the SOI leads the SST series.

Figure 3 shows the correlation between a detrended, deannualised SOI (data kindly provided by P. D. Jones, CRU, East Anglia) and the global mean SST for a range of lags. The horizontal axis shows the

number of months by which the SOI leads the SST series. A clear negative peak is observed with the SOI leading the SST at 4–5 months, as noted by Jones [8].

We reconstruct the component of the global SST which is “explained”, in a statistical sense, by the SOI, using a regression model with an 11-month running mean detrended, deannualised SOI as the independent variable and the detrended, deannualised SST as the dependent variable, and with the SOI leading the SST by 4 months. We then subtract this “ENSO signal” from the SST series and repeat the analysis above to see if removing this variability improves our ability to detect secular trends in global temperatures. Figure 4 shows the result. There is some improvement: we now only need an 11-year data-set to have an 80% chance of detecting a positive trend given the IPCC’s “best” estimate of the rate of warming (point a).

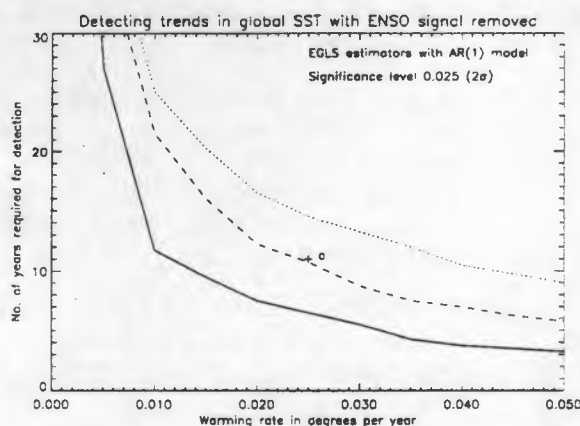


Figure 4: As previous figure but with ENSO signal removed from global mean SSTs by regression on an 11-month running mean SOI.

There will be some element of “artificial skill” in this improvement, since we have used the same data to construct the regression model on the 11-month running mean SOI as we subsequently use to test its impact on trend detection. The main point of figure 4 is to show that removing the ENSO signal from the global temperature record, if possible, is definitely worthwhile, but its impact is not dramatic.

So far, we have simply been addressing the question of whether *any* warming trend is detectable in global SST: in effect, whether the climate sensitivity to increased CO<sub>2</sub> levels is significantly different from zero. We can apply the same methodology to assess the number of years of data required to place upper and lower bounds on the rate of warming. Data requirements for lower bounds can be read off directly from figure 4. Instead of reading the horizontal axis as the absolute true warming rate, we can read it as the difference between the true warming rate and the lower bound which we wish to place on the warming

rate. Thus 11 years of data would be required, for example, for us to have an 80% chance of rejecting  $\mathcal{H}(b \leq 0.015^\circ\text{C per year})$  if the true warming rate was  $0.015 + 0.025 = 0.04^\circ\text{C per year}$ . In other words, with perfect observing system stability, 11 years would be required to begin to reject values of the warming rate at the lower end of the current uncertainty range if the warming rate is, in fact, at the higher end.

We have to repeat the analysis to assess the number of years of data required to place upper bounds on the rate of warming. Figure 5 is similarly calculated to the previous figure (i.e. ENSO signal removed) except that here we test the null hypothesis  $\mathcal{H}(b \geq 0.04^\circ\text{C per year})$ . We also need 11 years of data, with perfect observing system stability, to have an 80% chance of rejecting the values of the climate sensitivity at the upper end of the current uncertainty range if it is, in fact, at the lower end (point a). Had this number proved significantly different to that found in the previous paragraph it would have indicated that some stationary process was contributing to global temperatures which introduced a preferred direction in time, such as a saw-tooth wave. This would have clearly called into question the appropriateness of the AR(1) model and required further investigation. As it is, results are reassuringly symmetric.

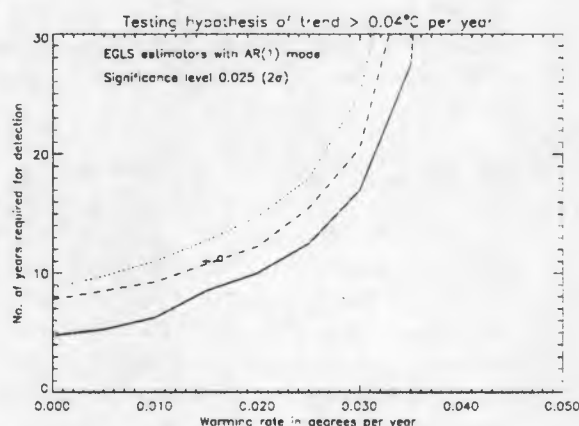


Figure 5: As previous figure but placing an upper bound on the rate of warming. Testing the hypothesis  $\mathcal{H}(b \geq 0.04^\circ\text{C per year})$ .

## 5. IMPACT OF OBSERVING SYSTEM STABILITY

The impact of uncertainty in the stability in our observing system on detection times can also be read off from figures 2, 4 and 5. If we can only be confident that the drift in the observing system is  $\leq 0.15^\circ\text{C per decade}$ , which is a very strong requirement, then the lines on figures 2 and 4 should be shifted by  $0.015^\circ\text{C per year}$  to the right. This implies that, with the ENSO signal removed, we would only have a 50% chance of rejecting  $\mathcal{H}(b = 0)$  with 11 years of data

if the true warming rate was  $0.025^{\circ}\text{C}$  per year – the current “best guess” value – and that we would have an 80% chance of rejection only if the true warming rate was  $0.04^{\circ}\text{C}$  per year – at the top of the current uncertainty range.

This clearly illustrates the importance of our being able to characterise and quantify any drift in the observing system. No presently-available instrument, either satellite-mounted or surface, can be expected to operate for 10 years delivering this level of stability. The only way we can begin to approach this level of confidence is through extensive cross-instrument validation and re-calibration campaigns.

## 6. IMPLICATIONS

This note has focussed on detection of trends in global mean SST. There are, clearly, other parameters which it would also be useful to monitor, not all of them directly related to temperature. Detection of the “correct” (model-predicted) pattern of change in a number of parameters (the “fingerprinting” technique) would clearly enhance our confidence in attributing a change to the enhanced greenhouse effect, but it has yet to be shown that such detection will necessarily take less time than the detection of a significant change in the global mean. Indeed, Santer *et al.* [13] find that the signal-to-noise ratios in centered detection statistics (i.e. those which do not depend directly on changes in global means) are generally lower than the S/N ratio in the global mean temperature.

Thus we conclude that natural, stationary sources of climate variability place a lower limit of 10–15 years on the length of a data-set for it to be useful for global change detection. Even a 10–15 year dataset will only be useful if quite stringent limits can be placed on observing system drift. These constraints are unlikely to be satisfied by any *unsupported* single instrument or array of similar instruments, indicating the need for intensive and continuous cross-instrument validation.

## References

- [1] I. J. Barton, A. M. Zavody, D. M. O'Brien, D. R. Cutten, R. W. Saunders, and D. T. Llewellyn-Jones. Theoretical Algorithms for Satellite-Derived Sea Surface Temperatures. *J. Geophys. Res.*, 94(D3):3365–3375, 1989.
- [2] M. Bottomley *et al.* *Global Ocean Surface Temperature Atlas*. H.M.S.O., London, 1990.
- [3] R. J. Charlson, J. Langner, H. Rodhe, C. B. Leovy, and S. G. Warren. Perturbation of the northern hemisphere radiative balance by backscattering from anthropogenic sulphate aerosols. *Tellus*, 43A-B:152–163, 1991.
- [4] M. H. A. Davis and B. B. Vinter. *Stochastic modelling and control*. Chapman and Hall, 1985.
- [5] J. Durbin and G. S. Watson. Testing for serial correlation in least squares regression ii. *Biometrika*, 38:159–178, 1951.
- [6] C. K. Folland and D. E. Parker. A physically-based technique for correcting historical sea surface temperature data. *Quart. J. Roy. Met. Soc.*, 1992.
- [7] J. T. Houghton *et al.*, editors. *Climate Change 1992, Supplement to the IPCC Scientific Assessment*. Cambridge Univ. Press, 1992.
- [8] P. D. Jones. *Climate Monitor*, 17:80–89, 1989.
- [9] T. R. Karl, R. W. Knight, and J. R. Christy. Global and hemispheric temperature trends: uncertainties related to inadequate spatial sampling. *J. Geophys. Res.*, 1993. submitted.
- [10] J. Kmenta. *Elements of Econometrics*. Macmillan, 2 edition, 1986.
- [11] J. F. B. Mitchell and J. M. Gregory. Climatic consequences of emissions and a comparison of is92a and sa90. In J. T. Houghton *et al.*, editors, *Climate Change, The IPCC Scientific Assessment*, chapter Annex, pages 173–175. Cambridge Univ. Press, 1990.
- [12] R. W. Reynolds, C. K. Folland, and D. E. Parker. Biases in satellite-derived sea surface temperature data. *Nature*, 341:728–731, 1989.
- [13] B. D. Santer, T. M. L. Wigley, and P. D. Jones. Correlation methods in fingerprint detection studies. *Climate Dynamics*, 1993.
- [14] R. W. Spencer and J. R. Christy. Precise monitoring of global temperature trends from satellites. *Science*, 247:1558–1562, 1990.
- [15] A. E. Strong. Greater global warming revealed by satellite-derived sea surface temperature trends. *Nature*, 338:642–645, 1989.
- [16] R. Vautard, P. Yiou, and M. Ghil. Singular Spectrum Analysis: a toolkit for short, noisy and chaotic series. *Physica D*, 58, 1992. to appear.
- [17] T. M. L. Wigley and T. P. Barnett. Detection of the greenhouse effect in the observations. In J. T. Houghton *et al.*, editors, *Climate Change, The IPCC Scientific Assessment*, chapter 8, pages 245–255. Cambridge Univ. Press, 1990.

## THE VALIDATION OF ATSR MEASUREMENTS WITH *IN SITU* SEA TEMPERATURES.

P. J. Minnett<sup>1</sup> and K. L. Stansfield<sup>2</sup>

<sup>1</sup>Oceanographic and Atmospheric Sciences, Brookhaven National Laboratory, P.O. Box 5000, Upton, N.Y. 11973-5000;

<sup>2</sup>Marine Sciences Research Center, State University of New York, Stony Brook, N.Y. 11794-5000

### Abstract

The largest source of uncertainty in the retrieval of SST (sea-surface temperature) from space-borne infrared radiometric measurements is in the correction for the effects of the intervening atmosphere. During a research cruise of the R/V *Alliance* measurements of sea-surface temperature, surface meteorological variables and surface infrared radiances were taken. SST fields were generated from the ATSR data using pre-launch algorithms derived by the ATSR Instrument Team (A.M. Zavody, personal communication), and the initial comparison between ATSR measurements and SST taken along the ship's track indicate that the dual-angle atmospheric correction is accurate in mid-latitude conditions.

Keywords: Infrared radiometry, ATSR, atmospheric correction, sea-surface temperature, shipboard measurements.

### 1. INTRODUCTION

During October and November, 1991, the NATO Research Vessel *Alliance* sailed from Amsterdam into the western Mediterranean Sea and during this time measurements were made for the validation of ATSR data. This reports the initial comparison between ATSR measurements and sea-surface temperatures (SSTs) taken along the ship's track by an *in situ* thermometer at a depth of about 3m.

### 2. ITINERARY

The ship sailed from Amsterdam on October 1 arriving at La Spezia on October 9. Apart from when the ship was in port from the 9 to 15 October, 18 October, and 21 to 24 October, measurements were made continuously until November 9.

The track of the ship for this period is shown in Fig. 1.

### 3. SHIP-BOARD INSTRUMENTATION

Measurements of sea-surface temperature, surface meteorological variables and surface infrared radiances were

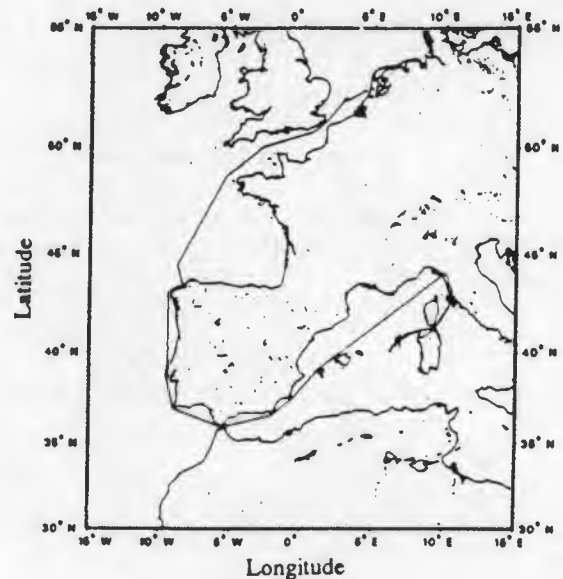


Figure 1. Track of the R/V *Alliance*, 1 October to 9 November, 1991.

taken by a set of instruments mounted on the ship and logged by computers.

The surface temperatures used here are from a Sea-Bird CTD (Conductivity-Temperature-Depth sensor) which was mounted through the hull so that it extended beyond the ship's boundary layer, at a depth of about 3m. It is acknowledged that these data are not ideal for the validation of ATSR as they may be decoupled from the true surface temperature by the skin effect and possible diurnal thermoclines, but at the time of writing they provide the temperatures in which I have most confidence. One minute averages of 1-second samples are used. At present, the data from the ship radiometer (R.A.L./S.I.L. type) are not ready for use, although it is anticipated that these will form the basis of a validation of ATSR using skin temperatures.

Atmospheric profiles of temperature and humidity were made using radiosondes, launched, when possible, so their ascents coincided with satellite overpasses when the sky was reasonably clear of cloud.

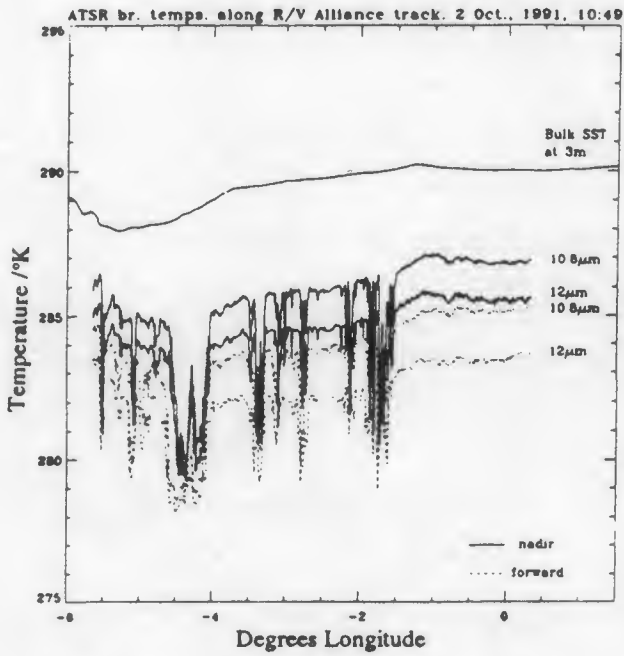


Figure 2. ATSR brightness temperature sections with the 3m *in situ* SST along the track of the ship for the image taken on October 2, 1991.

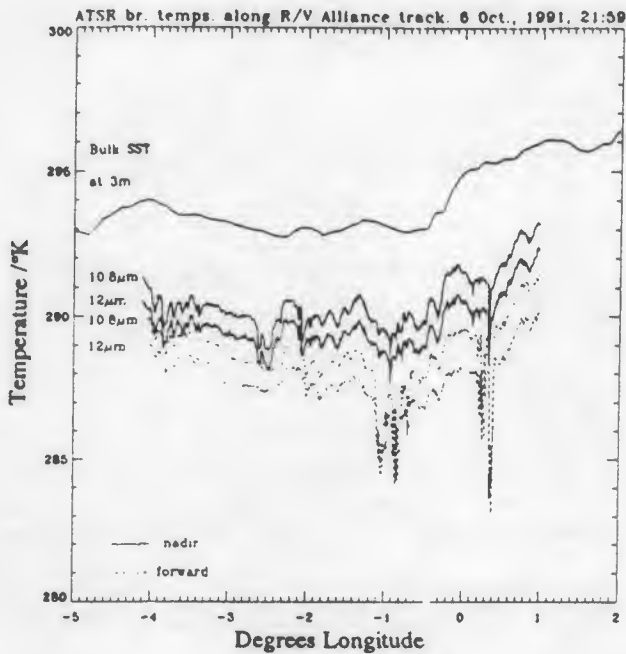


Figure 3. ATSR brightness temperature sections with the 3m *in situ* SST along the track of the ship for the image taken on October 6, 1991.

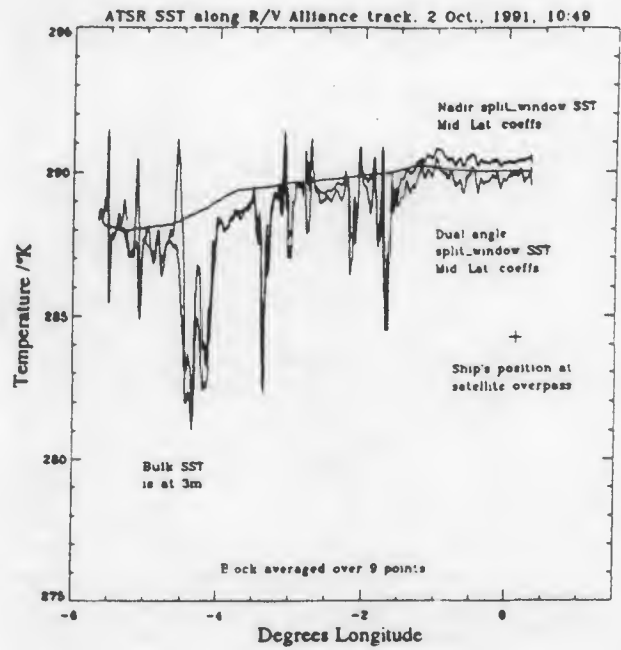


Figure 4. SSTs derived with the nadir split-window and dual-view split-window algorithms, smoothed by block averaging over 9 samples along the track. Mid-latitude atmospheric correction coefficients have been used. The 3m bulk temperature trace is also shown. The data are for the October 2 case.

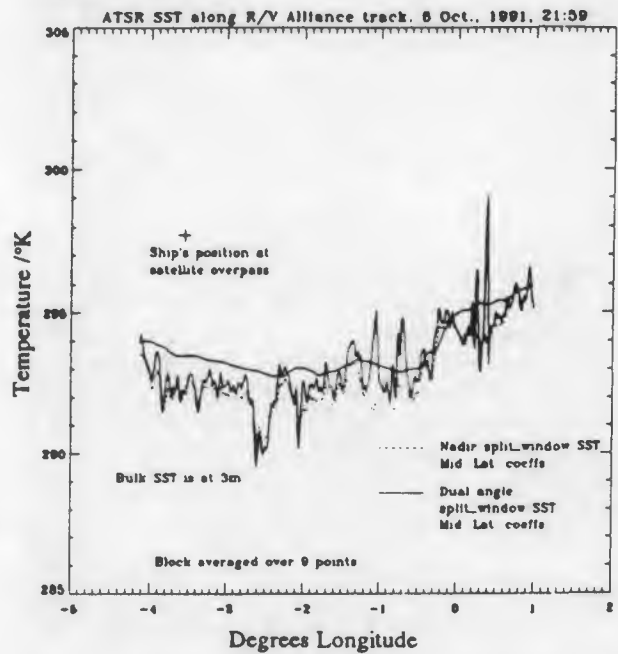


Figure 5. SSTs derived with the nadir split-window and dual-view split-window algorithms, smoothed by block averaging over 9 samples along the track. Mid-latitude atmospheric correction coefficients have been used. The 3m bulk temperature trace is also shown. The data are for the October 6 case.

temperature difference between the  $10.8\mu\text{m}$  and the  $12\mu\text{m}$  nadir measurements is comparable to that between the nadir and forward measurements at  $10.8\mu\text{m}$  (Figure 2). Towards the west the atmospheric conditions change and the  $10.8\mu\text{m}$  measurement becomes colder than that at  $12\mu\text{m}$  at nadir. Towards the east, the radiosonde launched from the ship shows that the atmosphere was anomalously dry at mid levels, between 1 and 2 km height. On October 6 (Figure 3), the brightness temperature difference between the  $10.8\mu\text{m}$  and the  $12\mu\text{m}$  nadir measurements is only about half of that between the nadir and forward measurements at  $10.8\mu\text{m}$ . The atmosphere was anomalously dry at higher levels, between 3 and 4 km height.

### 6.3 SST comparison

Comparison of ship SST and ATSR derived SST is encouraging. In the October 2 case, the split-window retrieval overcompensates the effect of the atmosphere and produces an SST retrieval that is warmer than the -3m bulk measurement (Figure 4). Given that the skin temperature is expected to be lower than the bulk temperature by a few tenths of a degree, the dual-angle SST retrieval looks to be very accurate indeed. The discrepancy between the two ATSR SST retrievals diminishes towards the west as the atmospheric conditions change. Note that the ship measurements can not be used to validate the satellite retrieval here because of the excessive time interval between the ship and satellite measurements. The comparison on October 6 does not show a clear advantage of the dual-angle retrieval (Figure 5).

The differences between the nadir-only and dual-angle SST retrievals can be significant (Table 1); it is presumed, but not demonstrated here, that the dual-angle retrieval is more accurate.

### 6.4 Noise levels in the SST fields

The nadir-only split-window SST images (not shown) are very clean and noise-free. The dual-angle split-window SST retrievals are significantly noisier than those derived from the nadir scans alone. This results from at least three effects: the SST is derived by the combination of four channels of information instead of two, and each channel contributes some noise to the retrieval; the coefficients in the dual-angle retrieval are larger than in the nadir-only retrieval and these magnify the noise levels; and the mismatch in the pixel sizes in the forward and nadir swaths. The last effect may be the most important, and is most readily corrected, as instead of mapping the forward view pixels into the nadir swath, which requires oversampling of the forward-view information, the nadir swath pixels could be mapped into the forward view image. Although this would lead to a loss of resolution it may reduce the noise level.

### 6.5 Effects of spatial averaging

Averaging the SST traces may produce a more stable estimate of the SST (Figure 6), but the standard deviation

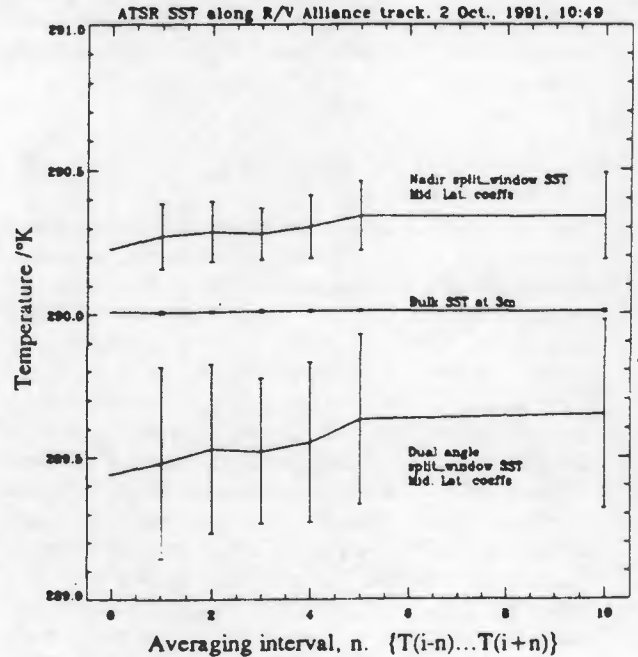


Figure 6. Effect on SST estimates of averaging along the track of the ship for the October 2 case. The error bars are the  $\pm$  one standard deviation in the averaging interval.

of the derived SSTs is consistently higher for the dual-angle retrieval compared to the split-window retrieval, by about a factor of two.

### 6.6 Effects of clouds

The effects of clouds are more pronounced in the dual angle retrievals. This is an inevitable consequence of the parallax in the forward view measurements.

## 7. CONCLUSIONS

The ATSR is performing well, and the atmospheric correction coefficients derived by Albin Zavody appear to function very well, although the sample presented here is too small to draw firm conclusions.

The inclusion of the information of the dual view in the atmospheric correction can result in changes in the estimate of the SST by over 0.5K. While it is presumed that the dual-view retrieval is more accurate, that cannot be demonstrated with this small data set. More comparisons must be made to confirm the benefits of the dual-angle atmospheric correction technique.

The variance of the SST in a given area is greater when the SST field has been derived using a dual-angle atmospheric correction, than that when using the nadir-only atmospheric correction.

Latitude, longitude, ship's speed, heading (gyrocompass reading) and course made good derived by the ship's navigation computer were archived at intervals of about one minute.

#### 4. ATSR ON ERS-1

The ATSR/M is a scanning four-channel infrared radiometer incorporating a two channel nadir-pointing microwave radiometer and is the first satellite instrument to have been designed for the accurate measurement of sea-surface temperature. (Refs. 1, 2). It uses the same infrared channels as the AVHRR (Advanced Very High Resolution Radiometer on the NOAA series of polar-orbiting satellites), but has a novel approach to the correction of the effects of the intervening atmosphere, in that the same 500 km swath of the ocean surface is measured twice through different atmospheric path lengths (Ref. 3). This information, coupled with the multichannel measurements, permits an improved atmospheric correction. In addition, rigorous pre-launch calibration (Refs. 4, 5), and improved internal black-body calibration targets (Ref. 6) enable a more accurate in-flight measurement, and detectors refrigerated to liquid nitrogen temperatures improve the signal to noise level.

#### 5. ATSR DATA

Six scenes of level 1.5 (brightness temperature) data were provided by RAL from the period of this cruise. Of these, only two contain the position of the ship, at the time of the satellite overpass, under clear skies. One of these is a daytime overpass (October 2), and the other is at night-time (October 6). Note that the time taken for the ship to complete the track across the image is nearly one day and comparisons must be restricted to that part of the ship's track close to the ship's position at the time of the satellite overpass (Ref. 7).

##### 5.1. Image navigation

The geographic location of individual pixels was calculated by bi-linear interpolation between the 25km grid provided in the image files. The accuracy of the grid was confirmed by overlaying coastal outlines; corrections were made where necessary.

##### 5.2 Atmospheric correction

The pixels along the position of the ship's track were sampled to extract the ATSR measured brightness temperatures in the nadir and forward views at 10.8  $\mu\text{m}$  and 12  $\mu\text{m}$ . Plots of these, as a function of longitude are shown together with the -3m SST in Figures 2 and 3. SSTs were calculated from these brightness temperatures using coefficients calculated by Albin Zavody (ATSR Project, Rutherford Appleton Laboratory, U.K.), for both the nadir swath multichannel split-window algorithm and the dual-angle multichannel algorithm. The coefficients as supplied were applicable to 50-km wide subswaths symmetrically

placed on each side of the sub-satellite track. These coefficients were used to generate values that change smoothly across the swath by a least-squares fourth-order polynomial fit. The resulting SST traces along the ship's track are shown in Figures 4 and 5.

Cloud free areas, about 50x50 km square, were selected in each scene and the differences between the nadir swath multichannel split-window algorithm and the dual-angle multichannel algorithm were calculated (Table 1). These are a function of the state of the atmosphere, and have mean values in excess of 0.5K. Drawing on the result of the comparison with the *in situ* measurements (see below), it is likely that the dual-angle multichannel algorithm produces a more accurate result.

Table 1. Discrepancies in SSTs between the nadir-only and dual-angle split-window retrieval in cloud-free areas.

Boundary of box	$\Delta\text{SST}$
pixels lines	mean $\pm$ 1 s.d.

October 2.

30: 89	150:209	0.670 $\pm$ 0.258
--------	---------	-------------------

October 6.

10: 59	230:279	-0.439 $\pm$ 0.441
110:159	110:159	-0.376 $\pm$ 0.213
260:309	150:199	-0.426 $\pm$ 0.215
235:284	245:294	-0.545 $\pm$ 0.276
370:419	180:229	-0.404 $\pm$ 0.230
450:499	420:469	-0.004 $\pm$ 0.325

#### 6. DISCUSSION

As a consequence of cloud cover, and also of the relatively narrow swath of the ATSR, the number of usable coincidences of satellite and ship data is distressingly small.

##### 6.1 General performance

The brightness temperature images are apparently free of instrumental noise. The temperature features observable in the ocean appear realistic and uncontaminated by instrumental effects.

##### 6.2 Brightness temperatures

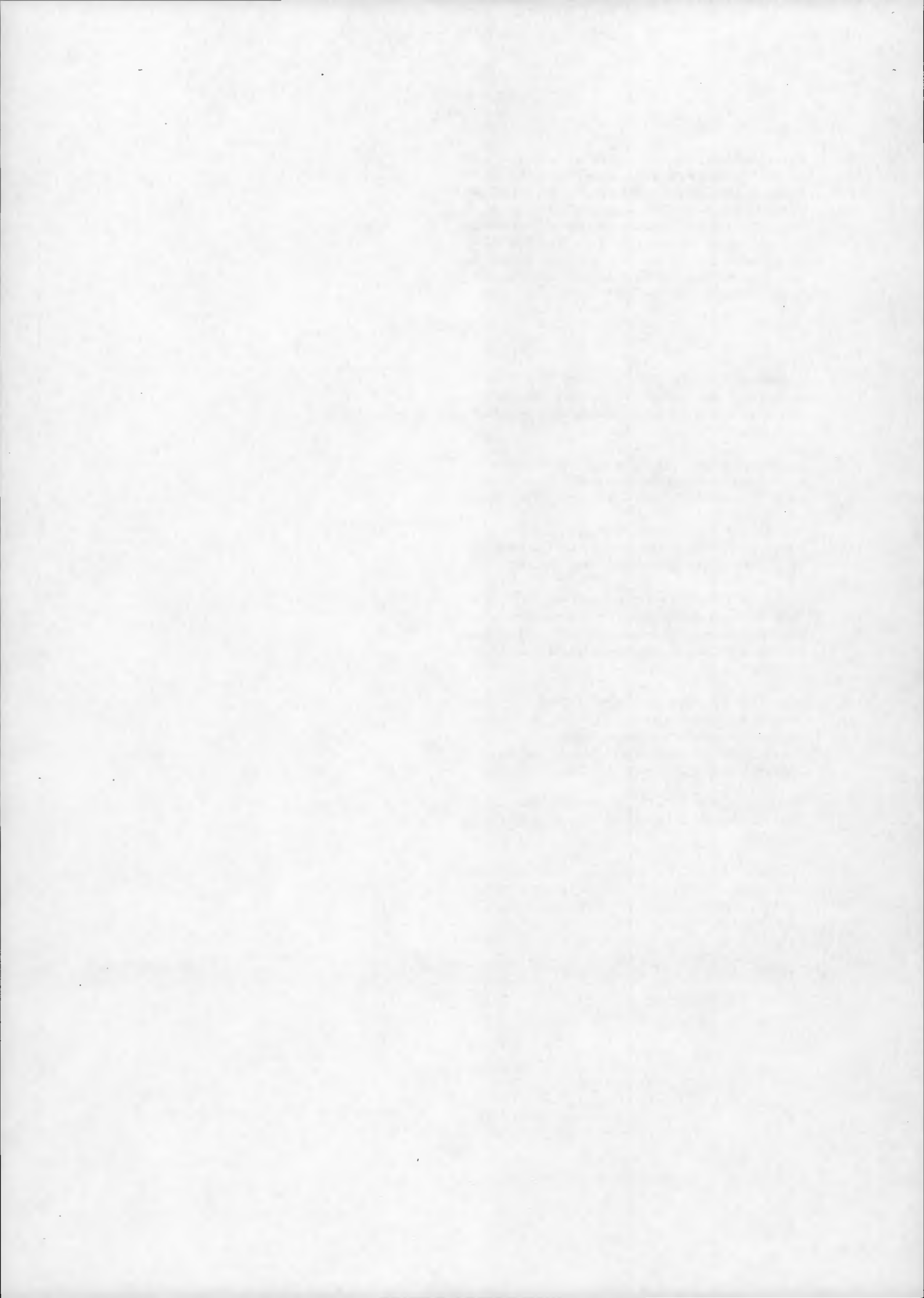
The traces of brightness temperatures along the ship's track appear to be entirely credible. The decreasing brightness temperatures with increasing wavelength and increasing atmospheric path length are as expected. The relative effects of the spectral brightness temperature gradient and the atmospheric path length gradient are different in the two cases reported here, due to the different atmospheric conditions on the two days. On October 2, the brightness

## 8. ACKNOWLEDGEMENTS

The support during the cruise of the ship's officers and crew and technical staff from the SACLANT Undersea Research Centre is appreciatively acknowledged. The ATSR data (©1991 by ESA and SERC) were provided by the ATSR Project Team at RAL. Support from the National Oceanic and Atmospheric Administration, Grant NA26GP0266-01, is acknowledged. This document was prepared under the auspices of the United States Department of Energy under Contract No. DE-AC02-76CH00016.

## 9. REFERENCES

- 1 Edwards T et al 1990, The Along Track Scanning Radiometer - Measurement of sea-surface temperature from ERS-1. *Journal of the British Interplanetary Society*, 43, 160-180.
- 2 Minnett P J 1993, The along-track scanning radiometer. In 'Oceanographic Application of Remote Sensing', edited by M. Ikeda and F. Dobson, C.R.C. Press. In the Press.
- 3 Prata A J F et al 1990, The Along-Track Scanning Radiometer for ERS-1 - scan geometry and data simulation. *IEEE Trans. Geoscience and Rem. Sens.*, 28,3-13.
- 4 Armitage S et al 1990, Test and calibration of the Along Track Scanning Radiometer (ATSR). *Proceedings of the International Symposium on Environmental Testing for Space Programmes - Test, Facilities and Methods*. ESA SP-304. 559-564.
- 5 Mason G 1991, Test and calibration of the Along Track Scanning Radiometer, a satellite borne infrared radiometer designed to measure sea-surface temperature. D. Phil. Thesis, Dept. of Atmospheric, Oceanic and Planetary Physics, University of Oxford, U.K.
- 6 Mason I M et al 1993, Black Body calibration sources of high accuracy for a spaceborne infrared radiometer. In preparation.
- 7 Minnett P J 1991, Consequences of sea surface temperature variability on the validation and applications of satellite measurements. *J. Geophys. Res.*, 96, 18,475-18,489.



# THE ALONG TRACK SCANNING RADIOMETER (ATSR) - GLOBAL VALIDATION RESULTS

C.T. Mutlow, D.T. Llewellyn-Jones and A.M. Závody

Rutherford Appleton Laboratory, Chilton, Didcot, Oxon., OX11 0QX  
UNITED KINGDOM

## ABSTRACT

Initial analysis of data from the Along Track Scanning Radiometer, launched in July 1991 on ERS-1, the European Space Agency's first remote sensing satellite, demonstrates sea-surface temperature can be measured from space with very high accuracy. The paper describes some early results from ATSR that provide quantitative evidence of the benefit of ATSR's 2-angle view of the Earth, its high radiometric performance and stable calibration targets. To assess data consistency an analysis of global SST data from ATSR was also carried out, whereby the ATSR global SST field was compared on a daily basis to the UK Meteorological Office's daily SST analysis field. The ATSR global field has been shown to be consistently within less than 1K of the analysis field - the night time data is typically within 0.3-0.4K of the UKMO analysis whereas the day time data is biased by about 0.8K. Further comparisons with drifting buoy will be described and possible interpretations of these differences are discussed.

Keywords: remote sensing, sea surface temperature, validation.

## 1. INTRODUCTION

The surface of the sea forms the boundary between the oceans and the atmosphere across which energy is exchanged between these two massive natural systems. SST is one of the most important geophysical parameters in climate studies, as the behaviour of the atmosphere is strongly coupled to the ocean temperature. Improved monitoring of this SST will lead to better understanding of short term climate anomalies such as El Niño and the Indian Monsoon, as well as enabling the early detection of the long-term warming which predictions show will be associated with the enhanced greenhouse effect.

With these facts in mind, the Along Track Scanning Radiometer (ATSR) was designed to provide observations of SST to the levels of accuracy now required for climate research (i.e. better than 0.3K). ATSR is an advanced infrared radiometer to measure the global sea-surface temperature from space, and to investigate the ultimate accuracy to which these measurements can be achieved using space-borne sensors.

ATSR was launched as part of the payload of ESA's ERS-1 satellite on 17th July 1991. Since 13th September 1991 when the instrument completed its in-flight commissioning period, ATSR has been producing high-quality thermal images and global gridded maps of sea-surface temperature.

There are three types of correlative measurements that are used that show the ATSR system (instrument plus ground processing) is achieving the appropriate level levels of accuracy. These are :-

1. comparison with ship-borne infrared radiometer measurements.
2. comparison with the UK Meteorological Office daily SST analysis.

3. comparison with SST measurements from the drifting buoy network.

This paper discusses the results from 2) and 3), validations that fall into category 1) are discussed in Ref. 1 and several other papers in the conference proceedings.

## 2. CALIBRATION AND VALIDATION

### 2.1. What are calibration and validation ?

The CEOS Working Group on Calibration and Validation have endorsed the following definitions:-

Calibration is the process of quantitatively defining the system response to known, controlled system inputs, whereas validation is the process of assessing by independent means the quality of the data products derived from the system outputs.

It should be noted that ATSR is a self-calibrating radiometer which measures the radiative temperature of a given scene against an absolute temperature reference (i.e. a pair of calibrated blackbody targets). The reliability and robustness of this calibration was established during extensive ground testing before the delivery of the ATSR instrument to ESA for launch.

The purpose of validation is to understand the physical reasons for any biases or significant disagreements in the ATSR data with respect to the *in situ* data, and to provide a correction for any mismatch based on this understanding. Therefore, the accuracy to which SST is retrieved from the ATSR brightness temperatures is a test of the quality of the atmospheric models used in the retrieval process, not of the calibration of the ATSR instrument.

### 2.2. Skin and bulk sea-surface temperature

The ATSR SST algorithms use theoretical models of atmospheric transmission to supply an estimate of the radiating temperature of the thin skin layer at the ocean surface. This skin temperature is usually less than that just below the surface due to radiative, conductive and evaporative cooling at the air-sea interface.

Previously, the operational algorithms for computing SST from other satellite data (i.e. AVHRR) have been derived by the regression of satellite-observed brightness temperatures to *in situ* data obtained by buoys. Satellite observations processed in this way are usually regarded as measurements of the bulk temperature of the ocean surface.

### 2.3. Validation of ATSR data products

The correct way to validate satellite skin temperature observations, such as those from ATSR, is by comparisons of the ATSR SST data with skin SST measurements from *in situ* infrared radiometers. The problem with this approach is, how-

ever, that these data are not available globally. Hence, the results from a limited number of dedicated *in situ* validation campaigns must be generalised through global quality assessments based on the observational fields of bulk temperature data.

The ATSR validation procedure is based on a series of dedicated validation campaigns using properly instrumented ships and aircraft, which have extrapolated globally using the available bulk observations. The following sections describe results from these global validation activities.

The ATSR data product that is validated in this study is the ATSR spatially-averaged SST data. This product is a  $\frac{1}{2}^\circ$  latitude-longitude average of the 1km resolution data record by the instrument.

### 2.3.1. Global Quality Assessment

Results from dedicated *in situ* validation cruises demonstrate the high accuracy in SST that ATSR can produce (see Refs. 1, 2 and 3 for instance). However, these data are only available over a very limited geographic region and we need to validate the ATSR data globally. This objective can only be achieved using a routinely available, high-quality global temperature data-set for comparison with the ATSR data. To provide this, the UK Meteorological Office's SST analysis (UKMOSST) field was used as the reference SST data-set for systematic comparisons with the ATSR spatially-averaged data.

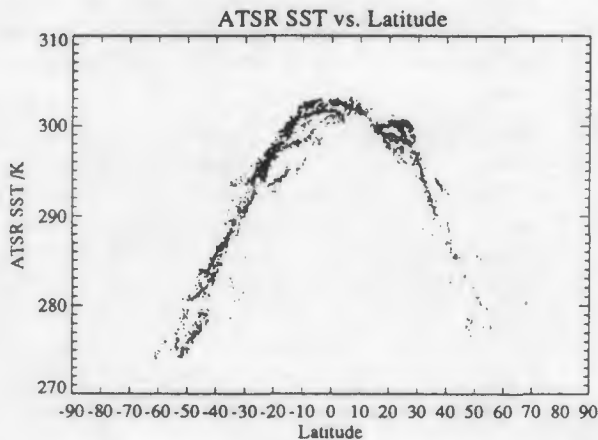


Fig. 1. ATSR Spatially-averaged SST data for the 28th April 1992 plotted as sea-surface temperature in Kelvin as a function of latitude.

The UKMOSST analysis is generated daily by the Meteorological Office from quality-controlled bulk SST observations (i.e. data from buoys, ships and XBTs). During the period chosen for study there was no satellite data in the SST analysis. The AVHRR MCSST data was excluded due to inability of this instrument, with a single nadir-only view, to provide an adequate correction for the anomalous atmospheric situation caused by the Pinatubo aerosol and still give accurate SST. With the sparse geographic coverage of bulk SST observations available from conventional sources, it is necessary for the analysis field to rely on climatological SST data from the historical analysis from Ref. 4.

Figures 1 and 2 show the SST data from the ATSR data and UKMOSST analysis, respectively, for 28th April 1992 plotted

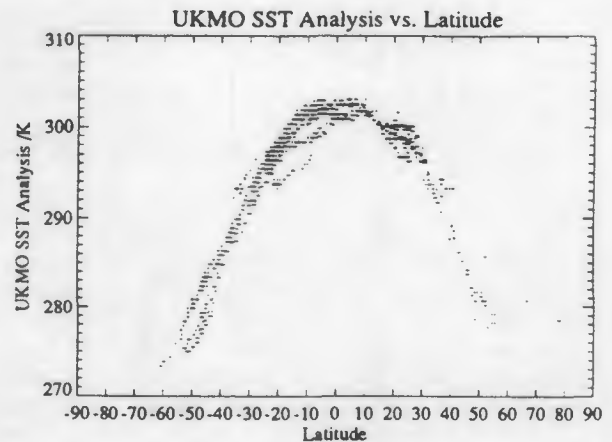


Fig. 2. UK Meteorological Office SST analysis for 28th April 1992 plotted as sea-surface temperature in Kelvin as a function of latitude.

as a function of latitude. Both plots reproduce the same broad features and show very similar detailed structure. The positions of the maximum and minima in the curves match closely, as do the absolute values of SST observed. The finer detail of the structure are also reproduced in both curves (i.e. the bifurcations in both hemispheres at high latitudes, the loops hanging down from the main curve between the equator and  $30^\circ\text{S}$  and the hump between  $20^\circ\text{S}$  and  $30^\circ\text{N}$ ). There are, however, a small num-

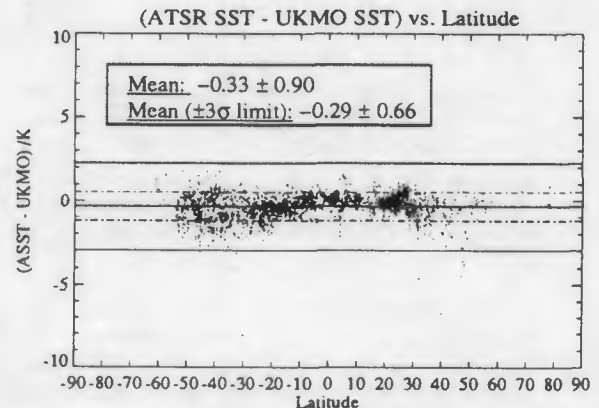


Fig. 3. Plot of the difference in the observed SST from the ATSR and the UKMO SST analysis as a function of latitude for the 28th April 1992. The dashed line is the  $\pm 1\sigma$  limit and the solid lines are the mean and the  $\pm 3\sigma$  limits, respectively.

ber of isolated cold values visible in the ATSR curve which are not seen in the UKMOSST curve. These values fall between 5–10K lower than the other SST values at the same latitude (e.g. the points beneath the main curve  $30^\circ\text{S}$ – $35^\circ\text{S}$ ). Investigation of these points shows that they result from small deficiencies in the ATSR cloud-clearing algorithm, which occur in regions where there are only a small number of SSTs contributing the  $\frac{1}{2}^\circ$  average. In these situations the effect of this small number of cloud contaminated SST values has a marked effect on the derived SST value, but they were easily rejected by applying a  $3\sigma$  filter to the data.

Figure 3 shows the difference between the data in figures 1 and 2 plotted as a function of latitude.

The global mean difference between the ATSR field and the UKMOSST is  $-0.29 \pm 0.66\text{K}$  for the 28th April 1992. This example is for a night time dual-view SST. The night time retrieval makes use of a three channel algorithm (i.e. 3.7, 10.8 and 12.0  $\mu\text{m}$ ), whereas the day time retrieval makes use of only the 10.8 and 12.0  $\mu\text{m}$  channel. Hence, the ATSR night time retrievals are more accurate. ATSR can also produce an AVHRR-like single view product which make use of the only the nadir view information from the instrument (this is the single view only SST data provided in the following tables).

The conclusions of a series of daily comparisons like the one shown in figure 3, but averaged over the month from 15th April 1992 to 15th May 1992 are shown in table 1. The data presented in this table require some explanation. Basically, the data consist of a tabulation of mean differences between the two SST fields (i.e. (ATSR SST - UKMOSST)) together with their standard deviations, negative values indicate that ATSR has produced an SST which is colder than the analysis. The results are presented separately for each of the four different ATSR algorithms (i.e. day single view, day dual view, night single view and night dual view). Column 1 is a key indicating whether the dual view or single view ATSR algorithm was used, column 2 the mean difference from the UKMO analysis and the associated standard deviation for night time observations, column 3 is the same as column 2 but for the day time observations, column 4 is the result of column 2 minus column 3 (i.e. the day/night) difference.

Algorithm type	Night SST Kelvin	Day SST Kelvin	Day-Night Difference
Dual view SST	$-0.33 \pm 0.7$	$-0.85 \pm 0.9$	-0.52
Single view SST	$-0.68 \pm 0.9$	$-0.89 \pm 0.9$	-0.21
Dual - Single difference	0.35	0.04	

TABLE 1. Results of Global comparisons of ATSR data with the UK Meteorological Office SST analysis for the period 15th April 1992 to 15th May 1992.

The results in this table reveal the advantages of along track scanning. For both the day time and the night time data the agreement with the UKMOSST is better for the dual view case than for the nadir view only.

The agreement between the UKMOSST and the ATSR data is closest for the night time data, and with the dual view data always producing the best result. The mean difference from 15th April - 15th May is  $-0.33\text{K}$  for the night time data (see table 1), this is colder than the analysis field. The deficit for the day time dual-view data is larger by approx.  $-0.5\text{K}$  with a value of about 0.85K cooler than the analysis.

The comparisons between the ATSR data and the UKMO data typically show a spread of  $\pm 0.7\text{K}$  at night and around  $\pm 0.9\text{K}$  during the day. At first sight this looks to be a poor result when compared to AVHRR which shows a scatter of  $-0.7\text{K}$  compared to buoy.

The local times of the ATSR observations are 10.40 am and 10.40 p.m. approx. The UKMO analysis is based on a climatology that is updated by the ship and buoy bulk temperature

observations collected throughout a 24 hour period. Thus in comparisons with these data there are implicit errors as it is not possible to separate the UKMO analysis into its day time and night time component. Studies at the UKMO using ATSR near-real-time data have also shown up other limitations in the data-set. There is consistent bias between the ship observations and the buoy data (see Ref. 5). The ship data is 0.1-0.5K warmer than the buoy temperatures with the buoy comparisons showing a standard deviation of approximately 0.5K (cf. 1.0K for ship observations).

However, it should be noted that the real spread in the ATSR comparisons is likely to be very much smaller than the values quoted above. The evidence for this is that the standard deviation of the daily mean bias computed by averaging the daily mean bias values for the study period is much less than 0.1K (cf. 0.7K computed from optimally combining the standard deviations from each day).

The fact that there are systematic errors in the comparison is not surprising, as it has not been possible to remove the effects of the variations of SST throughout the day in the way recommended by Ref. 6.

The principal reason for this consistent bias between the ATSR and the UKMOSST is because the UKMOSST field is derived from measurements of the water bulk temperature and the satellite, of course, measures the skin temperature. The differences found in this analysis are consistent with present understanding of the skin/bulk temperature difference, bearing in mind the the limitations of the analysis technique described above, and can be regarded as evidence of the consistency of ATSR's performance.

### 2.3.2. Comparisons with drifting buoy data

To improve our understanding of the results presented above, a limited study of ATSR spatially-averaged product against drifting buoy data has been undertaken for the period 15th April to 15th May 1992. It should be noted that although these comparisons are still of a bulk temperature to a skin temperature, more quality control can be applied to the data than was possible with the UKMO analysis fields.

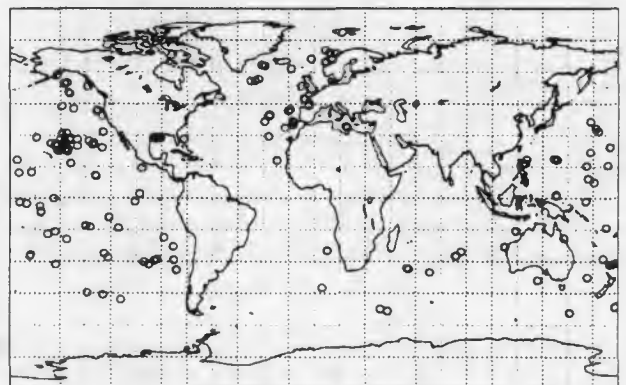


Fig. 4. Locations of the ATSR / Buoy coincidences for the case of night time dual view SST for the period 15th April to 15th May 1992 - 280 samples

The systematic errors were reduced by requiring that the coincident buoy data to be obtained within  $\pm 3$  hours of an ATSR overpass and at a position not more than  $\frac{1}{2}^\circ$  latitude or longitude away, following the recommendations of Ref. 6. The

drifting buoy data were provided by the UK Meteorological Office, together with extra information in the form of the differences in the buoy observations from the analysis field and climatology. These additional data were used to provide a further level of quality control. All the data from buoys that showed a consistently high bias with respect to the analysis and climatology fields were excluded from the comparison (this is a very similar procedure to that adopted by the UKMO in screening observations for inclusion into their analysis field). The quality control reduced the total number of coincidences by around 10%.

Figure 4 shows the locations of the successful buoy ATSR coincidences during the study period for the night time dual view SST. The results of the study for each of the ATSR algorithms

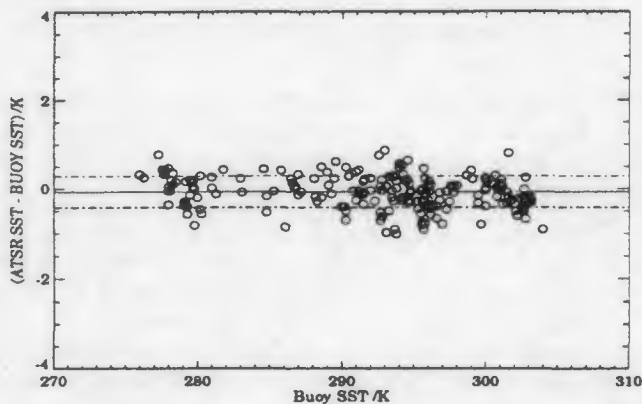


Fig. 5. Comparison of ATSR night time dual view SST with quality-controlled buoy data. All coincidences between 15th April 1992 and 15th May 1992- 280 samples.

Algorithm Type	Night SST Kelvin	Day SST Kelvin	Day-Night Difference
Dual view SST	$-0.07 \pm 0.35$ 280 samples	$-0.39 \pm 0.51$ 198 samples	-0.32
Single view SST	$-0.30 \pm 0.47$ 331 samples	$-0.56 \pm 0.50$ 336 samples	-0.26
Dual - single difference	0.23	0.17	

TABLE 2. Summary of the difference between ATSR and buoy SST for each ATSR SST algorithm. The last column is the day/night difference and last row is the single/dual view difference (dual view is warmer).

are summarised in table 3. The numbers presented in this table are the global mean of the difference between ATSR and the buoy SST field together with its standard deviation. The numbers in the last row and column of the table are the single view/dual difference and the day/night difference, respectively.

These results support the arguments offered in the previous section, and further demonstrate the capabilities of the ATSR instrument to deliver a high-quality SST product.

The dual view algorithm provides an improvement in retrieved SST of 0.2 to 0.3K over the single view algorithm. The RMS

errors of these comparisons show that the ATSR is delivering an RMS error in retrieved SST of less than 0.5K, just as it was designed to do. The noise in this comparisons seems to be dominated by the errors in the buoy data-set. The true RMS errors in the ATSR data are likely to be much less than these comparisons show and based on the *in situ* data radiometer comparisons described earlier is between 0.2 to 0.35K RMS error

Table 2 shows that the mean bias between the ATSR observations and the drifting buoy SST is between 0.1 and 0.3K at night time and between 0.4 and 0.6K during the day. These small relatively small differences can be explained in terms of the skin effect without having to invoke any other explanation.

### 3. SUMMARY OF RESULTS

The data discussed in the previous sections must be regarded as preliminary at this stage as the ATSR retrieval algorithms are still being developed and refined. Furthermore, to confirm these results a much more detailed and long-term analysis will be required. The ultimate quality of the ATSR data will depend on an extensive set of *in situ* radiometric measurements of SST under representative geographical areas and meteorological conditions. Such work forms part of an ongoing programme of validation for the ATSR instrument, further results from which are discussed in Refs. 1,2,3 and 7.

The comparisons with drifting buoy data show that ATSR is capable of generating very high-quality dual-view SST data with a mean bias with respect to drifting buoy data of  $-0.07K$  and an RMS deviation of 0.35K.

The day time dual-view algorithm, which only uses data from the 10.8 and 12.0 $\mu$ m channel, supported by cloud information from the 1.6 $\mu$ m channel, provides data with a mean bias of  $-0.4K$  and an RMS error of 0.5K. These data are of comparable quality to the night time single view data which are obtained using brightness temperatures from all three of ATSR's thermal infrared channels. This clearly demonstrates the benefit of the dual view, and shows that the addition of the forward view information to the day time retrieval provides an improvement in the SST retrieval similar to the addition of a third thermal channel to the two channel retrieval.

The night time dual-view SSTs are ATSR's highest quality data product. These data are produced using the maximum possible number of ATSR observations, as they are computed using the three-channel, dual-view algorithm (i.e. all six brightness temperatures). As expected, the instrument's worst results are the day time single view SST values computed using the two-channel, single-view algorithm (i.e. two brightness temperatures).

In the course of this study it has become clear that "along track scanning" provides a two-fold advantage in SST determination. The first of these advantages is the obvious one of the improved atmospheric correction resulting from the two different atmospheric path lengths in the forward and nadir view. The second advantage is less obvious and results from the ability of the ATSR's forward view, with its increased optical path through the atmosphere and increased size, to detect thin clouds and the edges of large clouds that are not obvious in the nadir view.

The present results show for the conditions prevailing at the time of these observations, the "along track scanning" provided additional information about atmospheric conditions

and cloud cover which can allow SST to be measured from space to an accuracy within 0.3°C of the *in situ* measurements.

Further refinement of the ATSR algorithms is now in progress; these include improvements in the cloud clearing algorithm, retrieval of water vapour and the development of more physically-based algorithms for SST determination that maximises the benefits of along track scanning.

#### 4. ACKNOWLEDGEMENTS

The Along Track Scanning Radiometer was provided to the European Space Agency by a consortium consisting of Rutherford Appleton Laboratory, Mullard Space Science Laboratory, Oxford University, UK Meteorological Office with contributions from Australia and France.

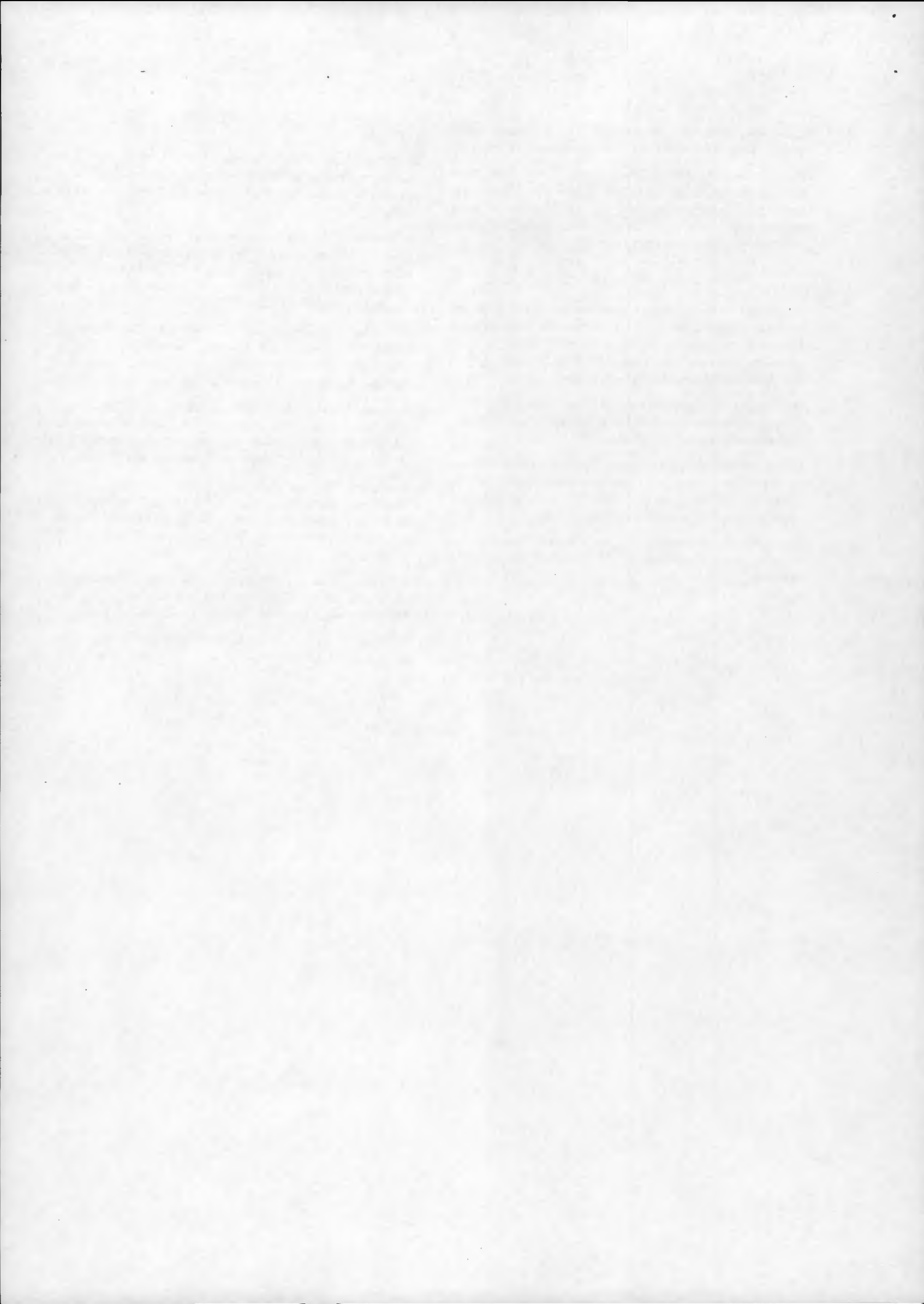
The work of the engineering teams at the collaborating institutes, who designed and built the ATSR instrument, is gratefully acknowledged by the authors.

The authors are also indebted to the UK Meteorological Office for supplying them with a globally representative set of radiosonde profiles, for access to their SST analysis fields, and for providing the drifting buoy data-set.

The ATSR data are copyright by the European Space Agency and are provided courtesy of SERC/Rutherford Appleton Laboratory.

#### 5. REFERENCES

1. Barton, I.J., C.T. Mutlow, A.M. Závody and D.T. Llewellyn-Jones, *Intercomparison of AVHRR and ATSR Data Products*, Proceedings ESA ERS-1 Conference Hamburg, 1993.
2. Forrester, T.N., P.G. Challenor and T.H. Guymer, *Validation of ATSR Sea Surface Temperatures near the Faroes*, Proc. of the 1st ERS-1 Symposium, SPACE AT THE SERVICE OF OUR ENVIRONMENT, Cannes 4-6th November 1992, ESA Publication SP-359, Vol. II, 807-811, 1993.
3. Mutlow, C.T., D.T. Llewellyn-Jones, A.M. Závody and I.J. Barton, *The Along Track Scanning Radiometer (ATSR) on ESA's ERS-1 Satellite — Early Results and Performance Analysis*, Submitted to J. Geophysical Research, 1993.
4. Bottomley, M., C.K. Folland, J. Hsiung, R.E. Newell, and D.E. Parker, *Global Ocean Surface Atlas*, Joint Project of the UK Meteorological Office and Massachusetts Institute of Technology, 20 pp, 313 plates, published by HMSO, 1990
5. Harrison, D.L. and C.P. Jones, *A User Appraisal of ATSR Near-real-time Products*, Proc. of the 1st ERS-1 Symposium, SPACE AT THE SERVICE OF OUR ENVIRONMENT, Cannes 4-6th November 1992, ESA Publication SP-359, Vol. II, 791-795, 1993.
6. Minnett, P.J., *Consequences of Sea Surface Temperature Variability on the Validation and Applications of Satellite Measurements*, J. Geophys. Res., 96, 18,475-18,489, 1991.
7. Mutlow, C.T. et al., *Validation Review Paper* in Preparation for submission, 1993..



The satellite integration started in January 1994. After payload and platform coupling, a series of electrical tests, including hardware/software compatibility and a system validation test with ESOC, were performed. Prior to the environmental test, the propulsion subsystem was checked for leak-tightness.

Vibration and acoustic testing were then carried out to demonstrate, successfully, that the ERS-2 satellite would not be adversely affected by the vibration and noise induced by the launch vehicle. That was followed by a deployment test, under onboard software and under ESOC control, of the SAR, the Scatterometer and the Microwave Radiometer antennas using special 'zero-gravity' rigs to simulate a realistic deployment.

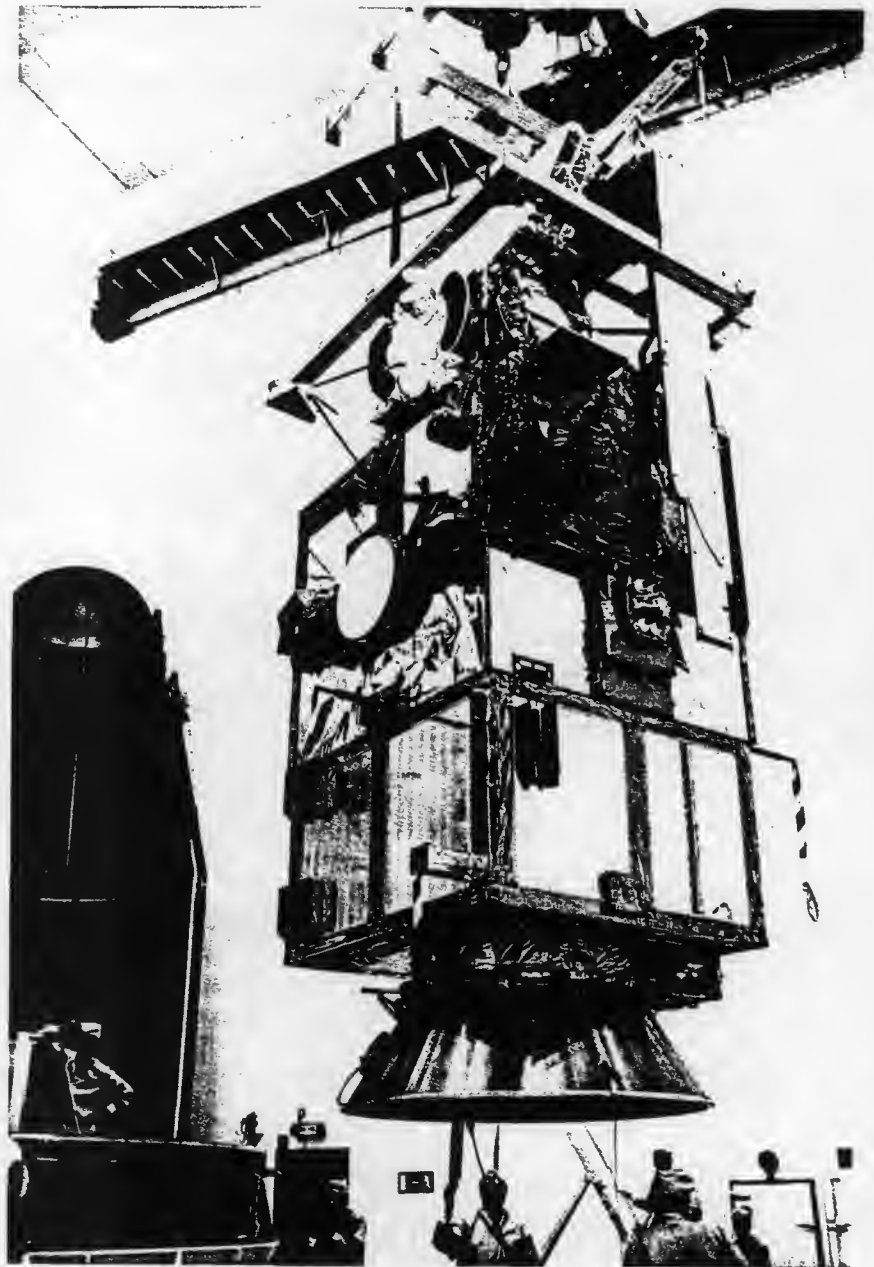
The satellite assembly, integration and test (AIT) activities concluded with a full functional performance test and a rehearsal of the launch site procedures in August 1994. The AIT programme was completed exactly on the date that had been originally planned at the beginning of the ERS-2 programme in 1990.

Following the flight acceptance review, the flight hardware and the associated ground support equipment were prepared for shipment to the launch range in Kourou, French Guiana. Five sea containers and two dedicated 747 cargo flights were used to transport the equipment to the launch site.

ERS-2 was planned to be launched on Ariane flight V72 in January 1995. The launch campaign started on 14 November 1994. After the set-up of the check-out equipment, the satellite mechanical preparations and the alignment, a post-transport functional performance test was performed. Immediately before the end of that test, on 30 November, however, the launch of Ariane flight V70 failed. The post-transport test of ERS-2 was completed but the satellite then had to be placed in storage until the preparations for flight V72 could be resumed. The satellite was protected by a dedicated tent, which was purged and the ambient conditions inside the tent were permanently monitored.

The launch campaign was interrupted for two months, from 19 December 1994 to 17 February 1995. Only a small 'babysitter' team remained in Kourou.

In February 1995, the campaign resumed with a short functional test, the integration of the solar array and the preparation for fuelling.



After further delays due to hydrogen and oxygen leaks in the third stage of the Ariane V71 launch vehicle, ERS-2 was transferred to the filling and encapsulation hall. Finally, on the night of 20 April 1995, ERS-2 was successfully launched.

**Figure 22. ERS-2 being prepared for encapsulation in the Ariane V72 fairing**

## ATSR-2: The Evolution in Its Design from ERS-1 to ERS-2

**N.C.M. Stricker & A. Hahne**

ESA Directorate for Observation of the Earth and Its Environment, ESTEC, Noordwijk, The Netherlands

**D.L. Smith, J. Delderfield, M.B. Oliver & T. Edwards**

Space Science Department, Rutherford Appleton Laboratory, Didcot, UK

The Along-Track Scanning Radiometer, or ATSR, was developed for the ERS-1 mission as an Announcement of Opportunity package by the United Kingdom and France. It consists of a four-band Infrared Radiometer (IRR) to measure the Sea Surface Temperature (SST), and a Microwave Radiometer (MWR) to measure the integrated (vapour and liquid) atmospheric water content. The IRR was developed by Rutherford Appleton Laboratory (RAL, UK) and the MWR by the Centre de Recherche en Physique de l'Environnement Terrestre et Planetaire (CRPE, F).

For the ATSR-2 on ERS-2, the IRR has been upgraded by adding three more bands in the visible part of the spectrum to provide data for vegetation studies (Fig 1). The MWR is identical to that used on ERS-1, but is provided by a different industrial contractor, namely Schrack Aerospace of Austria.

### The ATSR instrument on ERS-1

The IRR, an imaging radiometer equipped with four infrared channels operating at wavelengths of 1.6, 3.7, 11 and 12 microns, scans two 500 km swaths across the satellite's ground track, one being the nadir view and the other 800 km forward (47° with respect to the nadir) along the ground track (Fig. 2). Successive swaths are displaced by 1 km due to the satellite's orbital motion.

A rotating mirror scans the two tracks once every 150 ms, each scan being subdivided into 2000 pixels (each equivalent to 75 microsec), 555 of which contain nadir-view data and 371 forward-view data. The infrared

Figure 1. A 512 x 512 km section of the tropical rain forest in Rondonia (western Brazil), as seen by ATSR-2. This image combines three channels from ATSR-2, at 0.55  $\mu\text{m}$  (extracted as blue), 0.67  $\mu\text{m}$  (green) and 1.6  $\mu\text{m}$  (red). The regularly-shaped, pale cream patches are areas where the rain forest has already been felled

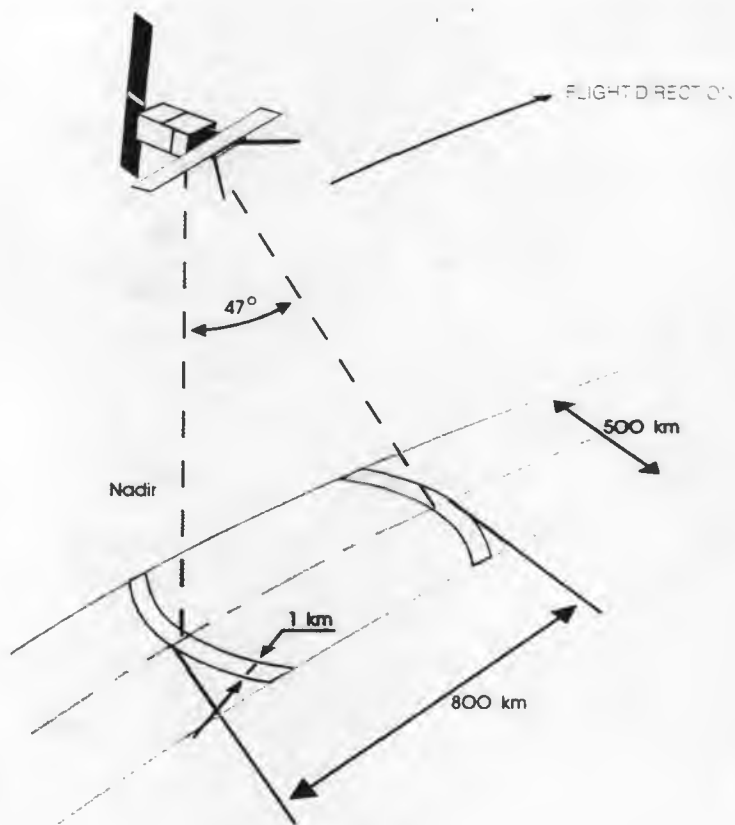


channels and associated electronics are calibrated using two black bodies, one hot and one cold, located in the path of the scanning mirror.

With the 555 pixels in the nadir view, a resolution of the order of 1 km x 1 km can be achieved. Averaging over 50 km x 50 km gives an absolute accuracy of better than 0.5 K in sea-surface temperature, assuming that 20% of the pixels within the area are cloud-free. For cloud-free pixels of 1 km x 1 km, the relative accuracy is about 0.2 K.

The scanning mirror directs the incoming radiation to an off-axis paraboloidal mirror (Fig. 3). A field stop positioned at the focus of the instrument determines the field of view. Beyond this field stop, the beam diverges into the Focal-Plane Assembly (FPA), where it is spectrally divided into four infrared channels. Three of the component beams, corresponding to the 3.7, 11 and 12 micron bands, are re-imaged by three off-axis ellipsoidal mirrors onto separate detectors. An aspherical zinc-sulphide lens re-images the fourth beam (1.6 micron) onto its detector (Fig. 4). Photoconductive cadmium-mercury telluride detectors are used for the 11 and 12 micron channels, and indium-antimonide photodiode detectors for the 1.6 and 3.7 micron channels.

A Stirling-cycle cooler keeps the Focal-Plane Assembly at 80 K, to provide the required low-noise performance for the detectors. Eight onboard pixel maps allow the selection and compression of IRR pixels for eight different data sets. After formatting, the



data are collected by the Instrument Data-Handling and Transmission Unit (IDHT) and transmitted to ground via the X-band link.

**Figure 2. Measurement principle of the Along-Track Scanning Radiometer (ATSR)**

The MWR instrument uses a 60 cm Cassegrain offset-fed antenna to view the Earth in the nadir direction at frequencies of 23.8 and 36.5 GHz. The signals received are compared with that from the reference source at a known temperature in order to minimise the effects of

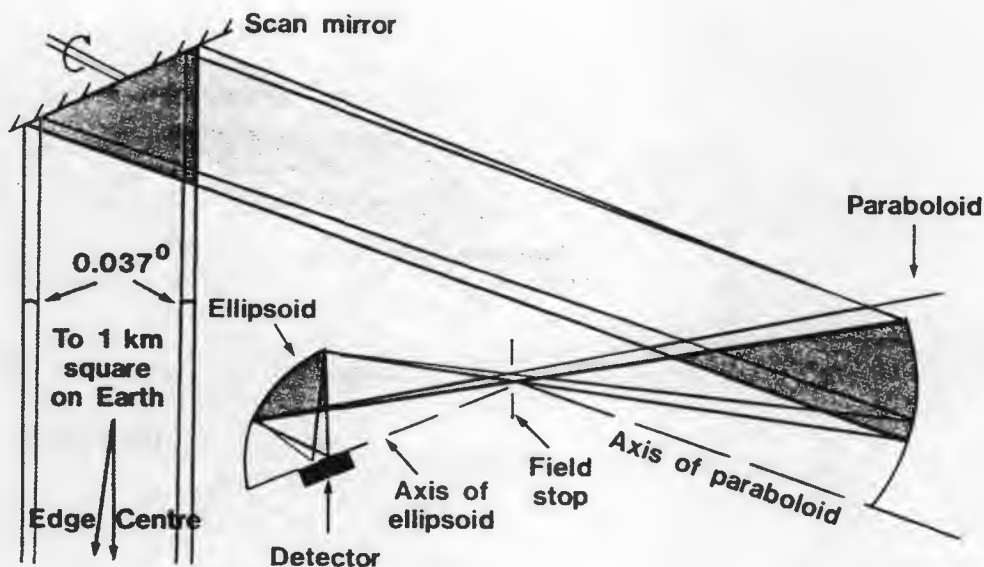
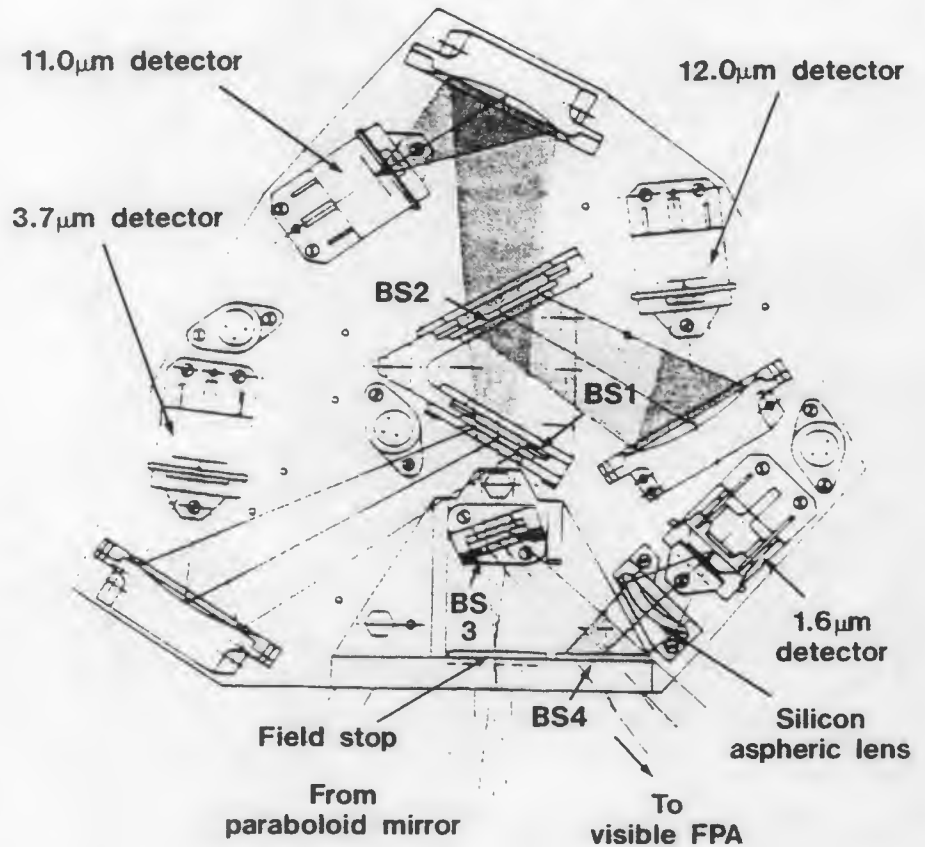


**Figure 3. The arrangement of the ATSR's optical components**

Figure 4. The optical layout of the Infrared Focal-Plane Assembly (IRFPA) for ATSR-2



short-term variations in the receiver-chain gain. To calibrate the MWR, additional features are used: the sky-horn antenna is pointed towards the very low cosmic background radiation of deep space at about 4 K for 'cold reference' measurements, while the 'hot reference' is obtained from measurements within the instrument itself.

by adding of a second Focal-Plane Assembly, with the constraint that it was not to impact adversely on the existing channels.

Figure 5. The optical layout of the Visible Focal-Plane Assembly (VFPA) for ATSR-2

**The ATSR-2 instrument on ERS-2**

In the ATSR aboard the ERS-2 mission, three additional visible channels are accommodated

The Infrared Focal-Plane Assembly (IRFPA) on ERS-2 differs somewhat from that on its predecessor ERS-1. The mirror used to reflect radiation into the 1.6 micron detector has been replaced by a dichroic beam-splitter. This allows the visible beam to pass out of the IRFPA (Fig. 4), via a sapphire window and radiation-resistant doublet relay lens, and enter the

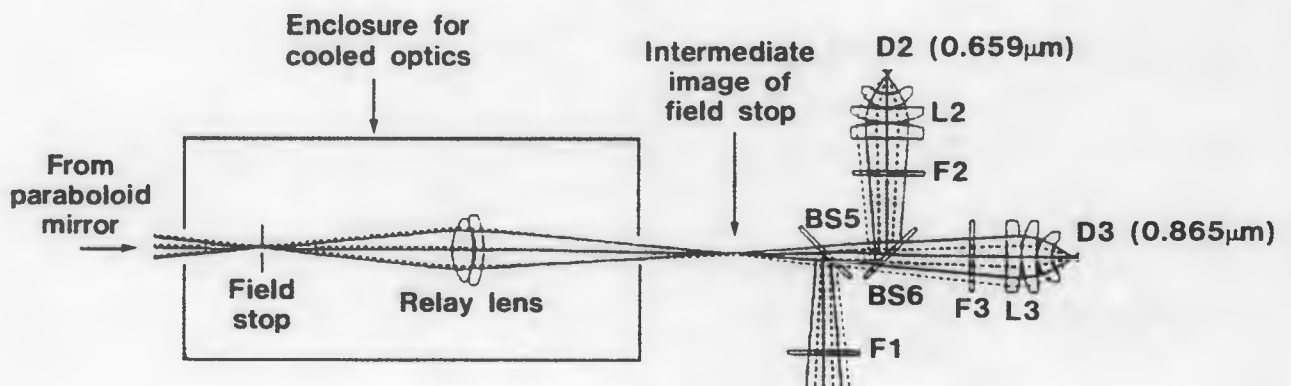


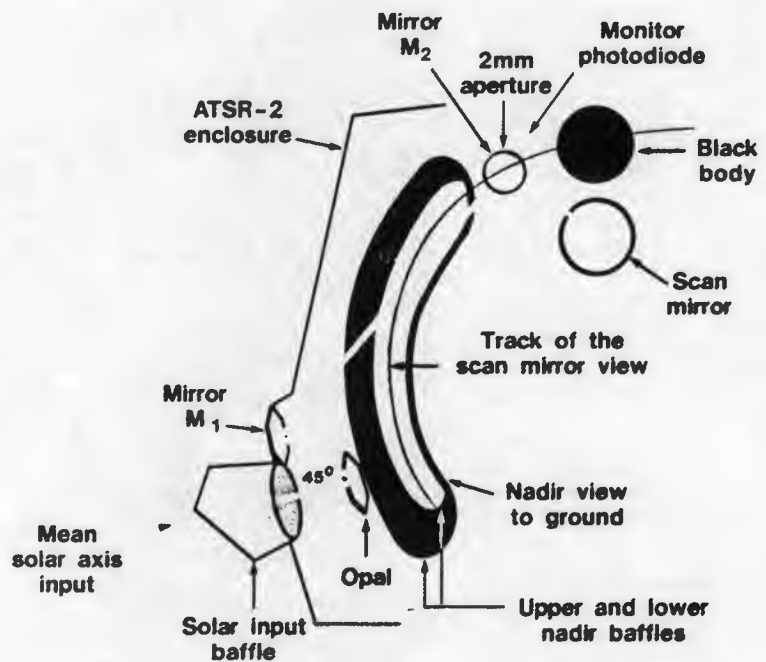


Figure 6. This ATSR-2 image, recorded on 8 May 1995 over Central Italy and Sicily, is a false-colour composite, compiled from the uncalibrated data in the 0.67  $\mu\text{m}$  (as a blue extract), 0.87  $\mu\text{m}$  (green) and 1.6  $\mu\text{m}$  (red) spectral channels

Figure 7. Optical components of the visible calibration system

Visible Focal-Plane Assembly (VFPA, Fig. 5). There the beam is split into three, using dichroic beam splitters, before being focussed by zinc-sulphide triplet lenses onto the visible-channel detectors. The centre wavelengths of these three channels are 0.555, 0.659 and 0.865 microns, respectively.

The visible channels are calibrated with a Visible Calibration Unit, as shown in Figure 7. The opal MS20 diffuser, located behind the solar input baffle and radiation-resistant glass window, is illuminated by the Sun during some parts of ERS-2's orbit. Mirror M1 reflects the diffuse beam onto the plane mirror M2, located between the nadir view and one of the black-body units in the path of the scanning mirror. The size of the M2 mirror determines the aperture stop in this calibration system, adding 16 visible-calibration pixels to the ATSR-2 data stream. Calibration takes place close to the time of local satellite sunset, when the Sun is  $13^\circ$  below the tangent to the Earth's surface at the satellite's nadir point. The nadir- and forward-viewing baffles are designed to exclude stray radiation from entering the



calibration system, which would degrade its accuracy.

Three new amplifiers have been added to the pre-amplifier unit to cope with the three visible channels on ATSR-2, and three corresponding Single Channel Processors have been incorporated into the electronic system.

The increased data flow on ATSR-2 called for a new set of data-compression algorithms. In addition, uncompressed infrared and visible data can be transmitted in a high-data-rate mode, which provides double the normal throughput. This mode is limited, however, to

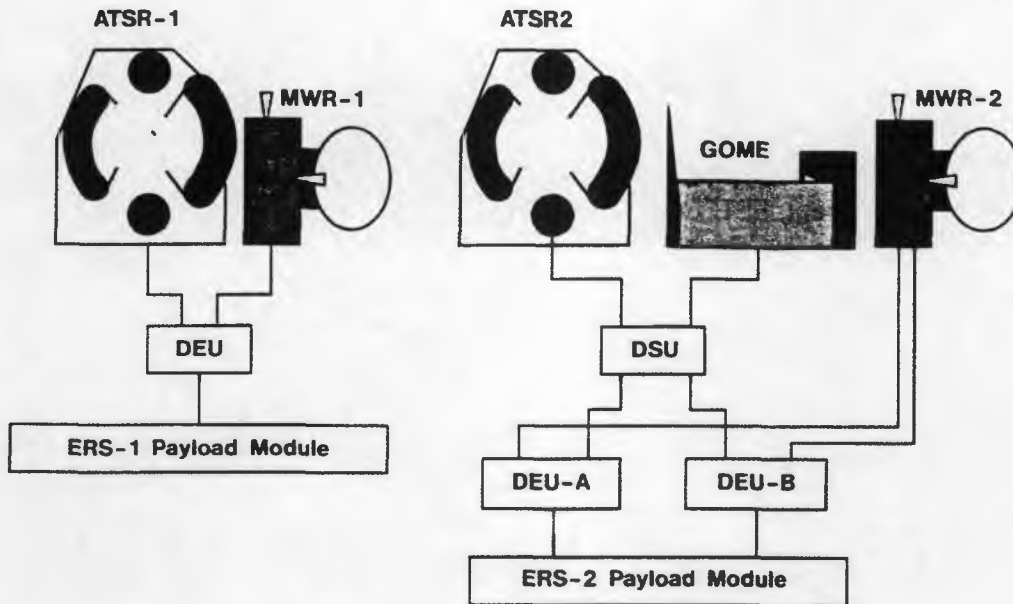
the periods when other payload instruments are not making full use of the X-band data capacity.

The possibility with the original ATSR of choosing between eight fixed pixel-selection maps is replaced for ATSR-2 by a facility for uploading different pixel formatting maps from the ground, thereby providing greater operational flexibility. Two pixel maps can be loaded at any given time, which allows two different maps to be used during an orbit, for example one over the sea and a different one over land. It also allows swath-width modulation and a reduction in the number of detector



**Figure 8. ATSR-2 view of the Gulf Stream, which gives Europe its temperate climate, acquired on 16 May 1995. It shows the eastern seaboard of North America, stretching from New York (at the top) to Charleston, South Carolina (at the bottom). Off the coast is the warm Gulf Stream (in red), which comes up from the south and meets the cold Labrador current off Cape Hatteras. The sometimes quite wide transition zones stand out very clearly, as do the swirling eddies and broken-up currents that occur further on. The varying colours of the clouds near the top and bottom edges of the picture are also due to temperature differences**

Figure 9. Schematic of the configurations of the IRR, MWR and DEU aboard ERS-1 and ERS-2



channels to be traded-off against better resolution in the remaining channels in low-data-rate mode.

Major mechanical modifications were made to the ATSR-2 Infrared Radiometer. The carbon-fibre structure has been substantially re-designed, the vestigial ATSR-1 optical bench has been removed, and all optical elements are now mounted directly onto the structure.

With the addition of the Global Ozone Monitoring Experiment (GOME) for the ERS-2 mission, and the need to interface this experiment to the satellite via the ATSR-2's Digital Electronics Unit (DEU), it became important to add more redundancy to the latter as it now interfaces with the IRR, the MWR and GOME. A second identical DEU was therefore added to the payload module, together with a DEU Switching Unit (DSU in Fig. 9).

### The ATSR products

The main application objectives for the original ATSR instrument aboard ERS-1 are:

- sea-surface temperature measurements
- cloud and atmospheric measurements
- lake measurements
- sea-ice measurements
- land-ice measurements
- deforestation measurements
- forest-fire detection.

With the new features that have been incorporated into the ATSR-2 instrument carried by ERS-2, the following additional objectives are being addressed:

- combined visible/infrared remote-sensing of vegetation in both the nadir- and along-track viewing directions
- improved spatial resolution and coverage in high-data-rate modes, when the Active Microwave Instrument (AMI) is in low-data-rate mode
- quantitative vegetation measurements, using the 0.65 and 0.85 micron channels
- leaf-moisture measurements, using the 0.85 and 1.6 micron channels
- vegetation state (growth stage and health) measurements, using all three visible channels.

